



Universität
Bremen

Kumulative Dissertation zur Erlangung des akademischen Grades eines Doktors
der Naturwissenschaften: Doctor rerum naturalium

– Dr. rer. nat. –

An dem Fachbereich für Geowissenschaften der Universität Bremen

**The response of calcareous nannofossils to carbon cycle
perturbations during the early Eocene**

Vorgelegt von: Bryan Niederbockstruck

Gutachter: Prof. Dr. Heiko Pälike und Prof. Dr. Blanca Ausín

Bremen, 26.06.2024

Versicherung an Eides Statt / *Affirmation in lieu of an oath*

gem. § 5 Abs. 5 der Promotionsordnung vom 28.04.2021 /
according to § 5 (5) of the Doctoral Degree Rules and Regulations of 28 April, 2021

Ich / I, Bryan Niederbockstruck

(Vorname / *First Name*, Name / *Name*, Anschrift / *Address*, ggf. Matr.-Nr. / *student ID no.*, if applicable)

versichere an Eides Statt durch meine Unterschrift, dass ich die vorliegende Dissertation selbständig und ohne fremde Hilfe angefertigt und alle Stellen, die ich wörtlich dem Sinne nach aus Veröffentlichungen entnommen habe, als solche kenntlich gemacht habe, mich auch keiner anderen als der angegebenen Literatur oder sonstiger Hilfsmittel bedient habe und die zu Prüfungszwecken beigelegte elektronische Version (PDF) der Dissertation mit der abgegebenen gedruckten Version identisch ist. / *With my signature I affirm in lieu of an oath that I prepared the submitted dissertation independently and without illicit assistance from third parties, that I appropriately referenced any text or content from other sources, that I used only literature and resources listed in the dissertation, and that the electronic (PDF) and printed versions of the dissertation are identical.*

Ich versichere an Eides Statt, dass ich die vorgenannten Angaben nach bestem Wissen und Gewissen gemacht habe und dass die Angaben der Wahrheit entsprechen und ich nichts verschwiegen habe. / *I affirm in lieu of an oath that the information provided herein to the best of my knowledge is true and complete.*

Die Strafbarkeit einer falschen eidesstattlichen Versicherung ist mir bekannt, namentlich die Strafandrohung gemäß § 156 StGB bis zu drei Jahren Freiheitsstrafe oder Geldstrafe bei vorsätzlicher Begehung der Tat bzw. gemäß § 161 Abs. 1 StGB bis zu einem Jahr Freiheitsstrafe oder Geldstrafe bei fahrlässiger Begehung. / *I am aware that a false affidavit is a criminal offence which is punishable by law in accordance with § 156 of the German Criminal Code (StGB) with up to three years imprisonment or a fine in case of intention, or in accordance with § 161 (1) of the German Criminal Code with up to one year imprisonment or a fine in case of negligence.*

Bremen, 26.06.2024

Ort / *Place*, Datum / *Date*

Unterschrift / *Signature*

Acknowledgements

Firstly, I would like to express my deepest gratitude to my supervisors, Ulla Röhl and Heiko Pälike. Your guidance allowed me to delve into Earth's history and explore the world of millions and millions of years ago. Thank you for your patience, especially during my first year when Covid-19 made an already challenging journey even more difficult. I am also grateful to Heather L. Jones for her huge support and assistance with all my tasks and challenges that I had to face. Additionally, I extend my thanks to all my co-authors for the enriching discussions and valuable contributions.

I extend my sincere thanks to Nele, who always made time for me, particularly during the first half of this journey. Your lovely handmade espresso mug became a symbol of my concentration and focus. A heartfelt thank you goes to the GeoKids for our classic 11 o'clock coffee meetings and the enjoyable chats about everything. Special thanks to Heather Johnstone, Maria, Luz Ma, and Nina Wichern for their friendship and support. I want to thank Jing for her endless support and love during all kinds of situations. Your company made every day brighter.

I am deeply grateful to Holger and Alex for sharing over 600 lunch breaks (and possibly more) with me over the past three years. I also want to thank my office mates, Nina Rohlf and Dominik Hülse, for their support and positivity when I faced struggles.

Thanks should also go to Chris, who dragged me away from my desk for several invigorating rides with our road bikes into the Blockland. Your enthusiasm helped me clear my mind and stay physically active. Special thanks to Dominik Nommensen, my former classmate during both my Bachelor's and Master's studies. You have always been a source of mental support, and I could always count on you.

A heartfelt thank you goes to all my friends outside of academia, who always kept an eye on me and reminded me to enjoy life amidst the demands of research.

I would also like to extend my gratitude to GLOMAR, not only for their invaluable training courses but even more for their support, their willingness to help doctoral candidates whenever possible, and for organizing the wonderful PhD days every year. Special thanks to Dierk, Tina, and Vivien for your dedication and hard work.

Final thanks go to my parents, who have always been unwavering in their support and encouragement. Your belief in me has been a constant source of strength.

Abstract

In view of the ongoing anthropogenic climate change and the resulting environmental changes, investigations that provide insight from the geological past regarding rapid warming can help us understand the potential consequences we may face in the near future. One such time interval is the early Eocene (ca. 56 to 49 Ma), when the Earth experienced conditions of extreme global warmth and elevated atmospheric carbon dioxide concentrations. These events are known as hyperthermals.

A common way to study the geological past is by investigating marine sediments, which serve as archives storing environmental changes throughout history. In 2020, the International Ocean Discovery Program Expedition 378 recovered Paleogene sediments at the Southern Campbell Plateau, south of New Zealand. To learn from the Earth's history, it is crucial to understand the duration and timing of extreme events recorded in these sediments. In the first part, I constructed a high-resolution age model that allows to track these warming events. By using a multi-proxy approach, I found a diachroneity of calcareous nannofossil datums, which are commonly used for early Eocene biostratigraphy. I emphasize the need to determine whether the diachroneity is a unique feature of the study site or a characteristic of early Paleogene high-latitude sites.

Calcareous nannoplankton contribute to carbon sequestration and form the base of the food web, making them a valuable component of the ecosystem. To determine if these organisms are affected by drastic climate changes, the second part focused on the composition of the assemblage during specific warming events. The investigation shows a response of the calcareous nannoplankton community linked to transient warming events. Additionally, I observed that the major assemblage change occurred around 120 kyr before the onset of the Early Eocene Climatic Optimum (EECO), a 4-million-year interval during which Earth's temperature was the highest in the Cenozoic.

Geochemical records prove that the climate recovered from the hyperthermals, pointing to a negative feedback mechanism in response to global warming. Potential mechanisms include silicate weathering and enhanced marine productivity, which are thought to consume CO₂ from the atmosphere and transport it to the seafloor, resulting in a cooling effect. Enhanced silica content for such events, which could be linked to hyperthermals, has so far only been found in the Atlantic Ocean. In the third part, I present evidence of enhanced silica content in South Pacific sediments coinciding with hyperthermals, pointing to a potentially global phenomenon.

Table of Content

Acknowledgements	I
Abstract	III
1. Introduction.....	1
1.1 Background and motivation	1
1.2 Study Site and oceanographic setting	3
2. Overview of the manuscripts	6
3. Methods	7
3.1. Stable carbon and oxygen isotope records	7
3.2. Calcareous nannofossil assemblage and biostratigraphy	7
3.3. Opal concentration.....	8
4. Author's contribution.....	8
5 Part I: Apparent Diachroneity of Calcareous Nannofossil Datums During the Early Eocene in the High-Latitude South Pacific Ocean	11
Abstract	11
5.1. Introduction.....	11
5.2. Materials and Methods	12
5.2.1. Site Location	12
5.2.2. Core Images and XRF Data	13
5.2.3. Stable Isotope Analyses.....	14
5.2.4. Calcareous Nannoplankton Biostratigraphy	14
5.2.5. Age Model	14
5.3. Results	15
5.3.1. Core Images and Geochemical Results.....	15
5.3.2. Biostratigraphy	15
5.4. Discussion	18
5.4.1. Correlation of Chemostratigraphic Data	18
5.4.2. Age Model Construction.....	19
5.4.3. Diachroneity of Early Eocene Calcareous Nannofossil Events in the High Latitude Southern Hemisphere	24
5.5. Conclusions.....	26
5.6. Data Availability Statement.....	26
5.7. References.....	26
6. Part II: Calcareous nannoplankton responded to short- and long-term warming during the early Eocene in the South Pacific	33
Abstract	33
6.1. Introduction.....	33

6.2. Environmental preferences of calcareous nannofossil genera	36
6.3 Material and Method	36
6.3.1. Study Site.....	36
6.3.2 Nannofossil assemblage counts	38
6.3.3. Statistical analyses.....	38
6.4. Results	39
6.4.1. Hierarchical Clustering	39
6.4.2 Principle Component Analyses.....	41
6.5. Discussion	44
6.5.1. Hyperthermals I1 and I2.....	46
6.5.2. Major shift in calcareous nannofossil assemblage and the onset of the EECO	46
6.5.3. Changing conditions is response to the K event in the Southwest Pacific.....	48
6.6. Conclusion	52
6.7. Acknowledgements.....	52
6.8. Data availability	52
6.9. References.....	53
7. Part III: Enhanced silica burial in the South Pacific during early Eocene warming events.....	63
Abstract	63
7.1. Introduction.....	63
7.2. Material and Methods.....	66
7.2.1. Material and Study Site	66
7.2.2. Opal measurement.....	67
7.2.3. High-resolution paleoproductivity record.....	67
7.2.4. Statistical analyses.....	68
7.3. Results	69
7.4. Discussion.....	72
7.4.1. The occurrence of siliceous horizons in early Eocene sediments	72
7.4.2. Astronomically paced silica productivity during hothouse climate?	74
7.5. Conclusion	78
7.6. Acknowledgements.....	78
7.7. Data availability	79
7.8. References.....	79
7.7. Supplemental material	89
8. Synthesis.....	92
9. Outlook.....	93
10. References.....	95

1. Introduction

1.1 Background and motivation

In recent decades, the Earth has experienced a significant increase in global temperatures, primarily attributed to anthropogenic activities, particularly the emission of carbon dioxide (CO₂). Before the industrial revolution in 1750, CO₂ concentration was around 270 ppm (Rubino et al., 2019) and has been rising since then, exceeding a mean of 420 ppm in the year 2023 (Keeling et al., 2001). This rapid increase is pushing the climate to warming conditions at a speed unprecedented in Earth's history. Under the "business as usual" scenario, the representative concentration pathway 8.5 (RCP8.5) model simulations predict CO₂ concentrations between 795 and 1145 ppm by the end of the century (Friedlingstein et al., 2014). Consequences of rising temperatures include sea level rise, intensification of weather phenomena, and deoxygenation of the oceans. Although the current climate change might be unique in its speed, the Earth's climate holds lessons from the geological past that can inform us about the potential consequences of rapid global warming. A time interval in the past when Earth experienced similarly high atmospheric CO₂ concentrations, comparable to the predicted scenarios, was the early Eocene (Burke et al., 2018; Tierney et al., 2020; Westerhold et al., 2020).

During the early Eocene (56–48 Ma), the Earth faced its warmest conditions of the entire Cenozoic (66–0 Ma) with the absence of permanent ice sheets (Zachos et al., 2001). The climate of the early Eocene was punctuated by several transient warming events, called hyperthermals. These hyperthermals were caused by carbon perturbations, with an excess of light carbon (¹²C) entering the oceanic-atmospheric system, lasting less than 100 kyr. The most significant and well-known of these events is the Paleocene-Eocene Thermal Maximum (PETM), first identified by a coupled decrease in δ¹³C and δ¹⁸O in foraminifera tests (Kennett and Stott, 1991). Many other hyperthermals have been identified in sediments from outcrop sections and deep-sea drilled cores (e.g., Cramer et al., 2003; Agnini et al., 2009; Galeotti et al., 2010; Kirtland Turner et al., 2014; Lauretano et al., 2015). Additionally, a long-term warming of approximately 4 million years occurred during the early Eocene, known as the Early Eocene Climate Optimum (EECO; 53.26 to 49.14 Ma; Westerhold et al., 2017). The climate of the early Eocene was characterized by high atmospheric CO₂ concentrations (Hönisch et al., 2012; Anagnostou et al., 2016, 2020). Model results indicate that mean surface temperatures during the EECO were approximately 14° ± 3°C warmer than pre-industrial times (Caballero & Huber, 2013), with the PETM at 31.6°C (27.2° to 34.5°C) and the EECO at 27.0°C (23.2° to 29.7°C), respectively (Inglis et al., 2020). Sea surface temperatures and deep-sea temperatures increased in parallel during both short-term hyperthermals and the long-term trend of the EECO, with greenhouse gas forcing thought to be the main driver of the warming (Anagnostou et al., 2016; Cramwinckel et al., 2018). Therefore, the early Eocene is one of the most promising time intervals to study concerning ongoing anthropogenic CO₂

emissions and their potential consequences for the future climate. Studying the hyperthermals allows us to understand how climate responds over timescales of 100-10,000 years following a massive injection of carbon into the atmosphere (Zachos et al., 2008) and the EECO providing insights into long-term climate change beyond orbital cycles.

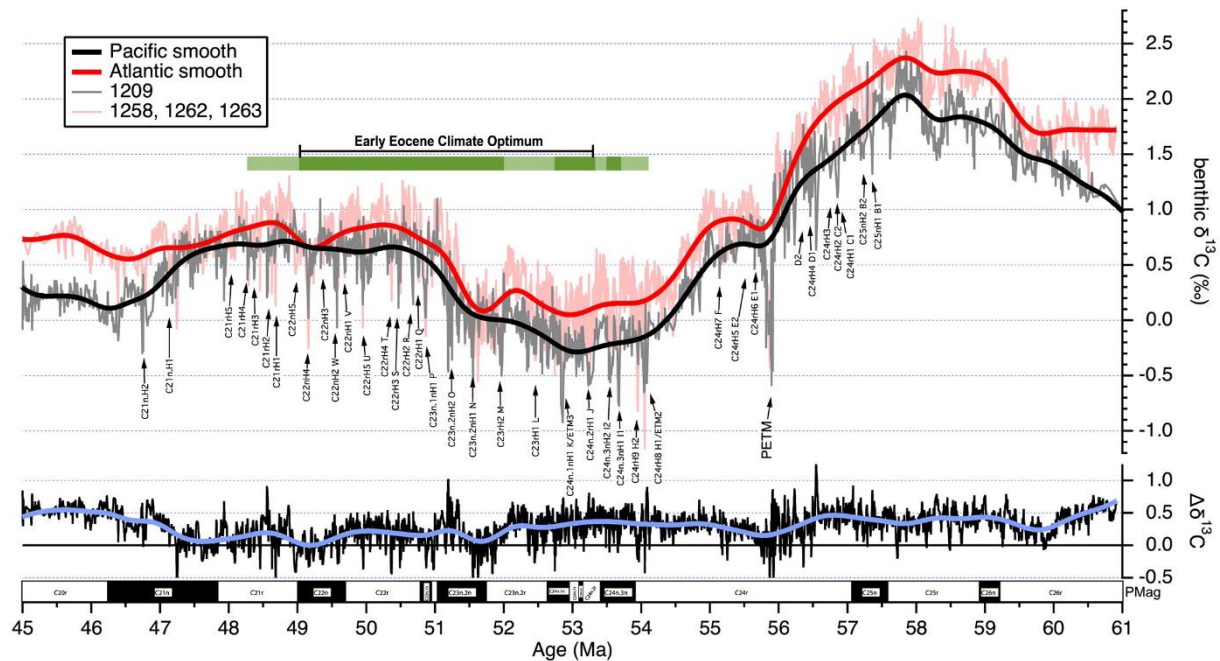


Figure 1.1. Benthic foraminifera $\delta^{13}\text{C}$ showing late Paleocene and early Eocene hyperthermals, taken from Westerhold et al. (2018). With hyperthermals labels from A-L (Cramer et al., 2003) and M-W (Lauretano et al., 2016). The magnetostratigraphy from form Atlantic sites are from Westerhold et al. (2008, 2017).

Recent satellite observations and paleoceanographic reconstructions show that high-latitude regions are particularly sensitive to climate perturbations, exhibiting elevated temperature rises compared to low- and mid-latitude areas (Holland & Bitz, 2003; Serreze et al., 2009; Taylor et al., 2013; Ito et al, 2020). With Site U1553, being even further south in the early Eocene, the sediment record provides a unique opportunity to study past oceanographic and climatic changes in response to warming events in high-latitude areas.

One key role in regulating the climate is hold by the marine phytoplankton. They are considered to contribute to more than half of atmospheric oxygen via photosynthesis (Falkowski et al., 1998; Sengupta et al., 2017). Equally important is their ability to sequester carbon from the atmosphere into their organic, thereby acting as a net CO_2 sink. When the remains sink to the ocean floor, carbon is transported out of the atmospheric-oceanic system which can act as a negative feedback to rising CO_2 levels and global warming. Among the phytoplankton, calcareous nanoplankton are of particular interest in paleoceanographic studies. Their fossils are commonly used for Paleogene biostratigraphy on sediment records (e.g., Aubry, 1986; Raffi et al., 2005; Agnini et al., 2006; Toffanin et al., 2013),

mostly following established biozonations (Martini 1971; Bukry, 1973; Agnini et al., 2014). Their organic and inorganic remains contain biogeochemical signals that allow the reconstruction of sea surface temperature (Brassel et al., 1986; Prahel and Wakeham 1987; Müller et al., 1998), that has been applied for the Paleogene (Bijl et al., 2010; Guitán and Stoll, 2021), productivity (Dedert et al., 2012) and atmospheric CO₂ concentration (Pagani, 2002; Zhang et al., 2013).

1.2 Study Site and oceanographic setting

Paleoceanographic and paleoclimatic conditions are stored in multiple ways in sedimentary archives which can be found as outcrops on land, or sediment cores that are recovered from drilling into the seafloor. In order to learn about the conditions of warming events from the early Eocene, I here make use of such an archive in the form of sediment cores that were recovered during the International Ocean Drilling Program (IODP) 378. Scientist set sail to the South Pacific on the research vessel *JOIDES Resolution* in the early 2020 to decipher oceanographic and climatic changes during intervals of chemical perturbations of the Paleogene. On the Southern Campbell Plateau, south of New Zealand, Site U1553 (-52.2240°N, 166.1916°E) (Röhl et al., 2022) was drilled in multiple holes and recovered Paleogene sediments, especially a nearly continuous record of the targeting interval for this thesis: the late Paleocene to early Eocene. Site U1553 was drilled next to legacy Deep Sea Drilling Project (DSDP) Site 277, where the first Cenozoic carbon and oxygen isotope composition were obtained by the work of Shackleton and Kennet (1975). However, DSDP Site 277 was drilled in a single, spot-cored hole, and does not provide a continuous archive of the Paleogene. The sedimentary archive of Site U1553 will build up on this work, expands and complete the findings of previous works.

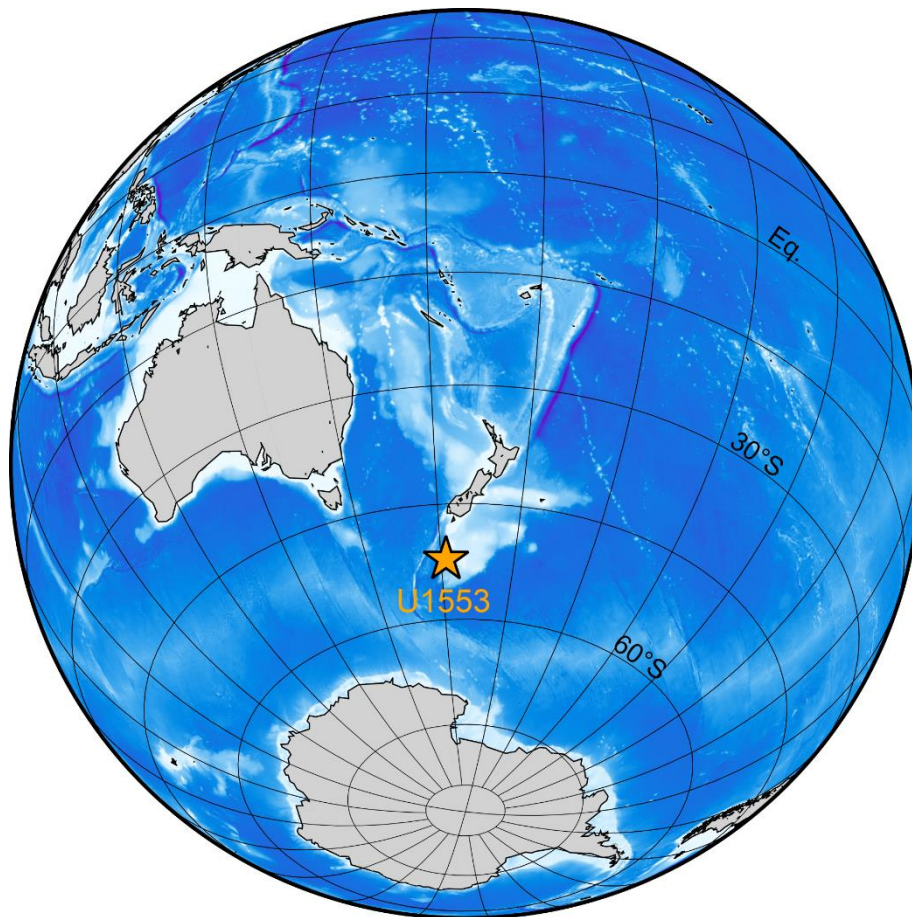


Figure 1.2. Location of International Ocean Drilling Program Site U1553 at the southern Campbell Plateau, south of New Zealand (orange star). The map was generated using software *The Generic Mapping Tools* (Wessel et al., 2019).

In the modern setting, the area around the southern Campbell Plateau is characterized by several constricted zones of three oceanic fronts between 40°S and 60°S: the Subtropical Front, the Subantarctic Front, and the Antarctic Front, which separate different water masses in between (Figure 3). A very strong oceanic front is the Subtropical Front, which crosses the Southern Campbell Plateau and separates the subtropical and subantarctic water masses with a sharp change in temperature of 4-5°C and salinity of 0.5 psu (Deacon, 1982; Carter et al., 2008). The Subantarctic Front separates the subantarctic surface water from the circumpolar surface water, the latter being characterized by a complex mixing with nearby water masses, typically with temperatures of 3-8°C and salinity of 34-34.4 psu (Carter et al., 2008). South of the Antarctic Polar Front, the Antarctic Surface Waters thrive between 50°S and 60°S, with temperatures typically below 0°C (Carter et al., 2008).

During the early Eocene, the palaeoceanographic setting of the Southwest Pacific differed significantly from today. The Tasmanian Gateway and Drake Passage were nearly closed, preventing the formation of a circumpolar current. The nature of the existing currents at that time remains a subject of debate (Huber et al., 2004). Characteristic oceanic fronts had not yet been established (Nelson and Cooke, 2001). There is no evidence of colder, northward-flowing Antarctic waters at the Southern Campbell

Plateau until the late Eocene, when a circumpolar current had become established (Nelson and Cooke, 2001). However, Jenkins (1993) suggested the presence of a transition zone from warm to cool subtropical waters, supported by fossil evidence (Hornibrook, 1992).

During the EECO, sea surface temperatures in the Southwest Pacific are thought to have exceeded 25°C based on planktic foraminifera Mg/Ca (Hines et al., 2017), and may have reached up to 34°C based on TEX86 data from the East Tasman Plateau (Bijl et al., 2009).

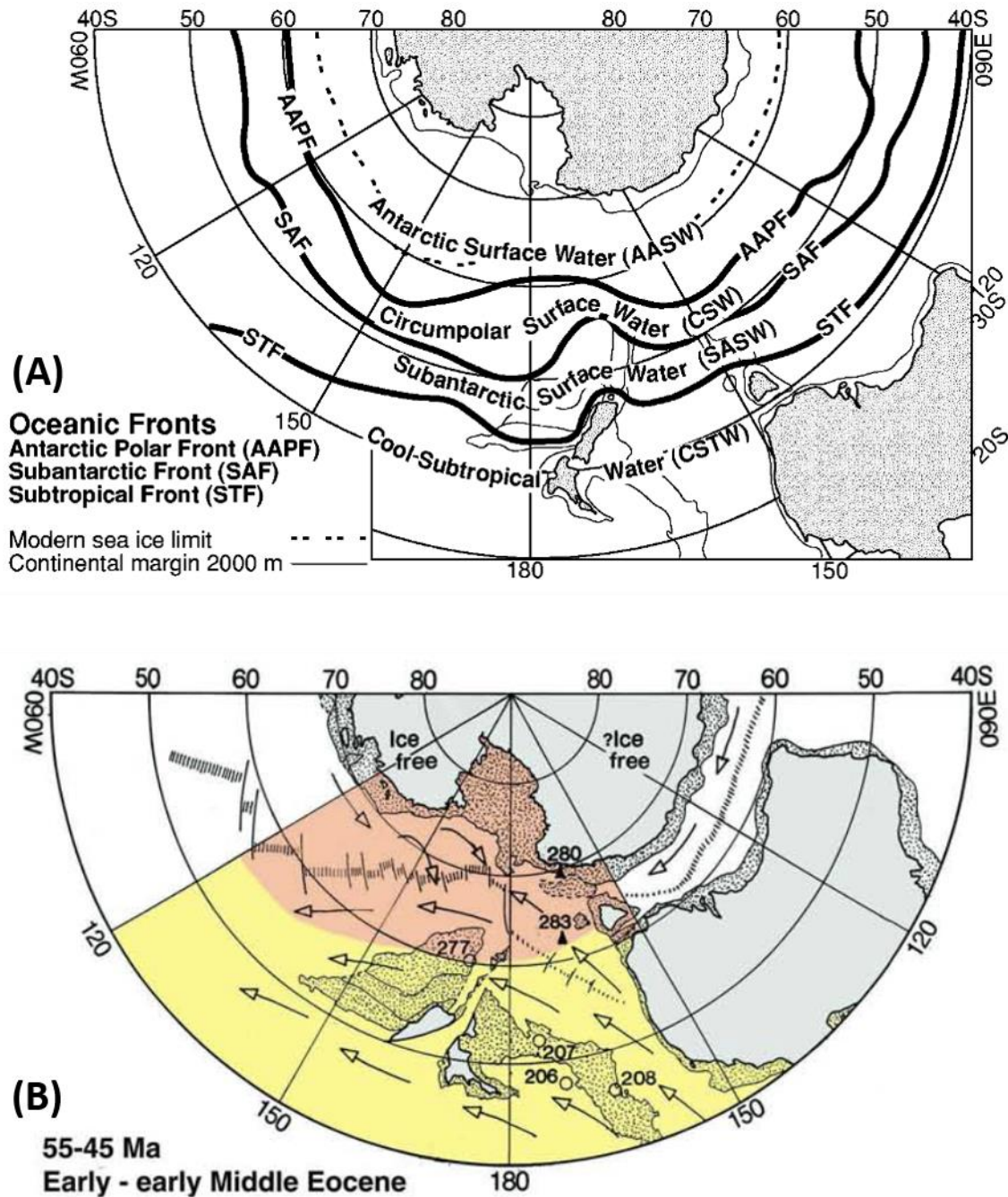


Figure 1.3. Modern and paleoceanographic map of the study area taken from Nelson and Cooke (2001). (a) The modern oceanic fronts adapted from Belkin & Gordon (1996). (b) Paleogeographic reconstruction adapted from Lawver et al. (1992). Yellow area: Warm subtropical water masses. Orange area: cool subtropical water masses. The numbers represent the Sites of the Deep Sea

Drilling Project, with DSDP Site 277 also marking the location of IODP Site U1553. Arrows indicate ocean surface currents. No oceanic fronts were suspected.

This thesis aims to shed light on the response of calcareous nannoplankton to the rapid release of CO₂ into the oceanic-atmospheric system and to examine how overall marine productivity and its potential ability to sequester CO₂ plays a role in regulating the climate during extreme warming events. To achieve these goals, the thesis will utilize the nearly continuous late Paleocene to early Eocene sediment record, which provides a new high-latitude archive of the Paleogene.

2. Overview of the manuscripts

Part I:

To evaluate any chemical and biotic responses to perturbations in the carbon cycle during the early Eocene, it is crucial to first identify these events and place them in the correct chronological order. Therefore, I refined the shipboard age model (Röhl et al., 2022) to achieve the temporal resolution necessary to identify hyperthermals in **Chapter 5**. Here, I employ a correlation of carbon stable isotope record from Site U1553 with astronomically tuned carbon stable isotope records from the Atlantic. The change in atmospheric CO₂ represents a global signal, expected to be consistent across different ocean basins and latitudes. Indeed, bulk sediment $\delta^{13}\text{C}$ and benthic foraminifera $\delta^{13}\text{C}$ records have been correlated from sediment records across the oceans. Moreover, since hyperthermals are characterized by a rapid increase in ^{12}C , a $\delta^{13}\text{C}$ -record allows not only for a high-resolution, globally applicable age model but also for the direct identification of hyperthermals. Due to the exceptional good recovery of rotary drilled sediments at Site U1553, I hypothesize that the record provides a valuable opportunity to study perturbations in the carbon cycle through the latest Paleocene and early Eocene.

This chapter got published in April 2024:

Niederbockstruck, B., Jones, H. L., Yasukawa, K., Raffi, I., Tanaka, E., Westerhold, T., Ikehara, M., & Röhl, U. (2024). Apparent Diachroneity of Calcareous Nannofossil Datums During the Early Eocene in the High-Latitude South Pacific Ocean. *Paleoceanography and Paleoclimatology*, 39(4), e2023PA004801. <https://doi.org/https://doi.org/10.1029/2023PA004801>

For the purpose of this dissertation, the paper is edited to follow the order of chapters.

Part II:

The response of calcareous nannoplankton to hyperthermals events has been mainly focused on the PETM (Bralower, 2002; Gibbs et al., 2006; Mutterlose et al., 2007; Raffi et al., 2008; Bown and Pearson, 2009; Jiang and Wise, 2009; Self-Trail et al., 2012; Schneider et al., 2013; Wang et al., 2022), and ETM2 (Dedert et al., 2012; Gibbs et al., 2012; D'Onofrio et al., 2016; Lei et al., 2016). However, the sensitivity of calcareous nannoplankton to climate perturbation remains under debate (Gibbs et al., 2006; Newsam et al., 2017). In order to better understand the response of calcareous nannoplankton

community to carbon perturbations, I investigated the assemblage in **Chapter 6** during hyperthermals of different magnitudes. I hypothesize that the nannoplankton community responded to hyperthermals. However, due to the generally extreme warm climate of the Eocene the main driver that causing changes in the nannoplankton community might not be temperature alone.

Part III:

Negative feedback mechanisms to rising atmospheric CO₂ include chemical weathering and marine carbon burial. Evidence for these feedbacks has been found in Atlantic sediments, where siliceous facies are attributed to hyperthermals, which have not been observed in other oceans (Penman et al., 2019). Since increased CO₂ emissions and warming should affect the Earth globally, particularly at high latitudes, I hypothesize that signals of chemical weathering and enhanced marine productivity are likely preserved in the sediment archives at IODP Site U1553. In **Chapter 7**, I examine geochemical data and line-scanned core images to identify silica-enriched sediments at Site U1553 and discuss the possible association to hyperthermals.

3. Methods

3.1. Stable carbon and oxygen isotope records

For stable oxygen and carbon isotopes on bulk sediment, samples were dried and grounded by hand with an agate mortar and pestle. The prepared samples were stored in labeled, transparent 1.5 mL centrifuge tubes. Analyses were conducted at the MARUM - Center for Marine Environmental Sciences, University of Bremen, utilizing a Finnigan 253plus gas isotope ratio mass spectrometer equipped with a Kiel IV automated carbonate preparation device. The laboratory staff, led by Dr. Henning Kuhnert, performed the stable isotope analyses. Data are presented in the conventional delta-notation ($\delta^{13}\text{C}$ and $\delta^{18}\text{O}$). relative to Vienna Peedee Belemnite (V-PDB). The instrument calibration was performed using the house standard (ground Solnhofen limestone), which was previously calibrated against NBS 19 calcite. The data was calculated as:

$\delta = (R_{\text{sample}}/R_{\text{standard}} - 1) * 1000$, with:

- $R = {}^{13}\text{C}/{}^{12}\text{C}$ for $\delta^{13}\text{C}$
- $R = {}^{18}\text{O}/{}^{16}\text{O}$ for $\delta^{18}\text{O}$.

3.2. Calcareous nannofossil assemblage and biostratigraphy

Analyses were done using a light microscope with 1200x magnification under transmitted and crossed-polarized light. Smear slides for microscopic analyses were prepared following the guidelines of Marsaglia et al. (2015): Glass slides were labeled with the Sample-ID on one side and pre-heated on a hotplate at moderate heat. A coverslip was moistened using a few drops of distilled water from a

pipette. Sediment of the sampling interval was picked on the top end of a wooden toothpick. In the next step, the sediment on the toothpick was placed on the coverslip to dilute the sediment and spread the slurry sediment on the coverslip. In the next step, the coverslip was placed with the slurry sediment facing upwards on the hot plate to dry. Then a few drops of an adhesive oil were placed on the labeled glass slide and the dried coverslip was carefully placed with the sediment on the oil of the glass slide. The air will be removed within seconds between the glass slide and the coverslip. Once the air has escaped the slides were placed for 10 min under UV light to cure the adhesive oil.

The calcareous nannofossil datums used for biostratigraphy, the species were identified using the taxonomic concepts of the online database Nannotax3 (<https://www.mikrotax.org/Nannotax3/>), and their occurrences were determined by counting the number of the respective specimens in a prefixed area (N/mm^2) (Backman & Shackleton, 1983). For the calcareous nannofossil assemblage analysis, 400 specimens per sample were counted and identified to the species level.

3.3. Opal concentration

For the determination of opal content in sediment samples, the automated leaching method of Müller and Schneider (1993) was employed. This method involves the extraction of biogenic silica (opal) using a 1 M NaOH solution at 85°C. The extraction is conducted in a stainless-steel vessel with constant stirring to ensure uniform temperature and effective leaching. This method has been validated on various biogenic silica sources including sponge spicules, radiolarian tests, and diatomaceous ooze, ensuring comprehensive recovery of biogenic opal in sediments. The process compensates for silica co-extracted from alumino-silicates using the applied extrapolation technique, maintaining a measurement uncertainty within ± 0.4 weight (wt) % SiO_2 , depending on the clay mineral composition and content. The laboratory staff, led by Dr. Oscar Romero and Marco Klann, performed the analyses.

4. Author's contribution

Part I (Chapter 5): For the first study, I wrote the drafts and created the figures. Isabella Raffi performed the biostratigraphy. Ulla Röhl grounded the samples for stable isotope analyses by hand with an agate mortar and pestle, before they were analyzed in the MARUM laboratories, led by Henning Kuhnert and his team. A second, independent set of stable isotope data were prepared and analyzed by Erika Tanaka, Kazutaka Yasukawa, Minoru Ikehara and the laboratory team of the Marine Core Research Institute, Kochi University. Thomas Westerhold helped in developing the age model. All co-authors contributed to the interpretation of the results, contributed to the discussions and reviewed the final draft version. The review process throughout the draft versions were especially guided by Heather L. Jones and Ulla Röhl.

Part II (Chapter 6): For the second study, I counted at least 400 specimens of calcareous nannofossils in 71 samples using an Olympus BX51 microscope. The smear slides were prepared by Heather L. Jones, who also taught me to identify calcareous nannofossils under plane and polarized light at the beginning of my doctoral studies. For the manuscript, I wrote the drafts, performed the calculations, and created the figures. Heather L. Jones and Ulla Röhl contributed to the interpretations of the results and reviewed the drafts.

Part III (Chapter 7): For the third study, opal measurements were conducted at the MARUM laboratories, led by Oscar Romero and his team. I wrote the drafts, performed the calculations, and created the figures. Heather L. Jones and Ulla Röhl contributed to the interpretation of the results and reviewed the drafts.

Paleoceanography and Paleoclimatology



RESEARCH ARTICLE

10.1029/2023PA004801

Special Section:

Illuminating a Warmer World:
Insights from the Paleogene

Key Points:

- A new chemostratigraphic age model (50.5–57.5 Ma) was developed for IODP Site U1553 in the high-latitude South Pacific Ocean
- Commonly used calcareous nannofossil datums show significant offsets at Site U1553 compared to records from lower latitude regions
- This study highlights the need to revise early Eocene calcareous nannofossil biostratigraphic datums to be applicable to high-latitude sites

Supporting Information:

Supporting Information may be found in the online version of this article.

Correspondence to:

B. Niederbockstruck,
bniederbockstruck@marum.de

Citation:

Niederbockstruck, B., Jones, H. L., Yasukawa, K., Raffi, I., Tanaka, E., Westerhold, T., et al. (2024). Apparent diachroneity of calcareous nannofossil datums during the early Eocene in the high-latitude South Pacific Ocean.

Paleoceanography and Paleoclimatology, 39, e2023PA004801. <https://doi.org/10.1029/2023PA004801>






Received 3 NOV 2023

Accepted 2 APR 2024

© 2024. The Authors.

This is an open access article under the terms of the [Creative Commons Attribution License](https://creativecommons.org/licenses/by/4.0/), which permits use, distribution and reproduction in any medium, provided the original work is properly cited.

5. Part I: Apparent Diachroneity of Calcareous Nannofossil Datums During the Early Eocene in the High-Latitude South Pacific Ocean

B. Niederbockstruck¹ , H. L. Jones¹, K. Yasukawa^{2,3} , I. Raffi⁴, E. Tanaka^{5,6}, T. Westerhold¹ , M. Ikehara⁵ , and U. Röhl¹ 

¹MARUM - Center for Marine Environmental Sciences, University of Bremen, Bremen, Germany, ²Frontier Research Center for Energy and Resources, School of Engineering, The University of Tokyo, Tokyo, Japan, ³Department of Systems Innovation, School of Engineering, The University of Tokyo, Tokyo, Japan, ⁴International Research School of Planetary Sciences (IRSPS), Università degli Studi “G. d’Annunzio” di Chieti-Pescara, Pescara, Italy, ⁵Marine Core Research Institute, Kochi University, Kochi, India, ⁶Ocean Resources Research Center for Next Generation, Chiba Institute of Technology, Chiba, Japan

Abstract The late Paleocene to early Eocene interval is characterized by a series of carbon perturbations that caused transient warming (hyperthermal) events, of which the Paleocene-Eocene Thermal Maximum (PETM) was the largest. These hyperthermals can be recognized in the pelagic sedimentary record as paired negative $\delta^{13}\text{C}$ and $\delta^{18}\text{O}$ excursions, in addition to decreased calcium carbonate and increased iron content caused by carbonate dissolution. However, current data are predominantly sourced from the equatorial-to subequatorial regions. Here we present a new high-latitude late Paleocene—early Eocene record, recovered during International Ocean Discovery Program (IODP) Expedition 378 on the Campbell Plateau off New Zealand, in the southwest Pacific Ocean. To construct an age model, we correlated our chemostratigraphic and biostratigraphic data to existing astronomically-tuned age models from Walvis Ridge (South Atlantic Ocean) and Demerara Rise (equatorial Atlantic Ocean). Our results indicate that the Site U1553 composite section spans ~ 7 million years of the latest Paleocene to early Eocene (50.5–57.5 Ma), and preserves many of the early Eocene hyperthermals; including a PETM interval that is more expanded than elsewhere in this region. However, construction of the age model also revealed discrepancies between the chemostratigraphic and biostratigraphic tie points used for correlation. This is likely due to latitudinal diachroneity in the calcareous nannofossil biostratigraphic datums, which are primarily based on low-to mid-latitude assemblages. Therefore, our study highlights the need to establish a revised calcareous nannofossil biozonation that is more appropriate for high-latitude age models.

5.1. Introduction

The early Eocene hothouse (ca. 47 to 56 Ma; Westerhold et al., 2020) was the warmest interval in the Cenozoic, with atmospheric carbon dioxide (CO_2) concentrations >800 ppmv providing highly valuable information about climate sensitivity (i.e., the extent to which CO_2 emissions have an impact on temperature change; e.g., Anagnostou et al., 2020, 2016; Burke et al., 2018; Hönisch et al., 2012). Numerous temperature proxy records and modeling approaches (Cramwinckel et al., 2018; Farnsworth et al., 2019; Inglis et al., 2020; Lunt et al., 2021; Sluijs et al., 2020) indicate that a general global warming trend during the early Eocene and the preceding latest Paleocene was punctuated by a series of transient warming episodes known as hyperthermals (Thomas et al., 2000; Zachos et al., 2010). The most pronounced and best-studied of these warming events—the Paleocene-Eocene Thermal Maximum (PETM); ca. 56 Ma—was first identified by a coupled $\sim 2\%$ decrease in the $\delta^{13}\text{C}$ and $\delta^{18}\text{O}$ values of planktonic foraminifera tests at Ocean Drilling Program (ODP) Site 690 in the Southern Ocean (Kennett & Stott, 1991), and has since been recognized in hundreds of outcrop sections and deep-sea sediment cores worldwide (e.g., Arenillas et al., 1999; Bains et al., 1999; Bralower et al., 1997; Hancock et al., 2003; Kaiho et al., 1996; Koch et al., 1992; Schmitz et al., 1996; Westerhold, Röhl, Wilkens, et al., 2018; Yasukawa et al., 2017; Zachos et al., 2005). The characteristic negative shift in $\delta^{13}\text{C}$ during the PETM indicates a massive release of isotopically light carbon into the ocean-atmosphere system, causing enhanced warming that lasted approximately 170–200 kyrs (Murphy et al., 2010; Röhl et al., 2007; Westerhold, Röhl, Wilkens, et al., 2018; Zeebe & Lourens, 2019), as well as possible surface ocean acidification (Babila et al., 2018; Gutjahr et al., 2017; Harper et al., 2020; Penman et al., 2014). The exact source of this isotopically light carbon has been heavily

debated, with methane from destabilized gas hydrates (e.g., Bowen, 2013; DeConto et al., 2012; Dickens et al., 1995) and carbon dioxide from North Atlantic volcanism (Gutjahr et al., 2017; Svensen et al., 2004) both being suggested as viable possibilities. Due to its similarities with modern climate change, the PETM is considered an adequate (if imperfect) analog for future climate states, with the caveat that anthropogenic carbon emission rates are 10 times higher than during the onset of the PETM (Bowen et al., 2015; Frieling et al., 2016; Gingerich, 2019; Zeebe et al., 2009).

Since the discovery of the PETM, numerous studies have reported similar but less pronounced paired negative shifts in $\delta^{13}\text{C}$ and $\delta^{18}\text{O}$ during the late Paleocene and early Eocene in both outcrop sections (e.g., Agnini et al., 2009; Coccioni et al., 2012; Galeotti et al., 2010; Slotnick et al., 2015) and within deep sea sediment cores (e.g., Cramer et al., 2003; Kirtland Turner et al., 2014; Lauretano et al., 2015; Littler et al., 2014; Stap et al., 2010; Westerhold et al., 2007; Westerhold et al., 2017; Zachos et al., 2010). These hyperthermals have been labeled from A to L (Cramer et al., 2003) and M to W (Lauretano et al., 2016), and can also be recognized as peaks in X-Ray fluorescence (XRF)-derived iron intensity data caused by carbonate dissolution (e.g., Röhl et al., 2000, 2007; Westerhold, Röhl, Donner, & Zachos, 2018; Zachos et al., 2010). More recently, labels based on the position of these events relative to magnetostratigraphy have also been assigned (Kirtland Turner et al., 2014; Westerhold et al., 2017). Although these smaller hyperthermals are relatively understudied compared to the PETM, previous research indicates that significant paleoceanographic and paleoecological changes also occurred during these warming events (e.g., Agnini et al., 2016; D'Onofrio et al., 2016; Gibbs et al., 2012; Harper et al., 2020; Jennions et al., 2015; Luciani et al., 2016; Thomas et al., 2018), and therefore can provide valuable information as to how the earth-ocean system responds to different magnitudes of carbon perturbation. However, before such analyses can be conducted, it is essential to have a robust age model that can be reliably used to constrain the pacing and timing of such changes.

Currently, our best astronomically-calibrated Paleogene age models are restricted to low- and mid-latitude sites such as Demerara Rise (ODP Leg 207; equatorial Atlantic Ocean), Walvis Ridge (ODP Leg 208; mid-latitude South Atlantic Ocean), and Shatsky Rise (ODP Leg 198; subtropical Pacific Ocean) (e.g., Barnett et al., 2019; Littler et al., 2014; Röhl et al., 2007; Westerhold et al., 2017; Westerhold, Röhl, Donner, & Zachos, 2018; Westerhold et al., 2020; Zachos et al., 2010). In comparison, higher latitude early Paleogene age models are scarce, although do exist for Maud Rise in the Atlantic sector of the Southern Ocean (ODP Sites 689 and 690; Bains et al., 1999; Cramer et al., 2003; Kennett & Stott, 1991; Röhl et al., 2007; Thomas et al., 1990), for the Kerguelen Plateau (ODP Sites 738 and 1135; Jiang & Wise, 2009) and the Mantelle Basin (International Ocean Discovery Program (IODP) Site U1514; Vahlenkamp et al., 2020) in the southern Indian Ocean, and for the Campbell Plateau in the South Pacific Ocean (Deep Sea Drilling Program (DSDP) 277; Hollis, 1997; Hollis et al., 2015; Shepherd et al., 2021). However, almost all of these age models are based on $\delta^{13}\text{C}$ data combined with low-resolution, shipboard biostratigraphic datums that may be unreliable. Furthermore, sediment cores from ODP Site 1135 and DSDP Site 277 were both spot-cored and do not provide a continuous record of the late Paleocene and early Eocene. IODP Site U1514 is the only high-latitude site with an astronomically tuned age model; however, this is based only on high-resolution XRF data as the carbon isotope data is of a very low-resolution (Vahlenkamp et al., 2020). In addition, some of the shipboard biostratigraphic datums from this site are inconsistent with the chemostratigraphically based age model interpretation. This highlights the need to use a combination of geochemical and biostratigraphic data to construct more reliable age models at the high-latitudes, so that the pacing and timing of paleoceanographic and paleoecological changes during the early Eocene hyperthermals can be better constrained.

For this reason, herein, we present a new chemostratigraphic and biostratigraphic record from the high-latitude southwest Pacific Ocean, spanning ~ 7 million years of the late Paleocene to early Eocene (50.5–57.5 Ma). The resultant age model allows us to evaluate the reliability of calcareous nannofossil biohorizons on a global scale. Furthermore, the new stable isotope record combined with our age model have the potential to provide new insights into high-latitude climate responses during carbon cycle perturbations, which will further our knowledge of early Paleogene paleoceanographic conditions.

5.2. Materials and Methods

5.2.1. Site Location

During IODP Expedition 378, Pleistocene to early Paleocene sediments were recovered from five holes at Site U1553, located on the Campbell Plateau off the south coast of New Zealand at $52^{\circ}13.4'S$, $166^{\circ}11.5'E$ (Röhl

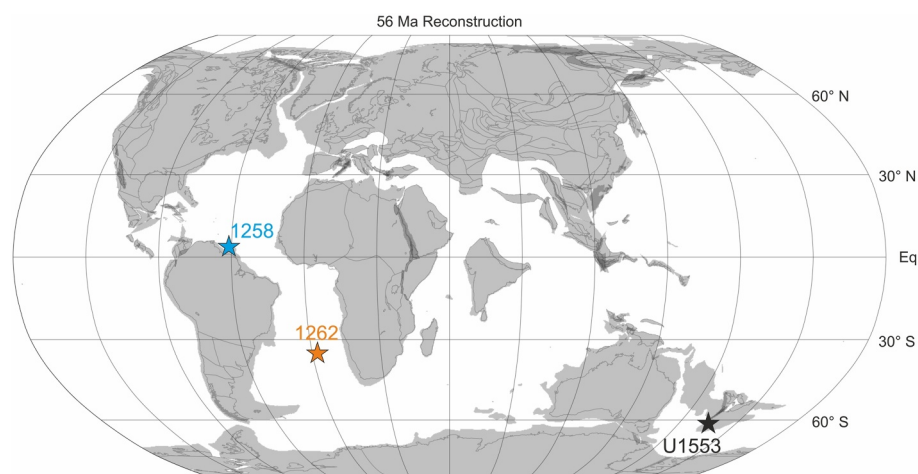


Figure 5.1. 56 Ma paleogeographic reconstruction in Robinson projection showing the position of IODP Site U1553 (black star—this study) and the reference low-to mid-latitude Ocean Drilling Program Sites 1258 (blue star) and 1262 (orange star) used for chemostratigraphic correlation. The reconstruction highlights the high-latitude position of Site U1553 at $\sim 60^{\circ}\text{S}$ during the early Eocene. Paleomap was generated with free software tool GPlates (Müller et al., 2018) by using the integrated combined rotation file (Cao et al., 2020; Müller et al., 2019; Torsvik et al., 2019; Young et al., 2019).

et al., 2022a). This new site was drilled very close to legacy DSDP Site 277, which consists of only one spot-cored hole with relatively low core recovery (Kennett et al., 1975; Shackleton & Kennett, 1975).

The late Paleocene to early Eocene sediments at Site U1553 were recovered from rotary-drilled Holes C and D between 409.21 and 461.7 m below sea-floor (mbsf), consisting of the lithological Subunit IIIb and lithological Unit IV (Röhl et al., 2022b). Lithological Subunit IIIb represents the top ~ 10 m of the study interval and consists of white, homogenous nannofossil chalk with foraminifera. The rest of the study interval is represented by lithological Unit IV, which is predominantly composed of limestones and is distinguished from Subunit IIIb by the increased lithification and variable degree of bioturbation (Röhl et al., 2022b). These sediments were deposited at high paleolatitudes (~ 59 – 61°S ; Figure 5.1) in lower to middle bathyal water depths based on the benthic foraminiferal assemblages ($\sim 1,000$ m; Hollis, 1997). The PETM interval at Site U1553 was first identified offshore within lithological Unit IV based on the nan-noplankton assemblages (Röhl et al., 2022b). At the onset of the PETM, there is an abrupt switch from white, non-bioturbated limestones to darker green, bioturbated limestones (Röhl et al., 2022b). Unlike at many other PETM sites there is no obvious dissolution horizon (e.g., Bralower et al., 2014; Zachos et al., 2005) indicating that sedimentation occurred above the calcite compensation depth (CCD) during the entire study interval.

High-resolution shipboard XRF core scanning data generated at the Gulf Coast Core Repository (GCR) was previously used to make a composite section (splice) of Holes U1553C and -D (Drury et al., 2022; Wilkens et al., 2022). The splice shows that the record from 440 to 496 m core composite depth below seafloor (CCSF) is relatively continuous, with minimal core recovery gaps (Figure 5.2a). This is particularly true of the interval between 450 and 491 m CCSF, where core recovery is generally $>83\%$: exceptional for a rotary-drilled hole. In comparison, the lowest and highest parts of the splice (below 491 m CCSF and above 450 m CCSF respectively) have poorer core recovery (35%–45%), due to the presence of more lithified limestones and/or cherts (Röhl et al., 2022b). Despite these challenges, our composite section still provides one of the most complete records of the early Paleogene from the high-latitude South Pacific to date.

5.2.2. Core-Images and XRF Data

Line-scanned core images and XRF shipboard data (Röhl et al., 2022b) can be used to identify hyperthermal events, which are reported to contain darker, carbonate-depleted sediment with higher XRF-Fe values (Röhl

et al., 2000; Westerhold et al., 2017; Zachos et al., 2005). To generate the core splice images of Holes C and D, we used the software tool *Code for Ocean Drilling Data* (Wilkens et al., 2017). XRF-Fe counts consist of 2025 data points, with an average spacing of 2.3 cm (Figure 5.2a).

2.3. Stable Isotope Analyses

Paired negative $\delta^{13}\text{C}$ and $\delta^{18}\text{O}$ excursions are arguably the best way to identify the early Eocene hyperthermal events. For this reason, we measured the bulk stable carbon and oxygen isotopes of 454 sediment samples from Holes U1553C and -D. Each sediment sample was dried, finely ground by hand with an agate mortar and pestle, and analyzed in the Stable Isotope Laboratory at MARUM—Center for Marine Environmental Sciences, University of Bremen on a Finnigan 253plus gas isotope ratio mass spectrometer with a Kiel IV automated carbonate preparation device. Data are reported in delta-notation versus Vienna Pee Dee Belemnite (V-PDB). The instrument was calibrated against the house standard (ground Solnhofen limestone), which in turn was calibrated against the NBS 19 calcite. Over the measurement period, the standard deviation of the house standard was 0.03‰ for $\delta^{13}\text{C}$ and 0.06‰ for $\delta^{18}\text{O}$.

Bulk stable carbon and oxygen isotope ratios for the same interval were independently analyzed at the Marine Core Research Institute, Kochi University. We analyzed 354 bulk sediment samples from Holes U1553C and -D, which is a different sample set from that analyzed at MARUM. The samples were freeze-dried and finely ground by hand with an agate mortar and pestle. The bulk carbon and oxygen isotopes of the powdered samples were measured using a GV Instruments IsoPrime with a Multicarb preparation system (Wythenshove, Manchester, United Kingdom). The calibration standard material was IAEA-603 (calcite, a reference material certified by International Atomic Energy Agency). The measured isotopic ratios were converted to delta-notation versus V-PDB. Repeated measurements ($n = 70$) of the IAEA-603 showed that the standard deviations of carbon and oxygen isotope ratios were 0.03 and 0.10‰, respectively. The total of 808 samples across a ~ 7 Ma long time interval represents an average sampling resolution of 15,000 to 20,000 years, respectively.

5.2.4. Calcareous Nannofossil Biostratigraphy

For the nannofossil biostratigraphy, we used the biohorizons of Agnini et al. (2007, 2014), which are based on the abundance patterns of several biostratigraphically-useful taxa. The stratigraphic positions of biohorizons in Holes U1553C and -D were obtained through analyses of the nannofossil assemblages observed in smear slide samples, which were processed using the standard procedures outlined in Bown and Young (1998). 80 Samples (52 in Hole U1553C, 28 in Hole U1553D) were analyzed at a ~ 30 cm sampling resolution in the intervals straddling the biohorizons, and another 25 samples were checked in the stratigraphic intervals between the biohorizons. Analyses were carried out using a light microscope at 1200 \times magnification under cross-polarized and transmitted light. The biostratigraphic markers were identified using the taxonomic concepts compiled in the online database Nannotax3 (<https://www.mikrotax.org/Nannotax3/>), and their occurrences were determined by counting the number of the respective specimens in a prefixed area (N/mm^2) (Backman & Shackleton, 1983). We added the taxonomic note “*cf.*” (=“confer,” in Latin) to *Fasciculithus tympaniformis*, as some specimens exhibit an anomalous morphology likely caused by overgrowth. Therefore, we are confident about their genus-level—but not their species-level—designations. This is unlikely to affect our interpretations, as the *Fasciculithus involutus* group (which includes *F. tympaniformis*) is the last *Fasciculithus* group to become extinct (e.g., Agnini et al., 2014).

5.2.5. Age Model

In order to construct a high-resolution age model using the full potential of the sediment records from both Holes C and D, we combined data from outside the splice with the in-splice data by applying the revised splice adjustment (Drury et al., 2022; Wilkens et al., 2022). To improve the reliability of the existing shipboard U1553 age model (Röhl et al., 2022b), we combined our new bulk sediment stable isotope data ($\delta^{13}\text{C}$) with the updated calcareous nannofossil datums. We then correlated our chemostratigraphic record to published astronomically tuned sections from ODP Site 1262 on the Walvis Ridge (Zachos et al., 2010) and Site 1258 on the Demerara Rise

(Kirtland Turner et al., 2014). The high-resolution records from both sites allow intuitive correlation with Site U1553 using the amplitude and shape of several carbon isotope excursions (CIEs). Calcareous nannofossil biostratigraphic events were also correlated to those at Site 1262 (Agnini et al., 2007) using the revised age model of Westerhold et al. (2017).

5.3. Results

5.3.1. Core Images and Geochemical Results

Core images from Site U1553 (Röhl et al., 2022b) generally show alternations of darker and lighter sediment layers, with thicknesses ranging from centimeters to decimeters (Figure 5.2a). Darker-colored sediments are more abundant in the lower part of the U1553 composite (late Paleocene to early Eocene section; 462–496 m CCSF), whilst lighter-colored sediments dominate the upper part (440–462 m CCSF). Concurrent with the change in sediment color, XRF-derived Fe content shows increased values in darker sediment layers and lower values in lighter sediment layers.

Bulk sediment $\delta^{13}\text{C}$ values during the late Paleocene to early Eocene interval range between -0.2 and 3.2‰ (Figure 5.2b). Overall, a long-term, gradual decrease in $\delta^{13}\text{C}$ is punctuated by several negative CIEs. The lower part of the record between 482 and 496 m CCSF is characterized by relatively high $\delta^{13}\text{C}$ values ranging from 2.2 to 3.2‰ , followed by the most prominent decrease of $\sim 2.5\text{‰}$ between 481 and 483 m CCSF (i.e., during the onset of the PETM). Between 450 and 481 m CCSF, average $\delta^{13}\text{C}$ values are 1.13‰ , but show several negative excursions, with a decrease of up to 0.76‰ at 451, 454, 461, 464, 468 and 472 m CCSF. The negative excursions at 468 and 472 m CCSF are both followed by a second smaller $\delta^{13}\text{C}$ decrease of less than 0.4‰ . The uppermost section (440–443.5 m CCSF) of the record is characterized by an overall increase in $\delta^{13}\text{C}$.

5.3.2. Biostratigraphy

The upper Paleocene to lower Eocene nannofossil biohorizons delineated at Site U1553 are summarized in Table 701, and comprise most of those considered by Agnini et al. (2007, 2014). However, it was not possible to confidently assign some of the biohorizons due to the poor preservation of the nannofossil assemblages, this being inconsistent between different depth intervals and showing variability from diffuse overgrowth to etching. For example, dissolution-resistant taxa (e.g., *Discoaster* and *Tribrachiatulus*) are often heavily overgrown, and interspersed among the well-preserved coccoliths of dominant taxa (e.g., *Toweius* and *Chiasmolithus*). For this reason, preservation problems hampered the recognition of the lowest occurrence biohorizons related to *Tribrachiatulus*, that is, base (B) *Tribrachiatulus bramlettei* and B *Tribrachiatulus contortus*.

Additional challenges in the designation of biohorizons stemmed from the rarity or inconsistent occurrence of many of the biostratigraphic marker species at the start and/or end of their stratigraphic ranges, as well as the occurrence of some taxa above their previously published last occurrences. For example, the stratigraphic range of *Fasciculithus* is well documented as becoming extinct shortly after the PETM at many early Eocene sites (e.g., Bralower, 2002; Raffi et al., 2005; Self-Trail et al., 2012; Westerhold et al., 2017). However, it extends to at least ~ 20 m above the PETM at Site U1553 (Figure 5.2c), causing the top (T) of the *Fasciculithus tympaniformis* biohorizon to appear significantly delayed with respect to its observed position at mid- and low-latitude sites (Agnini et al., 2014). This is largely due to the presence of *Fasciculithus* specimens with a non-typical morphology (i.e., *F. cf. tympaniformis*; Figure 5.3: 13–15), especially in the upper part of its extended range. These anomalous forms are unlikely to be a product of reworking, as reworked specimens of other late Paleocene taxa were not observed. Instead, the prolonged occurrence of *Fasciculithus* appears to be a primary paleobiological signal, which decreases the reliability of the top *Fasciculithus* biohorizon at Site U1553.

By comparing the biohorizons between Holes U1553C and -D, we observe that only a few of the events (the base of *Discoaster multiradiatus*, the top of *Tribrachiatulus contortus*, the tentative top of *Fasciculithus cf. tympaniformis* and the top of *Tribrachiatulus orthostylus*) are found at the same depth within uncertainty (Figure 5.2c). However, it is important to note that the oldest (B *D. multiradiatus*) and youngest (T *T.*

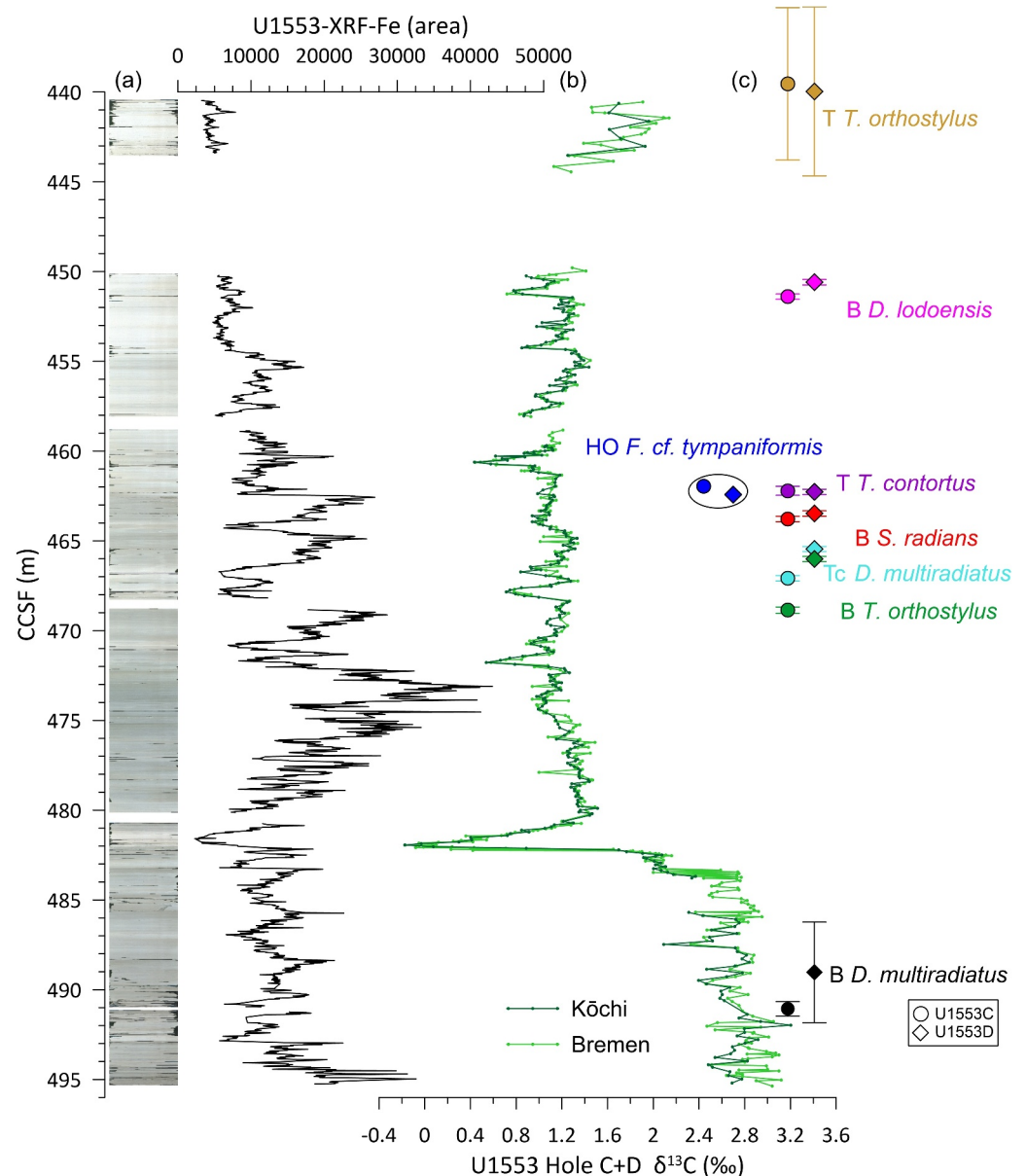


Figure 5.2. The late Paleocene—early Eocene record from IODP Site U1553: (a) Core images and XRF-Fe (Röhl et al., 2022b) of the splice from Holes U1553 Holes C and -D (Drury et al., 2022; Wilkens et al., 2022) (b) Bulk sediment $\delta^{13}\text{C}$ (c) Position of calcareous nannofossil biostratigraphic events. (T = Top occurrence, Tc = Top common occurrence, B= Bottom occurrence, cf. = confer). Genus names abbreviations are D.: *Discoaster*, F.: *Fasciculithus*, T.: *Tribrachiatus*, and S.: *Sphenolithus*. The highest observed occurrence (HO) of *F. cf. tympaniformis* is also shown (the true top of *F. cf. tympaniformis* expected to be even higher up but is not well constrained herein).

orthostylus) of these events have a higher range of uncertainty than the other biostratigraphic datums. The <2 m inter-hole depth discrepancies in the base of *Tribrachiatus orthostylus*, top common *Discoaster multiradiatus*, the base of *Sphenolithus radians* and the base of *Discoaster lodoensis*, may simply be a result of variable nannofossil preservation, the rarity of marker species at the beginning of their stratigraphic ranges and/or differences in core recovery and sampling intensity between holes during certain depth intervals.

Table 5.1
Sample Intervals of Calcareous Nannofossil Biostratigraphic Events at Site U1553 Holes C and -D, With T = Top Occurrence and B = Bottom Occurrence

Sample interval	CCSF adjusted (m)			Uncert. ±	Age (Ma)	Agnini et al. (2012)	Age (Ma)	Westerhold et al. (2017)	U1553C and -D	
	Top	Bottom	Midpoint						Datum	Datum
378-U1553C-25R-CC*	378-U1553C-26R-CC*	435.300	443.790	439.545	4.245	50.5	50.66	50.571 ± 0.135	T	Tribirachiatus orthostylus
378-U1553C-27R-2, 37	378-U1553C-27R-2, 67	451.249	451.536	451.393	0.143	53.7	52.64"	53.678 ± 0.010	B	Discoaster lodoensis
378-U1553C-28R-2, 120	378-U1553C-28R-3, 3	461.963	462.459	462.211	0.248	54.17	53.49	54.117 ± 0.006	T	Tribirachiatus contortus
378-U1553C-28R-3, 123	378-U1553C-28R-4, 2	463.635	463.935	463.785	0.150	54.17	53.53	54.169 ± 0.011	B	Sphenolithus radians
378-U1553C-28R-6, 9	378-U1553C-28R-6, 39	466.935	467.235	467.085	0.150	–	53.58	54.226 ± 0.00	Tc	Discoaster multiradiatus
378-U1553C-29R-1, 30	378-U1553C-29R-1, 60	468.685	469.028	468.856	0.172	54.37	54	54.321 ± 0.008	B	Tribirachiatus orthostylus
378-U1553C-32R-4, 86	378-U1553C-33R-1, 30	490.655	491.475	491.065	0.410	57.32	56.01	–	B	Discoaster multiradiatus
78-U1553D-2R-CC*	378-U1553D-3R-CC*	435.93	444.67	439.965	4.705	50.5	50.66	50.571 ± 0.135	T	Tribirachiatus orthostylus
378-U1553D-4R-1, 30	378-U1553D-4R-1, 60	450.445	450.745	450.595	0.150	53.7	52.64"	53.678 ± 0.010	B	Discoaster lodoensis
378-U1553D-5R-3, 62	378-U1553D-5R-3, 92	462.125	462.425	462.275	0.150	54.17	53.49	54.117 ± 0.006	T	Tribirachiatus contortus
378-U1553D-5R-4, 40	378-U1553D-5R-4, 70	463.326	463.626	463.476	0.150	54.17	53.53	54.169 ± 0.011	B	Sphenolithus radians
378-U1553D-5R-5, 114	378-U1553D-5R-6, 23	465.316	465.591	465.454	0.138	–	53.58	54.226 ± 0.008	Tc	Discoaster multiradiatus
378-U1553D-5R-6, 53	378-U1553D-5R-6, 84	465.867	466.151	466.009	0.142	54.37	54	54.321 ± 0.008	B	Tribirachiatus orthostylus
378-U1553D-7R-CC, 35	378-U1553D-8R-1, 1	486.235	491.835	489.035	2.800	57.32	56.01	–	B	Discoaster multiradiatus

Note. The biochronology from several studies is summarized (Agnini et al., 2014; Gradstein et al., 2012; Westerhold et al., 2017). *Shipboard data (Röhl et al., 2022b).

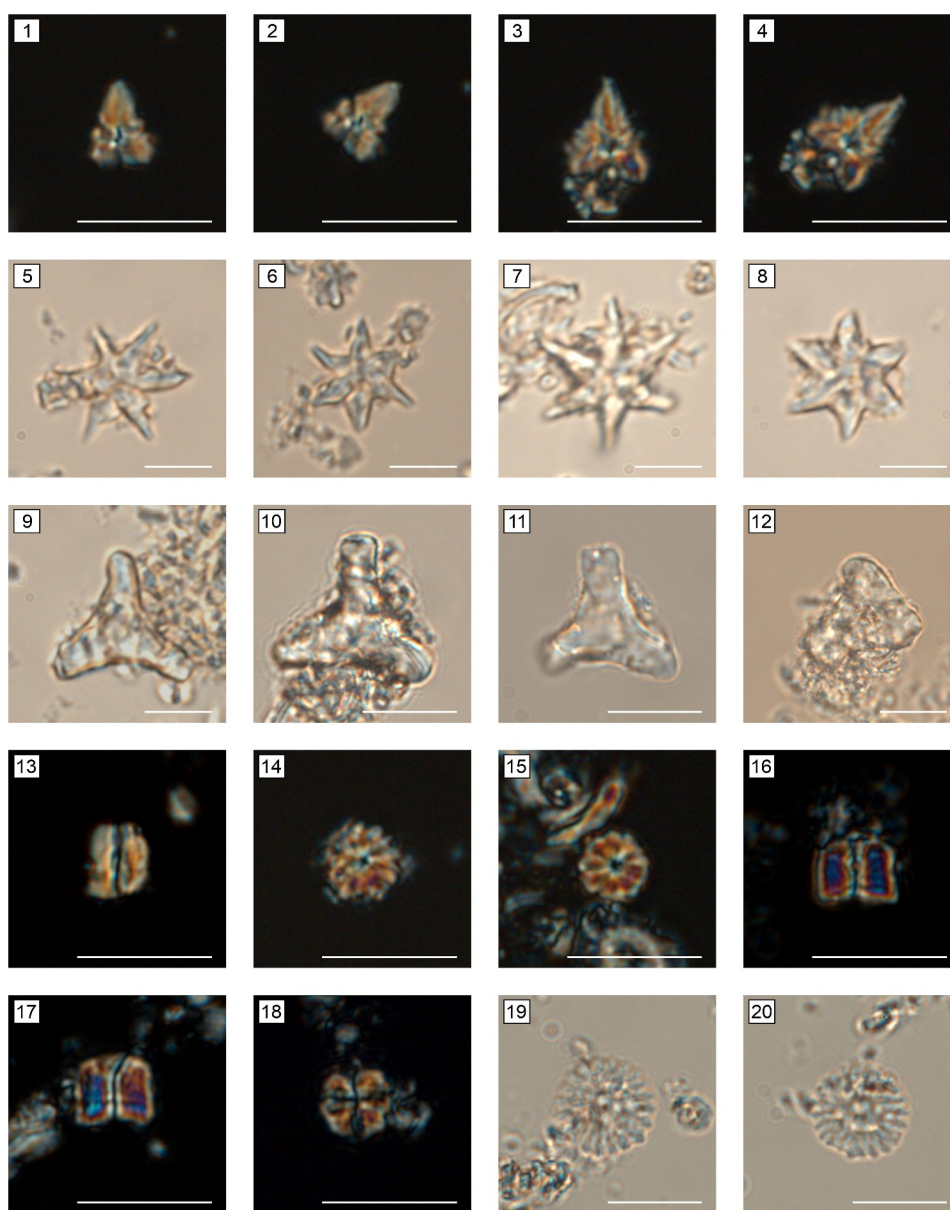


Figure 5.3. Images of selected calcareous nannofossil taxa used for biostratigraphy of the late Paleocene and early Eocene at Site U1553 under Parallel light (PL) and Cross-polarized light (XPL). Scale bar = 10 μ m. 1–4: *Sphenolithus radians*, XPL (U1553C-27R-1, 80 cm); 5–8: *Discoaster lodoensis*, PL (U1553D-3R-CC); 9: *Tibrachiatus orthostylus*, PL (U1553C-28R-4, 122 cm); 10: *Tibrachiatus orthostylus*, PL (U1553C-27R-2, 37 cm); 11: *Tibrachiatus orthostylus*, PL (U1553C-28R-5, 78 cm); 12: Overgrown specimen of *Tibrachiatus contortus*, PL (U1553C-28R-5, 61 cm); 13: *Fasciculithus cf. tympaniformis* side view, XPL (U1553C-29R-2, 89 cm); 14–15: *Fasciculithus cf. tympaniformis* basal view, XPL (U1553C-29R-2, 89 cm); 16–17: *Fasciculithus tympaniformis* side view, XPL (U1553C-31R-2, 34 cm); 18: *Fasciculithus tympaniformis* basal view, XPL (U1553C-31R-2, 30 cm); 19–20: *Discoaster multiradiatus*, PL (U1553D-6R-6, 132 cm). *cf.* (=“confer,” in Latin).

5.4. Discussion

5.4.1. Correlation of Chemostratigraphic Data

The late Paleocene to early Eocene hyperthermal events have been identified worldwide as negative CIEs, which are often coincident with darker sediment layers containing increased XRF-derived Fe intensities due to the dissolution of carbonate (e.g., Lourens et al., 2005; Röhl et al., 2007; Westerhold, Röhl, Donner, & Zachos, 2018;

Zachos et al., 2010). Although this relationship is observed at Walvis Ridge (Röhl et al., 2007; Westerhold et al., 2007; Zachos et al., 2005), Shatsky Rise and Demerara Rise (Westerhold et al., 2017), the correlation of higher Fe intensities with lower $\delta^{13}\text{C}$ values is not observed for the hyperthermal events at Site U1553. This decoupling between Fe and $\delta^{13}\text{C}$ is due to the shallower depositional water depth of Site U1553 (~1,221 m; Röhl et al., 2022a) compared to other pelagic sites of the early Eocene (2,387–4,755 m). For this reason, it is very likely that sediment deposition occurred above the CCD at Site U1553 and was not affected by the dissolution of calcium carbonate, even during the hyperthermals. Therefore, unlike in other studies (e.g., Röhl et al., 2007; Westerhold et al., 2007; Westerhold, Röhl, Donner, & Zachos, 2018; Zachos et al., 2005; Zachos et al., 2010), our XRF-derived Fe record cannot be reliably used to construct an age model.

Stable carbon isotope records have also previously been utilized to establish reliably calibrated orbital chronologies during the late Paleocene to early Eocene (Kirtland Turner et al., 2014; Zachos et al., 2010). For this reason, we correlated our bulk sediment stable carbon isotope data with those from two astronomically tuned sites in the Atlantic Ocean: ODP Site 1262 on the Walvis Ridge (Zachos et al., 2010) and ODP Site 1258 on the Demerara Rise (Kirtland Turner et al., 2014). In addition to their orbitally constrained age models (Westerhold et al., 2017), these sites have high-resolution bulk sediment $\delta^{13}\text{C}$ records that allow for the unique recognition and correlation of hyperthermal events.

For the detailed correlation, we compared the amplitude and shape of the different CIEs as well as the overall pattern of the stable isotope record (Figure 5.4). The PETM is widely known as the largest CIE in the late Paleocene to early Eocene interval. At Site 1262, it is characterized by an abrupt 2.25‰ decrease in $\delta^{13}\text{C}$ (Zachos et al., 2010). In the Site U1553 record, a comparable abrupt $\delta^{13}\text{C}$ decrease occurs at 482 m CCSF (Figure 5.4), marking our first tie point. The paired hyperthermal events H1, H2 and I1, I2 show the typical double minima (Lauretano et al., 2015) with the first CIE (i.e., H1 and I1) being slightly larger in both cases. We identified these paired excursions at 470–472 m CCSF and 466–468 m CCSF. The J event marks the onset of the Early Eocene Climate Optimum (Westerhold, Röhl, Donner, & Zachos, 2018). In the bulk sediment record of Site 1262, the J event has a similar amplitude to I2, but has a more gradual recovery. We correlate this to the decrease in $\delta^{13}\text{C}$ at 464 m CCSF at Site U1553. The K-event (Thomas et al., 2018) has an amplitude similar to H1, and was found in our record at 461 m CCSF (Figure 5.4). The L event has a lower amplitude signal compared to the K event. However, the onset of this event appears to be missing in the U1553 record due to a coring gap at around 459 m CCSF. The hyperthermals M and N are characterized by an asymmetric shape at Site 1258 with sharp onsets and gradual recovery, making them recognizable. We correlate these events to the negative carbon excursion at 454 m CCSF (M) and 451 m CCSF (N), respectively. By comparing the amplitudes, the alternation of more positive and negative $\delta^{13}\text{C}$ values and the relative position of the hyperthermal events O, P, Q, R and S in relation to the N event at Site 1258 (Figure 5.4), we correlate the CIE above the coring gap at 441 m CCSF to the S event. Besides the individual hyperthermal events, there are two prominent shifts in our $\delta^{13}\text{C}$ record: (a) a negative shift before H1 at ~476 m CCSF and (b) a positive shift of ~1‰ after the N-event at ~450 m CCSF. Both of these shifts are observed in the benthic foraminiferal $\delta^{13}\text{C}$ record of Site 1209 (Westerhold, Röhl, Donner, & Zachos, 2018), with the latter also being reported in the benthic *Nuttallides truempyi* $\delta^{13}\text{C}$ record from Site 1263 (Lauretano et al., 2016). This further strengthens the correlation of the hyperthermal events between sites. The less pronounced CIEs immediately before and after the PETM (D1, D2, E1, E2 and F) could not be identified, most likely because of their low amplitudes (Figure 5.4).

5.4.2. Age Model Construction

We compared our $\delta^{13}\text{C}$ record to the calcareous nannofossil datums in Table 5.2. However, doing so revealed multiple discrepancies between the chemo- and biostratigraphic tie points, especially above the PETM recovery (ca. 55.5 Ma). The most striking discrepancy is the top occurrence of *Fasciculithus cf. tympaniformis*, the highest observed occurrence of which is recorded shortly below the K event (~53 Ma; Figure 5.3; Figure S1 in Supporting Information S1) at Site U1553 and not during the recovery of the PETM as expected (55.531 Ma; Westerhold et al., 2017). Another major discrepancy is observed in the first occurrence of *Discoaster lodoensis* (53.68 Ma), which should occur prior to the K event (52.85 Ma), but occurs 10 m above it according to our chemostratigraphic correlation (Figure 5.4). We also observe a delay in the base of *Tribrachiatius orthostylus* (54.321 Ma), *Sphenolithus radians* (54.169 Ma) and the top of *Tribrachiatius contortus* (54.117 Ma). These three events are expected to be found prior to H1/ETM-2 (Agnini et al., 2007) but appear 9 m above H1/ETM-2 in the sediment records of U1553. The base of *Discoaster multiradiatus* prior to the PETM (57.32 Ma) agrees with the chemostratigraphic age model.

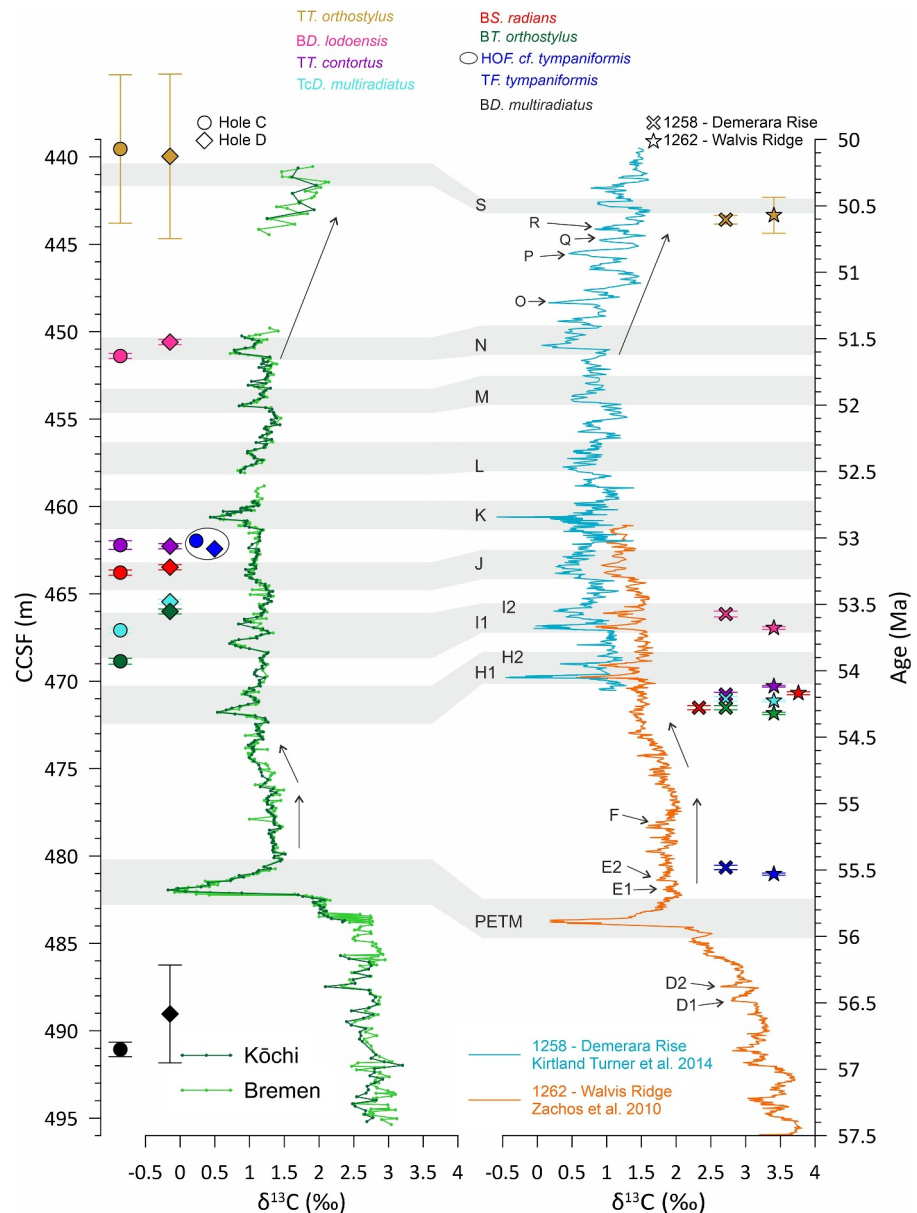


Figure 5.4. Correlation of the bulk sediment $\delta^{13}\text{C}$ record from IODP Site U1553 (green line—this study) to Ocean Drilling Program (ODP) Sites 1258 (blue line—Kirtland Turner et al., 2014) and 1262 (orange line—Zachos et al., 2010). Positions of the hyperthermals are highlighted in gray, after Cramer et al. (2003). The position of calcareous nannofossil biostratigraphic datums and their uncertainty are also shown as circle (U1553C), diamond (U1553D). Ages of calcareous nannofossil datums at ODP Site 1258 and 1262 from Westerhold et al. (2017). Abbreviations for the biohorizons are T = Top occurrence, Tc = Top common occurrence, cf. = confer, B = Bottom occurrence, HO = Highest observed occurrence. Genus names abbreviations are *D.*: *Discoaster*, *F.*: *Fasciculithus*, *T.*: *Tribrachiatulus*, and *S.*: *Sphenolithus*.

Due to these discrepancies, we evaluated the validity of two alternative age models (Figure 5.5a): one based on chemostratigraphic tie points (option 1; Table 5.2) and the other based only on the biostratigraphic tie points (option 2; Table 5.2). To represent the biostratigraphic age model for option 2, we applied the biohorizons from Hole C, as these datums generally have smaller uncertainties and are in slightly closer agreement to the $\delta^{13}\text{C}$ tie points than the datums from Hole D (Figure 5.5a). We also removed the *T. F. tympaniformis* datum as a tie point, as the presence of non-typical morphotypes (i.e., *F. cf. tympaniformis*) for tens of meters above the PETM means that precise delineation of this biostratigraphic event at Site U1553 is highly unreliable.

Table 5.2
List of Utilized Tie Points for the Early Eocene Site U1553 Age Model: Hyperthermal Events (Hyp; Cramer et al., 2003), Correlation of Bulk Sediment $\delta^{13}\text{C}$ ($\delta^{13}\text{C}$ Corr) and Calcareous Nannofossil Biohorizons (Bio) After Agnini et al. (2007)

Age (Ma)	Bulk sed. $\delta^{13}\text{C}$ (option 1) Hole C and D	Biostratigraphy (option 2)		Tie point (midpoint) CCSF adjusted (m)	Event	Name
		Hole C (Top)	Hole C (Bottom)			
50.485	378-U1553C-26R-1,40-41 cm	-	-	440.845	Hyp	S
50.571	-	378-U1553C-25R-CC*	378-U1553C-26R-CC*	439.545	Bio	T <i>Tribracliatius orthostylus</i>
50.67	378-U1553D-3R-2,60-61 cm	-	-	442.853	$\delta^{13}\text{C}$ corr	-
51.55	378-U1553C-27R-2,37-38 cm	-	-	451.249	Hyp	N
M51.97	378-U1553D-4R-3,125-126 cm	-	-	454.255	Hyp	M
52L.46	378-U1553D-4R-6,75-76 cm	-	-	457.945	Hyp	L
52.845	378-U1553D-5R-2,43-44 cm	-	-	460.625	Hyp	K/ETM-3
53.26	378-U1553C-28R-4,17-18 cm	-	-	464.085	Hyp	J
53.545	378-U1553C-28R-5,109-110 cm	-	-	466.515	Hyp	I2
53.665	378-U1553C-28R-6,99-100 cm	-	-	467.835	Hyp	I1
53.678	-	378-U1553C-27R-2, 37	378-U1553C-27R-2, 67	451.393	Bio	B <i>Discoaster lodoensis</i>
53.95	378-U1553C-29R-2,59-60 cm	-	-	470.905	Hyp	H2
54.05	378-U1553C-29R-3,8-9 cm	-	-	471.805	Hyp	H1/ETM-2
54.117	-	378-U1553C-28R-2, 120	378-U1553C-28R-3, 3	462.211	Bio	T <i>Tribracliatius contortus</i>
54.169	-	378-U1553C-28R-3, 123	378-U1553C-28R-4, 2	463.785	Bio	B <i>Sphenolithus radians</i>
54.321	-	378-U1553C-28R-6, 9	378-U1553C-28R-6, 39	467.085	Bio	Tc <i>Discoaster multiradiatus</i>
55.77	378-U1553D-7R-1,0-1 cm	-	-	468.856	Bio	B <i>Tribracliatius orthostylus</i>
55.93	378-U1553D-7R-2,5-6 cm	-	-	480.735	$\delta^{13}\text{C}$ corr	PETM rec end
55.98	378-U1553C-31R-2,47-48 cm	-	-	482.085	Hyp	PETM/ETM-1
56.379	378-U1553D-7R-3,71-72 cm	-	-	482.492	$\delta^{13}\text{C}$ corr	PETM onset
56.497	378-U1553D-7R-3,121-122 cm	-	-	484.235	$\delta^{13}\text{C}$ corr	-
56.69	378-U1553D-7R-9,35-36 cm	-	-	484.735	$\delta^{13}\text{C}$ corr	-
56.861	378-U1553C-32R-2,30-31 cm	-	-	486.235	$\delta^{13}\text{C}$ corr	-
57.22	378-U1553C-32R-3,129-130 cm	-	-	487.475	$\delta^{13}\text{C}$ corr	-
"57.32	-	378-U1553C-32R-4, 86	378-U1553C-33R-1, 30	489.675	$\delta^{13}\text{C}$ corr	-
				491.065	Bio	B <i>Discoaster multiradiatus</i>

Note: Ages for Hyp and Bio from Westerhold et al. (2017). *Age for B *Discoaster multiradiatus* from Gradstein et al. (2012). *Shipboard data (Röhl et al., 2022b).

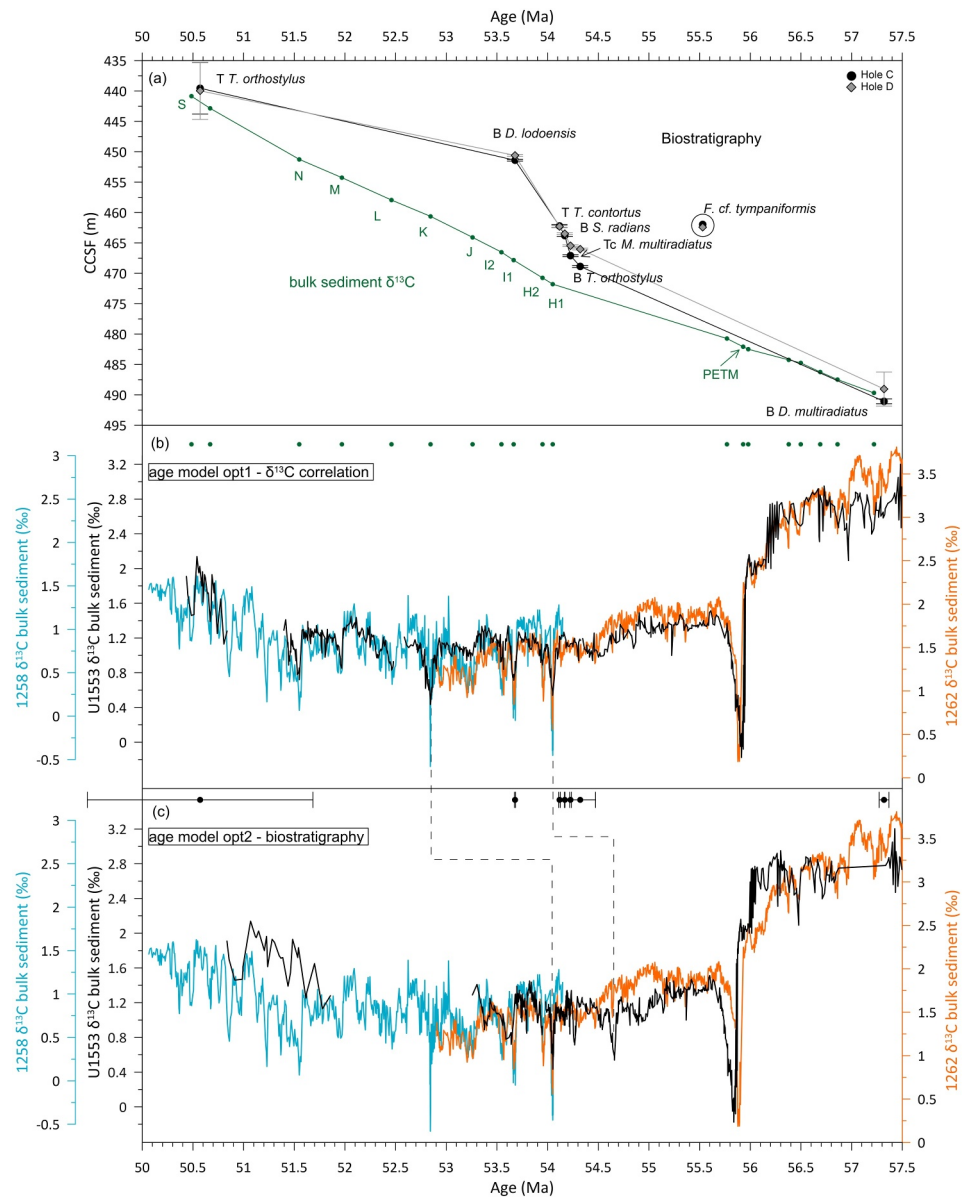


Figure 5.5. (a) Age-depth plot with tie points for the age model. Green: correlation of bulk sediment $\delta^{13}\text{C}$ –hyperthermal events, black: biostratigraphy of calcareous nannofossil events in U1553C and gray: U1553D. The circle shows the highest observed occurrence of *F. cf. tympaniformis* (b) Age model option 1: correlation of the bulk sediment $\delta^{13}\text{C}$ record from IODP Site U1553 (black line—this study), with Ocean Drilling Program (ODP) Site 1258 (blue line) and ODP Site 1262 (orange line). (c) Age model option 2: constructed using the calcareous nannofossil biozone datums from Site U1553 Hole C compared to the same datums from ODP Sites 1258 and 1262 against the bulk sediment $\delta^{13}\text{C}$ records for each site. The dashed lines indicate the substantial time offset between the two alternative age models.

In order to match our age models with those of ODP Sites 1258 and 1262, we offset all three vertical axes of $\delta^{13}\text{C}$ with a range of 3.5‰, but changed the absolute values in order to provide an overlap between all records (Figures 5.5b and 5.5c). Comparison of both options indicates that the CIE coinciding with option 1's K event, is shifted back by 1.2 Ma to the onset of H1 in age model option 2 (Figures 5.5b and 5.5c—dashed lines). Similarly, the negative excursion that coincides with H1 in option one is shifted back by 0.6 Ma in option 2. The large offsets for the K and the H1 event are a result of the delayed biostratigraphic events at Site U1553 (Figure 5.4) compared to ODP Sites 1258 and 1262 (Westerhold et al., 2017).

Overall, option 1 shows a very good correlation in the amplitude and shape of hyperthermal events before and after the PETM. Furthermore, the relatively stable $\delta^{13}\text{C}$ values after the PETM and the negative shift around

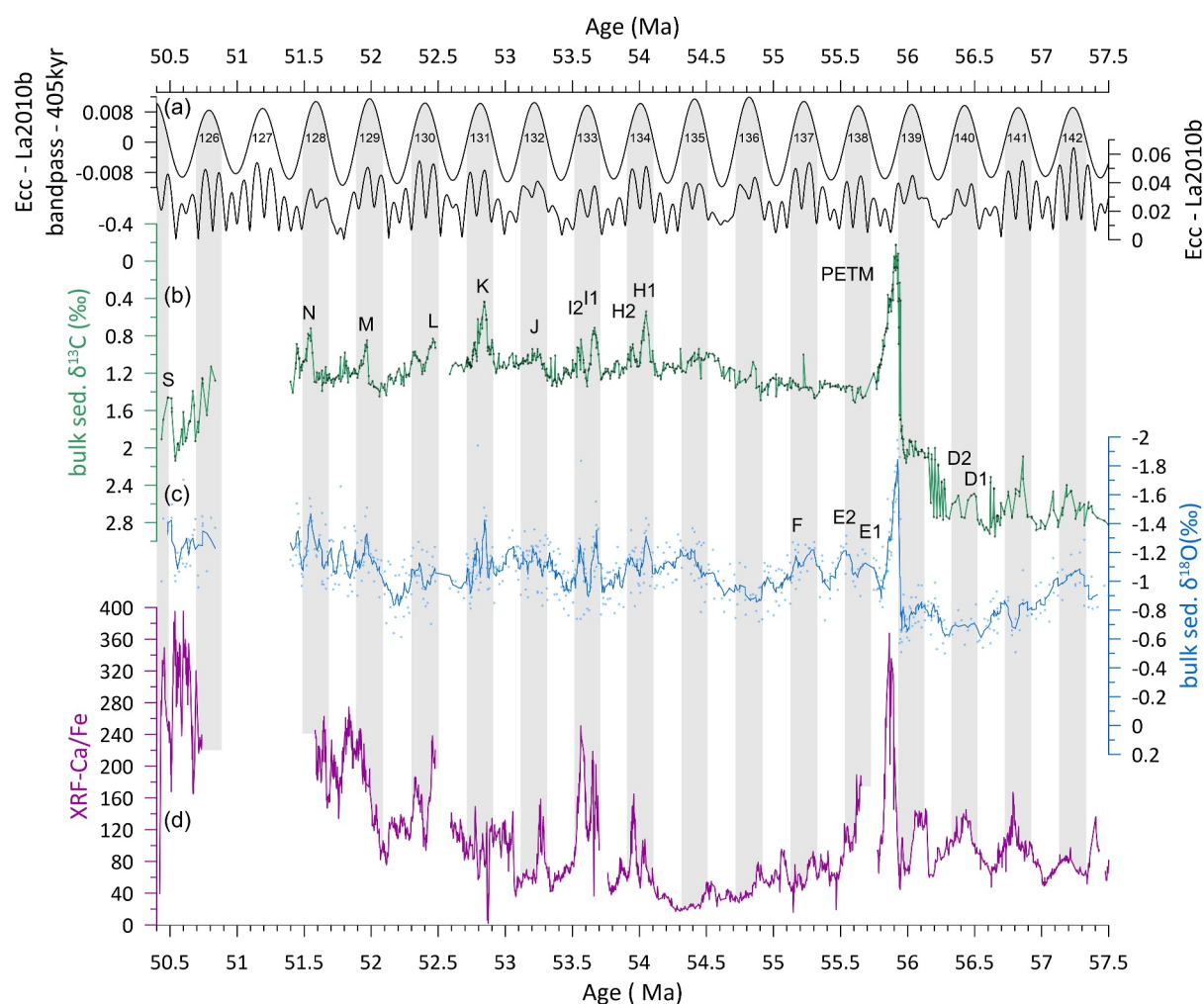


Figure 5.6. Earth eccentricity variability in comparison with Site U1553 data. (a) Earth eccentricity (La2010b) and its 405 kyr bandpass filter generated with Acycle (Li et al., 2019). The numbers reflect the long eccentricity cycles counted backwards from today. (b) Combined bulk sediment $\delta^{13}\text{C}$. (c) Combined bulk sediment $\delta^{18}\text{O}$, on which a five-point running average was applied to provide better visibility. (d) XRF Ca/Fe ratio.

54.8 Ma toward H1, are consistent with the Site 1262 record. In contrast, the isotope data from Site U1553 and ODP Site 1262 are anti-correlated between 54 and 55.5 Ma in option 2. For these reasons, our results indicate that the chemostratigraphic age model (option 1) is more reliable than the biostratigraphic age model (option 2).

Previous biostratigraphic work conducted on sediments from nearby DSDP Site 277, suggests the presence of a >1 Myr hiatus after the PETM. This is based on the short depth interval (approx. 40 cm) between the top of *Fasciculithus spp.* (55.64 Ma) and the base of *Tribrachiatulus orthostylus* (54.37 Ma). In addition, the presence of a shorter (~200 kyr) hiatus was proposed, based on the joint first occurrences of *Tribrachiatulus orthostylus* (54.37 Ma) and *Sphenolithus radians* (53.17 Ma) within the same sample (Hollis et al., 2015; Shepherd et al., 2021). However, our biostratigraphic work at Site U1553 does not support the presence of either one of these hiatuses. Therefore, the hypothesized hiatuses at DSDP Site 277, are likely a result of single-hole, spot coring and are not a true stratigraphic signal.

As described for many other late Paleocene to early Eocene sections worldwide, the U1553 record exhibits a pronounced cyclicity (e.g., Kirtland Turner et al., 2014; Littler et al., 2014; Vahlenkamp et al., 2020; Westerhold et al., 2017; Zachos et al., 2010). Therefore, we plotted the eccentricity according to Laskar et al. (2011) and added a bandpass filter to highlight the long eccentricity cycle of 405 kyr (Figure 5.6a). We also plotted bulk sediment $\delta^{18}\text{O}$ (as a rudimentary temperature proxy) and in-slice XRF-derived Ca/Fe data on our new chemostratigraphic age model to determine if paleoenvironmental trends were astronomically paced. As our $\delta^{18}\text{O}$

record has a low signal-to-noise ratio, likely due to diagenetic overprinting (Hollis et al., 2015; Schrag, 1999; Schrag et al., 1995; Sexton et al., 2006), we applied a five-point running average (Figure 76c). Overall, the $\delta^{13}\text{C}$ and $\delta^{18}\text{O}$ isotopic signatures of the hyperthermal events closely follow the short and long eccentricity cycle with the exception of the PETM (Figures 76a–76c), which is consistent with previous studies. The $\delta^{18}\text{O}$ signal reveals negative values during all of the hyperthermals and therefore demonstrates the expected warming during these events. In addition, the smaller hyperthermal events E1, E2 and F, which cannot be identified within our $\delta^{13}\text{C}$ record, show clear negative excursions in the $\delta^{18}\text{O}$ record, which coincides with the long eccentricity cycles 137 and 138 (Figure 76c). XRF-derived Fe on its own exhibits the dilution of carbonate (represented by Ca). To minimize the dilution effect, we applied the Ca/Fe ratio as shown in Figure 76d. The high positive Ca/Fe values during all hyperthermal events suggests either higher carbonate productivity and/or confirms that the sediments at Site U1553 were deposited above the CCD during the late Paleocene and early Eocene. Overall, our new age model and its comparability to stable isotope records of ODP Sites 1258 and 1262, highlights its applicability, and demonstrates the value of Site U1553 for future paleoceanographic research.

5.4.3. Diachroneity of Early Eocene Calcareous Nannofossil Events in the High Latitude Southern Hemisphere

Our Site U1553 age model provides strong evidence for the diachroneity of calcareous nannofossil bioevents between Site 1262 (Agnini et al., 2007; Westerhold et al., 2017) and Site U1553. A possible explanation for this diachroneity is the latitudinal difference between sites with well-defined biostratigraphic tie points (Agnini et al., 2007, 2014) and Site U1553. Indeed, the traditionally used Paleogene calcareous nannofossil biozones are predominantly based on low- to mid-latitude assemblages (Agnini et al., 2014; Martini, 1971; Okada & Bukry, 1980) and therefore include many warm-water taxa (e.g., *Discoaster* spp.) that only have rare or spotty occurrences at high latitude sites such as U1553. Despite the apparent latitudinal diachroneity of nannofossil datums, it is striking that the sequence of biostratigraphic events at Site U1553 is identical to those at low- and mid-latitude sites. This suggests that the first and last occurrences of biostratigraphically important nannofossil taxa relative to one another were the same on a global scale, but that this evolutionary sequence occurred geologically later at Site U1553 compared to lower latitude sites. One of the most surprising results of our study is the >2.5 Myr delay in the highest observed occurrence of *Fasciculithus* at Site U1553 compared to ODP Site 1262 (Table 70). Although not explicitly stated in the literature, data from Maud Rise (ODP 690) in the high-latitude South Atlantic Ocean, also show that *Fasciculithus* is present until ~20 m above the PETM interval (within nannofossil biozone NP10), and for this reason, this marker taxon could not be used to delineate the Paleocene/Eocene boundary (Cramer et al., 2003; Pospichal & Wise, 1990). Rare *Fasciculithus* specimens were also consistently observed above this reported last occurrence, although these specimens were described as reworked. The reasons why these *Fasciculithus* specimens were considered reworked are unclear, and may simply be a result of the authors deciding that this taxon had already extended too far above its previously reported stratigraphic range. For this reason, it is possible that the delayed extinction of *Fasciculithus* at Site U1553 is a primary ecological signal, which might also be a feature of other high-latitude sites.

As *Fasciculithus* is commonly interpreted to have preferred warmer surface waters (e.g., Bralower, 2002; Gibbs et al., 2006; Mutterlose et al., 2007), it is particularly unusual that it persists for longer than its previously documented stratigraphic range at a high-latitude site such as Site U1553. Although our study is the first to observe possible diachroneity in the top occurrence of *Fasciculithus*, its bottom occurrence during the Paleocene was shown to have a <1 Myr discrepancy between four different basins sampling a range of paleolatitudes (Fuqua et al., 2008). This previous study found that temperature only had a secondary control on the origination of this genus, with its first occurrence observed earlier at a higher-latitude site on the Exmouth Plateau, Indian Ocean (ODP Site 761, paleolatitude of ~40°S) compared to a low-latitude site on the Shatsky Rise, Pacific Ocean (ODP Site 1209; paleolatitude of ~15°N). It was therefore hypothesized that the first occurrence of *Fasciculithus* was primarily controlled by a decrease in surface ocean nutrient levels, which in turn was driven by increased biological pump efficiency. The complex interplay of processes that govern the efficiency of the biological pump are known to vary greatly over various spatial and temporal scales (see review in Honjo et al., 2014), therefore, it is reasonable to expect this mechanism to drive diachroneity in the occurrences of nannofossil taxa (in this case *Fasciculithus*) that had an ecological preference for specific surface ocean nutrient conditions. As it is likely that surface water nutrient availability was the primary control on the first occurrence of *Fasciculithus*, it is plausible that it also had a greater influence than temperature on the last occurrence of this taxon during the early Eocene.

Table 5.3

Calculated Ages After the Chemostratigraphic Age Model (Option 1) for Biostratigraphic Events and Their Time Difference Compared to Ages of Westerhold et al. (2017)

U1553C and -D Datum			Age (Ma)			Westerhold et al. (2017)	
	Top	Bottom	Top	Bottom	Midpoint	Age (Ma)	Δt (Myr)
T <i>Tribrachiatulus orthostylus</i>	378-U1553C-25R-CC*	378-U1553C-26R-CC*	49.582	50.768	50.175	50.571 ± 0.135	-0.396
B <i>Discoaster lodoensis</i>	378-U1553C-27R-2, 37	378-U1553C-27R-2, 67	51.550	51.590	51.570	53.678 ± 0.010	-2.108
T <i>Tribrachiatulus contortus</i>	378-U1553C-28R-2, 120	378-U1553C-28R-3, 3	53.005	53.065	53.035	54.117 ± 0.006	-1.082
B <i>Sphenolithus radians</i>	378-U1553C-28R-3, 123	378-U1553C-28R-4, 2	53.206	53.242	53.224	54.169 ± 0.011	-0.945
Tc <i>Discoaster multiradiatus</i>	378-U1553C-28R-6, 9	378-U1553C-28R-6, 39	53.583	53.610	53.597	54.226 ± 0.008	-0.629
B <i>Tribrachiatulus orthostylus</i>	378-U1553C-29R-1, 30	378-U1553C-29R-1, 60	53.748	53.782	53.765	54.321 ± 0.008	-0.556
HO <i>Fasciculithus cf. tympaniformis</i>	378-U1553C-28R-2, 120	–	–	–	53.005	55.531 ± 0.008	-2.526
B <i>Discoaster multiradiatus</i>	378-U1553C-32R-4, 86	378-U1553C-33R-1, 30	57.380	57.514	57.447	“57.32	0.127
T <i>Tribrachiatulus orthostylus</i>	378-U1553D-2R-CC*	378-U1553D-3R-CC*	49.685	50.860	50.273	50.571 ± 0.135	-0.298
B <i>Discoaster lodoensis</i>	378-U1553D-4R-1, 30	378-U1553D-4R-1, 60	51.466	51.497	51.481	53.678 ± 0.010	-2.197
T <i>Tribrachiatulus contortus</i>	378-U1553D-5R-3, 62	378-U1553D-5R-3, 92	53.025	53.061	53.043	54.117 ± 0.006	-1.074
B <i>Sphenolithus radians</i>	378-U1553D-5R-4, 40	378-U1553D-5R-4, 70	53.169	53.205	53.187	54.169 ± 0.011	-0.982
Tc <i>Discoaster multiradiatus</i>	378-U1553D-5R-5, 114	378-U1553D-5R-6, 23	53.404	53.437	53.421	54.226 ± 0.008	-0.805
B <i>Tribrachiatulus orthostylus</i>	378-U1553D-5R-6, 53	378-U1553D-5R-6, 84	53.469	53.502	53.486	54.321 ± 0.008	-0.835
HO <i>Fasciculithus cf. tympaniformis</i>	378-U1553D-5R-3-92	–	–	–	53.061	55.531 ± 0.008	-2.470
B <i>Discoaster multiradiatus</i>	378-U1553D-7R-CC, 35	378-U1553D-8R-1, 1	56.690	57.572	57.131	“57.32	-0.189

Note. T, Top occurrence; Tc, Top common occurrence; cf, Confer; B, Bottom occurrence; HO, Highest observed occurrence. “Age for B *Discoaster multiradiatus* from Gradstein et al. (2012). *Shipboard data (Röhl et al., 2022b).

This is supported by data indicating that the latitudinal temperature gradient was almost non-existent during the early Eocene (Bijl et al., 2009), suggesting that alternative environmental variables (other than temperature) had a larger control on nannofossil distribution patterns at this time. Unfortunately, independent temperature and/or nutrient availability proxy data do not currently exist for the early Eocene interval at Site U1553, so we are unable to properly test this hypothesis. However, it is an interesting possibility that should be explored more fully in the future, both at Site U1553 and at other early Eocene sites.

Other nannofossil biozones were also shown to be diachronous at Site U1553, with the most extreme example being the base of *Discoaster lodoensis*. At ODP Sites 1258 and 1262—low to mid-latitude sites with orbital age control—this datum is placed before the I2 event (Westerhold et al., 2017), but occurs >2 Myr later at Site U1553 (Table 7B). Some of this apparent diachroneity could be explained by the relatively low core recovery of U1553C-27R (about 30%, Röhl et al., 2022b), but this alone cannot explain the entire discrepancy. Like *Fasciculithus*, the genus *Discoaster* is interpreted as a warm-water taxon (e.g., Aubry, 1998; Bralower, 2002; Tremolada & Bralower, 2004); therefore, the delay in the first occurrence of *D. lodoensis* at high versus low-to mid-latitude sites is not unexpected. However, detailed scrutiny of the literature revealed that the first occurrence of *Discoaster lodoensis* is globally heterogeneous, even for sites that sample similarly high paleolatitudes. For example, the FO of *Discoaster lodoensis* at IODP Site U1514 and ODP Site 752 (Huber et al., 2019; Millen, 2012) is also delayed when compared to ODP Sites 1258 and 1262, but is observed much earlier (below ETM-2; ~54.05 Ma) at ODP Site 690 (Pospichal & Wise, 1990). This heterogeneity could partially be explained by: (a) the low sampling resolution of the biostratigraphic analyses that have been conducted at Sites U1513, 752 and 690, (b) the rare and “spotty” occurrence of *Discoaster* at high-latitude sites, and/or (c) the common poor-preservation of *Discoaster* specimens (generally due to overgrowth) that makes taxonomic identification to species-level challenging. Future research should therefore establish the extent to which the diachroneity of the *Discoaster lodoensis* datum is a primary signal.

In addition to these more extreme examples, the base of *Tribraehiatus orthostylus*, the top common of *Discoaster multiradiatus*, the base of *Sphenolithus radians* and the top of *Tribraehiatus contortus*, all occur shortly before the onset of the H1 event (54.05) at ODP Site 1262 (Westerhold et al., 2017), but occur 0.5 to 1 Ma later at Site U1553 (Table 7B). As reported in the IODP Expedition 378 Proceedings volume (Röhl et al., 2022b), the preservation of calcareous nannofossils is generally moderate to good. However, during a few restricted (cm-scale) intervals, the preservation of nannofossils decreased, perhaps due to the presence of thin layers that are enriched in silica (e.g., cherts) or were more affected by post-depositional processes such as cementation and recrystallization. Although this made it challenging to confidently identify taxa that are more susceptible to overgrowth (e.g., *Tribraehiatus contortus* and *Discoaster lodoensis*), these poorly-preserved intervals are too short and sporadic to explain the multiple >0.5 Myr-long diachroneities that we observe in the nannofossil datums. Therefore, despite ruling out various potential causes of the apparent diachroneity in calcareous nannofossil biostratigraphic events at Site U1553, the lack of comparable data from nearby high-latitude sites means that it is not currently possible to determine the exact drivers of this phenomenon. For this reason, future work should focus on developing further high-latitude age models to determine whether the apparent latitudinal diachroneity in nannofossil bioevents is characteristic of all early Paleogene high-latitude sites, or whether it is a specific feature of Site U1553.

5.5. Conclusions

Here, we present a new late Paleocene to early Eocene age model (50.5–57.5 Ma), reconstructed using sediments recovered from two holes at IODP Site U1553 in the high-latitude southwest Pacific Ocean. Our chemostratigraphic correlation reveals several characteristic paired negative carbon and oxygen isotope excursions, indicative of the early Eocene hyperthermals, underlining the global impact of carbon perturbations. In addition, the Site U1553 age model represents one of the most stratigraphically complete late Paleocene—early Eocene sections from this region to date. Therefore, our new record will be critical for future research on paleoenvironmental and paleoecological changes during warmer worlds at understudied high-latitude sites. Our study highlights that the traditionally used calcareous nannofossil biostratigraphic datums—calibrated to low- and mid-latitude assemblages—cannot be reliably utilized at the high southern latitudes. Future biostratigraphic work should focus on devising a high-latitude biozonation scheme that can be calibrated to astronomically tuned records from lower latitude sites. Critically, the results of our study underline the necessity to check other high-latitude records, to determine whether the latitudinal diachroneity of calcareous nannofossils is the rule rather than the exception.

Data Availability Statement

Data sets for this research are available online in Niederbockstruck et al. (2024). Shipboard data used in the study is available in Röhl et al. (2022b).

References

- Agnini, C., Fornaciari, E., Raffi, I., Catanzariti, R., Pälike, H., Backman, J., & Rio, D. (2014). Biozonation and biochronology of Paleogene calcareous nannofossils from low and middle latitudes. *Newsletters on Stratigraphy*, 47(2), 131–181. <https://doi.org/10.1127/0078-0421/2014/0042>
- Agnini, C., Fornaciari, E., Raffi, I., Rio, D., Röhl, U., & Westerhold, T. (2007). High-resolution nannofossil biochronology of middle Paleocene to early Eocene at ODP Site 1262: Implications for calcareous nannoplankton evolution. *Marine Micropaleontology*, 64(3), 215–248. <https://doi.org/10.1016/j.marmicro.2007.05.003>
- Agnini, C., Macri, P., Backman, J., Brinkhuis, H., Fornaciari, E., Giusberti, L., et al. (2009). An early Eocene carbon cycle perturbation at ~52.5 Ma in the Southern Alps: Chronology and biotic response. *Paleoceanography*, 24(2). <https://doi.org/10.1029/2008PA001649>
- Agnini, C., Spofforth, D. J. A., Dickens, G. R., Rio, D., Pälike, H., Backman, J., et al. (2016). Stable isotope and calcareous nannofossil assemblage record of the late Paleocene and early Eocene (Cicogna section). *Climate of the Past*, 12(4), 883–909. <https://doi.org/10.5194/cp-12-883-2016>
- Anagnostou, E., John, E. H., Babila, T., Sexton, P., Ridgwell, A., Lunt, D. J., et al. (2020). Proxy evidence for state-dependence of climate sensitivity in the Eocene greenhouse. *Nature Communications*, 11(1), 1–9. <https://doi.org/10.1038/s41467-020-17887-x>
- Anagnostou, E., John, E. H., Edgar, K. M., Foster, G. L., Ridgwell, A., Inglis, G. N., et al. (2016). Changing atmospheric CO₂ concentration was the primary driver of early Cenozoic climate. *Nature*, 533(7603), 380–384. <https://doi.org/10.1038/nature17423>
- Arenillas, I., Molina, E., & Schmitz, B. (1999). Plankton foraminiferal and ¹³C isotopic changes across the Paleocene/Eocene boundary at Possagno (Italy). *International Journal of Earth Sciences*, 88(2), 352–364. <https://doi.org/10.1007/s005310050270>
- Aubry, M.-P. (1998). Early Paleogene calcareous nannoplankton evolution: A tale of climatic amelioration. Late Paleocene-early Eocene climatic and biotic events. In *The marine and terrestrial records* (pp. 158–203).
- Babila, T. L., Penman, D. E., Hönisch, B., Kelly, D. C., Bralower, T. J., Rosenthal, Y., & Zachos, J. C. (2018). Capturing the global signature of surface Ocean acidification during the Palaeocene–Eocene Thermal Maximum. *Philosophical Transactions of the Royal Society A: Mathematical, Physical & Engineering Sciences*, 376(2130), 20170072. <https://doi.org/10.1098/rsta.2017.0072>

Acknowledgments

This research used samples and/or data provided by the International Ocean Discovery Program (IODP). We thank the crew and scientists of IODP 378 “S Pacific Paleogene Climate.” We owe a great debt of gratitude to Laurel Childress and colleagues, Texas A&M University, for XRF-scanning all U1553 cores during pandemic’s lockdown phases and the Gulf Coast Repository (GCR) team for taking our samples during times, when nobody could travel or get to a lab abroad. We thank Henning Kuhnert and his team for stable isotope analyses at MARUM, University of Bremen. The stable isotope analyses in Kochi were supported by cooperative research program at Center for Advanced Marine Core Research (CMCR), Kochi University (Nos. 21A007, 21B007, 22A003, and 22B002). We thank Tom Dunkley Jones and another anonymous reviewer for their constructive comments, which helped to improve the quality of the manuscript. This study is funded by the Deutsche Forschungsgemeinschaft (DFG, German Research Foundation) under Germany’s Excellence Strategy EXC-2077-390741603, and by the Japan Society for the Promotion of Science (JSPS) KAKENHI Grant 20H02678. Open Access funding enabled and organized by Projekt DEAL.

- Backman, J., & Shackleton, N. J. (1983). Quantitative biochronology of Pliocene and early Pleistocene calcareous nannofossils from the Atlantic, Indian and Pacific oceans. *Marine Micropaleontology*, 8(2), 141–170. [https://doi.org/10.1016/0377-8398\(83\)90009-9](https://doi.org/10.1016/0377-8398(83)90009-9)
- Bains, S., Corfield, R. M., & Norris, R. D. (1999). Mechanisms of climate warming at the end of the Paleocene. *Science*, 285(5428), 724–727. <https://doi.org/10.1126/science.285.5428.724>
- Barnet, J. S. K., Littler, K., Westerhold, T., Kroon, D., Leng, M. J., Bailey, I., et al. (2019). A high-fidelity benthic stable isotope record of late cretaceous–early Eocene climate change and carbon-cycling. *Paleoceanography and Paleoclimatology*, 34(4), 672–691. <https://doi.org/10.1029/2019PA003556>
- Bijl, P. K., Schouten, S., Sluijs, A., Reichert, G. J., Zachos, J. C., & Brinkhuis, H. (2009). Early Palaeogene temperature evolution of the southwest Pacific Ocean. *Nature*, 461(7265), 776–779. <https://doi.org/10.1038/nature08399>
- Bowen, G. J. (2013). Up in smoke: A role for organic carbon feedbacks in paleogene hyperthermals. *Global and Planetary Change*, 109, 18–29. <https://doi.org/10.1016/j.gloplacha.2013.07.001>
- Bowen, G. J., Maibauer, B. J., Kraus, M. J., Röhl, U., Westerhold, T., Steimke, A., et al. (2015). Two massive, rapid releases of carbon during the onset of the Palaeocene–Eocene thermal maximum. *Nature Geoscience*, 8(1), 44–47. <https://doi.org/10.1038/ngeo2316>
- Bown, P., & Young, J. (1998). *Techniques. U: Bown P.(ur.): Calcareous Nannofossil biostratigraphy*. Chapman and Hall, Kluwer Academic.
- Bralower, T. J. (2002). Evidence of surface water oligotrophy during the Paleocene-Eocene thermal maximum: Nannofossil assemblage data from Ocean Drilling Program Site 690, Maud rise, Weddell sea. *Paleoceanography*, 17(2). <https://doi.org/10.1029/2001PA000662>
- Bralower, T. J., Kelly, D. C., Gibbs, S., Farley, K., Eccles, L., Lindemann, T. L., & Smith, G. J. (2014). Impact of dissolution on the sedimentary record of the Paleocene–Eocene thermal maximum. *Earth and Planetary Science Letters*, 401, 70–82. <https://doi.org/10.1016/j.epsl.2014.05.055>
- Bralower, T. J., Thomas, D. J., Zachos, J. C., Hirschmann, M. M., Röhl, U., Sigurdsson, H., et al. (1997). High-resolution records of the late Paleocene thermal maximum and circum-Caribbean volcanism: Is there a causal link? *Geology*, 25(11), 963–966. [https://doi.org/10.1130/0091-7613\(1997\)025<0963:Hrrot>2.3.Co;2](https://doi.org/10.1130/0091-7613(1997)025<0963:Hrrot>2.3.Co;2)
- Burke, K. D., Williams, J. W., Chandler, M. A., Haywood, A. M., Lunt, D. J., & Otto-Bliesner, B. L. (2018). Pliocene and Eocene provide best analogs for near-future climates. *Proceedings of the National Academy of Sciences*, 115(52), 13288–13293. <https://doi.org/10.1073/pnas.1809600115>
- Cao, X., Zahirovic, S., Li, S., Suo, Y., Wang, P., Liu, J., & Müller, R. D. (2020). A deforming plate tectonic model of the South China Block since the Jurassic. *Gondwana Research*, 102, 3–16. <https://doi.org/10.1016/j.gr.2020.11.010>
- Coccioni, R., Bancalà, G., Catanzariti, R., Fornaciari, E., Frontalini, F., Giusberti, L., et al. (2012). An integrated stratigraphic record of the Palaeocene–lower Eocene at Gubbio (Italy): New insights into the early Palaeogene hyperthermals and carbon isotope excursions. *Terra Nova*, 24(5), 380–386. <https://doi.org/10.1111/j.1365-3121.2012.01076.x>
- Cramer, B. S., Wright, J. D., Kent, D. V., & Aubry, M.-P. (2003). Orbital climate forcing of $\delta^{13}C$ excursions in the late Paleocene–early Eocene (chrons C24n–C25n). *Paleoceanography*, 18(4). <https://doi.org/10.1029/2003PA000909>
- Cramwinckel, M. J., Huber, M., Kocken, I. J., Agnini, C., Bijl, P. K., Bohaty, S. M., et al. (2018). Synchronous tropical and polar temperature evolution in the Eocene. *Nature*, 559(7714), 382–386. <https://doi.org/10.1038/s41586-018-0272-2>
- DeConto, R. M., Galeotti, S., Pagani, M., Tracy, D., Schaefer, K., Zhang, T., et al. (2012). Past extreme warming events linked to massive carbon release from thawing permafrost. *Nature*, 484(7392), 87–91. <https://doi.org/10.1038/nature10929>
- Dickens, G. R., O’Neil, J. R., Rea, D. K., & Owen, R. M. (1995). Dissociation of oceanic methane hydrate as a cause of the carbon isotope excursion at the end of the Paleocene. *Paleoceanography*, 10(6), 965–971. <https://doi.org/10.1029/95PA02087>
- D’Onofrio, R., Luciani, V., Fornaciari, E., Giusberti, L., Boscolo Galazzo, F., Dallanave, E., et al. (2016). Environmental perturbations at the early Eocene ETM2, H2, and I1 events as inferred by Terthyan calcareous plankton (Terche section, northeastern Italy). *Paleoceanography*, 31(9), 1225–1247. <https://doi.org/10.1002/2016PA002940>
- Drury, A. J., Westerhold, T., Wilkens, R. H., & Röhl, U. (2022). Data report: Splice adjustment for site U1553. In U. Röhl, D. J. Thomas, L. B. Childress, & Expedition 378 Scientists (Eds.), *South Pacific Paleogene climate. Proceedings of the International Ocean Discovery Program* (Vol. 378). International Ocean Discovery Program. <https://doi.org/10.14379/iodp.proc.378.201.2022>
- Farnsworth, A., Lunt, D. J., O’Brien, C. L., Foster, G. L., Inglis, G. N., Markwick, P., et al. (2019). Climate sensitivity on geological timescales controlled by nonlinear feedbacks and ocean circulation. *Geophysical Research Letters*, 46(16), 9880–9889. <https://doi.org/10.1029/2019GL083574>
- Frieling, J., Svensen, H. H., Planke, S., Cramwinckel, M. J., Selnes, H., & Sluijs, A. (2016). Thermogenic methane release as a cause for the long duration of the PETM. *Proceedings of the National Academy of Sciences*, 113(43), 12059–12064. <https://doi.org/10.1073/pnas.1603348113>
- Fuqua, L. M., Bralower, T. J., Arthur, M. A., & Patzkowsky, M. E. (2008). Evolution of calcareous nannoplankton and the recovery of marine food webs after the Cretaceous–Paleocene mass extinction. *PALAIOS*, 23(4), 185–194. <https://doi.org/10.2110/palo.2007.p07-004r>
- Galeotti, S., Krishnan, S., Pagani, M., Lanci, L., Gaudio, A., Zachos, J. C., et al. (2010). Orbital chronology of early Eocene hyperthermals from the Contessa Road section, central Italy. *Earth and Planetary Science Letters*, 290(1), 192–200. <https://doi.org/10.1016/j.epsl.2009.12.021>
- Gibbs, S. J., Bown, P. R., Murphy, B. H., Sluijs, A., Edgar, K. M., Pälike, H., et al. (2012). Scaled biotic disruption during early Eocene global warming events. *Biogeosciences*, 9(11), 4679–4688. <https://doi.org/10.5194/bg-9-4679-2012>
- Gibbs, S. J., Bown, P. R., Sessa, J. A., Bralower, T. J., & Wilson, P. A. (2006). Nannoplankton extinction and origination across the Paleocene–Eocene thermal maximum. *Science*, 314(5806), 1770–1773. <https://doi.org/10.1126/science.1133902>
- Gingerich, P. D. (2019). Temporal scaling of carbon emission and accumulation rates: Modern anthropogenic emissions compared to estimates of PETM onset accumulation. *Paleoceanography and Paleoclimatology*, 34(3), 329–335. <https://doi.org/10.1029/2018PA003379>
- Gradstein, F. M., Ogg, J. G., Schmitz, M. D., & Ogg, G. M. (2012). *The geologic time scale 2012*. Elsevier.
- Gutjahr, M., Ridgwell, A., Sexton, P. F., Anagnostou, E., Pearson, P. N., Pälike, H., et al. (2017). Very large release of mostly volcanic carbon during the Palaeocene–Eocene thermal maximum. *Nature*, 548(7669), 573–577. <https://doi.org/10.1038/nature23646>
- Hancock, H. J. L., Dickens, G. R., Strong, C. P., Hollis, C. J., & Field, B. D. (2003). Foraminiferal and carbon isotope stratigraphy through the Paleocene-Eocene transition at Dee Stream, Marlborough, New Zealand. *New Zealand Journal of Geology and Geophysics*, 46(1), 1–19. <https://doi.org/10.1080/00288306.2003.9514992>
- Harper, D. T., Hönisch, B., Zeebe, R. E., Shaffer, G., Haynes, L. L., Thomas, E., & Zachos, J. C. (2020). The magnitude of surface ocean acidification and carbon release during Eocene Thermal Maximum 2 (ETM-2) and the Paleocene-Eocene Thermal Maximum (PETM). *Paleoceanography and Paleoclimatology*, 35(2), e2019PA003699. <https://doi.org/10.1029/2019PA003699>
- Hollis, C. J. (1997). Integrated Paleogene biostratigraphy of DSDP Site 277 (Leg 29): Foraminifera, calcareous nannofossils, Radiolaria, and palynomorphs. *Institute of Geological & Nuclear Sciences Science Report*, 97(07), 1–87.

- Hollis, C. J., Hines, B. R., Littler, K., Villasante-Marcos, V., Kulhanek, D. K., Strong, C. P., et al. (2015). The Paleocene–Eocene thermal maximum at DSDP Site 277, Campbell Plateau, southern Pacific Ocean. *Climate of the Past*, *11*(7), 1009–1025. <https://doi.org/10.5194/cp-11-1009-2015>
- Hönisch, B., Ridgwell, A., Schmidt, D. N., Thomas, E., Gibbs, S. J., Sluijs, A., et al. (2012). The geological record of ocean acidification. *Science*, *335*(6072), 1058–1063. <https://doi.org/10.1126/science.1208277>
- Honjo, S., Eglinton, T. I., Taylor, C. D., Ulmer, K. M., Sievert, S. M., Bracher, A., et al. (2014). Understanding the role of the biological pump in the global carbon cycle. An imperative for Ocean Science. *Oceanography*, *27*(3), 10–16. <https://doi.org/10.5670/oceanog.2014.78>
- Huber, B. T., Hobbs, R. W., & Bogus, K. A. (Eds.). (2019). Site U1516. In *Proceedings of the International Ocean Discovery Program* (Vol. 369, pp. 1–36). IODP. <https://doi.org/10.14379/iodp.proc.369.101.2019>
- Inglis, G. N., Bragg, F., Burls, N. J., Cramwinckel, M. J., Evans, D., Foster, G. L., et al. (2020). Global mean surface temperature and climate sensitivity of the Early Eocene Climatic Optimum (EECO), Paleocene–Eocene Thermal Maximum (PETM), and latest Paleocene. *Climate of the Past*, *16*(5), 1953–1968. <https://doi.org/10.5194/cp-16-1953-2020>
- Jennions, S. M., Thomas, E., Schmidt, D. N., Lunt, D., & Ridgwell, A. (2015). Changes in benthic ecosystems and ocean circulation in the Southeast Atlantic across Eocene Thermal Maximum 2. *Paleoceanography*, *30*(8), 1059–1077. <https://doi.org/10.1002/2015PA002821>
- Jiang, S., & Wise, S. W. (2009). Distinguishing the influence of diagenesis on the paleoecological reconstruction of nannoplankton across the Paleocene/Eocene Thermal Maximum: An example from the Kerguelen Plateau, southern Indian Ocean. *Marine Micropaleontology*, *72*(1), 49–59. <https://doi.org/10.1016/j.marmicro.2009.03.003>
- Kaiho, K., Arinobu, T., Ishiwatari, R., Morgans, H. E. G., Okada, H., Takeda, N., et al. (1996). Latest Paleocene benthic foraminiferal extinction and environmental changes at Tawanui, New Zealand. *Paleoceanography*, *11*(4), 447–465. <https://doi.org/10.1029/96PA01021>
- Kennett, J., Houtz, R., & Kennet, J. (1975). Introduction and explanatory remarks. In *Initial reports of the deep sea Drilling project* (Vol. 29, pp. 3–16). US Govt.
- Kennett, J. P., & Stott, L. D. (1991). Abrupt deep-sea warming, palaeoceanographic changes and benthic extinctions at the end of the Palaeocene. *Nature*, *353*(6341), 225–229. <https://doi.org/10.1038/353225a0>
- Kirtland Turner, S., Sexton, P. F., Charles, C. D., & Norris, R. D. (2014). Persistence of carbon release events through the peak of early Eocene global warmth. *Nature Geoscience*, *7*(10), 748–751. <https://doi.org/10.1038/ngeo2240>
- Koch, P. L., Zachos, J. C., & Gingerich, P. D. (1992). Correlation between isotope records in marine and continental carbon reservoirs near the Palaeocene/Eocene boundary. *Nature*, *358*(6384), 319–322. <https://doi.org/10.1038/358319a0>
- Laskar, J., Fienga, A., Gastineau, M., & Manche, H. (2011). La2010: A new orbital solution for the long-term motion of the Earth*. *A&A*, *532*, A89. <https://doi.org/10.1051/0004-6361/201116836>
- Lauretano, V., Hilgen, F., Zachos, J. C., & Lourens, L. J. (2016). Astronomically tuned age model for the early Eocene carbon isotope events: A new high-resolution delta C-13 (benthic) record of ODP Site 1263 between similar to 49 and similar to 54 Ma. *Newsletters on Stratigraphy*, *49*(2), 383–400. <https://doi.org/10.1127/nos/2016/0077>
- Lauretano, V., Littler, K., Polling, M., Zachos, J. C., & Lourens, L. J. (2015). Frequency, magnitude and character of hyperthermal events at the onset of the Early Eocene Climatic Optimum. *Climate of the Past*, *11*(10), 1313–1324. <https://doi.org/10.5194/cp-11-1313-2015>
- Li, M., Hinnov, L., & Kump, L. (2019). Acycle: Time-series analysis software for paleoclimate research and education. *Computers & Geosciences*, *127*, 12–22. <https://doi.org/10.1016/j.cageo.2019.02.011>
- Littler, K., Röhl, U., Westerhold, T., & Zachos, J. C. (2014). A high-resolution benthic stable-isotope record for the South Atlantic: Implications for orbital-scale changes in Late Paleocene–Early Eocene climate and carbon cycling. *Earth and Planetary Science Letters*, *401*, 18–30. <https://doi.org/10.1016/j.epsl.2014.05.054>
- Lourens, L. J., Sluijs, A., Kroon, D., Zachos, J. C., Thomas, E., Röhl, U., et al. (2005). Astronomical pacing of late Palaeocene to early Eocene global warming events. *Nature*, *435*(7045), 1083–1087. <https://doi.org/10.1038/nature03814>
- Luciani, V., Dickens, G. R., Backman, J., Fornaciari, E., Giusberti, L., Agnini, C., & D’Onofrio, R. (2016). Major perturbations in the global carbon cycle and photosymbiont-bearing planktic foraminifera during the early Eocene. *Climate of the Past*, *12*(4), 981–1007. <https://doi.org/10.5194/cp-12-981-2016>
- Lunt, D. J., Bragg, F., Chan, W. L., Hutchinson, D. K., Ladant, J. B., Morozova, P., et al. (2021). DeepMIP: Model intercomparison of Early Eocene Climatic Optimum (EECO) large-scale climate features and comparison with proxy data. *Climate of the Past*, *17*(1), 203–227. <https://doi.org/10.5194/cp-17-203-2021>
- Martini, E. (1971). Standard Tertiary and Quaternary calcareous nannoplankton zonation. In *Proceedings second planktonic conference, Rome*.
- Millen, H. T. (2012). Biostratigraphy and comparison of Paleocene to lower Eocene calcareous Nannofossils from broken ridge and ninety-east ridge: Ocean drilling program Leg 121, 752–758.
- Müller, R. D., Cannon, J., Qin, X., Watson, R. J., Gurnis, M., Williams, S., et al. (2018). GPlates: Building a virtual Earth through deep time. *Geochemistry, Geophysics, Geosystems*, *19*(7), 2243–2261. <https://doi.org/10.1029/2018GC007584>
- Müller, R. D., Zahirovic, S., Williams, S. E., Cannon, J., Seton, M., Bower, D. J., et al. (2019). A global plate model including lithospheric deformation along major rifts and Orogens since the Triassic. *Tectonics*, *38*(6), 1884–1907. <https://doi.org/10.1029/2018TC005462>
- Murphy, B. H., Farley, K. A., & Zachos, J. C. (2010). An extraterrestrial ³He-based timescale for the Paleocene–Eocene Thermal Maximum (PETM) from Walvis Ridge, IODP Site 1266. *Geochimica et Cosmochimica Acta*, *74*(17), 5098–5108. <https://doi.org/10.1016/j.gca.2010.03.039>
- Mutterlose, J., Linnert, C., & Norris, R. (2007). Calcareous nannofossils from the Paleocene–Eocene thermal maximum of the equatorial Atlantic (ODP Site 1260B): Evidence for tropical warming. *Marine Micropaleontology*, *65*(1), 13–31. <https://doi.org/10.1016/j.marmicro.2007.05.004>
- Niederbockstruck, B., Jones, H. L., Yasukawa, K., Raffi, I., Tanaka, E., Westerhold, T., et al. (2024). Late Paleocene to early Eocene stable isotope records and calcareous nannofossil datums at IODP Site U1553 [Dataset]. *PANGAEA*. <https://doi.org/10.1594/PANGAEA.963554>
- Okada, H., & Bukry, D. (1980). Supplementary modification and introduction of code numbers to the low-latitude coccolith biostratigraphic zonation (Bukry, 1973; 1975). *Marine Micropaleontology*, *5*, 321–325. [https://doi.org/10.1016/0377-8398\(80\)90016-X](https://doi.org/10.1016/0377-8398(80)90016-X)
- Penman, D. E., Hönisch, B., Zeebe, R. E., Thomas, E., & Zachos, J. C. (2014). Rapid and sustained surface ocean acidification during the Paleocene–Eocene Thermal Maximum. *Paleoceanography*, *29*(5), 357–369. <https://doi.org/10.1002/2014PA002621>
- Pospichal, J. J., & Wise, S. W., Jr. (1990). Paleocene to middle Eocene calcareous nannofossils of ODP Sites 689 and 690, Maud rise, Weddell sea. *Proceedings of the Ocean Drilling Program, Scientific Results*, *113*, 613–631.
- Raffi, I., Backman, J., & Pálíke, H. (2005). Changes in calcareous nannofossil assemblages across the Paleocene/Eocene transition from the paleo-equatorial Pacific Ocean. *Palaeogeography, Palaeoclimatology, Palaeoecology*, *226*(1), 93–126. <https://doi.org/10.1016/j.palaeo.2005.05.006>
- Röhl, U., Thomas, D. J., Childress, L. B., Anagnostou, E., Ausín, B., Borba Dias, B., et al. (2022b). Site U1553. In U. Röhl, D. J. Thomas, L. B. Childress, & Expedition 378 Scientists (Eds.), *South Pacific Paleogene climate. Proceedings of the International Ocean Discovery Program* (Vol. 378). International Ocean Discovery Program. <https://doi.org/10.14379/iodp.proc.378.103.2022>

- Röhl, U., Thomas, D. J., Childress, L. B., Anagnostou, E., Ausín, B., Borba Dias, B., et al. (2022a). Expedition 378 summary. In U. Röhl, D. J. Thomas, L. B. Childress, & Expedition 378 Scientists (Eds.), *South Pacific Paleogene climate. Proceedings of the International Ocean Discovery Program* (Vol. 378). International Ocean Discovery Program. <https://doi.org/10.14379/iodp.proc.378.101.2022>
- Röhl, U., Westerhold, T., Bralower, T. J., & Zachos, J. C. (2007). On the duration of the Paleocene-Eocene thermal maximum (PETM). *Geochemistry, Geophysics, Geosystems*, 8(12). <https://doi.org/10.1029/2007GC001784>
- Röhl, U., Bralower, T. J., Norris, R. D., & Wefer, G. (2000). New chronology for the late Paleocene thermal maximum and its environmental implications. *Geology*, 28(10), 927–930. [https://doi.org/10.1130/0091-7613\(2000\)28<927:Ncftlp>2.0.Co;2](https://doi.org/10.1130/0091-7613(2000)28<927:Ncftlp>2.0.Co;2)
- Schmitz, B., Speijer, R. P., & Aubry, M.-P. (1996). Latest Paleocene benthic extinction event on the southern Tethyan shelf (Egypt): Foraminiferal stable isotopic ($\delta^{13}\text{C}$, $\delta^{18}\text{O}$) records. *Geology*, 24(4), 347–350. [https://doi.org/10.1130/0091-7613\(1996\)024<0347:Lpbeeo>2.3.Co;2](https://doi.org/10.1130/0091-7613(1996)024<0347:Lpbeeo>2.3.Co;2)
- Schrag, D. P. (1999). Effects of diagenesis on the isotopic record of late paleogene tropical sea surface temperatures. *Chemical Geology*, 161(1), 215–224. [https://doi.org/10.1016/S0009-2541\(99\)00088-1](https://doi.org/10.1016/S0009-2541(99)00088-1)
- Schrag, D. P., DePaolo, D. J., & Richter, F. M. (1995). Reconstructing past sea surface temperatures: Correcting for diagenesis of bulk marine carbonate. *Geochimica et Cosmochimica Acta*, 59(11), 2265–2278. [https://doi.org/10.1016/0016-7037\(95\)00105-9](https://doi.org/10.1016/0016-7037(95)00105-9)
- Self-Trail, J. M., Powars, D. S., Watkins, D. K., & Wandless, G. A. (2012). Calcareous nannofossil assemblage changes across the Paleocene–Eocene Thermal Maximum: Evidence from a shelf setting. *Marine Micropaleontology*, 92–93, 61–80. <https://doi.org/10.1016/j.marmicro.2012.05.003>
- Sexton, P. F., Wilson, P. A., & Pearson, P. N. (2006). Microstructural and geochemical perspectives on planktic foraminiferal preservation: “Glassy” versus “Frosty”. *Geochemistry, Geophysics, Geosystems*, 7(12). <https://doi.org/10.1029/2006GC001291>
- Shackleton, N. J., & Kennett, J. P. (1975). Paleotemperature history of the Cenozoic and the Initiation of Antarctic Glaciation: Oxygen and carbon isotope analyses in DSDP Sites 277. 279–281.
- Shepherd, C. L., Kulhanek, D. K., Hollis, C. J., Morgans, H. E., Strong, C. P., Pascher, K. M., & Zachos, J. C. (2021). Calcareous nannoplankton response to early Eocene warmth, southwest Pacific Ocean. *Marine Micropaleontology*, 165, 101992. <https://doi.org/10.1016/j.marmicro.2021.101992>
- Slotnick, B. S., Dickens, G. R., Hollis, C. J., Crampton, J. S., Percy Strong, C., & Phillips, A. (2015). The onset of the early Eocene climatic optimum at Branch Stream, Clarence river valley, New Zealand. *New Zealand Journal of Geology and Geophysics*, 58(3), 262–280. <https://doi.org/10.1080/00288306.2015.1063514>
- Sluijs, A., Frieling, J., Inglis, G. N., Nierop, K. G. J., Peterse, F., Sangiorgi, F., & Schouten, S. (2020). Late Paleocene–early Eocene Arctic Ocean sea surface temperatures: Reassessing biomarker paleothermometry at Lomonosov ridge. *Climate of the Past*, 16(6), 2381–2400. <https://doi.org/10.5194/cp-16-2381-2020>
- Stap, L., Lourens, L. J., Thomas, E., Sluijs, A., Bohaty, S., & Zachos, J. C. (2010). High-resolution deep-sea carbon and oxygen isotope records of Eocene Thermal Maximum 2 and H2. *Geology*, 38(7), 607–610. <https://doi.org/10.1130/g30777.1>
- Svensen, H., Planke, S., Malthe-Sørenssen, A., Jamtveit, B., Myklebust, R., Rasmussen Eidem, T., & Rey, S. S. (2004). Release of methane from a volcanic basin as a mechanism for initial Eocene global warming. *Nature*, 429(6991), 542–545. <https://doi.org/10.1038/nature02566>
- Thomas, E., Barrera, E., Hamilton, N., Huber, B., Kennett, J., O’Connell, S., et al. (1990). 51. Upper Cretaceous–Paleogene stratigraphy of sites 689 and 690, Maud rise (Antarctica).
- Thomas, E., Boscolo-Galazzo, F., Balestra, B., Monechi, S., Donner, B., & Röhl, U. (2018). Early Eocene thermal maximum 3: Biotic response at Walvis Ridge (SE Atlantic Ocean). *Paleoceanography and Paleoclimatology*, 33(8), 862–883. <https://doi.org/10.1029/2018PA003375>
- Thomas, E., Zachos, J. C., & Bralower, T. J. (2000). Deep-sea environments on a warm earth: Latest Paleocene–Early Eocene.
- Torsvik, T. H., Steinberger, B., Shephard, G. E., Doubrovine, P. V., Gaina, C., Domeier, M., et al. (2019). Pacific–panthalassic reconstructions: Overview, Errata and the way forward. *Geochemistry, Geophysics, Geosystems*, 20(7), 3659–3689. <https://doi.org/10.1029/2019GC008402>
- Tremolada, F., & Bralower, T. J. (2004). Nannofossil assemblage fluctuations during the Paleocene–Eocene thermal maximum at Sites 213 (Indian Ocean) and 401 (North Atlantic Ocean): Palaeoceanographic implications. *Marine Micropaleontology*, 52(1), 107–116. <https://doi.org/10.1016/j.marmicro.2004.04.002>
- Vahlenkamp, M., De Vleeschouwer, D., Batenburg, S. J., Edgar, K. M., Hanson, E., Martinez, M., et al. (2020). A lower to middle Eocene astrochronology for the Mentelle Basin (Australia) and its implications for the geologic time scale. *Earth and Planetary Science Letters*, 529, 115865. <https://doi.org/10.1016/j.epsl.2019.115865>
- Westerhold, T., Marwan, N., Drury, A. J., Liebrand, D., Agnini, C., Anagnostou, E., et al. (2020). An astronomically dated record of Earth’s climate and its predictability over the last 66 million years. *Science*, 369(6509), 1383–1387. <https://doi.org/10.1126/science.aba6853>
- Westerhold, T., Röhl, U., Donner, B., & Zachos, J. C. (2018). Global extent of early Eocene hyperthermal events: A new Pacific benthic foraminiferal isotope record from Shatsky rise (ODP Site 1209). *Paleoceanography and Paleoclimatology*, 33(6), 626–642. <https://doi.org/10.1029/2017PA003306>
- Westerhold, T., Röhl, U., Frederichs, T., Agnini, C., Raffi, I., Zachos, J. C., & Wilkens, R. H. (2017). Astronomical calibration of the Ypresian timescale: Implications for seafloor spreading rates and the chaotic behavior of the solar system? *Climate of the Past*, 13(9), 1129–1152. <https://doi.org/10.5194/cp-13-1129-2017>
- Westerhold, T., Röhl, U., Laskar, J., Raffi, I., Bowles, J., Lourens, L. J., & Zachos, J. C. (2007). On the duration of magnetochrons C24r and C25n and the timing of early Eocene global warming events: Implications from the Ocean Drilling Program Leg 208 Walvis Ridge depth transect. *Paleoceanography*, 22(2), PA2201. <https://doi.org/10.1029/2006PA001322>
- Westerhold, T., Röhl, U., Wilkens, R. H., Gingerich, P. D., Clyde, W. C., Wing, S. L., et al. (2018). Synchronizing early Eocene deep-sea and continental records – Cyclostratigraphic age models for the Bighorn Basin Coring Project drill cores. *Climate of the Past*, 14(3), 303–319. <https://doi.org/10.5194/cp-14-303-2018>
- Wilkens, R. H., Drury, A. J., Westerhold, T., & Röhl, U. (2022). Data report: Depths of site U1553 off-splice data adjusted to the site U1553 splice, IODP Expedition 378. In U. Röhl, D. J. Thomas, L. B. Childress, & Expedition 378 Scientists (Eds.), *South Pacific Paleogene climate. Proceedings of the International Ocean Discovery program* (Vol. 378). International Ocean Discovery Program. <https://doi.org/10.14379/iodp.proc.378.202.2022>
- Wilkens, R. H., Westerhold, T., Drury, A. J., Lyle, M., Gorgas, T., & Tian, J. (2017). Revisiting the Ceara rise, equatorial Atlantic Ocean: Isotope stratigraphy of ODP Leg 154 from 0 to 5 Ma. *Climate of the Past*, 13(7), 779–793. <https://doi.org/10.5194/cp-13-779-2017>
- Yasukawa, K., Nakamura, K., Fujinaga, K., Ikehara, M., & Kato, Y. (2017). Earth system feedback statistically extracted from the Indian Ocean deep-sea sediments recording Eocene hyperthermals. *Scientific Reports*, 7(1), 11304. <https://doi.org/10.1038/s41598-017-11470-z>
- Young, A., Flament, N., Maloney, K., Williams, S., Matthews, K., Zahirovic, S., & Müller, R. D. (2019). Global kinematics of tectonic plates and subduction zones since the late Paleozoic Era. *Geoscience Frontiers*, 10(3), 989–1013. <https://doi.org/10.1016/j.gsf.2018.05.011>

- Zachos, J. C., McCarren, H., Murphy, B., Röhl, U., & Westerhold, T. (2010). Tempo and scale of late Paleocene and early Eocene carbon isotope cycles: Implications for the origin of hyperthermals. *Earth and Planetary Science Letters*, 299(1), 242–249. <https://doi.org/10.1016/j.epsl.2010.09.004>
- Zachos, J. C., Röhl, U., Schellenberg, S. A., Sluijs, A., Hodell, D. A., Kelly, D. C., et al. (2005). Rapid acidification of the ocean during the Paleocene-Eocene thermal maximum. *Science*, 308(5728), 1611–1615. <https://doi.org/10.1126/science.1109004>
- Zeebe, R. E., & Lourens, L. J. (2019). Solar System chaos and the Paleocene–Eocene boundary age constrained by geology and astronomy. *Science*, 365(6456), 926–929. <https://doi.org/10.1126/science.aax0612>
- Zeebe, R. E., Zachos, J. C., & Dickens, G. R. (2009). Carbon dioxide forcing alone insufficient to explain Palaeocene–Eocene Thermal Maximum warming. *Nature Geoscience*, 2(8), 576–580. <https://doi.org/10.1038/ngeo578>

Supporting Information for

Apparent diachroneity of calcareous nannofossil datums during the early Eocene in the high-latitude South Pacific Ocean

B. Niederbockstruck¹, H. L. Jones¹, K. Yasukawa^{2,3}, I. Raffi⁴, E. Tanaka^{5,6}, T. Westerhold¹, M. Ikehara⁵, U. Röhl¹

¹MARUM - Center for Marine Environmental Sciences, University of Bremen

²Frontier Research Center for Energy and Resources, School of Engineering, The University of Tokyo

³Department of Systems Innovation, School of Engineering, The University of Tokyo

⁴International Research School of Planetary Sciences (IRSPS), Università degli Studi "G. d'Annunzio" di Chieti-Pescara

⁵Marine Core Research Institute, Kochi University

⁶Ocean Resources Research Center for Next Generation, Chiba Institute of Technology

Contents of this file

Figures S1 to S1

Introduction

This study shows apparent diachroneity of calcareous nannofossil datums used for biostratigraphy at IODP Site U1553. The supporting Figure S1 shows the abundance pattern of the species which are relevant for the biostratigraphy of this study.

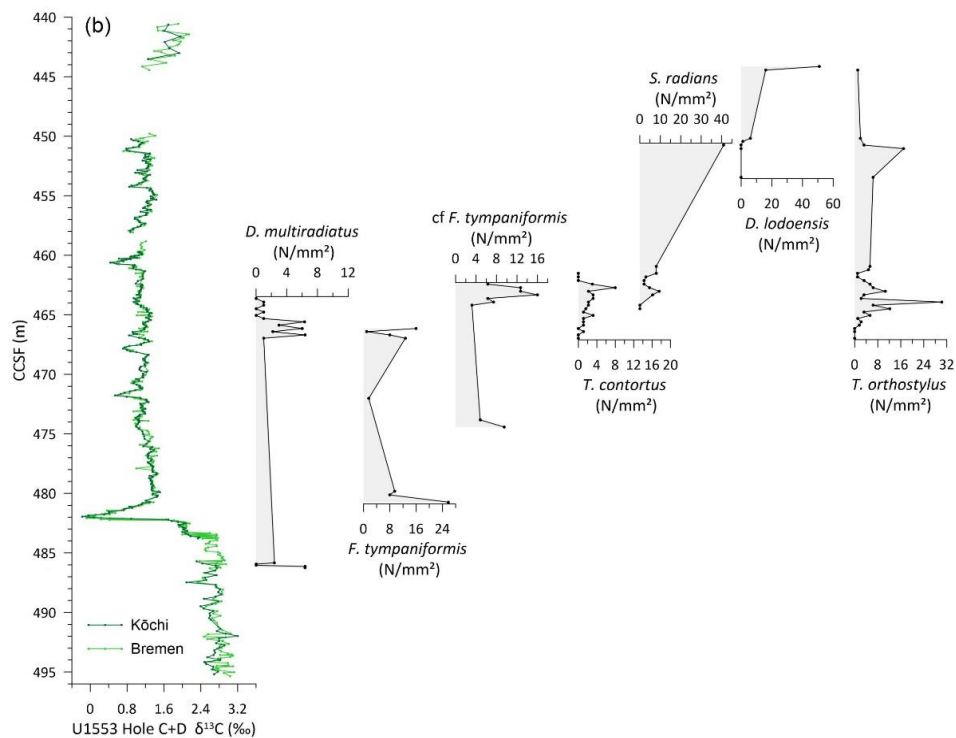
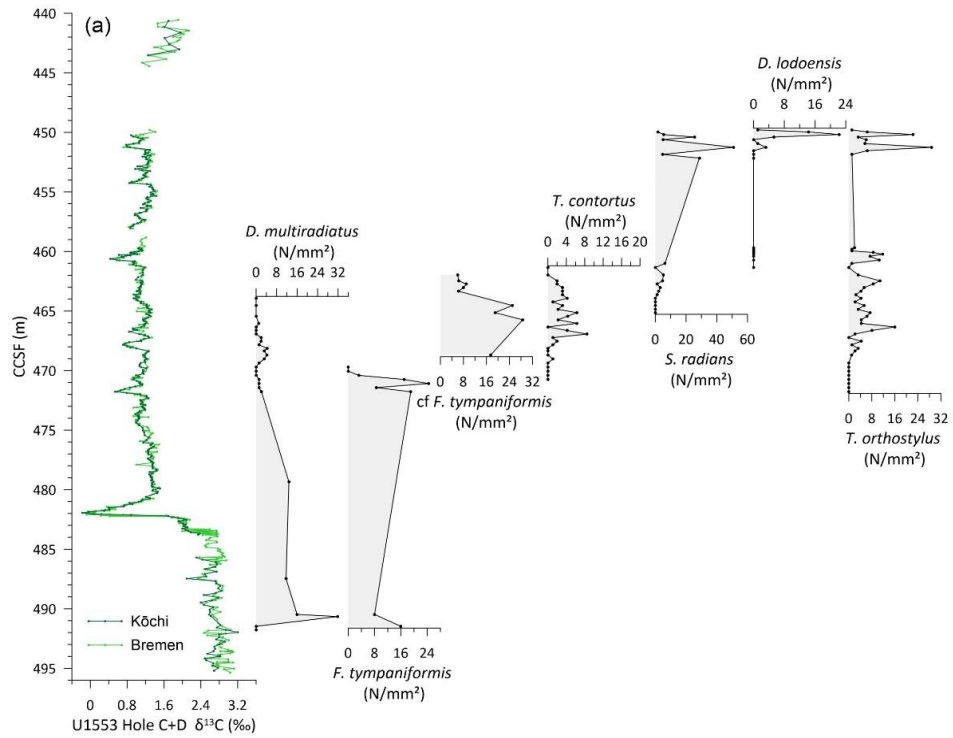


Figure S1. Abundance pattern of calcareous nannofossil species used for biostratigraphy. a) IODP Site U1553 Hole C. b) IODP Site U1553 Hole D.

6. Part II: Calcareous nannoplankton responded to short- and long-term warming during the early Eocene in the South Pacific

Bryan Niederbockstruck¹, Heather L. Jones¹, Ursula Röhl¹

¹MARUM - Center for Marine Environmental Sciences, University of Bremen, Bremen, Germany,

Abstract

Calcareous nannofossils are crucial for identifying past environmental conditions. The early Eocene was marked by perturbations in the carbon cycle, leading to warming events known as hyperthermals, which provide unique opportunities to study environmental changes driven by high atmospheric CO₂. While most studies on early Eocene calcareous nannofossils focus on long-term scales, few target hyperthermals at high resolution. Existing high-resolution studies primarily address the Paleocene-Eocene Thermal Maximum and Eocene Thermal Maximum 2. Here, we present a high-resolution assemblage record from 53.8 to 52.7 Ma, encompassing several hyperthermals of varying magnitudes. Our results reveal a significant shift in the calcareous nannofossil assemblage approximately 120 kyr before the onset of the Early Eocene Climate Optimum. We conclude that these changes are primarily driven by nutrient levels rather than temperature. The assemblage shifts are characterized by an interplay between *Zygrhablithus* and *Chiasmolithus*, with *Chiasmolithus* showing increased abundance during hyperthermal events, likely due to enhanced nutrient supply. This study enhances our understanding of calcareous nannoplankton responses to extreme warming conditions and indicates a non-linear response to the magnitude of carbon perturbations. Our findings raise the question of whether the major changes in the assemblage observed at Site U1553, particularly the interactions between *Zygrhablithus* and *Chiasmolithus*, are unique to this site or can be observed elsewhere, and whether these changes could serve as indicators for the onset of the EECO.

6.1. Introduction

The early Eocene (56 to 48 Ma) was a geological time interval of exceptionally high temperatures (Cramwinckel et al., 2018; Farnsworth et al., 2019; Sluijs et al., 2020; Lunt et al., 2021) and elevated atmospheric CO₂ concentrations (Anagnostou et al., 2016, 2020) with no permanent ice sheets, leading to it being described as a 'Hothouse climate' (Westerhold et al., 2020). The early Eocene was marked by transient warming events known as hyperthermals, where sudden releases of isotopically light carbon significantly altered the oceanic-atmospheric system (e.g., Dickens et al., 1995; Thomas and Shackleton, 1996; Thomas et al., 2000). The source of light carbon is still under debate with two potential candidates that are volcanic activity (Svensen et al., 2004; Gutjahr et al., 2017), or dissociation of gas hydrates (Dunkley Jones et al., 2010, DeConto et al., 2012; Bowen, 2013). The

sudden releases of isotopically light carbon lead to further increased temperatures and ocean acidification (Penman et al., 2014; Gutjahr et al., 2017; Babila et al., 2018; Harper et al., 2020). As hyperthermals are characterized by increases in both atmospheric ^{12}C and temperature, they can be recognized in the sedimentary record as paired negative $\delta^{13}\text{C}$ and $\delta^{18}\text{O}$ excursions in outcrop sections (e.g., Agnini et al., 2009; Galeotti et al., 2010; Coccioni et al., 2012; Slotnick et al., 2015) and deep-sea sediments (e.g., Cramer et al., 2003; Westerhold et al., 2007; Kirtland Turner et al., 2014; Littler et al., 2014; Westerhold et al., 2017).

The three most prominent early Eocene hyperthermals are the Eocene Thermal Maximum (ETM) 1, also known as the Paleocene-Eocene Thermal Maximum (PETM; Kennett and Scott, 1991; Norris and Röhl, 1999; Röhl et al., 2007; Zachos et al., 2010) dated to 55.930 Ma, followed by ETM2 (Lourens et al. 2005, Nicolo et al. 2007) at 54.050 Ma (Westerhold et al., 2017) and ETM3 (also known as the 'X' event; Röhl et al., 2005, Thomas et al., 2018) at 52.845 Ma (Westerhold et al., 2017). Smaller carbon cycle perturbations of varying magnitudes occurred in-between and around these major events, and were initially labeled from A to L (Cramer et al., 2003) and M to W (Lauretano et al., 2016). In addition to the hyperthermals, this geological interval includes the Early Eocene Climate Optimum (EECO): a critical, about 4 Ma long interval (Westerhold et al., 2018), when the Earth experienced its warmest long-term state of the Cenozoic with exceptionally high general mean surface temperature of 23.2° to 29.7°C (Inglis et al, 2020) and sea surface temperature based on Mg/Ca and biomarker paleothermometry reaching 34°C in the Southwest Pacific (Bijl et al., 2009; Hines et al., 2017). Although some studies indicate that the onset of the EECO (Ca. 53 Ma) cannot globally defined (e.g., Luciani et al., 2016) others suggest that it coincides approximately with the onset of the J hyperthermal event based on benthic foraminiferal stable isotope data (Lauretano et al., 2015; Westerhold et al., 2018), changes in planktic foraminifera assemblage (Luciani et al., 2017) and lithological changes in sediment sections (Slotnick et al., 2012). From the J event, the EECO extends until the first occurrence of the calcareous nannofossil species *Discoaster Sublodeonsis* (Luciani et al., 2016) from 53.26 to 49.14 (Westerhold et al., 2018).

Both, short- and long-term warming would be expected to have a profound impact on marine organisms, with those that precipitate calcium carbonate shells (e.g., calcareous nannoplankton) likely being more susceptible to the associated biogeochemical changes. During the K-Pg boundary, 90% of the calcareous nannofossil species became extinct (Bown et al., 2004), followed by a reestablishment of new families in the early Paleocene (Perch-Nielsen, 1985). Those evolutionary trends, marked by periods of decline and diversification through the Cenozoic, make them a valuable tool for biostratigraphy (Agnini et al., 2017; Raffi and Backman, 2022). As the early Eocene is thought to be a reasonable and most closely resemble analog for modern climate change (Burke et al, 2018), this time interval provides the opportunity to examine the responses of calcareous nannoplankton to extreme

environmental conditions such as elevated SSTs or ocean acidification on timescales that go beyond experimental or observational data.

Many high-resolution studies on calcareous nannofossil assemblage changes during the early Eocene exist, but almost all exclusively focus primarily on the PETM (eg.: Bralower, 2002; Gibbs et al., 2006; Mutterlose et al., 2007; Raffi et al., 2008; Bown and Pearson, 2009; Jiang and Wise, 2009; Self-Trail et al., 2012; Schneider et al., 2013; Wang et al., 2022) or ETM2 (Dedert et al., 2012; Gibbs et al., 2012; D’Onofrio et al., 2016; Lei et al., 2016). Very few examine the longer-term early Eocene record and not many examine the smaller hyperthermals. However, there are some studies that have looked at them. A study, that compiled calcareous nannofossil assemblage records of several sites (Schneider et al., 2011) find out that a major global turnover in the assemblage started with the onset of the EECO, coinciding with thermal destratification and a weakening in the efficiency of the biological pump. Shepherd et al. (2021) investigated the calcareous nannofossil assemblage change for a 15 Ma long record at DSDP Sites 207 and 277, and concluded that the assemblage pointed to warm, temperate conditions around New Zealand during the EECO with a warm proto-East Australian current extended to at least 55°S. A long-term time series of calcareous nannofossil investigation at ODP Site 1209, suggest that a negative carbon excursion need to overcome a threshold value, as it did in ETM1, ETM2 and I1, in order to cause significant biotic disruptions (Gibbs et al., 2012). A similar conclusion derives from the Cicogna section, where only the PETM seems to cause a major difference in the assemblage with other CIEs only causing limited variation in the assemblage during the latest Paleocene to early Eocene (Agnini et al., 2016). Recently, Alegret et al. (2021) investigated calcareous nannofossil assemblages in the EECO including hyperthermal events ETM3, S, T and U at Site U1510 in the Tasman Sea. They observed warm-water taxa dominating the calcareous nannoplankton assemblage, that were most abundant during ETM3, the most prominent hyperthermal of the EECO.

Although these studies indicate a response of calcareous nannoplankton to carbon perturbations, we are still uncertain about the threshold it needs to initiate these changes and if these are globally the same or differ between high and low latitudes. Most of our current high-resolution age models - that are essential for reliably identifying the hyperthermal events and the onset of the EECO - are from the low to mid-latitudes. In comparison, ecological responses at the high latitudes are poorly understood.

Here we present a high-resolution calcareous nannofossil assemblage data from the IODP Site U1553 in the Southwest Pacific Ocean spanning a 1.1 Ma-long interval of the early Eocene (52.7 to 53.8 Ma), including hyperthermal events I1, I2, J and K and the onset of the EECO. The aim of this study is to better understand the response of calcareous nannoplankton to carbon perturbations of different magnitudes in a warmer world, which in turn could be used to predict how future calcareous nannoplankton communities will be affected by anthropogenic warming. These results may exhibit

possible changes of calcareous phytoplankton in the near future regarding the ongoing CO₂ rising. Studying the response of plankton beyond the major perturbations of ETM1-2 may help further to understand if the magnitude of biotic response is linked to the magnitude of perturbations.

6.2. Environmental preferences of calcareous nannofossil genera

The sensitivity of calcareous nannoplankton in response to environmental changes has been discussed in several studies, highlighting their potential as indicators for paleoceanographic reconstructions (e.g., Wei and Wise, 1990; Erba et al., 2010; Self-Trail et al., 2012).

Coccolithus is a cosmopolitan genus, appearing at any latitudes during the early Eocene. *Coccolithus pelagicus*, is considered to prefer temperate waters (Jiang and Wise, 1990) and eutrophic conditions (Villa et al., 2014). A species that is thought to prefer warm water is *Coccolithus formosa* (Villa et al., 2008).

Toweius is thought to have preferred cooler waters with mesotrophic to eutrophic conditions (Bralower, 2002; Tremolada and Bralower, 2004; Self-Trail et al., 2012) but is a cosmopolitan and abundant across all latitudes (Haq and Lohmann, 1976).

Zygrhablithus preferred warm and oligotrophic conditions (Aubry, 1998, Bralower, 2002; Agnini et al., 2007; Cappelli et al., 2019) and is mainly presented in near shore environments (Villa et al., 2008).

Chiasmolithus is thought to favor cool water (Bralower, 2002; Persico and Villa, 2004; Villa et al., 2008) and mesotrophic to eutrophic conditions (Aubry, 1998).

Discoaster is considered to be a warm water genus, preferring oligotrophic conditions (Aubry, 1992; Monechi et al., 2000; Bralower, 2002; Bown and Pearson, 2009; Gibbs et al., 2006 -Science). It is represented in low abundance at high latitudes (Bukry, 1973).

Sphenolithus is considered have similar preferences as *Discoaster* and being an indicator for warm and oligotrophic conditions (Aubry, 1998; Bralower, 2002; Gibbs et al., 2004; Jiang and Wise, 2006).

Cyclicargolithus is thought to be a cosmopolitan genus (Haq et al., 1977) which favor temperate-water and nutrient-rich conditions (Wei and Wise, 1990, Aubry, 1992), but Persico and Villa (2004) suggest that *Cyclicargolithus* has no temperature affinity.

6.3 Material and Method

6.3.1. Study Site

Samples investigated for this study were retrieved from sediment cores drilled in the Southwestern Pacific Ocean during IODP Expedition 378 at Site U1553 on the southern Campbell Plateau (Röhl et al.,

2022) (Figure 6.1). At Site U1553, five parallel holes recovered sediments from the Pleistocene to the early Paleocene. Site U1553 was drilled close to legacy DSDP Site 277, which retrieved Eocene sediments only in a spot-cored, single hole with overall low recovery (Kennett et al., 1975). Early Eocene sediments were retrieved from parallel Holes U1553C and -D, resulting in a continuously-cored and stratigraphically complete composite record from these two holes. Stable isotope analyses on bulk sediment and the resulting chronostratigraphy (Niederbockstruck et al., 2024) revealed the presence of many of the hyperthermal events and the absence of stratigraphic hiatuses within the study interval. The early Eocene sediments at Site U1553 for the studied interval belong to lithological Subunit IV (ca 52-62 Ma), which is generally summarized as limestone with increased lithification downwards. In more detail, the calcium carbonate concentration decreases from 90 to 63% downwards through the Subunit IV. The presence of nannofossils, quartz and micas is common to abundant (Röhl et al., 2022). Towards the base, XRD analysis identified an increase of siliclastic material such as clay. Nevertheless, calcite is the dominant mineral.

During the early Eocene, sediments were deposited at a paleolatitude of around 60°S, at a water depth of 1000 m, based on benthic foraminifera assemblages (Hollis, 1997). At this time, both the continental configuration and oceanographic conditions were significantly different from today, with the study area was thought to be bathed in subtropical waters (Nelson and Cooke, 2001), derived from the lower-latitude proto-East Australian Current (Kennett and Exon, 2004). The sediments appear to have been deposited above the CCD, with no lithological evidence for pervasive dissolution during the hyperthermals.

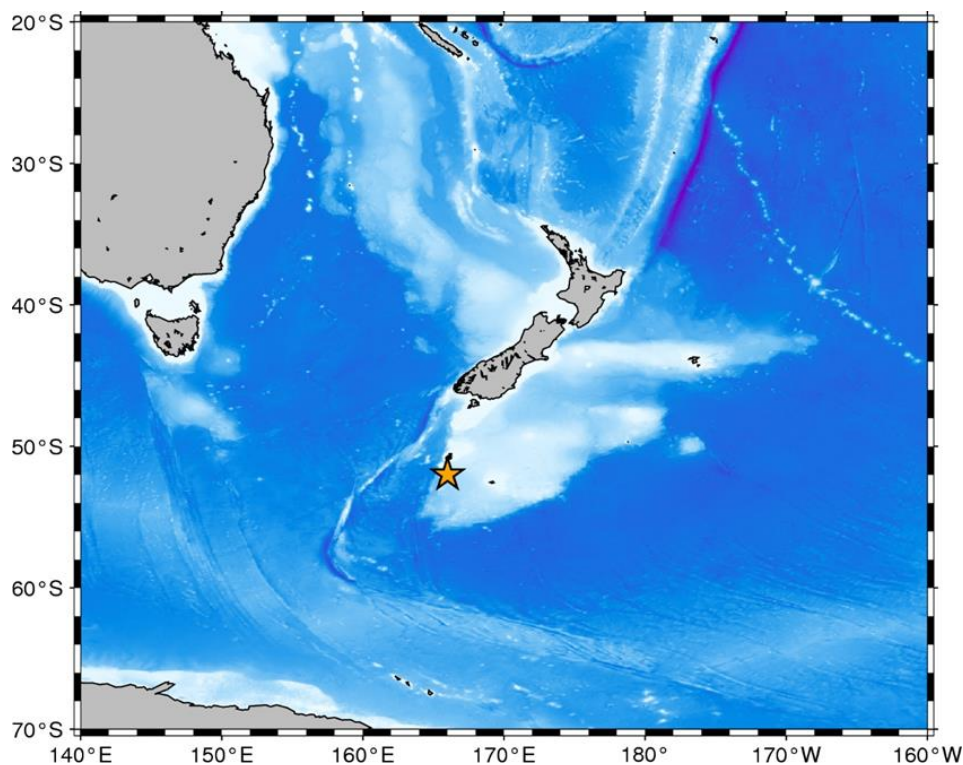


Figure 6.1. Location of International Ocean Drilling Program (IODP) Site U1553 at the Southern Campbell Plateau (orange star). The Map is made by using free software *The Generic Mapping Tools* (Wessel et al., 2019).

6.3.2 Nannofossil assemblage counts

Smear slides for calcareous nannofossil assemblage counts were prepared using the standard procedures outlined in Bown and Young (1998), predominantly from residues of the sediments used for bulk stable isotope analyses. 71 samples were taken from Site U1553, Hole C and investigations of Niederbockstruck et al. (2024) indicates that the studied interval, covering the hyperthermals K and I1, are located at 459.962 to 469.343 m CCSF, resulting in an average resolution of 13.2 cm/ 15.5 kyr. All slides were examined at 1200x magnification under plane-polarized and cross-polarized light with an Olympus BX51 microscope. At least 400 specimens were counted and identified to species level in each sample, using the taxonomic concepts compiled in the online database Nannotax3 (<https://www.mikrotax.org/Nannotax3/>).

6.3.3. Statistical analyses

As rare taxa tend to produce outliers in multivariate analyses, all genera with a relative mean abundance of < 1% were removed prior to statistical analyses. The seven genera: *Coccolithus*, *Toweius*, *Zygrhablithus*, *Chiasmolithus*, *Sphenolithus*, *Discoaster* and *Cyclicargolithus* represent 98.19% of the assemblage. However, the relative abundance is heterogeneously distributed with three genera of very high abundance, each of above 23% and four genera with low abundance of less than 10%.

To decrease the influence of dominant genera for the hierarchical clustering, the relative abundance data was standardized/scaled using z-scores as follows:

$$z = (x - \mu) / \sigma$$

With x = value of the genus in a sample, μ = the mean of the genus and σ = the standard deviation of the genus.

The hierarchical clustering was performed with Python using the *Scikit-learn* package (Pedregosa et al., 2011). The Euclidean distance measure and Ward's linkage method was utilized to generate more clear and compact groups compared to other methods (McCune and Grace, 2002).

To examine the main components that are responsible for assemblage changes, we performed a Principal Component Analyses (PCA) on the relative abundance of the genera. The PCA was made for normal distributed data, so that a dataset should be normalized towards a more symmetric distribution for interpretation (Legendre and Legendre, 2012). Strong deviations from a symmetric dataset will affect the result of the PCA in a negative way (Hammer and Harper, 2007). Our dataset of the relative nannofossil assemblage is more positive than negative skewed (see Chapter 11). A normalizing

transformation reshapes the distribution towards a Gaussian distribution. For a positive skewness, root transformation and for negative skewness a log-transformation is suggested (Bialik et al., 2021). In our case we apply a square-root transformation on the relative abundance data to reduce the positive skewing. The square-root transformation and the PCA were performed using python package *Scikit-learn* (Pedregosa et al., 2011).

We constructed a correlation matrix using the Pearson correlation coefficient r , which measures the linear relationship between variables with $r= 1$ positive linear relationship, $r= -1$ negative linear relationship and $r= 0$ meaning no linear relationship. The scores of the datasets were not standardized since the linear relationship is not affected by the scale of the scores. The correlation matrix was performed using the Python package *pandas* (The pandas development team, 2024).

We used XRF-derived elements (Röhl et al., 2022) to calculate Ca/Fe and Si/Fe ratio as they are used as rough estimates of paleoproductivity (Marsh et al., 2007; Agnihotri et al., 2008; Boulila et al., 2018; Vahlenkamp et al., 2020).

6.4. Results

Although we identified all specimens to species-level, we chose to statistically analyze our data at the genus-level, as this has been shown to provide more reliable, robust and meaningful results that are more comparable to other sites (Gibbs et al., 2012). Nannofossil assemblages during the early Eocene (52.7 to 53.8 Ma) at Site U1553 consist of 26 genera, of which only 7 genera (*Coccolithus*, *Toweius*, *Zygrhablithus*, *Chiasmolithus*, *Sphenolithus*, *Discoaster* and *Cyclicargolithus*) have a mean abundance of > 1%. Together, these 7 genera represent 98.19% of the overall assemblage. The preservation of the calcareous nannofossils is moderate to good without no major variance observed.

6.4.1. Hierarchical Clustering

The hierarchical clustering separates the calcareous nannofossil genera into two main groups along the x-axis (A and B; Figure 6.2). Group A consists of *Zygrhablithus* and *Sphenolithus*, while Group B is further divided into subgroups: [*Coccolithus* and *Chiasmolithus*], both belonging to the order Coccolithales; [*Toweius* and *Cyclicargolithus*], belonging to the order Isochrysidales; and [*Discoaster*], closely linked to the subgroup of [*Toweius* and *Cyclicargolithus*].

Along the y-axis, samples are divided into two main groups (Figure 6.2) with 30 samples belonging to assemblage Group 1 (brown) and 41 samples belonging to assemblage Group 2 (blue).

Group 1 is characterized by a relatively low abundance of *Zygrhablithus* and a generally high abundance of *Chiasmolithus*. Group 1 is further divided into three subgroups. Subgroup 1.1 contains

only three samples, characterized by the highest relative abundance of *Cyclicargolithus* in the record. Subgroup 1.2 represents the main body of Group 1, distinguished by the low abundance of *Zygrhablithus* and the notable presence of both *Chiasmolithus* and *Coccolithus*. Subgroup 1.3 includes samples with the highest abundance of *Discoaster* and a few samples with low abundance of *Chiasmolithus* within Group 1.

In contrast, Group 2 is characterized by a relatively high abundance of *Zygrhablithus*. Group 2.1 shows a relatively high abundance of *Coccolithus* along with a low abundance of *Sphenolithus*; however, the relative abundance of *Zygrhablithus* is lower compared to the other subgroups of Group 2. Group 2.2 is marked by the dominance of *Zygrhablithus* compared to other genera. Contrary to Group 2.1, Group 2.3 contains samples with the lowest abundance of *Coccolithus* but a relatively high abundance of *Sphenolithus*. Within Group 2, which generally exhibits a low abundance of *Toweius*, samples 67 and 70 stand out, containing the highest relative abundance of *Toweius* in the entire record.

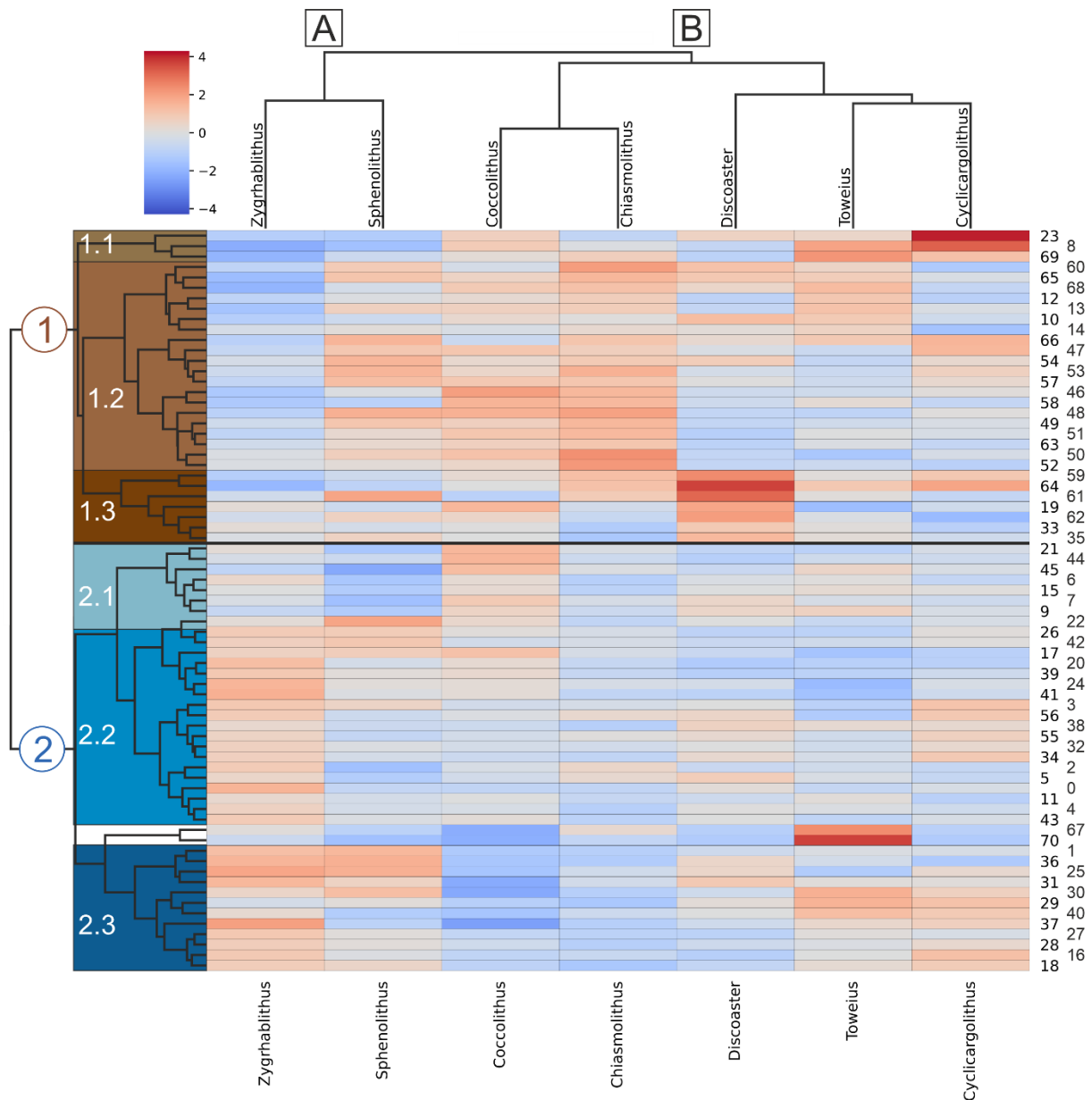


Figure 6.2. Two-way cluster analysis on scaled calcareous nannofossil assemblage with clustering of the genera along the horizontal axis and the clustering of the samples on the vertical axis.

6.4.2 Principle Component Analyses

The PCA reveals that the first two axis 1 and 2 explain more than two-thirds of the assemblage variance (Table 6.1). The PCA shows that the first two principal components contribute to two-thirds of the variance (Table 6.1). PC1 (46.75%) is mainly characterized by a negative loading of *Zygrhablithus* (-0.85) and, to a lesser extent, positive loadings of *Chiasmolithus* (0.36), *Toweius* (0.29), and *Coccolithus* (0.25) (Figure 6.3). *Discoaster*, *Sphenolithus*, and *Cyclicargolithus* have minor contributions of 0.08, -0.06, and 0.05, respectively. The negative and positive loadings reflect nannofossil Groups A and B. The scores of PC1 show a decrease in the studied interval at 53.42 Ma and an increase between 52.86 and 52.75 Ma.

Table 6.1 Summary of the PCA showing Eigenvalues and relative Variance.

Axis	Eigenvalue	Expl. Variance %	Cumulative %
1	0.0095973	46.752045	46.752045
2	0.00431412	21.015716	67.767761
3	0.00271599	13.230621	80.998382
4	0.00184641	8.994548	89.99293
5	0.00107942	5.258242	95.251172
6	0.00093965	4.577392	99.828564
7	3.5192E-05	0.171436	100

PC2 (21.02%) is mainly characterized by positive loadings of *Toweius* (0.72) and negative loadings of *Coccolithus* (-0.53), *Chiasmolithus* (-0.39), and *Sphenolithus* (-0.19). To a lesser extent, PC2 is characterized by *Cyclicargolithus*, *Zygrhablithus*, and *Discoaster* with 0.06, -0.06, and 0.01, respectively. The scores of PC2 are elevated twice between 53.67 and 53.32 Ma and 53.13 and 52.89 Ma, with negative scores in between.

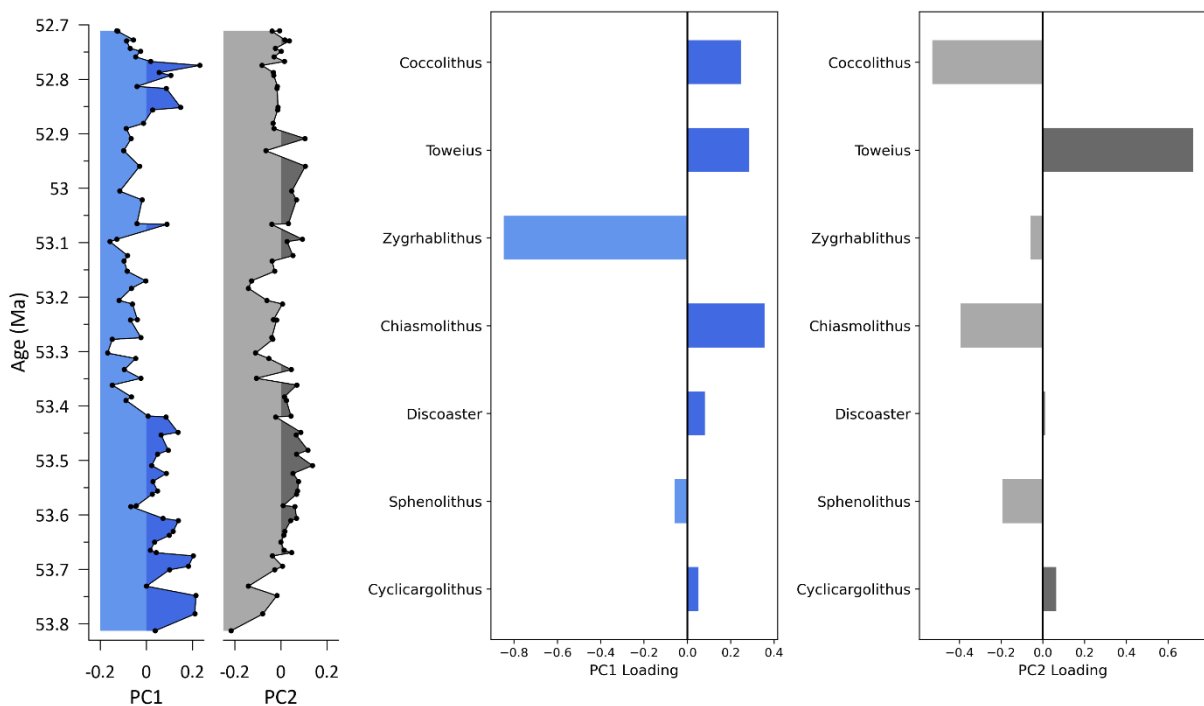


Figure 6.3. Results of Principle Component Analyses on calcareous nannofossil assemblage. On the left: Distribution of PC1 (blue) and PC2 (grey) along the studied interval. On the right: The loading plots of PC1(blue) and PC2 (grey).

The calcareous nannofossil assemblage shows changes throughout the 1.1 Ma interval (Figure 6.4). The relative abundance of *Coccolithus* varies between 24% and 48%. *Toweius* has its highest

abundance at 53.8 Ma with more than 48%, but decreases to around 24% at 53.5 Ma and remains relatively low for the rest of the record.

Zygrhablithus ranges between 7% and 40%, with low abundances at the beginning of the record and an increase towards younger times.

Chiasmolithus never exceeds a relative abundance of 9% of the assemblage. *Chiasmolithus* is relatively abundant during the first 400 kyr from 53.8 to 53.4 Ma. From that point onward, its relative abundance stays rather low until 52.7 Ma.

Similar to *Chiasmolithus*, *Discoaster* never exceeds a relative abundance of 9%, with its highest relative abundance between 53.75 and 53.55 Ma.

Sphenolithus shows no major trend except a decline at 53.45 Ma, fluctuating between 0% and 5% throughout the record.

Cyclicargolithus appears to be the most constant genus among the seven, with no major increase or decrease, ranging between 1% and 6%.

We observe that the major change from positive to negative scores in PC1 around 53.42 Ma coincides with the change from Group 1 (brown) dominated assemblage to Group 2 (blue) dominated assemblage, that is mainly characterized by the increase of *Zygrhablithus* and decrease in *Chiasmolithus* in the calcareous nannofossil assemblage (Figure 6.4 – dashed horizontal line). The scores of PC2 resembles positively the trend of *Coccolithus* and negatively the trend of *Toweius*.

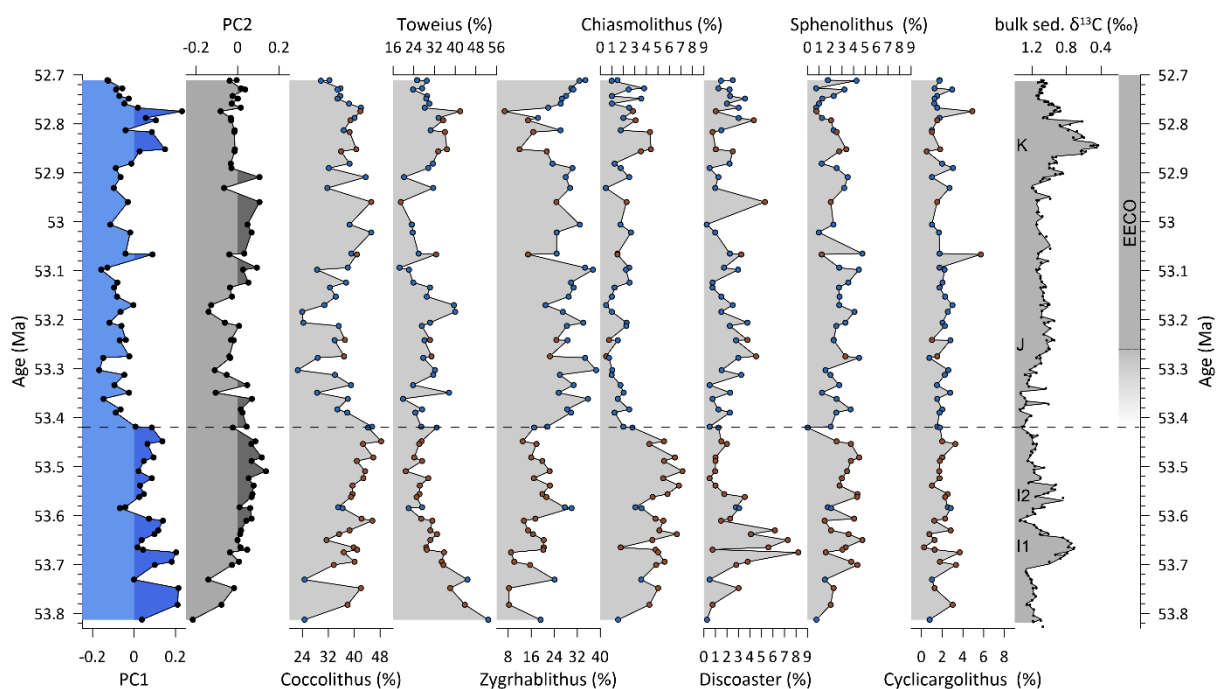


Figure 6.4. PC1 and PC2 scores along the relative calcareous nannofossil assemblage along the studied time interval. The blue and brown dots refer two Group1 and Group 2 of the hierarchical clustering. Note the different scales on the x-axis. Bulk sediment $\delta^{13}\text{C}$ on a 3point running average are from (Niederbockstruck et al., 2024). Onset of the EECO at 53.26 Ma according to Westerhold et al. (2017).

6.5. Discussion

The productivity of calcareous nannoplankton is not hampered during CIEs as studies have shown for the PETM (Gibbs et al., 2006; Stoll et al., 2007; Gibbs et al., 2010) or H1 (Dedert et al., 2012), leading to the assumption of a generally high resilience of calcareous nannoplankton to carbon perturbations (Newsam et al., 2017; Slater et al., 2022). However, several studies across the oceans show that despite their productivity, certain taxa and the assemblages are associated to certain environmental conditions during the early Eocene (e.g., Wei and Wise, 1990; Aubry, 1998; Bralower, 2002; Villa et al., 2008; Schneider et al., 2011, 2013; D’Onofrio et al., 2016). Our analysis reveals a dominance of the genera *Coccolithus* and *Toweius* in the assemblage at Site U1553, with *Coccolithus* identified as the most abundant overall. The dominance within the assemblage of both genera is also observed at Walvis Ridge around the H1 event (Dedert et al., 2012), and for the PETM in the western Tarim Basin (Wang et al., 2023). At low- mid-latitude ODP Site 1260b on Walvis Ridge, *Coccolithus pelagicus* and *Toweius* spp. emerged as the predominant taxa of the assemblage during the calcareous nannofossil zones NP9 and NP10 (~ 54 to 57 Ma), suggesting similar ecological preferences (Mutterlose et al., 2007). Their dominance within different oceans from low to high latitudes through the Eocene underscores the high ubiquity and adaptation to environmental conditions. However, a notable negative correlation (-0.64; Mutterlose et al., 2007) between *Coccolithus* and *Toweius* shows the competition of both genera, with the interpretation that *C. pelagicus* favored comparatively warmer surface waters than *Toweius* (Mutterlose et al., 2007) while both may have bloomed under eutrophic conditions (Self-Trail et al., 2012; Villa et al., 2014). Our observations agree to those findings, with a negative correlation of *Coccolithus* and *Toweius* (-0.38)(Figure 6.5) and strong opposite loadings on PC2 (Figure 6.3). *Coccolithus* is the sole genus among the seven still extant in the oceans today, further highlighting its ecological adaptability. Presently, *Coccolithus pelagicus* is classified as a cold-water species, predominating in assemblages within (sub)Arctic regions (Baumann et al., 2000; Balestra et al., 2004).

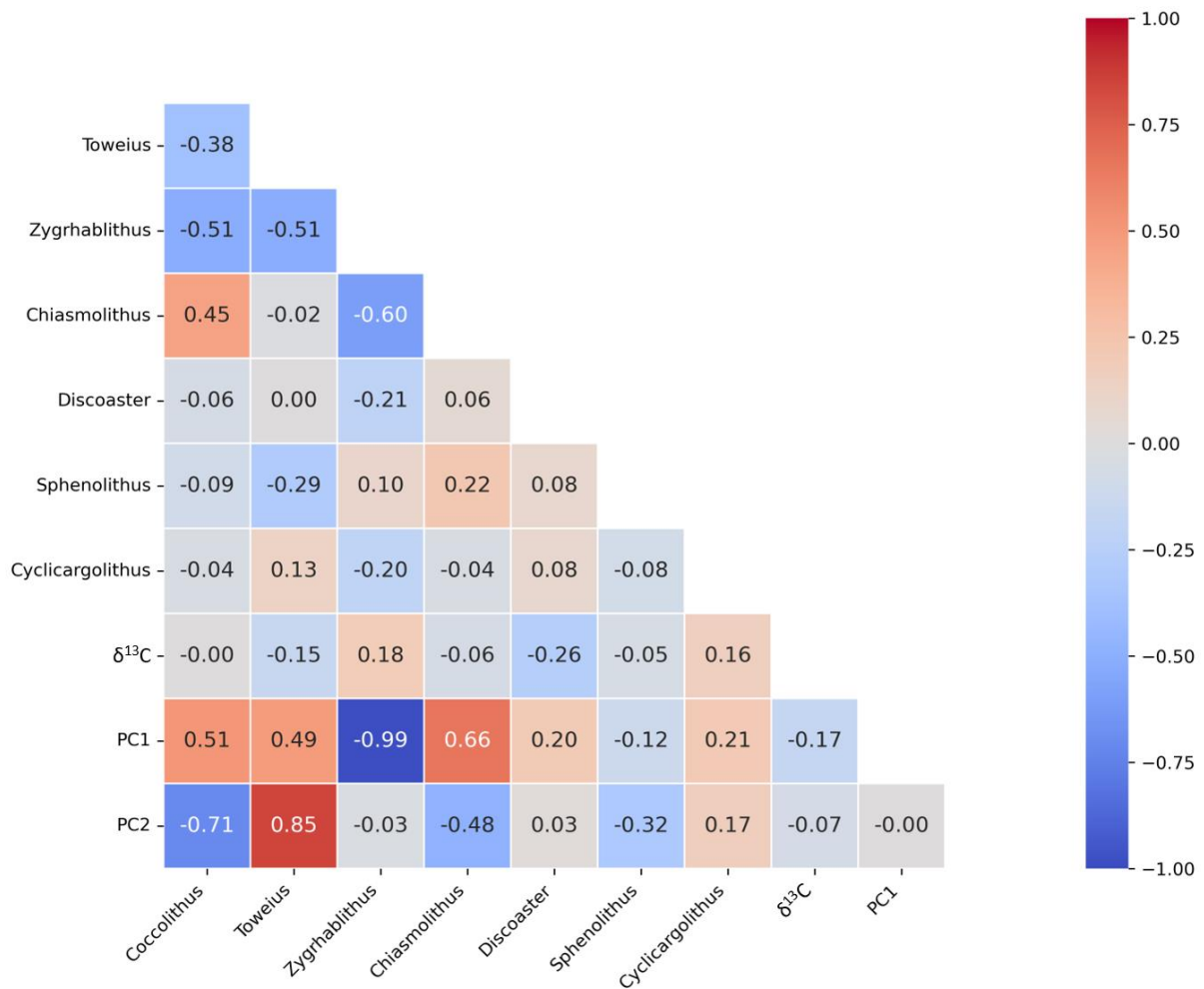


Figure 6.5. Pearson correlation of the seven genera, linear interpolated $\delta^{13}\text{C}$ of bulk sediment and scores of PC1 and PC2. Red colors indicate positive correlation with 1 meaning a fully linear correlation and -1 a perfect negative linear correlation.

Our findings indicate a pronounced increase in the relative abundances of warm water taxa such as *Discoaster* during the I1 and J event, and an increase in *Sphenolithus* during the hyperthermal events I2 and K. Both taxa were often combined as a proxy for warm water conditions (e.g., Shepherd et al., 2021). Further, *Coccolithus* is considered to favor warm water (Aubry, 1998) and eutrophic conditions (Jiang and Wise, 2006; Villa et al., 2014) and has high abundance during the hyperthermals and lower abundance during background conditions prior and past the J event at Site U1553. These patterns, combined with a noted prevalence of *Chiasmolithus* during I1, I2 and K points to warm and eutrophic conditions during the CIEs. In addition, the oligotrophic genus *Zygrhablithus* (Villa et al., 2008; Agnini et al., 2009) shows decreased abundances during I1, I2, during the peak of J event and during the K event. This observation lead to the hypothesis, that ocean surface conditions during CIEs were warm and eutrophic at Site U1553. A study from the Terche section (northeastern Italy) observe similar findings with increased warm and eutrophic taxa during the hyperthermals H1, H2 and I1 (D’Onofrio et al., 2016). Additionally, the nutrient enrichment is further supported by the occurrence of

radiolarians, pointing to nutrient supply and enhanced siliceous productivity in the surface waters (D'Onofrio et al., 2016). Analogous to the Terche section (D'Onofrio et al., 2016), there is evidence of enhanced nutrient supply, siliceous and carbonate productivity at Site U1553 by increased XRF Si/Ti and Ca/Fe (Figure 6.6), which peaks during the hyperthermal events I1, I2, J and K. A productivity optimum of calcareous nannoplankton during the hyperthermal event H1 is also indicated for the South Atlantic from Sr/Ca measurements (Dedert et al., 2012).

6.5.1. Hyperthermals I1 and I2

The interval of the paired hyperthermals I1 and I2 is the main period during which Group 1 is present. During the I1 hyperthermal, we observed the highest abundance of the warm-water taxon *Discoaster* throughout the entire record. This is surprising given that the K event is the largest of the Carbon Isotope Excursions (CIEs), and it was expected to see the highest abundance of *Discoaster* during that event. The correlation between bulk $\delta^{13}\text{C}$ and relative abundance is generally quite low, with the highest being for *Discoaster* (-0.26). This weak correlation suggests that the calcareous nannofossil assemblage is less sensitive to environmental perturbations and/or is not primarily affected by temperature. This interval of the paired hyperthermals is especially characterized by the high abundance of *Chiasmolithus* and the low abundance of *Zygrhablithus*. *Chiasmolithus* was found to be nearly absent at low- to mid-latitude sites throughout the Eocene, but present at high-latitude sites, indicating a preference for cooler waters. A comprehensive study by Schneider et al. (2011) revealed that *Chiasmolithus* became more dominant at high-latitude sites during the early Eocene, including the EECO and early part of the middle Eocene, before decreasing in abundance towards the late Eocene. Although *Chiasmolithus* exhibits its highest abundance at high-latitude sites, it tends to increase its relative abundance during hyperthermals and the generally warmer conditions. This suggests a more complex interplay between environmental conditions and competition. Self-Trail et al. (2012) proposed that the increased abundance of *Chiasmolithus* during the Paleocene-Eocene Thermal Maximum (PETM) at Maud Rise, Site 690 (Bralower, 2002), could be attributed to a refugium effect, where high-latitude sites provided a retreat during periods of extreme global warmth. However, the relatively high abundance of *Chiasmolithus* during I1 and I2, which only reappeared briefly (< 50 kyrs) during the K event, implies that either: 1) *Chiasmolithus* is not predominantly affected by temperature, or 2) the surface waters of the Southwest Pacific were eutrophic, which was a more controlling factor compared to temperature for *Chiasmolithus*.

6.5.2. Major shift in calcareous nannofossil assemblage and the onset of the EECO

Although EECO records are found around the world, the onset and duration are still challenging and not absolutely defined (Luciani et al., 2016; Westerhold et al., 2018). Nevertheless, the onset of the EECO has been associated with the J event, by a decrease of benthic foraminifera $\delta^{13}\text{C}$ and $\delta^{18}\text{O}$ at Site

1263 (Lauretano et al., 2015) and a lithological change from limestone to marl at Mead Stream, New Zealand (e.g., Slotnick et al., 2012). Increased warming conditions might challenge the planktic taxa for adaptation as it is observed in turnover of planktic foraminifera assemblage close to the J event on the Walvis Ridge and the Possagno section (Luciani et al., 2016, 2017). In both studies, planktic foraminifera assemblage changes with the onset of the J event, highlighted by the abundance switch of *Morozovella* and *Acarinina*. In addition, a distinct decrease of *Morozovella* ~20 kyr before the J event is observed (D’Onofrio et al., 2020). The biggest change in the calcareous nannofossil assemblage is the switch from assemblage Group 1 to Group 2 at ~53.42 Ma, coinciding with the major change in PC1: 120 kyrs before the onset of the J event. This major assemblage shift is predominantly driven by changes of *Zygrhablithus*, as seen in the loadings of PC1 (Figure 6.3), the negative linear correlation (-0.99) for *Zygrhablithus* and PC1, the relative abundances of *Zygrhablithus* and *Chiasmolithus* (Figure 6.4) and their ratio (Figure 6.6). The decrease and near-absence of *Chiasmolithus* towards the EECO and the high abundance of *Zygrhablithus* implies general environmental change, which possibly overprints the potential effect of hyperthermals. That could also explain the reduced response of the calcareous nannofossil assemblage during the J and K event, compared to I1 and I2. Another explanation for a reduced response of calcareous nannoplankton to the J event might be the magnitude of an environmental perturbation. At the equatorial Pacific at ODP Site 1209, significant changes in calcareous nannofossil assemblages during the early Eocene are associated with CIEs greater than 0.6 ‰ (Gibbs et al. 2012) which does not apply for the J event. The EECO is characterized by lithological changes, rising temperatures, and shifts in planktic foraminifera assemblages, particularly associated with the J event (Lauretano et al., 2015; Slotnick et al., 2015; D’Onofrio et al., 2016; Westerhold et al., 2018). Although concrete evidence of a response by calcareous nannofossils to the onset of the EECO is lacking, it is notable that the major assemblage change is observed approximately 120 kyrs before the J event. This change is marked by a decrease in *Chiasmolithus* and an increase in *Zygrhablithus* (Figure 6). Our observation raises the question of whether the assemblage change is triggered by an unknown event between I2 and J, or if it can be linked to the long-term perturbation of the EECO, occurring 120 kyrs before the suggested onset that is coinciding with the J event.

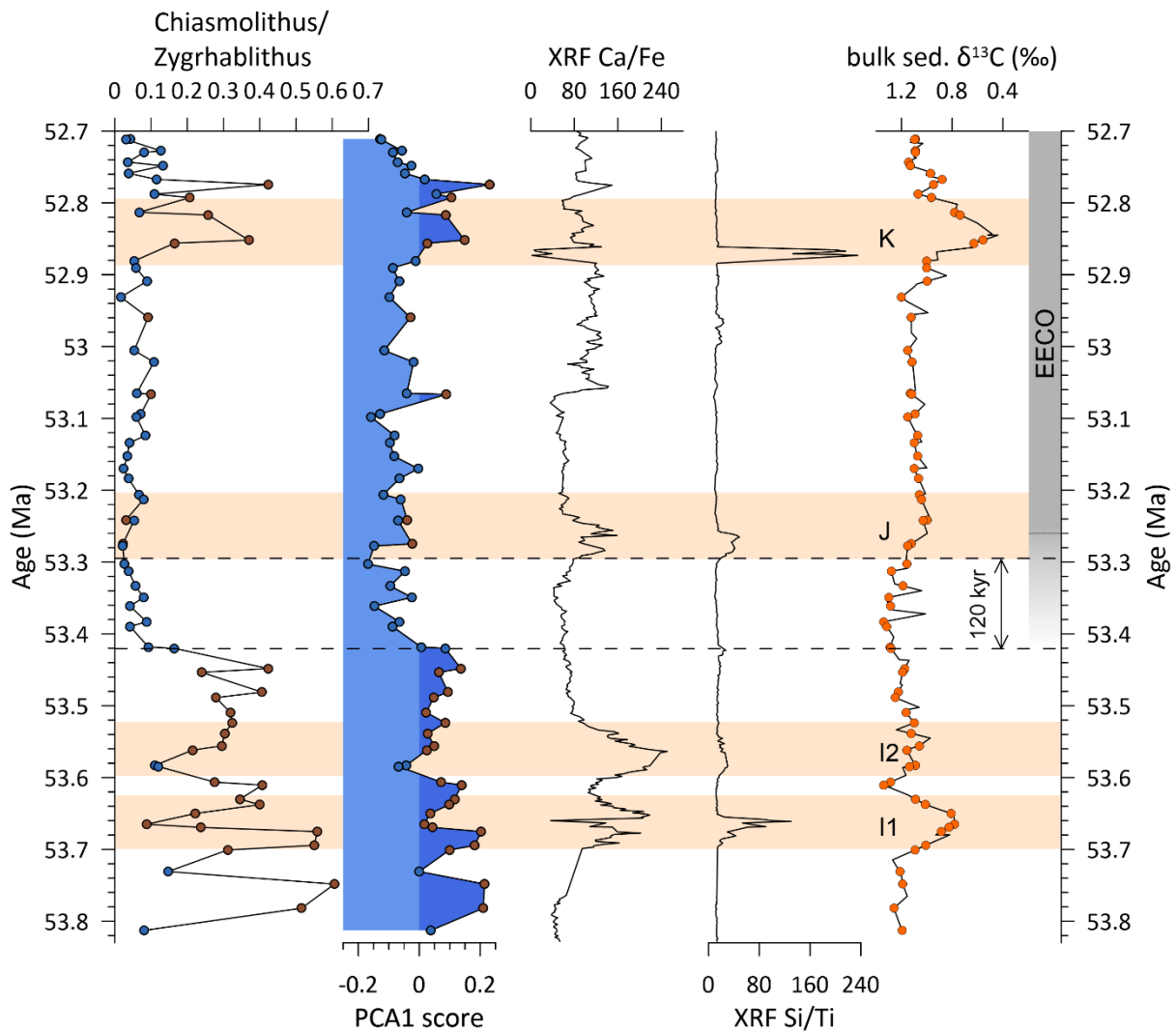


Figure 6.6. Ratio of the genera *Chiasmolithus* and *Zygrhablithus*, a distinct characteristic of the assemblage Group 1 (brown dots) and 2 (blue dots). PC1 scores with highlighted Group 1 and 2. XRF derived Ca/Fe and Si/Ti as indicator for carbonate and siliceous productivity. Bulk sediment $\delta^{13}\text{C}$ and the linear interpolated values of $\delta^{13}\text{C}$ for each sample (orange dots). Onset of the EECO at 53.26 Ma according to Westerhold et al. (2018).

6.5.3. Changing conditions in response to the K event in the Southwest Pacific

Although long-term records spanning several million years from the Eocene have been documented for the Southwest Pacific (Shepherd et al., 2021), high-resolution assemblage studies on orbital timescales remain limited. Alegret et al. (2021) conducted a detailed high-resolution study of calcareous nannofossil assemblages during the K, S, T, and U hyperthermal events at the Lord Howe Rise, Site U1510. The high carbonate content at Site U1553 (Röhl et al., 2022) and Site U1510 (Alegret et al., 2021) provides a good opportunity for comparison without the possible impact of carbonate dissolution (Alegret et al., 2021). This study revealed notable similarities in the relative abundances of seven genera during the K event, thereby enhancing confidence in the interpretation of regional responses of the assemblage to hyperthermal events.

A comparison of both sites shows a high relative abundance of *Sphenolithus*, *Chiasmolithus*, and *Toweius*, alongside a decrease in *Discoaster* during the peak of the K event (Figure 6.7). However, the abundance pattern of *Zygrhablithus* diverged between the records. At Site U1553, *Zygrhablithus* showed a decrease during the peak of the K event and an increase before and after, whereas at Site U1510, the pattern appeared inverted. This discrepancy may be attributed to carbonate overgrowth at Site U1510 (Alegret et al., 2021) which occurs during hyperthermal events (Kelly et al., 2005). Nevertheless, the relative abundance of *Zygrhablithus* at Site U1510 during the K event remained lower compared to its post-event increase. The observed increase in *Sphenolithus* suggests a response to enhanced warming, whereas the rise in *Chiasmolithus* and *Toweius* indicates a shift towards more mesotrophic/eutrophic conditions. This is consistent with the observed decrease in *Zygrhablithus*, which is typically associated with oligotrophic surface waters.

The presence of eutrophic nannofossil assemblages during the early Eocene CIEs has been observed at several shelf/shallow marine sites, while, in contrast, open-ocean sites generally suggest a decrease in surface ocean nutrients due to enhanced thermal stratification (Stoll and Bains, 2003; Gibbs et al., 2006; Dedert et al., 2012). The warm, high-nutrient surface oceans conditions suggested by calcareous nannofossil assemblages at Site U1553 support these observations, as the southern Campbell Plateau had a relatively shallow paleowater depth (< 1000 m; Hollis 1997), located south of New Zealand. Although *Discoaster* is generally considered to favor warmer waters, its reduced abundance at both sites during the peak of the K event, similar to I2, suggests the increased influence of nutrient availability over temperature on nannofossil community composition at Site U1553. These findings are interesting since temperature is often cited as a primary driver for changes in calcareous nannofossil assemblage (e.g., Wei and Wise, 1990; Clark and Watkins, 2020). However, our observation agrees with studies from the North Atlantic, in which middle Eocene calcareous nannofossil assemblages are not primarily driven by temperature, but rather controlled by the nutrient level (Newsam et al., 2017) and the increase of terrigenous input and the intensification of the hydrological cycle (Intxauspe-Zubiaurre et al., 2017).

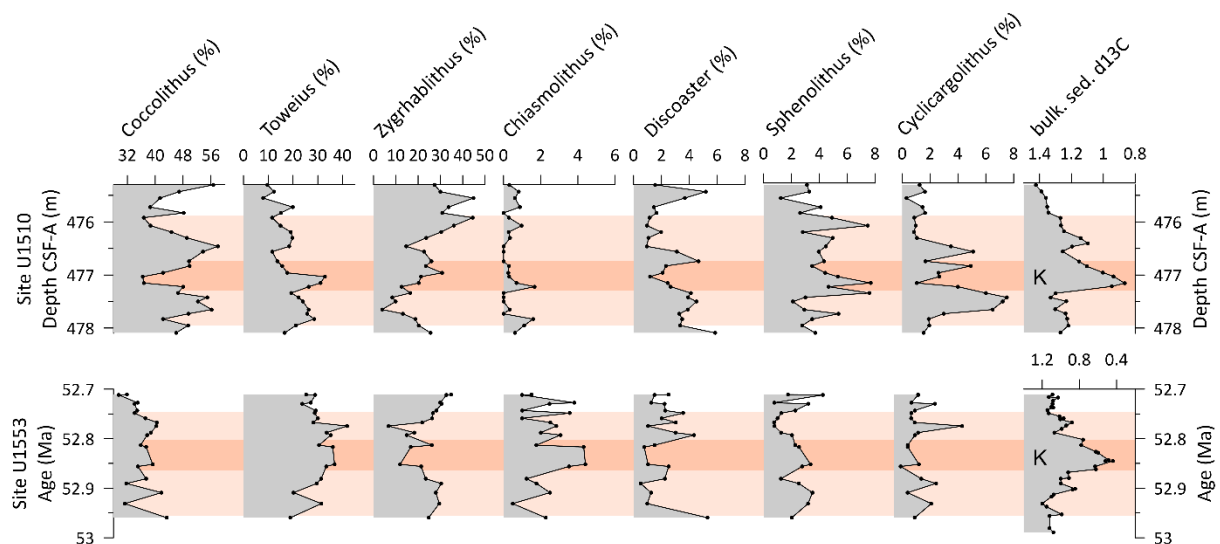


Figure 6.7. Relative abundance of the calcareous nannofossil assemblage for the South Pacific at Site U1510 (Alegret et al., 2021) and Site U1553 (this study) during the hyperthermal event K. Light background show the correlated interval and dark background highlight peak conditions of the K event.

Overall, the congruence in the pattern of relative abundance among several genera across both sites before, during, and after the K event, with the exception of *Coccolithus*, suggests that similar environmental conditions prevailed at both sites. Under modern conditions, the Southwest Pacific surface waters are characterized by oceanic fronts, separating Site U1510, located in subtropical waters, and Site U1553, located in subantarctic waters, divided by the Subtropical Front. However, the presence of oceanic fronts during the early Eocene is under debate. Nelson and Cooke (2001) detected a separation of subtropical and subantarctic waters only after the late Eocene (35 Ma) at $\sim 65^{\circ}\text{S}$. Conversely, other studies discuss the presence of a cool, northward-flowing Tasman Current during the early Eocene, with Jenkins (1993) suggesting a transition zone at least separating warm and cool subtropical waters during this period.

Sites U1510 and U1553 might have been influenced by the same warm proto-East Australian Current, based on the ratio of warm and cool water taxa of calcareous nannofossils at nearby sites DSDP 207 and 277 (Shepherd et al., 2021). Our findings, which show similar trends in the calcareous nannofossil assemblage during the K event, support this conclusion and indicate similar surface water conditions at both sites (Figure 6.8). The idea of an expanded warm proto-East Australian Current is further supported by reconstructions of sea surface temperatures along a 10° latitudinal transect of Zealandia, indicating the absence of a meridional SST gradient during the early Eocene (Hines et al., 2017), with SSTs around 30°C (Hines et al., 2017; Crouch et al., 2020).

The response of calcareous nannoplankton to the K event remains less pronounced compared to the paired hyperthermals I1 and I2. Compared to the J event, the K event exceeds the proposed threshold of 0.6‰ in $\delta^{13}\text{C}$ (Gibbs et al., 2012). Like the J event, the K event lies within the EECO and is dominated

by the assemblage Group 2. Similar to our observation in the Southwest Pacific, the response of calcareous nannofossils is also lower during the K event compared to ETM1 and ETM2 in the Southeast Atlantic (Thomas et al., 2018). The response of the calcareous nannoplankton to the K event might be diminished by the long-term increasing trend of sea surface temperatures and CO₂ during the onset of the EECO, which reduced the impact on environmental conditions during the K event. Alternatively, it is possible that calcareous nannoplankton developed increased resilience to hyperthermal events over time. It is also conceivable that there is a non-linear response of calcareous nannoplankton to the magnitude of hyperthermal events, where smaller hyperthermals might exert an equal or greater impact on assemblage composition.

53 Ma reconstruction

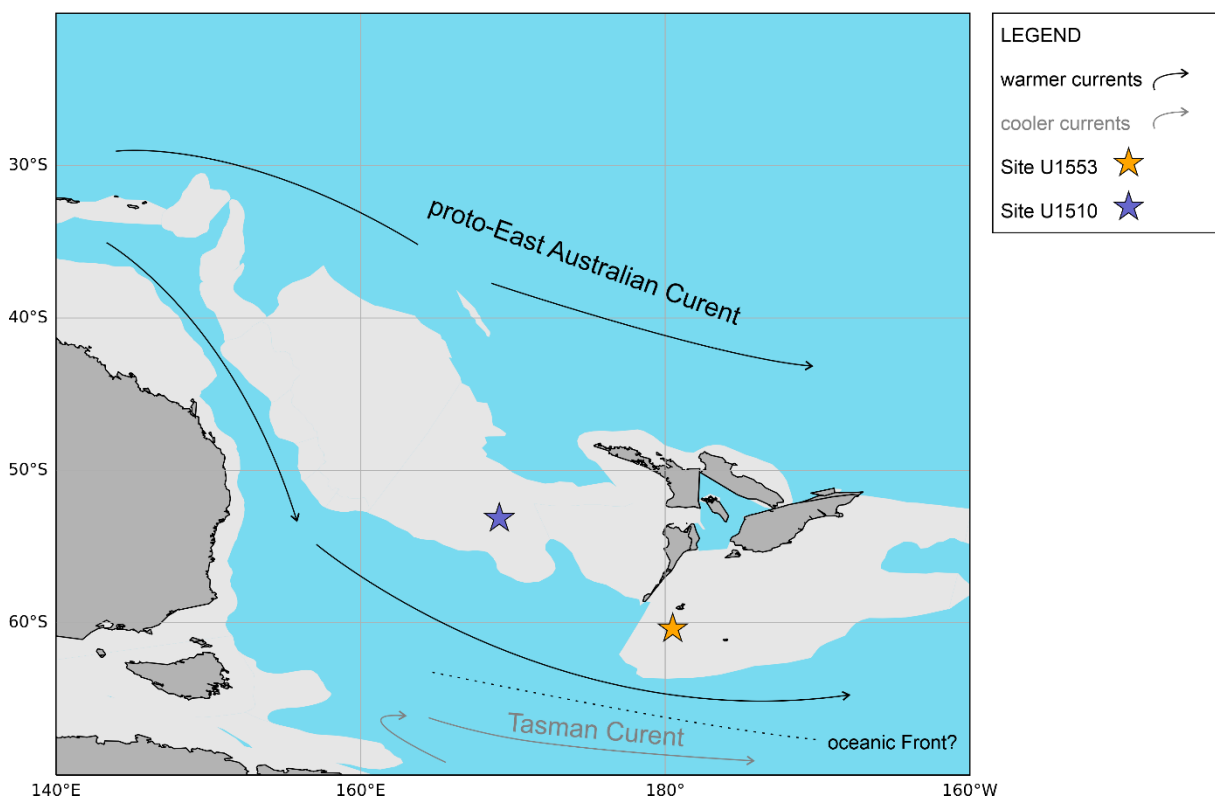


Figure 6.8. Paleoceanographic reconstruction of the Southwest Pacific. Light grey colors represent areas of continental crust. Dark grey areas show the present land and their paleo location. Paleomap is based on Hines et al. (2017), showing the expanded warm proto-East Australian Current and a potential cool Tasman current after Jenkins (1993). The reconstruction is made by using free software tool *GPlates* (Müller et al., 2018) by using the integrated combined rotation file (Cao et al., 2020; Müller et al., 2019; Torsvik et al., 2019; Young et al., 2019).

Several studies have indicated that changes in calcareous nannofossil assemblages are linked to environmental changes. However, we did not observe a clear response of calcareous nannoplankton to hyperthermal events, where the abundance of certain genera typically follows the trends of the bulk sediment $\delta^{13}\text{C}$ record, representative of hyperthermal events. The highest linear correlation with the $\delta^{13}\text{C}$ records was found in *Discoaster*, with a relatively low value of -0.26. Despite this, we observed a

preference for assemblage Group 1 during hyperthermal events I1, I2, and the onset of J and K. Additionally, positive scores of PC1 were noted from 53.82 to 53.44 Ma, including hyperthermals I1 and I2, and from 52.86 to 52.78 Ma, encompassing the K event, while the scores between these intervals were negative and dominated by Group 2. While Site U1553 was bathed in subtropical surface waters of the proto-Early Australian current throughout the studied interval, and the assemblage change was characterized by the interplay of *Zygrhablithus* and *Chiasmolithus*, we suggest that not temperature but the nutrient level of surface water was the main driver shaping the assemblage.

6.6. Conclusion

We present calcareous nannofossil assemblage record from 53.8 to 52.7 Ma from the western South Pacific at IODP Site U1553 to evaluate the response of marine biota to perturbations in the carbon cycle. The calcareous nannofossil assemblage can be divided into two main groups with Group 1 dominating the samples during the hyperthermal events I1, I2 and K, characterize by the relative high abundance of *Chiasmolithus* and low abundance of *Zygrhablithus*. Our data suggest that nutrient levels, rather than temperature, might be the primary driver for the changes in the assemblage. Our relative abundance data agrees with the study of IODP Site U1510, Tasman Sea, suggestion similar surface water conditions and supporting the idea of an intensified warm proto-East Australian current. Interestingly the major change in the assemblage appeared to between the two hyperthermals I2 and K around 53.44 Ma, ca 120 kyr before the onset of the EECO, leading to the hypothesis of an early signal of the EECO.

6.7. Acknowledgements

The samples for this study are provided by the International Ocean Discovery Program (IODP). We thank the crew and scientists of IODP Expedition 378 “South Pacific Paleogene Climate”. This study is funded by the Deutsche Forschungsgemeinschaft (DFG, German Research Foundation) under Germany's Excellence Strategy EXC-2077-390741603.

6.8. Data availability

Data of calcareous nannofossil assemblage can be found in chapter 11. Appendix.

Data sets of Alegret et al. (2021) are available online (<http://doi.org/10.17605/OSF.IO/H43WS>).

6.9. References

- Agnihotri, R., Altabet, M. A., Herbert, T. D., & Tierney, J. E. (2008). Subdecadally resolved paleoceanography of the Peru margin during the last two millennia. *Geochemistry, Geophysics, Geosystems*, 9(5). <https://doi.org/https://doi.org/10.1029/2007GC001744>
- Agnini, C., Fornaciari, E., Raffi, I., Rio, D., Röhl, U., & Westerhold, T. (2007). High-resolution nannofossil biochronology of middle Paleocene to early Eocene at ODP Site 1262: Implications for calcareous nanoplankton evolution. *Marine Micropaleontology*, 64(3), 215-248. <https://doi.org/https://doi.org/10.1016/j.marmicro.2007.05.003>
- Agnini, C., Macrì, P., Backman, J., Brinkhuis, H., Fornaciari, E., Giusberti, L., Luciani, V., Rio, D., Sluijs, A., & Speranza, F. (2009). An early Eocene carbon cycle perturbation at ~52.5 Ma in the Southern Alps: Chronology and biotic response. *Paleoceanography*, 24(2). <https://doi.org/https://doi.org/10.1029/2008PA001649>
- Agnini, C., Monechi, S., & Raffi, I. (2017). Calcareous nannofossil biostratigraphy: historical background and application in Cenozoic chronostratigraphy. *Lethaia*, 50(3), 447-463. <https://doi.org/https://doi.org/10.1111/let.12218>
- Agnini, C., Spofforth, D. J. A., Dickens, G. R., Rio, D., Pälike, H., Backman, J., Muttoni, G., & Dallanave, E. (2016). Stable isotope and calcareous nannofossil assemblage record of the late Paleocene and early Eocene (Cicogna section). *Clim. Past*, 12(4), 883-909. <https://doi.org/10.5194/cp-12-883-2016>
- Alegret, L., Harper, D. T., Agnini, C., Newsam, C., Westerhold, T., Cramwinckel, M. J., Dallanave, E., Dickens, G. R., & Sutherland, R. (2021). Biotic Response to Early Eocene Warming Events: Integrated Record From Offshore Zealandia, North Tasman Sea. *Paleoceanography and Paleoclimatology*, 36(8). <https://doi.org/10.1029/2020pa004179>
- Anagnostou, E., John, E. H., Babila, T., Sexton, P., Ridgwell, A., Lunt, D. J., Pearson, P. N., Chalk, T., Pancost, R. D., & Foster, G. (2020). Proxy evidence for state-dependence of climate sensitivity in the Eocene greenhouse. *Nature communications*, 11(1), 1-9.
- Anagnostou, E., John, E. H., Edgar, K. M., Foster, G. L., Ridgwell, A., Inglis, G. N., Pancost, R. D., Lunt, D. J., & Pearson, P. N. (2016). Changing atmospheric CO₂ concentration was the primary driver of early Cenozoic climate. *Nature*, 533(7603), 380-384. <https://doi.org/10.1038/nature17423>
- Aubry, M.-P. (1992). 13. Late Paleogene Calcareous Nanoplankton Evolution: A Tale of Climatic Deterioration. In R. P. Donald & A. B. William (Eds.), *Eocene-Oligocene Climatic and Biotic Evolution* (pp. 272-309). Princeton University Press. <https://doi.org/doi:10.1515/9781400862924.272>
- Aubry, M.-P. (1998). Early Paleogene calcareous nanoplankton evolution: a tale of climatic amelioration. *Late Paleocene-Early Eocene climatic and biotic events in the marine and terrestrial records*, 158-203.
- Babila, T. L., Penman, D. E., Hönisch, B., Kelly, D. C., Bralower, T. J., Rosenthal, Y., & Zachos, J. C. (2018). Capturing the global signature of surface ocean acidification during the Palaeocene–Eocene Thermal Maximum. *Philosophical Transactions of the Royal Society A: Mathematical, Physical and Engineering Sciences*, 376(2130), 20170072. <https://doi.org/doi:10.1098/rsta.2017.0072>
- Balestra, B., Ziveri, P., Monechi, S., & Troelstra, S. (2004). Coccolithophorids from the Southeast Greenland Margin (Northern North Atlantic): production, ecology and the surface sediment record. *Micropaleontology*, 50(Suppl_1), 23-34. https://doi.org/10.2113/50.Suppl_1.23

- Baumann, K. H., Andruleit, H., & Samtleben, C. (2000). Coccolithophores in the Nordic Seas: comparison of living communities with surface sediment assemblages. *Deep Sea Research Part II: Topical Studies in Oceanography*, 47(9), 1743-1772. [https://doi.org/https://doi.org/10.1016/S0967-0645\(00\)00005-9](https://doi.org/https://doi.org/10.1016/S0967-0645(00)00005-9)
- Bialik, O. M., Jarochovska, E., & Grossowicz, M. (2021). Ordination analysis in sedimentology, geochemistry and palaeoenvironment—Background, current trends and recommendations. *The Depositional Record*, 7(3), 541-563. <https://doi.org/https://doi.org/10.1002/dep2.161>
- Bijl, P. K., Schouten, S., Sluijs, A., Reichart, G. J., Zachos, J. C., & Brinkhuis, H. (2009). Early Palaeogene temperature evolution of the southwest Pacific Ocean. *Nature*, 461(7265), 776-779. <https://doi.org/10.1038/nature08399>
- Boulila, S., Vahlenkamp, M., De Vleeschouwer, D., Laskar, J., Yamamoto, Y., Pälike, H., Kirtland Turner, S., Sexton, P. F., Westerhold, T., & Röhl, U. (2018). Towards a robust and consistent middle Eocene astronomical timescale. *Earth and Planetary Science Letters*, 486, 94-107. <https://doi.org/https://doi.org/10.1016/j.epsl.2018.01.003>
- Bowen, G. J. (2013). Up in smoke: A role for organic carbon feedbacks in Paleogene hyperthermals. *Global and Planetary Change*, 109, 18-29. <https://doi.org/https://doi.org/10.1016/j.gloplacha.2013.07.001>
- Bown, P., & Pearson, P. (2009). Calcareous plankton evolution and the Paleocene/Eocene thermal maximum event: New evidence from Tanzania. *Marine Micropaleontology*, 71(1), 60-70. <https://doi.org/https://doi.org/10.1016/j.marmicro.2009.01.005>
- Bown, P., & Young, J. (1998). Techniques. U: Bown P.(ur.): Calcareous Nannofossil Biostratigraphy. In: Chapman and Hall, Kluwer Academic, London.
- Bown, P. R., Lees, J. A., & Young, J. R. (2004). Calcareous nannoplankton evolution and diversity through time. In H. R. Thierstein & J. R. Young (Eds.), *Coccolithophores: From Molecular Processes to Global Impact* (pp. 481-508). Springer Berlin Heidelberg. https://doi.org/10.1007/978-3-662-06278-4_18
- Bralower, T. J. (2002). Evidence of surface water oligotrophy during the Paleocene-Eocene thermal maximum: Nannofossil assemblage data from Ocean Drilling Program Site 690, Maud Rise, Weddell Sea. *Paleoceanography*, 17(2), 13-11-13-12. <https://doi.org/https://doi.org/10.1029/2001PA000662>
- Bukry, D. (1973). Low-attitude coccolith biostratigraphic zonation. Washington, DC, Initial Reports of the Deep Sea Drilling Project, 15, 127-149.
- Burke, K. D., Williams, J. W., Chandler, M. A., Haywood, A. M., Lunt, D. J., & Otto-Bliesner, B. L. (2018). Pliocene and Eocene provide best analogs for near-future climates. *Proceedings of the National Academy of Sciences*, 115(52), 13288-13293.
- Cao, X., Zahirovic, S., Li, S., Suo, Y., Wang, P., Liu, J., & Müller, R. D. (2020). A deforming plate tectonic model of the South China Block since the Jurassic. *Gondwana Research*, 102, 3–16. <https://doi.org/10.1016/j.gr.2020.11.010>
- Cappelli, C., Bown, P. R., Westerhold, T., Bohaty, S. M., de Riu, M., Lobba, V., Yamamoto, Y., & Agnini, C. (2019). The Early to Middle Eocene Transition: An Integrated Calcareous Nannofossil and Stable Isotope Record From the Northwest Atlantic Ocean (Integrated Ocean Drilling Program Site U1410).

Paleoceanography and Paleoclimatology, 34(12), 1913-1930.

<https://doi.org/https://doi.org/10.1029/2019PA003686>

Clark, W. B., & Watkins, D. K. (2020). A quantitative analysis of calcareous nannofossils across a late oligocene paleolatitudinal transect of the North Atlantic Ocean. *Marine Micropaleontology*, 158, 101892. <https://doi.org/https://doi.org/10.1016/j.marmicro.2020.101892>

Coccioni, R., Bancalà, G., Catanzariti, R., Fornaciari, E., Frontalini, F., Giusberti, L., Jovane, L., Luciani, V., Savian, J., & Sprovieri, M. (2012). An integrated stratigraphic record of the Palaeocene–lower Eocene at Gubbio (Italy): new insights into the early Palaeogene hyperthermals and carbon isotope excursions. *Terra Nova*, 24(5), 380-386. <https://doi.org/https://doi.org/10.1111/j.1365-3121.2012.01076.x>

Cramer, B. S., Wright, J. D., Kent, D. V., & Aubry, M.-P. (2003). Orbital climate forcing of $\delta^{13}\text{C}$ excursions in the late Paleocene–early Eocene (chrons C24n–C25n). *Paleoceanography*, 18(4). <https://doi.org/https://doi.org/10.1029/2003PA000909>

Cramwinckel, M. J., Huber, M., Kocken, I. J., Agnini, C., Bijl, P. K., Bohaty, S. M., Frieling, J., Goldner, A., Hilgen, F. J., Kip, E. L., Peterse, F., van der Ploeg, R., Röhl, U., Schouten, S., & Sluijs, A. (2018). Synchronous tropical and polar temperature evolution in the Eocene. *Nature*, 559(7714), 382-386. <https://doi.org/10.1038/s41586-018-0272-2>

Crouch, E. M., Shepherd, C. L., Morgans, H. E. G., Naafs, B. D. A., Dallanave, E., Phillips, A., Hollis, C. J., & Pancost, R. D. (2020). Climatic and environmental changes across the early Eocene climatic optimum at mid-Waipara River, Canterbury Basin, New Zealand. *Earth-Science Reviews*, 200, 102961. <https://doi.org/https://doi.org/10.1016/j.earscirev.2019.102961>

D'Onofrio, R., Luciani, V., Fornaciari, E., Giusberti, L., Boscolo Galazzo, F., Dallanave, E., Westerhold, T., Sprovieri, M., & Telch, S. (2016). Environmental perturbations at the early Eocene ETM2, H2, and I1 events as inferred by Tethyan calcareous plankton (Terche section, northeastern Italy). *Paleoceanography*, 31(9), 1225-1247. <https://doi.org/https://doi.org/10.1002/2016PA002940>

DeConto, R. M., Galeotti, S., Pagani, M., Tracy, D., Schaefer, K., Zhang, T., Pollard, D., & Beerling, D. J. (2012). Past extreme warming events linked to massive carbon release from thawing permafrost. *Nature*, 484(7392), 87-91. <https://doi.org/10.1038/nature10929>

Dedert, M., Stoll, H. M., Kroon, D., Shimizu, N., Kanamaru, K., & Ziveri, P. (2012). Productivity response of calcareous nannoplankton to Eocene Thermal Maximum 2 (ETM2). *Clim. Past*, 8(3), 977-993. <https://doi.org/10.5194/cp-8-977-2012>

Dickens, G. R., O'Neil, J. R., Rea, D. K., & Owen, R. M. (1995). Dissociation of oceanic methane hydrate as a cause of the carbon isotope excursion at the end of the Paleocene. *Paleoceanography*, 10(6), 965-971. <https://doi.org/https://doi.org/10.1029/95PA02087>

Dunkley Jones, T., Ridgwell, A., Lunt, D. J., Maslin, M. A., Schmidt, D. N., & Valdes, P. J. (2010). A Palaeogene perspective on climate sensitivity and methane hydrate instability. *Philosophical Transactions of the Royal Society A: Mathematical, Physical and Engineering Sciences*, 368(1919), 2395-2415. <https://doi.org/doi:10.1098/rsta.2010.0053>

Erba, E., Bottini, C., Weissert, H. J., & Keller, C. E. (2010). Calcareous Nannoplankton Response to Surface-Water Acidification Around Oceanic Anoxic Event 1a. *Science*, 329(5990), 428-432. <https://doi.org/doi:10.1126/science.1188886>

Farnsworth, A., Lunt, D. J., O'Brien, C. L., Foster, G. L., Inglis, G. N., Markwick, P., Pancost, R. D., & Robinson, S. A. (2019). Climate Sensitivity on Geological Timescales Controlled by Nonlinear Feedbacks

and Ocean Circulation. *Geophysical Research Letters*, 46(16), 9880-9889. <https://doi.org/https://doi.org/10.1029/2019GL083574>

Galeotti, S., Krishnan, S., Pagani, M., Lanci, L., Gaudio, A., Zachos, J. C., Monechi, S., Morelli, G., & Lourens, L. (2010). Orbital chronology of Early Eocene hyperthermals from the Contessa Road section, central Italy. *Earth and Planetary Science Letters*, 290(1), 192-200. <https://doi.org/https://doi.org/10.1016/j.epsl.2009.12.021>

Gibbs, S., Shackleton, N., & Young, J. (2004). Orbitally forced climate signals in mid-Pliocene nannofossil assemblages. *Marine Micropaleontology*, 51(1), 39-56. <https://doi.org/https://doi.org/10.1016/j.marmicro.2003.09.002>

Gibbs, S. J., Bown, P. R., Murphy, B. H., Sluijs, A., Edgar, K. M., Pälike, H., Bolton, C. T., & Zachos, J. C. (2012). Scaled biotic disruption during early Eocene global warming events. *Biogeosciences*, 9(11), 4679-4688. <https://doi.org/10.5194/bg-9-4679-2012>

Gibbs, S. J., Bown, P. R., Sessa, J. A., Bralower, T. J., & Wilson, P. A. (2006). Nannoplankton Extinction and Origination Across the Paleocene-Eocene Thermal Maximum. *Science*, 314(5806), 1770-1773. <https://doi.org/doi:10.1126/science.1133902>

Gibbs, S. J., Bralower, T. J., Bown, P. R., Zachos, J. C., & Bybell, L. M. (2006). Shelf and open-ocean calcareous phytoplankton assemblages across the Paleocene-Eocene Thermal Maximum: Implications for global productivity gradients. *Geology*, 34(4), 233-236. <https://doi.org/10.1130/g22381.1>

Gutjahr, M., Ridgwell, A., Sexton, P. F., Anagnostou, E., Pearson, P. N., Pälike, H., Norris, R. D., Thomas, E., & Foster, G. L. (2017). Very large release of mostly volcanic carbon during the Palaeocene–Eocene Thermal Maximum. *Nature*, 548(7669), 573-577. <https://doi.org/10.1038/nature23646>

Hammer, Ø. & Harper, D.A.T. (2007) Paleontological data analysis. Hoboken, New Jersey, United States: Blackwell Publishing Ltd. <https://doi.org/10.1002/9780470750711>

Haq, B. U., & Lohmann, G. P. (1976). Early Cenozoic calcareous nannoplankton biogeography of the Atlantic Ocean. *Marine Micropaleontology*, 1, 119-194. [https://doi.org/https://doi.org/10.1016/0377-8398\(76\)90008-6](https://doi.org/https://doi.org/10.1016/0377-8398(76)90008-6)

Haq, B. U., Premoli-Silva, I., & Lohmann, G. P. (1977). Calcareous plankton paleobiogeographic evidence for major climatic fluctuations in the early Cenozoic Atlantic Ocean. *Journal of Geophysical Research (1896-1977)*, 82(27), 3861-3876. <https://doi.org/https://doi.org/10.1029/JC082i027p03861>

Harper, D. T., Hönisch, B., Zeebe, R. E., Shaffer, G., Haynes, L. L., Thomas, E., & Zachos, J. C. (2020). The Magnitude of Surface Ocean Acidification and Carbon Release During Eocene Thermal Maximum 2 (ETM-2) and the Paleocene-Eocene Thermal Maximum (PETM). *Paleoceanography and Paleoclimatology*, 35(2), e2019PA003699. <https://doi.org/https://doi.org/10.1029/2019PA003699>

Hines, B. R., Hollis, C. J., Atkins, C. B., Baker, J. A., Morgans, H. E. G., & Strong, P. C. (2017). Reduction of oceanic temperature gradients in the early Eocene Southwest Pacific Ocean. *Palaeogeography, Palaeoclimatology, Palaeoecology*, 475, 41-54. <https://doi.org/https://doi.org/10.1016/j.palaeo.2017.02.037>

Hollis, C. J. (1997). Integrated Paleogene biostratigraphy of DSDP site 277 (Leg 29): foraminifera, calcareous nanofossils, Radiolaria, and palynomorphs. *Inst. Geol. Nuc. Sci. Rept.* 97/07, 1-87.

Inglis, G. N., Bragg, F., Burls, N. J., Cramwinckel, M. J., Evans, D., Foster, G. L., Huber, M., Lunt, D. J., Siler, N., Steinig, S., Tierney, J. E., Wilkinson, R., Anagnostou, E., de Boer, A. M., Dunkley Jones, T., Edgar,

- K. M., Hollis, C. J., Hutchinson, D. K., & Pancost, R. D. (2020). Global mean surface temperature and climate sensitivity of the early Eocene Climatic Optimum (EECO), Paleocene–Eocene Thermal Maximum (PETM), and latest Paleocene. *Clim. Past*, 16(5), 1953-1968. <https://doi.org/10.5194/cp-16-1953-2020>
- Intxauspe-Zubiaurre, B., Payros, A., Flores, J.-A., & Apellaniz, E. (2017). Changes to sea-surface characteristics during the middle Eocene (47.4 Ma) C21r-H6 event: evidence from calcareous nannofossil assemblages of the Gorrondatxe section (western Pyrenees). *Newsletters on stratigraphy*, 50(3), 245-267.
- Jenkins, D. G. (1993). The Evolution of the Cenozoic Southern High- and Mid-Latitude Planktonic Foraminiferal Faunas. In *The Antarctic Paleoenvironment: A Perspective on Global Change: Part Two* (pp. 175-194). <https://doi.org/https://doi.org/10.1002/9781118668061.ch9>
- Jiang, S., & Wise, S. W. (2006). Surface-water chemistry and fertility variations in the tropical Atlantic across the Paleocene/Eocene Thermal Maximum as evidenced by calcareous nanoplankton from ODP Leg 207, Hole 1259B. *Revue de Micropaléontologie*, 49(4), 227-244. <https://doi.org/https://doi.org/10.1016/j.revmic.2006.10.002>
- Jiang, S., & Wise, S. W. (2009). Distinguishing the influence of diagenesis on the paleoecological reconstruction of nanoplankton across the Paleocene/Eocene Thermal Maximum: An example from the Kerguelen Plateau, southern Indian Ocean. *Marine Micropaleontology*, 72(1), 49-59. <https://doi.org/https://doi.org/10.1016/j.marmicro.2009.03.003>
- Kelly, D. C., Zachos, J. C., Bralower, T. J., & Schellenberg, S. A. (2005). Enhanced terrestrial weathering/runoff and surface ocean carbonate production during the recovery stages of the Paleocene-Eocene thermal maximum. *Paleoceanography*, 20(4). <https://doi.org/https://doi.org/10.1029/2005PA001163>
- Kennett, J., Houtz, R., & Kennet, J. (1975). Introduction and explanatory remarks. In *Initial Reports of the Deep Sea Drilling Project*, 29 (pp. 3-16). US Govt. Printing Office Washington, DC.
- Kennett, J. P., & Stott, L. D. (1991). Abrupt deep-sea warming, palaeoceanographic changes and benthic extinctions at the end of the Palaeocene. *Nature*, 353(6341), 225-229. <https://doi.org/10.1038/353225a0>
- Kennett, J.P. and Exon, N.F. (2004). Paleoceanographic evolution of the Tasmanian Seaway and its climatic implications. In: Exon, N.F., Kennett, J.P. and M. J. Malone, M.J. (Eds.), *The Cenozoic Southern Ocean: Tectonics, Sedimentation, and Climate Change Between Australia and Antarctica*, American Geophysical Union, Washington, D.C., Geophysical Monograph Series 151, 345-367.
- Kirtland Turner, S., Sexton, P. F., Charles, C. D., & Norris, R. D. (2014). Persistence of carbon release events through the peak of early Eocene global warmth. *Nature Geoscience*, 7(10), 748-751. <https://doi.org/10.1038/ngeo2240>
- Lauretano, V., Littler, K., Polling, M., Zachos, J. C., & Lourens, L. J. (2015). Frequency, magnitude and character of hyperthermal events at the onset of the Early Eocene Climatic Optimum. *Clim. Past*, 11(10), 1313-1324. <https://doi.org/10.5194/cp-11-1313-2015>
- Lauretano, V., Zachos, J. C., & Lourens, L. J. (2018). Orbitally Paced Carbon and Deep-Sea Temperature Changes at the Peak of the Early Eocene Climatic Optimum. *Paleoceanography and Paleoclimatology*, 33(10), 1050-1065. <https://doi.org/https://doi.org/10.1029/2018PA003422>

- Legendre, P. & Legendre, L. (2012) Ordination in reduced space. *Developments in Environmental Modelling*, 24, 425–520. <https://doi.org/10.1016/B978-0-444-53868-0.50009-5>
- Lei, Y., Jiang, S., Wise, S. W., Cui, Y., & Wang, Y. (2016). Contrasting response of the calcareous nannoplankton communities after the Eocene hyperthermal events in the tropical Atlantic Ocean. *Marine Micropaleontology*, 129, 24-31. <https://doi.org/https://doi.org/10.1016/j.marmicro.2016.11.001>
- Littler, K., Röhl, U., Westerhold, T., & Zachos, J. C. (2014). A high-resolution benthic stable-isotope record for the South Atlantic: Implications for orbital-scale changes in Late Paleocene–Early Eocene climate and carbon cycling. *Earth and Planetary Science Letters*, 401, 18-30. <https://doi.org/https://doi.org/10.1016/j.epsl.2014.05.054>
- Lourens, L. J., Sluijs, A., Kroon, D., Zachos, J. C., Thomas, E., Röhl, U., Bowles, J., & Raffi, I. (2005). Astronomical pacing of late Palaeocene to early Eocene global warming events. *Nature*, 435(7045), 1083-1087. <https://doi.org/10.1038/nature03814>
- Luciani, V., D'Onofrio, R., Dickens, G. R., & Wade, B. S. (2017). Did Photosymbiont Bleaching Lead to the Demise of Planktic Foraminifer *Morozovella* at the Early Eocene Climatic Optimum? *Paleoceanography*, 32(11), 1115-1136. <https://doi.org/https://doi.org/10.1002/2017PA003138>
- Luciani, V., Dickens, G. R., Backman, J., Fornaciari, E., Giusberti, L., Agnini, C., & D'Onofrio, R. (2016). Major perturbations in the global carbon cycle and photosymbiont-bearing planktic foraminifera during the early Eocene. *Clim. Past*, 12(4), 981-1007. <https://doi.org/10.5194/cp-12-981-2016>
- Lunt, D. J., Bragg, F., Chan, W. L., Hutchinson, D. K., Ladant, J. B., Morozova, P., Niezgodzki, I., Steinig, S., Zhang, Z., Zhu, J., Abe-Ouchi, A., Anagnostou, E., de Boer, A. M., Coxall, H. K., Donnadieu, Y., Foster, G., Inglis, G. N., Knorr, G., Langebroek, P. M., . . . Otto-Bliesner, B. L. (2021). DeepMIP: model intercomparison of early Eocene climatic optimum (EECO) large-scale climate features and comparison with proxy data. *Clim. Past*, 17(1), 203-227. <https://doi.org/10.5194/cp-17-203-2021>
- Marsh, R., Mills, R. A., Green, D. R. H., Salter, I., & Taylor, S. (2007). Controls on sediment geochemistry in the Crozet region. *Deep Sea Research Part II: Topical Studies in Oceanography*, 54(18), 2260-2274. <https://doi.org/https://doi.org/10.1016/j.dsr2.2007.06.004>
- McCune, B., Grace, J., & Urban, D. (2002). *Analysis of ecological communities: Gleneden Beach, Oregon*, MJM Software Design.
- Monechi, S., Angori, E., & von Salis, K. (2000). Calcareous nannofossil turnover around the Paleocene/Eocene transition at Alamedilla (southern Spain). *Bulletin de la Société Géologique de France*, 171(4), 477-489. <https://doi.org/10.2113/171.4.477>
- Müller, R. D., Cannon, J., Qin, X., Watson, R. J., Gurnis, M., Williams, S., et al. (2018). GPlates: Building a virtual Earth through deep time. *Geochemistry, Geophysics, Geosystems*, 19(7), 2243–2261. <https://doi.org/10.1029/2018GC007584>
- Müller, R. D., Zahirovic, S., Williams, S. E., Cannon, J., Seton, M., Bower, D. J., et al. (2019). A global plate model including lithospheric deformation along major rifts and Orogens since the Triassic. *Tectonics*, 38(6), 1884–1907. <https://doi.org/10.1029/2018TC005462>
- Mutterlose, J., Linnert, C., & Norris, R. (2007). Calcareous nannofossils from the Paleocene–Eocene Thermal Maximum of the equatorial Atlantic (ODP Site 1260B): Evidence for tropical warming. *Marine Micropaleontology*, 65(1), 13-31. <https://doi.org/https://doi.org/10.1016/j.marmicro.2007.05.004>

- Nelson, C. S., & Cooke, P. J. (2001). History of oceanic front development in the New Zealand sector of the Southern Ocean during the Cenozoic—a synthesis. *New Zealand Journal of Geology and Geophysics*, 44(4), 535-553. <https://doi.org/10.1080/00288306.2001.9514954>
- Newsam, C., Bown, P. R., Wade, B. S., & Jones, H. L. (2017). Muted calcareous nannoplankton response at the Middle/Late Eocene Turnover event in the western North Atlantic Ocean. *Newsletters on Stratigraphy*, 50(3), 297-309. <https://doi.org/10.1127/nos/2016/0306>
- Nicolo, M. J., Dickens, G. R., Hollis, C. J., & Zachos, J. C. (2007). Multiple early Eocene hyperthermals: Their sedimentary expression on the New Zealand continental margin and in the deep sea. *Geology*, 35(8), 699-702. <https://doi.org/10.1130/g23648a.1>
- Niederbockstruck, B., Jones, H. L., Yasukawa, K., Raffi, I., Tanaka, E., Westerhold, T., Ikehara, M., & Röhl, U. (2024). Apparent Diachroneity of Calcareous Nannofossil Datums During the Early Eocene in the High-Latitude South Pacific Ocean. *Paleoceanography and Paleoclimatology*, 39(4), e2023PA004801. <https://doi.org/https://doi.org/10.1029/2023PA004801>
- Norris, R. D., & Röhl, U. (1999). Carbon cycling and chronology of climate warming during the Palaeocene/Eocene transition. *Nature*, 401(6755), 775-778. <https://doi.org/10.1038/44545>
- Pedregosa, F., Varoquaux, G., Gramfort, A., Michel, V., Thirion, B., Grisel, O., Blondel, M., Prettenhofer, P., Weiss, R., Dubourg, V., Vanderplas, J., Passos, A., Cournapeau, D., Brucher, M., Perrot, M., & Duchesnay, E. (2011). Scikit-learn: Machine learning in Python. *Journal of Machine Learning Research*, 12, 2825-2830.
- Penman, D. E., Hönisch, B., Zeebe, R. E., Thomas, E., & Zachos, J. C. (2014). Rapid and sustained surface ocean acidification during the Paleocene-Eocene Thermal Maximum. *Paleoceanography*, 29(5), 357-369. <https://doi.org/https://doi.org/10.1002/2014PA002621>
- Perch-Nielsen, K. (1985). Cenozoic calcareous nannofossils. *Plankton stratigraphy*, 427-455.
- Persico, D., & Villa, G. (2004). Eocene–Oligocene calcareous nannofossils from Maud Rise and Kerguelen Plateau (Antarctica): paleoecological and paleoceanographic implications. *Marine Micropaleontology*, 52(1), 153-179. <https://doi.org/https://doi.org/10.1016/j.marmicro.2004.05.002>
- Raffi, I., & Backman, J. (2022). The role of calcareous nannofossils in building age models for Cenozoic marine sediments: a review. *Rendiconti Lincei. Scienze Fisiche e Naturali*, 33(1), 25-38. <https://doi.org/10.1007/s12210-022-01048-x>
- Raffi, I., & De Bernardi, B. (2008). Response of calcareous nannofossils to the Paleocene–Eocene Thermal Maximum: Observations on composition, preservation and calcification in sediments from ODP Site 1263 (Walvis Ridge — SW Atlantic). *Marine Micropaleontology*, 69(2), 119-138. <https://doi.org/https://doi.org/10.1016/j.marmicro.2008.07.002>
- Röhl, U., Westerhold, T., Monechi, S., Thomas, E., Zachos, J. C., & Donner, B. (2005). The third and final early Eocene thermal maximum: Characteristic, timing, and mechanisms of the “X” event, *Geological Society of America, Abstracts and Programs*, 37, 264.
- Röhl, U., Westerhold, T., Bralower, T. J., & Zachos, J. C. (2007). On the duration of the Paleocene-Eocene thermal maximum (PETM). *Geochemistry, Geophysics, Geosystems*, 8(12). <https://doi.org/https://doi.org/10.1029/2007GC001784>
- Röhl, U., Thomas, D. J., Childress, L. B., Anagnostou, E., Ausín, B., Borba Dias, B., et al. (2022). Site U1553. In U. Röhl, D. J. Thomas, L. B. Childress, & Expedition 378 Scientists (Eds.), *South Pacific*

Paleogene climate. Proceedings of the International Ocean Discovery Program (Vol. 378). International Ocean Discovery Program. <https://doi.org/10.14379/iodp.proc.378.103.2022>

Schneider, L. J., Bralower, T. J., & Kump, L. R. (2011). Response of nannoplankton to early Eocene ocean de-stratification. *Palaeogeography, Palaeoclimatology, Palaeoecology*, 310(3), 152-162. <https://doi.org/https://doi.org/10.1016/j.palaeo.2011.06.018>

Schneider, L. J., Bralower, T. J., Kump, L. R., & Patzkowsky, M. E. (2013). Calcareous nannoplankton ecology and community change across the Paleocene-Eocene Thermal Maximum. *Paleobiology*, 39(4), 628-647. <https://doi.org/10.1666/12050>

Self-Trail, J. M., Powars, D. S., Watkins, D. K., & Wandless, G. A. (2012). Calcareous nannofossil assemblage changes across the Paleocene–Eocene Thermal Maximum: Evidence from a shelf setting. *Marine Micropaleontology*, 92-93, 61-80. <https://doi.org/https://doi.org/10.1016/j.marmicro.2012.05.003>

Shepherd, C. L., Kulhanek, D. K., Hollis, C. J., Morgans, H. E., Strong, C. P., Pascher, K. M., & Zachos, J. C. (2021). Calcareous nannoplankton response to early Eocene warmth, Southwest Pacific Ocean. *Marine Micropaleontology*, 165, 101992.

Slotnick, B. S., Dickens, G. R., Hollis, C. J., Crampton, J. S., Percy Strong, C., & Phillips, A. (2015). The onset of the Early Eocene Climatic Optimum at Branch Stream, Clarence River valley, New Zealand. *New Zealand Journal of Geology and Geophysics*, 58(3), 262-280. <https://doi.org/10.1080/00288306.2015.1063514>

Slotnick, B. S., Dickens, G. R., Nicolo, M. J., Hollis, C. J., Crampton, J. S., Zachos, J. C., & Sluijs, A. (2012). Large-Amplitude Variations in Carbon Cycling and Terrestrial Weathering during the Latest Paleocene and Earliest Eocene: The Record at Mead Stream, New Zealand. *The Journal of Geology*, 120(5), 487-505. <https://doi.org/10.1086/666743>

Sluijs, A., Frieling, J., Inglis, G. N., Nierop, K. G. J., Peterse, F., Sangiorgi, F., & Schouten, S. (2020). Late Paleocene–early Eocene Arctic Ocean sea surface temperatures: reassessing biomarker paleothermometry at Lomonosov Ridge. *Clim. Past*, 16(6), 2381-2400. <https://doi.org/10.5194/cp-16-2381-2020>

Stoll, H. M., Shimizu, N., Archer, D., & Ziveri, P. (2007). Coccolithophore productivity response to greenhouse event of the Paleocene–Eocene Thermal Maximum. *Earth and Planetary Science Letters*, 258(1), 192-206. <https://doi.org/https://doi.org/10.1016/j.epsl.2007.03.037>

Svensen, H., Planke, S., Malthe-Sørensen, A., Jamtveit, B., Myklebust, R., Rasmussen Eidem, T., & Rey, S. S. (2004). Release of methane from a volcanic basin as a mechanism for initial Eocene global warming. *Nature*, 429(6991), 542-545. <https://doi.org/10.1038/nature02566>

The pandas development team. (2024). pandas-dev/pandas: Pandas (v2.1.4). Zenodo. <https://doi.org/10.5281/zenodo.10957263>

Thomas, E., Boscolo-Galazzo, F., Balestra, B., Monechi, S., Donner, B., & Röhl, U. (2018). Early Eocene Thermal Maximum 3: Biotic Response at Walvis Ridge (SE Atlantic Ocean). *Paleoceanography and Paleoclimatology*, 33(8), 862-883. <https://doi.org/https://doi.org/10.1029/2018PA003375>

Thomas, E., & Shackleton, N. J. (1996). The Paleocene-Eocene benthic foraminiferal extinction and stable isotope anomalies. Geological Society, London, Special Publications, 101(1), 401-441. <https://doi.org/doi:10.1144/GSL.SP.1996.101.01.20>

- Thomas, E., Zachos, J. C., & Bralower, T. J. (2000). Deep-sea environments on a warm earth: latest Paleocene-early Eocene.
- Torsvik, T. H., Steinberger, B., Shephard, G. E., Doubrovine, P. V., Gaina, C., Domeier, M., et al. (2019). Pacific-panthalassic reconstructions: Overview, Errata and the way forward. *Geochemistry, Geophysics, Geosystems*, 20(7), 3659–3689. <https://doi.org/10.1029/2019GC008402>
- Tremolada, F., & Bralower, T. J. (2004). Nannofossil assemblage fluctuations during the Paleocene–Eocene Thermal Maximum at Sites 213 (Indian Ocean) and 401 (North Atlantic Ocean): palaeoceanographic implications. *Marine Micropaleontology*, 52(1), 107-116. <https://doi.org/https://doi.org/10.1016/j.marmicro.2004.04.002>
- Vahlenkamp, M., De Vleeschouwer, D., Batenburg, S. J., Edgar, K. M., Hanson, E., Martinez, M., Pälike, H., MacLeod, K. G., Li, Y.-X., Richter, C., Bogus, K., Hobbs, R. W., & Huber, B. T. (2020). A lower to middle Eocene astrochronology for the Mentelle Basin (Australia) and its implications for the geologic time scale. *Earth and Planetary Science Letters*, 529, 115865. <https://doi.org/https://doi.org/10.1016/j.epsl.2019.115865>
- Villa, G., Fioroni, C., Pea, L., Bohaty, S., & Persico, D. (2008). Middle Eocene–late Oligocene climate variability: Calcareous nannofossil response at Kerguelen Plateau, Site 748. *Marine Micropaleontology*, 69(2), 173-192. <https://doi.org/https://doi.org/10.1016/j.marmicro.2008.07.006>
- Villa, G., Fioroni, C., Persico, D., Roberts, A. P., & Florindo, F. (2014). Middle Eocene to Late Oligocene Antarctic glaciation/deglaciation and Southern Ocean productivity. *Paleoceanography*, 29(3), 223-237. <https://doi.org/https://doi.org/10.1002/2013PA002518>
- Wang, Y., Cui, Y., Su, H., Jiang, J., Wang, Y., Yang, Z., Hu, X., & Jiang, S. (2022). Response of calcareous nannoplankton to the Paleocene–Eocene Thermal Maximum in the Paratethys Seaway (Tarim Basin, West China). *Global and Planetary Change*, 217, 103918. <https://doi.org/https://doi.org/10.1016/j.gloplacha.2022.103918>
- Wei, W., & Wise, S. W. (1990). Biogeographic gradients of middle Eocene-Oligocene calcareous nannoplankton in the South Atlantic Ocean. *Palaeogeography, Palaeoclimatology, Palaeoecology*, 79(1), 29-61. [https://doi.org/https://doi.org/10.1016/0031-0182\(90\)90104-F](https://doi.org/https://doi.org/10.1016/0031-0182(90)90104-F)
- Wessel, P., Luis, J. F., Uieda, L., Scharroo, R., Wobbe, F., Smith, W. H. F., & Tian, D. (2019). The Generic Mapping Tools version 6. *Geochemistry, Geophysics, Geosystems*, 20, 5556–5564. <https://doi.org/10.1029/2019GC008515>
- Westerhold, T., Marwan, N., Drury, A. J., Liebrand, D., Agnini, C., Anagnostou, E., Barnet, J. S. K., Bohaty, S. M., De Vleeschouwer, D., Florindo, F., Frederichs, T., Hodell, D. A., Holbourn, A. E., Kroon, D., Laurentano, V., Littler, K., Lourens, L. J., Lyle, M., Pälike, H., . . . Zachos, J. C. (2020). An astronomically dated record of Earth’s climate and its predictability over the last 66 million years. *Science*, 369(6509), 1383-1387. <https://doi.org/doi:10.1126/science.aba6853>
- Westerhold, T., Röhl, U., Donner, B., & Zachos, J. C. (2018). Global Extent of Early Eocene Hyperthermal Events: A New Pacific Benthic Foraminiferal Isotope Record From Shatsky Rise (ODP Site 1209). *Paleoceanography and Paleoclimatology*, 33(6), 626-642. <https://doi.org/https://doi.org/10.1029/2017PA003306>
- Westerhold, T., Röhl, U., Frederichs, T., Agnini, C., Raffi, I., Zachos, J. C., & Wilkens, R. H. (2017). Astronomical calibration of the Ypresian timescale: implications for seafloor spreading rates and the chaotic behavior of the solar system? *Clim. Past*, 13(9), 1129-1152. <https://doi.org/10.5194/cp-13-1129-2017>

Westerhold, T., Röhl, U., Laskar, J., Raffi, I., Bowles, J., Lourens, L. J., & Zachos, J. C. (2007). On the duration of magnetochrons C24r and C25n and the timing of early Eocene global warming events: Implications from the Ocean Drilling Program Leg 208 Walvis Ridge depth transect. *Paleoceanography*, 22(2). <https://doi.org/https://doi.org/10.1029/2006PA001322>

Young, A., Flament, N., Maloney, K., Williams, S., Matthews, K., Zahirovic, S., & Müller, R. D. (2019). Global kinematics of tectonic plates and subduction zones since the late Paleozoic Era. *Geoscience Frontiers*, 10(3), 989–1013. <https://doi.org/10.1016/j.gsf.2018.05.011>

Zachos, J. C., McCarren, H., Murphy, B., Röhl, U., & Westerhold, T. (2010). Tempo and scale of late Paleocene and early Eocene carbon isotope cycles: Implications for the origin of hyperthermals. *Earth and Planetary Science Letters*, 299(1), 242-249. <https://doi.org/https://doi.org/10.1016/j.epsl.2010.09.004>

7. Part III: Enhanced silica burial in the South Pacific during early Eocene warming events

Bryan Niederbockstruck¹, Heather L. Jones¹, Ursula Röhl¹

¹MARUM - Center for Marine Environmental Sciences, University of Bremen, Bremen, Germany,

Abstract

Multiple short-term transient warming events of less than 100,000 years called hyperthermals punctuated the early Eocene climate. In addition to these events, a long-term warming trend (ca. 4 Ma) occurred known as the Early Eocene Climate Optimum (EECO). Both, short and long-term warming were caused by perturbations in the carbon cycle, resulting in a release of isotopically light carbon into the atmosphere. Each rise in atmospheric CO₂ during the hyperthermals initiated a recovery phase, indicating a negative feedback mechanism that sequesters carbon from the system. One potential mechanism is the chemical weathering of silicate minerals, which consumes CO₂ and results in a cooling effect. Although silicate-rich sediments have been recovered from many early Eocene deep-sea drilling sites they have only been correlated to the early Eocene hyperthermal events in the Atlantic Ocean, raising the question of whether this is a regional feature or a global phenomenon. Here, we present evidence of eccentricity-paced silica burial in early Eocene sediments from the Southwest Pacific, recovered during International Ocean Discovery Program (IODP) Expedition 378. We show that these silica-enriched sediments, as indicated by X-Ray Fluorescence (XRF)-derived element ratios, appeared in a 100 kyr cycle and coincide with the timing of many early Eocene hyperthermals. Furthermore, the opal concentration within the sediments also increased during hyperthermals, especially during the Paleocene Eocene Thermal Maximum (PETM), the I1 and K events. The latter two, are associated to the formation of chert nodules within the generally carbonate rich sediments. In addition, marine productivity also appears to increase at the onset of the EECO. Our results support evidence from the Atlantic Ocean that silicate weathering is a plausible mechanism to explain the global drawdown of CO₂ following the early Eocene hyperthermal events and. We emphasize the need to further study the correlation of early Eocene $\delta^{13}\text{C}$ records to silica preservation in deep-sea sediments, particularly at sites that were significantly influenced by riverine influx.

7.1. Introduction

The early Eocene, spanning from 48 to 56 Ma, was the warmest interval of the Cenozoic and is often referred to as a 'hothouse' climate state (Zachos et al., 2001; Westerhold et al., 2020). This period was marked by transient warming events known as hyperthermals (Thomas et al., 2000), with the most

significant being the Paleocene-Eocene Thermal Maximum (PETM) around 56 Ma (Kennett and Scott, 1991; Norris and Röhl, 1999; Röhl et al., 2007). Several less pronounced hyperthermals have been identified in marine sediments and outcrops worldwide, characterized by paired negative excursions of $\delta^{13}\text{C}$ and $\delta^{18}\text{O}$ (e.g., Agnini et al., 2009; Galeotti et al., 2010; Coccioni et al., 2012; Slotnick et al., 2015; Cramer et al., 2003; Westerhold et al., 2007; Kirtland Turner et al., 2014; Littler et al., 2014; Westerhold et al., 2017). The hyperthermals are believed to have been caused by perturbations in the carbon system, involving the massive release of isotopically light carbon (^{12}C) into the ocean-atmosphere system (e.g., Dickens et al., 1995; Thomas and Shackleton, 1996; Thomas et al., 2000). It is estimated that several thousand petagrams of carbon were released into the ocean-atmosphere system during the PETM (Panchuk et al., 2008; Zeebe et al., 2009). These carbon perturbations are considered to be paced by orbital cycles, especially the long and short eccentricity cycles of 400 and 100 kyr, respectively (Lourens et al., 2005; Kirtland Turner et al., 2014), except for the PETM (Röhl et al., 2007; Zachos et al., 2010). The hyperthermals of the late Paleocene to early Eocene are labeled from A to L (Cramer et al., 2003) and M to W (Lauretano et al., 2016), with the Early Eocene Thermal Maximum (ETM) 2 as H1 and ETM3 as K. The carbon isotope excursions (CIE's) for these hyperthermals indicate individual event durations of 50 to 200 kyr (Zachos et al., 2001; Sluijs et al., 2009), with increased $\delta^{13}\text{C}$ in the so called 'recovery' phase of each event suggesting a natural negative feedback mechanism in which carbon was sequestered back out of the system. Potential mechanisms for carbon sequestration include carbon burial through increased marine organic productivity and/or enhanced chemical weathering. The aforementioned hyperthermals were superimposed on a long-term warming trend that culminated in the Early Eocene Climate Optimum (EECO): a time interval of ca. 4 Myr, identified by a negative shift in benthic foraminifera $\delta^{18}\text{O}$ (Kirtland Turner et al., 2014; Lauretano et al., 2015). Although the exact timing for the start of the EECO is poorly-constrained, it was shown to coincide with the onset of the J event (53.26 Ma) on Ocean Drilling Program (ODP) Site 1209 (Shatsky Rise) in the low-latitude North Pacific (Westerhold et al., 2018).

It is hypothesized that chemical weathering represents a significant sink for atmospheric CO_2 over geologic timescales, functioning as a negative feedback to elevated atmospheric CO_2 concentrations (Raymo and Ruddiman, 1992; Misra and Froelich, 2012; Hessler et al., 2017; Caves et al., 2019; Penman et al., 2020). The intensification of the chemical weathering is thought to be controlled by increased atmospheric CO_2 and temperature (Berner et al., 1997; Walker et al., 1981; Fang et al., 2019) which has also been observed in laboratory and field experiments (Brady & Walther, 1992; Kump et al., 2000; Hartmann et al., 2010). During this process, carbon derived from atmospheric or soil-respired CO_2 reacts with water to form carbonic acid (H_2CO_3). This reaction then proceeds to interact with silicate minerals, such as wollastonite, as described by Garrels and Berner (1983). Consequently, this reaction results in the production of silicic acid, dissolved inorganic carbon (DIC) in the form of bicarbonate

(HCO₃⁻), and cations of magnesium, potassium, or sodium in dissolved form. Subsequently, these products are transported via river runoff into the oceans (Gaillardet et al., 1999). The bicarbonate and calcium cations participate as carbonate, while silicic acid, cations and other nutrients that got into the ocean stimulates the marine productivity. When both inorganic carbon in carbonates and organic carbon are restored to the ocean floor, atmospheric CO₂ is removed from the system.

The modern ocean is generally undersaturated in silica (Nelson et al., 1995; Rickert et al., 2002). However, in the geological past, evidence in the form of siliceous sediments proves that, at least temporarily, the silica concentration was high (e.g., Macellari & D. Vries, 1987; Mitchell et al., 2008; Penman et al., 2016, 2019). During the early Eocene, numerous silica-rich sediment depositions have been observed since the very first Deep Sea Drilling Project (DSDP) Leg 1 (Calvert, 1971). Silica in sediments appears in different forms such as chert, which is microcrystalline quartz (Smith, 1960; von Rad et al., 1978), or porcelanite, which is fine-grained cristobalite (Ernst and Calvert, 1969; Riech et al., 1979). Cristobalite represents an intermediate stage in the transformation of biogenic silica to chert (Calvert et al., 1977). Regardless of their mineralogical composition, they all exhibit an increased concentration of silica in the sediment layers.

Tanaka et al. (2022) reported increased continental chemical weathering during multiple early Eocene hyperthermals in the South Indian Ocean by analyzing osmium isotopes. Their findings indicate that chemical weathering played a significant role in responding to transient global warming events beyond the PETM. A link between enhanced river runoff, nutrient delivery, and CO₂ drawdown due to increased marine productivity has been suggested for the PETM (John et al., 2008; Bowen and Zachos, 2010; Penman et al., 2016, 2019) and for smaller hyperthermals such as I1, I2, H1, H2, J, and K (Kazutaka et al., 2017). Although silica burial has been widely reported across ocean basins, the association of these siliceous sediments with hyperthermal events has been confirmed only in the Atlantic. It has been stated that, so far, no association of silica burial and hyperthermal events has been found in the Pacific (Penman et al., 2019). Penman et al. (2019) linked the widespread presence of chert and other siliceous sediments in the early Eocene Atlantic record to these hyperthermal events. Their work proposed a model in which increased silicate weathering, driven by global warming, necessitated a rapid increase in marine silica burial, particularly in the Atlantic.

At South Pacific IODP Site U1510, early Eocene sediments of lithological Unit IIc consist of homogeneous calcareous chalk with chert (Sutherland et al., 2019). The chert nodules damaged XCB drill bits, leading to poor core recovery (Alegret et al., 2021). Among these chert layers, one was formed during a hyperthermal event. However, the occurrence of chert layers and their possible association with hyperthermal events in the Tasman Sea and South Pacific has not been thoroughly investigated, highlighting the need for further studies (Alegret et al., 2021). In 2020, IODP Site U1553 was drilled

south of New Zealand at the Southern Campbell Plateau, where core descriptions again reported the occurrence of chert nodules within early Eocene sediments (Röhl et al., 2022). Furthermore, the occurrence of radiolarians varies between rare, few, and common, with poor preservation in early Eocene sediments (Röhl et al., 2022). Sponge spicules are common throughout Eocene sediments (Röhl et al., 2022).

So far, the occurrence of siliceous sediment deposited during the early Eocene has been documented across different ocean basins but has been linked to hyperthermal events only in the Atlantic (Penman et al., 2016, 2019). If the deposition of siliceous sediments is associated with hyperthermal events, which are known to be global phenomena, we hypothesize that this phenomenon occurred globally and is not limited to the Atlantic Ocean. Therefore, this study aims to identify early Eocene siliceous sediments in the South Pacific and analyze their relationship to hyperthermal events.

7.2. Material and Methods

7.2.1. Material and Study Site

The samples and data used in this study are from sediments of IODP 378 at Site U1553, south of New Zealand at the southern Campbell Plateau (-52.22400°N, 166.19160°E; Röhl et al., 2022) (Figure 7.1). At Site U1553, five holes were drilled and retrieved sediments between the Pleistocene and early Paleocene. Sediments of the latest Paleocene to early Eocene were recovered in the holes C and D of lithological Unit IV which mainly consist of limestone with an increased downwards lithification (Röhl et al., 2022). The PETM was first identified by calcareous nannoplankton and a change from non-bioturbated sediments to bioturbated sediments. A more detailed age model was then generated by a correlation of high-resolution $\delta^{13}\text{C}$ isotope record, to astronomically calibrated records of Ocean Drilling Program (ODP) Sites 1258 (Kirtland Turner et al., 2014) and 1262 (Zachos et al., 2010) by Niederbockstruck et al. (2024a), which is applied to the data used in this study. The studied interval from the latest Paleocene to early Eocene lie between 450.21 to 486.29 m core composite depth below sea-floor (CCSF). For the purpose of the study, we choose Site U1553 not only because of its age model, but also because 1) the sediment archive of Site U1553 does not show a carbonate dissolution horizon at the PETM unlike many other sediment archives (e.g., Thomas et al., 1999; Zachos et al., 2005) and 2) the relatively good core recovery of generally > 83% during the studied interval (Röhl et al., 2022), which cannot be taken for granted considering the nearby single hole, sport-cored drilled Deep Sea Drilling Program (DSDP) Site 277 with low recovery (Kennett et al., 1975; Shackleton & Kennett, 1975), or IODP Site U1510 (Sutherland et al., 2019), which reports poor recovery for the EECO with 51% and 47% in Cores 51X and 52X (Alegret et al., 2021).

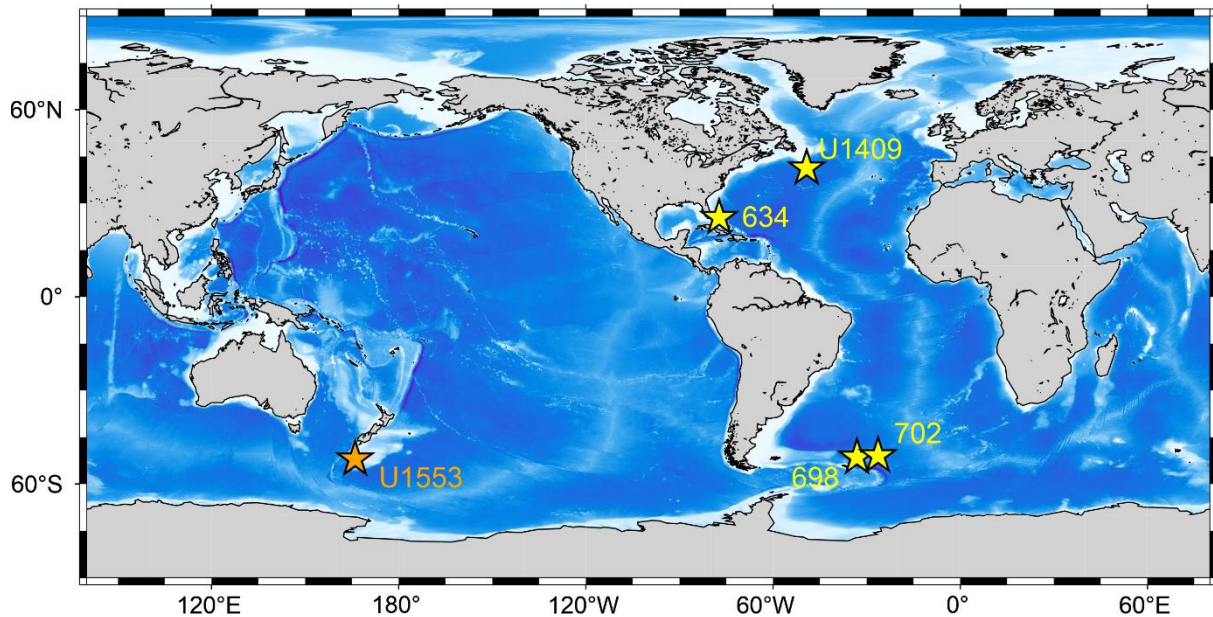


Figure 7.1. Bathymetric map with the locations of International Ocean Discovery Program (IODP) Site U1553 (orange, this study) and the four Atlantic sites with silica burial associated with early Eocene hyperthermal events (Penman et al., 2019): IODP Site U1409, Ocean Drilling Program (ODP) Site 634, 698, 702 (yellow). The map was generated using the *Generic Mapping Tool* (Wessel et al., 2019).

7.2.2. Opal measurement

To find out if the silica burial, associated to early Eocene hyperthermals is caused by siliceous productivity, we measured the opal concentration (weight (wt) %). Therefore, 48 samples were measured with 23 samples in Hole U1553C and 25 samples in Hole U1553D. 39 samples are from the more pronounced and well-known hyperthermals ETM1 (PETM), ETM2 (H1), ETM3 (K) and on slightly smaller hyperthermals H2, I1, I2, and J. The other 9 samples were taken from sediments before the PETM or between PETM and H1 to get background opal data.

Biogenic silica was determined at Laboratory of MARUM–Center for Marine Environmental Sciences, University of Bremen by an automated leaching technique using 1 M NaOH solution at 85°C (Müller and Schneider, 1993).

7.2.3. High-resolution paleoproductivity record

In order to get a continuous data record to track siliceous burial and potential productivity, we used XRF scanning data (Röhl et al., 2022) from the splice for Site U1553, Holes C and -D (Drury et al., 2022; Wilkens et al., 2022) which consists 1539 datapoints with an average resolution of 2.3 cm or 3.3 kyr, respectively. High-resolution XRF core scanning derived elemental intensities and ratios are used as indicators for sediment composition and element variability with some elements pointing to surface ocean paleoproductivity across different oceans and timescales. For this study, we used the elements Al, Si, K, Ca, Ti, Fe, Br and Ba. The carbonate and silica productivity can be indicated by calcium (Ca) and silicon (Si) concentrations, respectively. Because these elements can also be transported from the continents into the oceans as fluvial or aeolian input, the ratios of Ca and Si against other terrigenous

elements (e.g., Al, K, Ti, Fe), are utilized to reflect the increased or decreased marine-biogenic produced Si and Ca. Higher ratios indicate the (former) presence of siliceous and carbonate microfossils (e.g., Marsh et al., 2007; Agnihotri et al., 2008; Ingram et al., 2010). Another element for organic productivity is Bromine (Br), which is mainly concentrated in organic matter and known to be produced more by marine organisms compared to fresh water organisms (Malcolm and Price 1984; Gribble et al., 2003; Mayer et al., 2007). Therefore, XRF Br and Br/Ti ratio are used as an indicator for marine organic productivity (Agnihotri et al., 2008; Ren et al., 2009; Caley et al., 2011).

A possible dilution effect of Ca caused by carbonate dissolution, associated with several hyperthermal events elsewhere (Zachos et al., 2005) is unlikely at Site U1553 because early Eocene sediments were deposited well above the carbonate compensation depth (Hollis, 1997; Röhl et al., 2022), which is thought to be around 3200 m to 3600 m in the equatorial Pacific during the early Eocene (van Andel et al., 1975; Rea and Lyle, 2005, Pälike et al., 2012).

7.2.4. Statistical analyses

Single Spectral Analysis was performed using python package *Pyleoclim* (Khider et al., 2022). We applied the multitaper method (Thomson, 1982) which is widely used in cyclostratigraphic and paleoceanographic studies (e.g., Rao and Hamed, 2003; Agnihotri et al., 2008; Westerhold et al., 2018; Li et al., 2019; Lyu et al., 2023). The multitaper method requires equal spacing. XRF-Si/Fe data was equally spaced by its average resolution of 3.3 kyr (Figure 7.2) and then standardized. To detect statistically significant cycles, an autoregressive process (AR(1)) was computed to show the 95% threshold.

To quantify linear relationships within the XRF data, the Pearson correlation was calculated using the Python package *pandas* (The pandas development team, 2024). With the coefficient, $r = 1$ is a perfect positive linear relationship and $r = -1$ is a perfect negative linear relationship. This implies that the two variables move together identically in the same ($r=1$) or in the opposite ($r=-1$) direction, with $r = 0$ signifying no linear relationship.

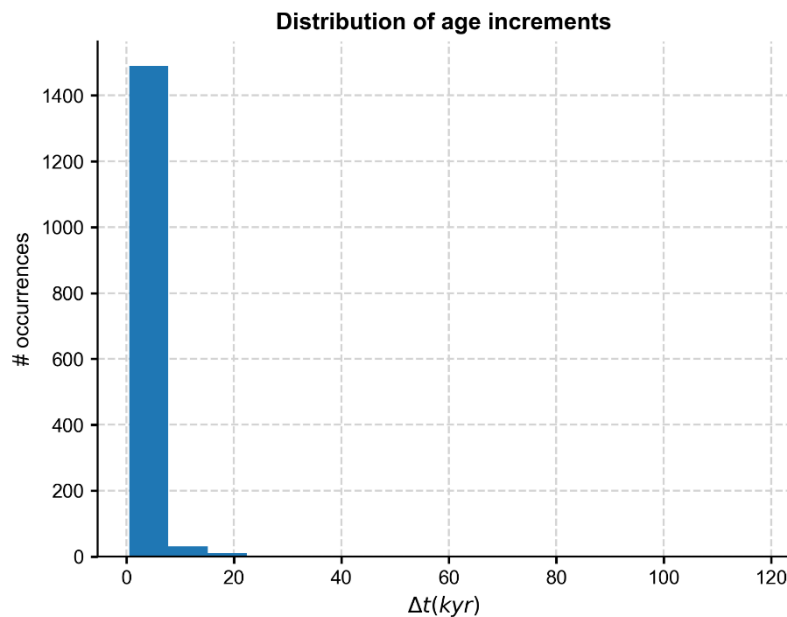


Figure 7.2. Distribution of age increments of XRF data of this study interval, showing the consistent sampling resolution in age.

7.3. Results

The splice sediment bulk $\delta^{13}\text{C}$ record is used to highlight the hyperthermal events on which opal was measured (Figure 7.3a). The visual core description as well as linescan images from the surface of sections from the Holes C and D (Röhl et al., 2022) exhibit several parts with non- or less-disturbed intervals, however not a single section is free of these disturbances. The most extreme examples are from the lowest sections U1553D-7R-1 and U1553D-7R-2 with the sediment being broken into several pieces (Figure 7.3b). Chert nodules of several centimeters formed during the I1 and K event. The XRF-Ca shows in general high intensities throughout the record with most fluctuations in the sections U1553D-7R-1 and U1553-7R-2 and the most constant values in the top part in U1553D-5R-1 and U1553D-7R-2. Despite the general high XRF-Ca intensities we observe several drops during the hyperthermal events H2, I1, J and K (Figure 3b, grey bars). The XRF-Ca intensities are fluctuating between higher and lower values during and above/below the PETM. During H1, there are two minor lows at 471.7 and 472 m CCSF. During the I2 event the XRF-Ca intensities are constant. Contrary to the XRF-Ca, the XRF-Si intensity is in general low but peaks during the hyperthermals I1, H2, J and K as already visible looking at the core sections (Figure 7.3b). XRF-Si intensity is more fluctuating the PETM, exhibits two small spikes during H1 at 471.7 and 472 m CCSF and no variability during I2. The most prominent peaks of XRF-Si intensity occur in K and I1, where the lithological Unit IV contains chert nodules at 460.8 and 467.8 m CCSF.

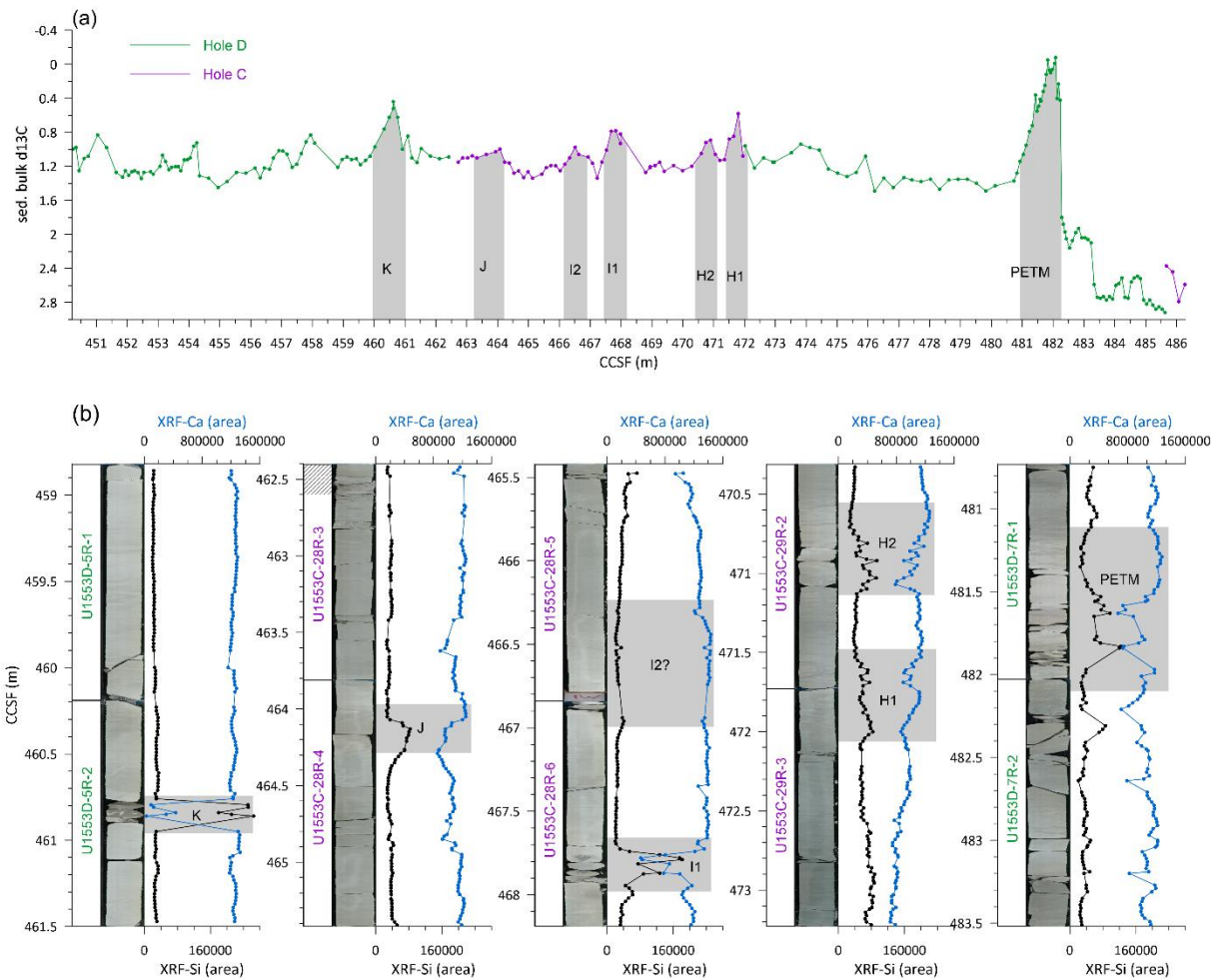


Figure 7.3. (a) Spliced bulk sediment $\delta^{13}\text{C}$ record from Holes U1553 Hole C and -D (Niederbockstruck et al., 2024b), (b) XRF- Si and Ca intensities and linescan images (Röhl et al., 2022) of selected hyperthermals.

The investigated 3.5 Ma long record shows multiple XRF-Si peaks throughout and this independent from highlighted hyperthermal events (Figure 7.4). The strongest peaks occurred during the onset of I1 and K. Between the PETM and I1, the XRF-Si increase and decrease again, indicating a relative increase of Si within the sediments after the PETM before decreasing to pre-PETM conditions. To understand the relative increase of Si intensities compared to other terrigenous elements we compared the ratios of Si over Al, K, Ti and Fe (Figure 7.4). The peaks of all these ratios highly correlate to the XRF-Si intensity. However, long-term trends are not present, different from the Si intensities, with low and constant background values. At 51.81 Ma there is one Si/K peak of 1831 while values below and above are all below 100.

The average relative weight of opal contents of the analyzed samples is 6.63 wt% with a minimum of 0.22 wt% at 53.33 Ma (Sample U1553C-28R-4, 77 cm) and a maximum 26.06 wt% at 55.86 Ma (Sample U1553D-7R-1, 119 cm). As with the XRF-derived Si values, higher opal concentrations tend to occur during hyperthermal events. Another high concentration of opal is found at 55.19 Ma with 19.98 wt%. Very low opal concentration (> 4 wt%) occurred mostly just before and after the hyperthermal events.

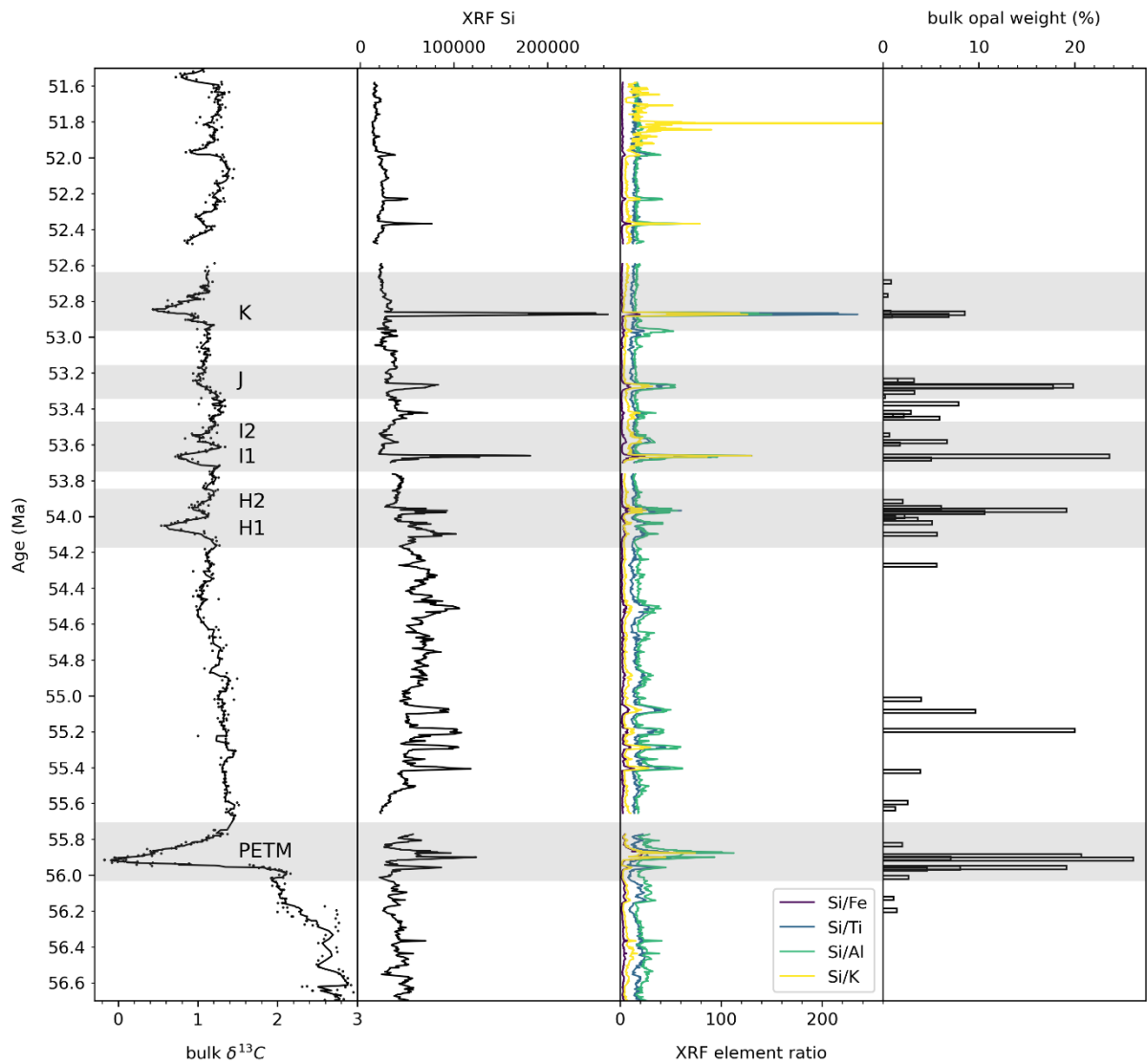


Figure 7.4. Bulk sediment $\delta^{13}\text{C}$ with a 3point running average (from Niederbockstruck et al., 2024). XRF-Si intensities and the ratio of XRF Si to over terrigenous elements. Opal concentration in wt%.

The Pearson correlation of XRF-derived elements show a very high correlation of up to 0.93 among Al, Si, K, Ti, Fe and Ba, which are indicated in red (Figure 7.5). These elements are anti-correlated to Ca, Br, Ca/Fe and Si/Fe. While Si is positively correlated to Al, Ti, Fe and Ba the Si/Fe ratio indicative for biogenic produced silica, only positive correlated to Si, but anti-correlated to the terrigenous elements Al, Ti, Fe and Ba.

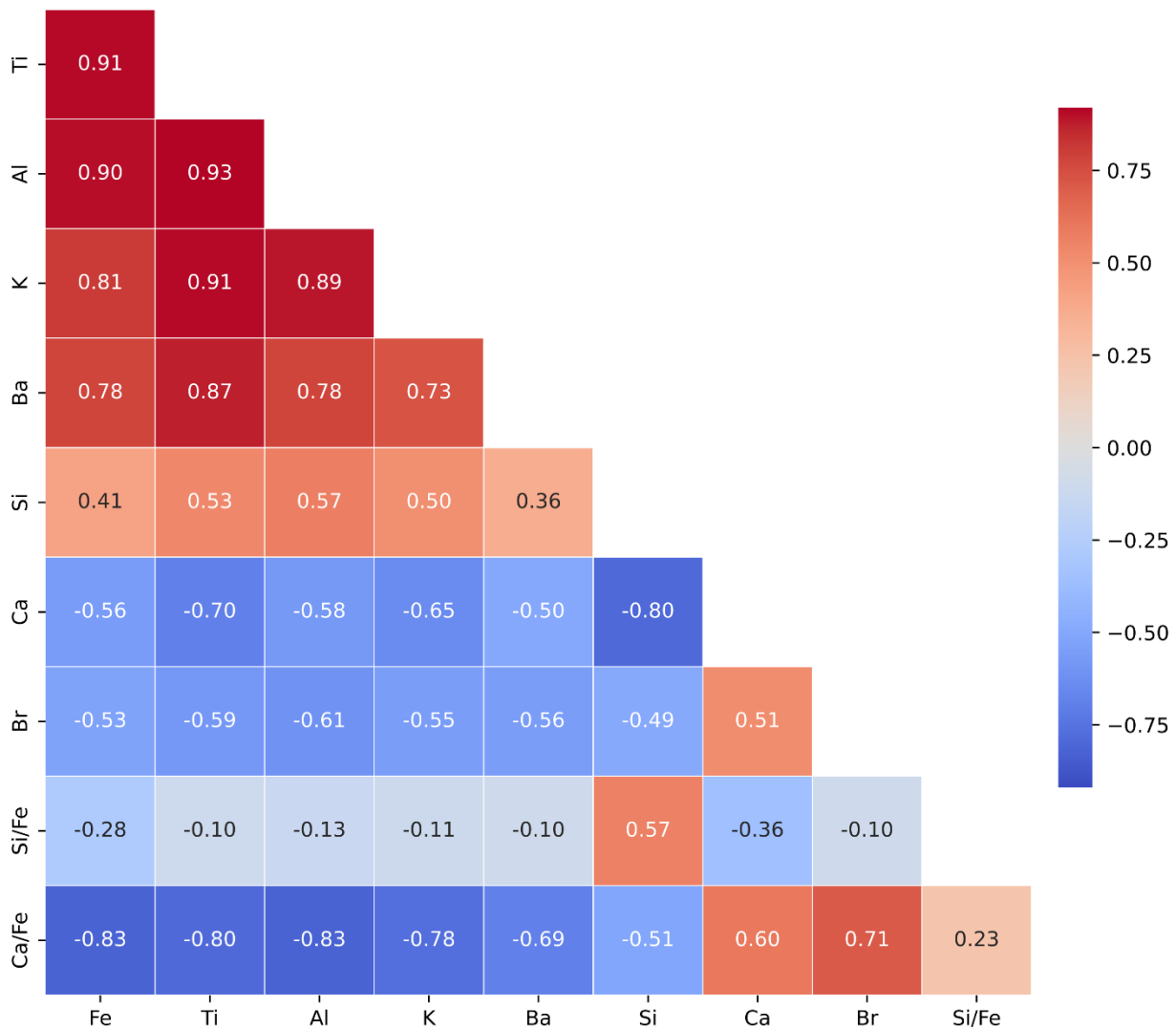


Figure 7.5. Pearson Correlation of XRF scanning derived elemental intensities of Site U1553 data. Red colors indicate positive correlation with 1 meaning a fully linear correlation and -1 a perfect negative linear correlation.

7.4. Discussion

7.4.1. The occurrence of siliceous horizons in early Eocene sediments

Since the initial Deep Sea Drilling Project (DSDP) Legs 1 and 2, chert layers have been documented in marine sediment cores (JOIDES, 1967), with those from Leg 2 being attributed to the early to middle Eocene (Gartner et al., 1970). Notably, during the early Eocene hyperthermals, significant silica burial has been particularly observed in the Atlantic (Penman et al., 2016, 2019). While observations may be biased by the number and location of drill sites, the distribution of silica-rich layers in the sediments cannot be solely explained by these factors. Instead, it is suggested to be a more widespread phenomenon (Muttoni and Kent, 2007). Although chert layers have been identified at several locations in the North and South Atlantic, their absence at Pacific Site 1183 raises questions about the occurrence of silica burial in the Pacific Ocean that are linked to the early Eocene hyperthermals (Penman et al., 2019). Higher silica concentrations in Pacific sediments from the early Eocene have

been found near the equator. At DSDP Site 316, a relatively variable sediment composition, including chert, siliceous and calcareous chalk, as well as limestone, was documented for the early to middle Eocene (Schlanger et al., 1976). Additional evidence was provided by ODP Leg 199 (Moore et al., 2008). In the outcrop section at Mead Stream, New Zealand, siliceous limestone appeared between the Paleocene-Eocene Thermal Maximum (PETM) and Eocene Thermal Maximum 1 (ETM1), as well as during the Early Eocene Climatic Optimum (EECO) (Hollis et al., 2005; Slotnick et al., 2012). However, those siliceous sediments were not directly associated with hyperthermals. It is hypothesized that silica weathering is enhanced during periods of high atmospheric CO₂, thereby consuming CO₂ and acting as a negative feedback mechanism (Walker et al., 1981; Berner et al., 1983; Elliot Smith et al., 2008; Fang et al., 2019). This negative feedback is also observed in carbon cycling models during transient warming events, such as hyperthermals, and long-term warming intervals like the EECO (Dickens et al., 1991; Penman et al., 2016, 2020). Increased runoff of dissolved silica into the surface ocean can enhance siliceous productivity, thereby increasing the supply of siliceous tests to the seafloor and improving the preservation of opal (Johnson, 1976). Another possibility is the silica supply from older, nutrient-rich bottom water via upwelling. Although hothouse conditions typically imply a more stratified surface layer, this does not preclude ventilation throughout the water column (de Boer et al., 2007). However, there is no consensus on early Eocene ocean circulation, which may have been fundamentally different from modern conditions due to the nearly closed Drake and Tasmanian passages (Zhang et al., 2020). Associations between early Eocene hyperthermals and ocean circulations were investigated using an intermediate complexity Earth system model (cGENIE), which revealed a weakening of overturning circulations in response to transient warmings (Kirtland Turner et al., 2024). Boxmodel experiments (LOSiCAR) indicates an increase in North Pacific deep-water formation and a reduction of Southern Ocean deep-water formation coinciding with a switch to younger less corrosive, nutrient-poor [H₄SiO₄] Pacific subsurface seawater and an upwelling of silica-rich subsurface water in the North Atlantic during the PETM (Penman et al., 2019). That upwelling then is thought to fuel the opal production in the Atlantic. Regardless of how dissolved silica got to the surface ocean waters, the LOSiCAR simulations predict silica-enriched surface waters as a key mechanism for the climate to recover from carbon release events like hyperthermals (Penman et al., 2016, 2019). Without any indication of increased upwelling south of Zealandia, we favor the hypothesis of enhanced silicate weathering, as being the main supplier for dissolved silicate in the upper water column via enhanced river runoff, as discussed in several studies (e.g., Bowen et al., 2004; Nicolo et al., 2007; Hessler et al., 2017). Besides the silica supply for opal formation, changes in silica productivity alone cannot be used to understand opal formation and preservation (Archer et al., 1993). Opal normally occurs in sediments from the Miocene or older (Riech & von Rad, 1979; Bohrmann et al., 1994) at temperatures above 18°C (Pisciotta, 1981). Such high bottom water temperatures seemed to be realistic at least during peak

hyperthermal conditions as indicated for ETM2/H1 with high bottom water temperatures of $16.9 \pm 2.3^\circ\text{C}$ (95% CI) derived from clumped isotope thermometry (Agterhuis et al., 2022). Next to an increased supply from the ocean surface, the bottom water and pore water chemistry control the formation and preservation of opal.

The formation of opal seems to favor a reduced proportion of detrital minerals and organic material (Bohrmann et al., 1994), and develops faster in carbonates compared to clayey sediments (Lancelot, 1973) which is indicated at Site U1553 interval by the high Si in relation to other terrigenous elements in the sediment, that mainly consists of limestone (Röhl et al., 2022) The proximal position of Site U1553 to Zealandia and thus enhanced river runoff and silica supply, high bottom water temperatures during the early Eocene and the low organic content makes the sediments of Site U1553 a suitable archive to preserve silica burial in the South Pacific.

7.4.2. Astronomically paced silica productivity during hothouse climate?

Many, though not all, observations of chert or other siliceous phases have been associated with hyperthermal events during the early Eocene in the Atlantic Ocean (Penman et al., 2019). These hyperthermal events, marked by paired negative excursions of $\delta^{13}\text{C}$ and $\delta^{18}\text{O}$, are largely paced by astronomical cycles, particularly eccentricity (e.g., Zachos et al., 2010; Kirtland Turner et al., 2014; Westerhold et al., 2017). The occurrence of chert decreases after the early Eocene as the climate underwent a global shift towards cooler conditions (Miller et al., 2005).

The origin of these siliceous sediments has been widely discussed (Gibson and Towe, 1971; Hesse, 1988; Muttoni and Kent, 2007). At Site U1553, the data suggest that silica burial is, if not solely, at least partially, caused by biogenic siliceous productivity. This is evidenced by 1) the presence of chert nodules in the sediment of the studied interval and the enhanced opal concentrations of up to 28 wt% within the sediments and 2) the chert nodules also contain radiolarians and sponge spicules (Röhl et al., 2022). Our data reveals a decrease in Ca when Si increases during the hyperthermals PETM, H1, H2, I1, J, and K (Fig. 2b). This pattern is most pronounced in sections where chert nodules are visible in the sediment core, coinciding with hyperthermals K and I1 at 460.8 and 467.8 m CCSF, respectively. While the accumulation of silica in the sediment does not always result in chert nodules, the XRF-Si peaks, and particularly the Si-ratios, appear multiple times throughout the studied interval, indicating an increased supply of biogenic silica to the seafloor, further supported by the presence of opal (Figure 7.4).

To understand if siliceous paleoproductivity and thus the foundation of silica burial appeared periodically or rather random in the South Pacific, a single spectrum analysis was performed. Because of the high positive correlation among the terrigenous elements Al, Ti, Fe, and K (0.81 to 0.93; Figure 7.5), we here use Si/Fe, representative for the ratio of silica over the other terrigenous elements which

indicates changes in biogenic silica. The multitaper power spectrum show a statistically significant peak at around a 100 kyr and 31 kyr cycle (Figure 7.6) and a stronger though not statistically significant (95% CL) 405 kyr cycle in the wavelet analyses (see Figure S7.2).

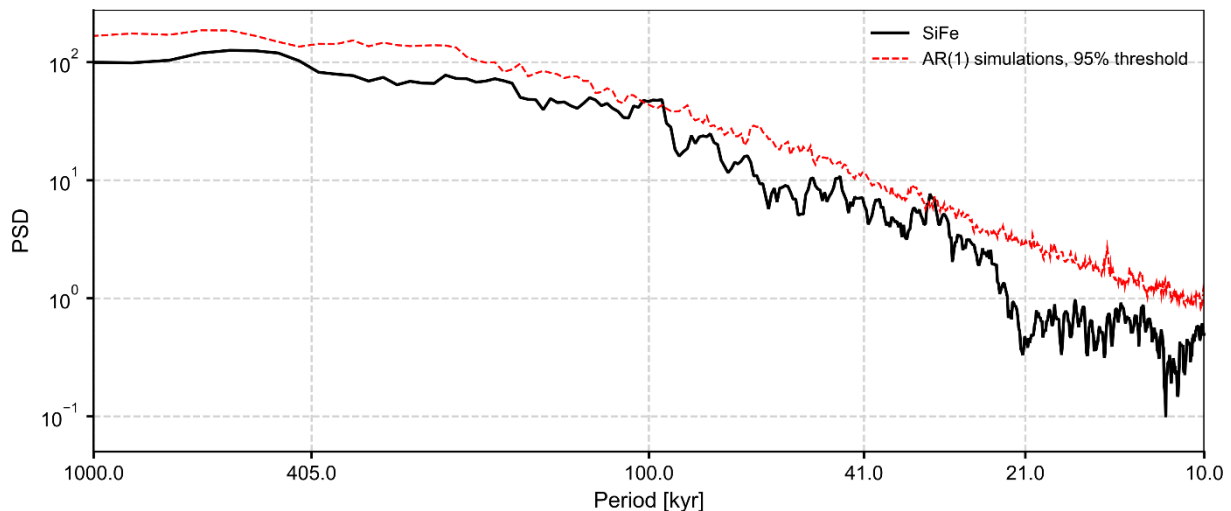


Figure 7.6. Periodogram of single spectrum analysis using the multitaper method on the XRF-Si/Fe ratio (black line), as an indicator for paleoproductivity at Site U1553. Note the log-scale of the y-axis of the Power Spectral Density (PSD), showing the power of a certain periodicity. An autoregressive simulation was performed to highlight statistically significant cycles above a 95% confidence level (red line). Analysis was performed using the Python package *Pyleoclim* (Khider et al., 2022).

Siliceous productivity during the late Paleocene and early Eocene at Site U1553 peaks at a 100 kyr cycle, coinciding with eccentricity maxima and associated hyperthermal events, as well as the PETM: a hyperthermal that is not paced by the long eccentricity cycle (Figure 7.7). Although not all eccentricity maxima result in the deposition of chert (as it did during the I1 and K events) this indicates that the increased silica burial, represented by the Si/(Al, K, Ti, Fe) ratio is paced by the 100 kyr eccentricity cycle (Figure 7.6). One of the clearest examples of eccentricity paced Si productivity appeared between 55.5 – 55.0 Ma (Figure 7.7), which can also be seen in the wavelet analysis (Figure S7.2) of which one coincides with the F event. Our data show some peculiarities; for example, the XRF-derived Si ratios show a more significant increase during the H2, I1 and K events than during the H1 event, despite the latter having the highest magnitude of CIE out of these four hyperthermals. Furthermore, opal concentrations during the low-magnitude hyperthermals H2, I1, I2 and J are higher than during H1, suggesting a possible disconnection between the magnitude of the carbon cycle perturbation and the earth system response. In addition, at Site U1553, we find a relatively low increase in opal (8 wt%), with a large increase in Si ratios during the K event. This supports Os isotope data that suggests less pronounced chemical weathering in the southern Indian Ocean during the K event compared to the H1 and I1 events (Tanaka et al., 2022) This inconsistency might be caused by the low resolution and/or a non-linear feature between XRF-derived Si ratios to opal. Another possible reason might be the

change in background conditions, which were already enhanced during the EECO, therefore reducing the impact of changes in chemical signals during the K event in the sediment, relative to its background signal. Compared to the 100 kyr cyclicity, we are not aware of any climatic cycle of 31 kyr (Figure 7.6). We speculate that this might be a superposition of obliquity (~40 kyr) and precession (~21 kyr), resulting in a mixed signal of both.

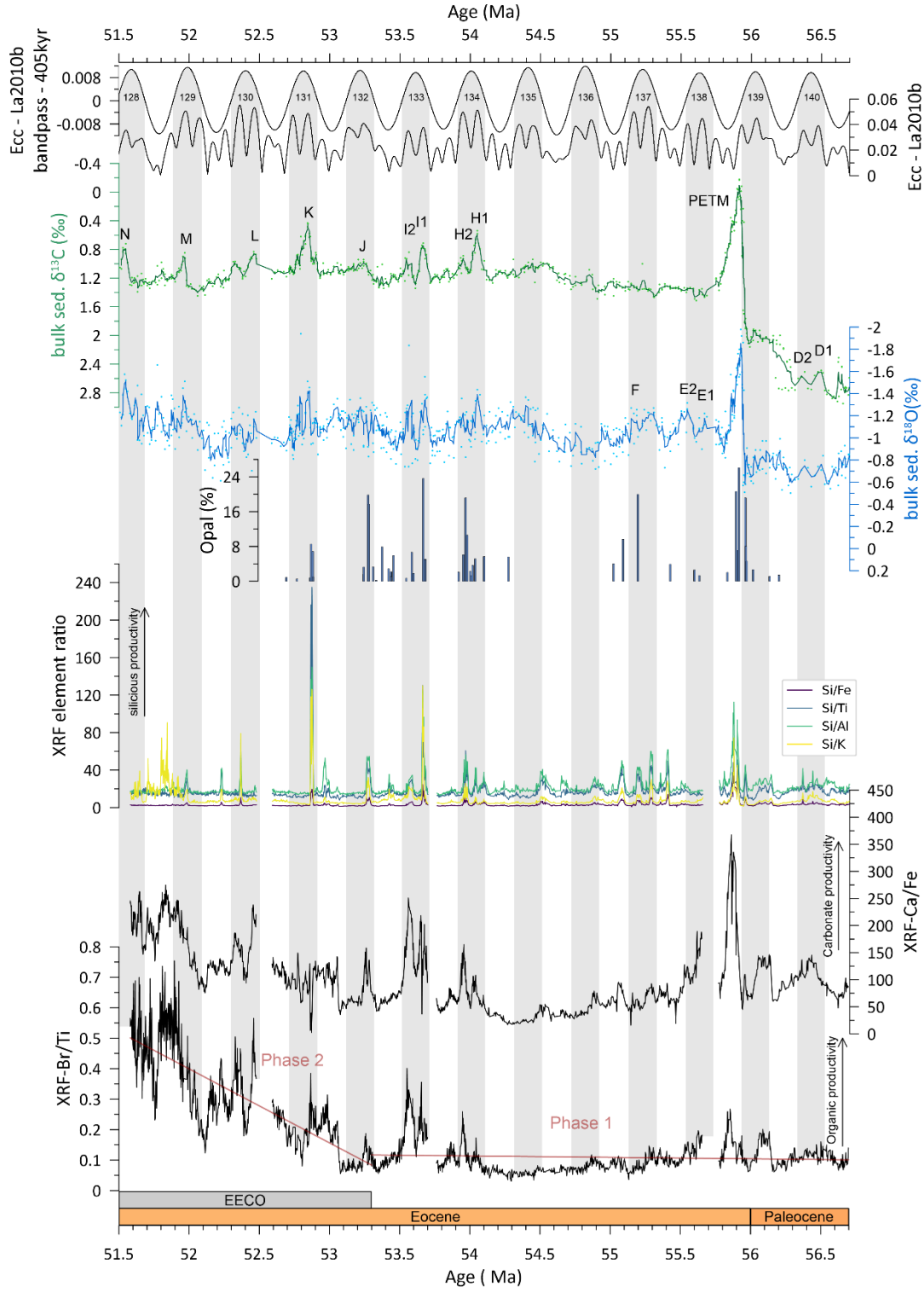


Figure 7.7. From top to bottom: Short-term Eccentricity (~100 kyr; Lascar et al., 2011) and 405 kyr filter. Bulk sediment $\delta^{13}\text{C}$ (green) and $\delta^{18}\text{O}$ (blue) with both applied a 3point running average of Niederbockstruck et al. (2024b). Siliceous productivity proxy, indicated by opal wt% (vertical bars) and XRF element ratios of Si over terrigenous elements. Carbonate productivity indicated by XRF Ca/Fe and organic productivity indicated by XRF Br/Ti. For the XRF Br/Ti, a linear fit was performed for before the EECO (Phase 1) and from the onset of the EECO (Phase 2)(red lines).

The carbonate productivity (Ca/Fe) increased during hyperthermal events D1, D2, H1, H2, I1, I2, J, K, L, M and N but was rather low in-between the E2 and H1 events (54.1 to 55.6 Ma). This supports previous research suggesting that the productivity of calcareous nannoplankton was possibly cyclic and orbitally-paced, as indicated by Sr/Ca ratios (Dedert et al., 2012). On several sites for the PETM, H1, H2 and I1, studies point to enhanced or at least unhindered productivity of calcareous nannoplankton, indicated by warm and eutrophic favored assemblages of calcareous nannoplankton and planktonic foraminifera and the occurrence of radiolarians (Gibbs et al., 2006; Stoll et al., 2007; Gibbs et al., 2010; D’Onofrio et al., 2016; Wang et al., 2022). However, this trend might not apply globally as Sr/Ca measurements on samples at sites with open ocean settings, as found in subtropical gyres indicate a reduced productivity (Dedert et al., 2012).

The marine organic productivity, as represented by the Br/Ti ratio, can be divided into two distinct phases. The Phase 1, spanning from 56.67 Ma to 53.3 Ma, is characterized by relatively low and constant productivity. During this phase, an increase in Br/Ti occurred during the 139th long eccentricity cycle and the recovery phase of the PETM (Figure 7.7). This stability persisted until 54.1 Ma, after which Br/Ti peaks coincided with hyperthermals H1, H2, I1, I2, J, and L (Figure 7.7). In contrast, Phase 2, from 53.3 Ma to 51.5 Ma, shows a continuous increase in marine organic productivity. This trend cannot be attributed to a relative decrease in terrigenous elements (Ti) because, parallel to the Br/Ti ratio, Br values also increased while terrigenous elements decreased (Figure S7.1). This observation supports the interpretation of enhanced organic productivity during this period. Interestingly, the state change between Phase 1 and Phase 2 coincides with the possible start of the EECO. This shift in productivity is illustrated by linear fits in the Br/Ti ratio for both phases, as shown by the red lines in Figure 7.7. The slope of the linear fit before the EECO is visually dependent on the axes' lengths in Figure 7.7. To provide a neutral perspective, the slopes were converted into angles in radians and then into degrees, resulting in angles of -0.27° and -13.65° , respectively (Table S1; Figure S7.3). The EECO is known to be the warmest interval of the Cenozoic with high bottom water temperatures (Friedrich et al., 2012; Lauretano et al., 2018) and sea surface temperatures (Friedrich et al., 2012; Lauretano et al., 2018). This interval is characterized by lithological changes in the sediment (Slotnick et al., 2012), benthic foraminifera stable isotope excursion (Lauretano et al., 2015) and assemblage change of planktic foraminifera (Luciani et al., 2016, 2017; D’Onofrio et al., 2020). Based on our observations, changes in surface water conditions with the onset of the EECO initiated an increase of marine organic productivity at Site U1553. This general trend in Phase 2 might overprint a response of younger

hyperthermals, as seen for the M event being in the slope of a long-term increase in Br/Ti (Figure 7.7). The rise in organic productivity is accompanied by increased carbonate productivity, indicated by the Ca/Fe ratio, consistently high Ca values, and generally light-colored sediments in Section U1553D-5R-1 and 2 (Figure 7.3). Our observations indicate increased productivity coinciding with the onset of the EECO that are in contrast to investigations at the succession at mid-Waipara River, Canterbury Basin, New Zealand of Crouch et al. (2020), where no change in productivity during the onset of the EECO was observed as indicated by the relatively constant abundance of calcareous nannofossils and dinocysts, which are considered to be indicators for productivity.

To summarize, our high-latitude Southwest Pacific data indicate that silica burial is generally associated with early Eocene hyperthermal events, both of which were paced by the short eccentricity cycle of ~100 kyr. Therefore, enhanced silica burial is likely caused by an increased marine productivity in response to both, the short-term hyperthermals and the long-term warming trend of the EECO. Hereby we provide evidence that the observation of silica burial associated with early Eocene hyperthermals are not just a feature of the Atlantic Ocean as previously thought.

7.5. Conclusion

Silica burial has been previously associated with early Eocene hyperthermal events in the Atlantic Ocean, raising the question of whether this is a regionally restricted or a global phenomenon. In this study, we provide evidence indicating that hyperthermal events and enhanced siliceous production both occurred during the same short eccentricity maxima. While hyperthermals did not occur during every eccentricity maximum, siliceous productivity also increased during periods not associated with hyperthermal events. The opal concentration was highest during the PETM, the I1, and K events.

In addition to the eccentricity-paced siliceous productivity, we observe a major change in overall marine productivity based on Br/Ti ratios from relatively stable values to a continuous increase starting at 53.3 Ma, which coincides with the potential start of the EECO at Site U1553. This emphasizes the need to examine if silica burial in early Eocene sediments is linked to hyperthermal events, as we suggest it is a signal captured globally in marine sediment archives that record the climate response to carbon perturbations.

7.6. Acknowledgements

The samples and data for this study are provided by the International Ocean Discovery Program (IODP). We thank the crew and scientists of IODP Expedition378 “South Pacific Paleogene Climate”. We express our profound gratitude to Laurel Childress and colleagues at Texas A&M University, for XRF-scanning the U1553 cores during the pandemic lockdowns and the Gulf Coast Repository (GCR) team

for taking our samples during times, when travel and access to labs abroad were restricted. We thank Oscar Romero and Marco Klann for opal analyses. This study is funded by the Deutsche Forschungsgemeinschaft (DFG, German Research Foundation) under Germany's Excellence Strategy EXC-2077-390741603.

7.7. Data availability

Bulk sediment $\delta^{13}\text{C}$, $\delta^{18}\text{O}$ and tie points for the age model are available online in Niederbockstruck et al. (2024b).

XRF data and line-scanned core images can be found here: <https://web.iodp.tamu.edu/OVERVIEW/>

Opal concentration can be found in chapter 11. Appendix.

7.8. References

- Agnihotri, R., Altabet, M. A., Herbert, T. D., & Tierney, J. E. (2008). Subdecadally resolved paleoceanography of the Peru margin during the last two millennia. *Geochemistry, Geophysics, Geosystems*, 9(5). <https://doi.org/https://doi.org/10.1029/2007GC001744>
- Agnini, C., Macrì, P., Backman, J., Brinkhuis, H., Fornaciari, E., Giusberti, L., Luciani, V., Rio, D., Sluijs, A., & Speranza, F. (2009). An early Eocene carbon cycle perturbation at ~52.5 Ma in the Southern Alps: Chronology and biotic response. *Paleoceanography*, 24(2). <https://doi.org/https://doi.org/10.1029/2008PA001649>
- Agterhuis, T., Ziegler, M., de Winter, N. J., & Lourens, L. J. (2022). Warm deep-sea temperatures across Eocene Thermal Maximum 2 from clumped isotope thermometry. *Communications Earth & Environment*, 3(1), 39. <https://doi.org/10.1038/s43247-022-00350-8>
- Alegret, L., Harper, D. T., Agnini, C., Newsam, C., Westerhold, T., Cramwinckel, M. J., Dallanave, E., Dickens, G. R., & Sutherland, R. (2021). Biotic Response to Early Eocene Warming Events: Integrated Record From Offshore Zealandia, North Tasman Sea. *Paleoceanography and Paleoclimatology*, 36(8). <https://doi.org/10.1029/2020pa004179>
- Archer, D., Lyle, M., Rodgers, K., & Froelich, P. (1993). What Controls Opal Preservation in Tropical Deep-Sea Sediments? *Paleoceanography*, 8(1), 7-21. <https://doi.org/https://doi.org/10.1029/92PA02803>
- Berner, R. A., & Caldeira, K. (1997). The need for mass balance and feedback in the geochemical carbon cycle. *Geology*, 25(10), 955-956. [https://doi.org/10.1130/0091-7613\(1997\)025<0955:Tnfmba>2.3.Co;2](https://doi.org/10.1130/0091-7613(1997)025<0955:Tnfmba>2.3.Co;2)
- Berner, R. A., Lasaga, A. C., & Garrels, R. M. (1983). The carbonate-silicate geochemical cycle and its effect on atmospheric carbon dioxide over the past 100 million years. *American Journal of Science*, 283(7), 641–683. <https://doi.org/10.2475/ajs.283.7.641>
- Bohrmann, G., Abelmann, A., Gersonde, R., Hubberten, H., & Kuhn, G. (1994). Pure siliceous ooze, a diagenetic environment for early chert formation. *Geology*, 22(3), 207-210. [https://doi.org/10.1130/0091-7613\(1994\)022<0207:Psoade>2.3.Co;2](https://doi.org/10.1130/0091-7613(1994)022<0207:Psoade>2.3.Co;2)

- Bowen, G. J., Beerling, D. J., Koch, P. L., Zachos, J. C., & Quattlebaum, T. (2004). A humid climate state during the Palaeocene/Eocene thermal maximum. *Nature*, 432(7016), 495-499. <https://doi.org/10.1038/nature03115>
- Bowen, G. J., & Zachos, J. C. (2010). Rapid carbon sequestration at the termination of the Palaeocene–Eocene Thermal Maximum. *Nature Geoscience*, 3(12), 866-869. <https://doi.org/10.1038/ngeo1014>
- Brady, P. V., & Walther, J. V. (1992). Surface chemistry and silicate dissolution at elevated temperatures. *American Journal of Science*, 292(9), 639-658. <https://doi.org/10.2475/ajs.292.9.639>
- Caley, T., Malaizé, B., Zaragosi, S., Rossignol, L., Bourget, J., Eynaud, F., Martinez, P., Giraudeau, J., Charlier, K., & Ellouz-Zimmermann, N. (2011). New Arabian Sea records help decipher orbital timing of Indo-Asian monsoon. *Earth and Planetary Science Letters*, 308(3), 433-444. <https://doi.org/https://doi.org/10.1016/j.epsl.2011.06.019>
- Calvert, S. E. (1971). Composition and origin of North Atlantic deep sea cherts. *Contributions to Mineralogy and Petrology*, 33(4), 273-288. <https://doi.org/10.1007/BF00382569>
- Calvert, S. E., Burns, R. G., Smith, J. V., Kempe, D. R. C., Horne, J. E. T., & Dunham, K. C. (1977). Mineralogy of silica phases in deep-sea cherts and porcelanites. *Philosophical Transactions of the Royal Society of London. Series A, Mathematical and Physical Sciences*, 286(1336), 239-252. <https://doi.org/doi:10.1098/rsta.1977.0115>
- Caves Rugenstein, J. K., Ibarra, D. E., & von Blanckenburg, F. (2019). Neogene cooling driven by land surface reactivity rather than increased weathering fluxes. *Nature*, 571(7763), 99-102. <https://doi.org/10.1038/s41586-019-1332-y>
- Coccioni, R., Bancalà, G., Catanzariti, R., Fornaciari, E., Frontalini, F., Giusberti, L., Jovane, L., Luciani, V., Savian, J., & Sprovieri, M. (2012). An integrated stratigraphic record of the Palaeocene–lower Eocene at Gubbio (Italy): new insights into the early Palaeogene hyperthermals and carbon isotope excursions. *Terra Nova*, 24(5), 380-386. <https://doi.org/https://doi.org/10.1111/j.1365-3121.2012.01076.x>
- Cramer, B. S., Wright, J. D., Kent, D. V., & Aubry, M.-P. (2003). Orbital climate forcing of $\delta^{13}\text{C}$ excursions in the late Paleocene–early Eocene (chrons C24n–C25n). *Paleoceanography*, 18(4). <https://doi.org/https://doi.org/10.1029/2003PA000909>
- Crouch, E. M., Shepherd, C. L., Morgans, H. E. G., Naafs, B. D. A., Dallanave, E., Phillips, A., Hollis, C. J., & Pancost, R. D. (2020). Climatic and environmental changes across the early Eocene climatic optimum at mid-Waipara River, Canterbury Basin, New Zealand. *Earth-Science Reviews*, 200, 102961. <https://doi.org/https://doi.org/10.1016/j.earscirev.2019.102961>
- D'Onofrio, R., Luciani, V., Fornaciari, E., Giusberti, L., Boscolo Galazzo, F., Dallanave, E., Westerhold, T., Sprovieri, M., & Telch, S. (2016). Environmental perturbations at the early Eocene ETM2, H2, and I1 events as inferred by Tethyan calcareous plankton (Terche section, northeastern Italy). *Paleoceanography*, 31(9), 1225-1247. <https://doi.org/https://doi.org/10.1002/2016PA002940>
- D'Onofrio, R., Luciani, V., Dickens, G. R., Wade, B. S., & Kirtland Turner, S. (2020). Demise of the Planktic Foraminifer Genus *Morozovella* during the Early Eocene Climatic Optimum: New Records from ODP Site 1258 (Demerara Rise, Western Equatorial Atlantic) and Site 1263 (Walvis Ridge, South Atlantic). *Geosciences*, 10(3), 88. <https://www.mdpi.com/2076-3263/10/3/88>

- de Boer, A. M., Sigman, D. M., Toggweiler, J. R., & Russell, J. L. (2007). Effect of global ocean temperature change on deep ocean ventilation. *Paleoceanography*, 22(2).
<https://doi.org/https://doi.org/10.1029/2005PA001242>
- Dedert, M., Stoll, H. M., Kroon, D., Shimizu, N., Kanamaru, K., & Ziveri, P. (2012). Productivity response of calcareous nannoplankton to Eocene Thermal Maximum 2 (ETM2). *Clim. Past*, 8(3), 977-993. <https://doi.org/10.5194/cp-8-977-2012>
- Dickens, G. R., O'Neil, J. R., Rea, D. K., & Owen, R. M. (1995). Dissociation of oceanic methane hydrate as a cause of the carbon isotope excursion at the end of the Paleocene. *Paleoceanography*, 10(6), 965-971. <https://doi.org/https://doi.org/10.1029/95PA02087>
- Drury, A. J., Westerhold, T., Wilkens, R. H., & Röhl, U. (2022). Data report: Splice adjustment for site U1553. In U. Röhl, D. J. Thomas, L. B. Childress, & Expedition 378 Scientists (Eds.), *South Pacific Paleogene climate. Proceedings of the International Ocean Discovery Program (Vol. 378)*. International Ocean Discovery Program. <https://doi.org/10.14379/iodp.proc.378.201.2022>
- Elliot Smith, M., Carroll, A. R., & Mueller, E. R. (2008). Elevated weathering rates in the Rocky Mountains during the Early Eocene Climatic Optimum. *Nature Geoscience*, 1(6), 370-374. <https://doi.org/10.1038/ngeo205>
- Ernst, W., & Calvert, S. E. (1969). An experimental study of the recrystallization of porcelanite and its bearing on the origin of some bedded cherts. *Am. J. Sci*, 267, 114-133.
- Fang, X., Galy, A., Yang, Y., Zhang, W., Ye, C., & Song, C. (2019). Paleogene global cooling–induced temperature feedback on chemical weathering, as recorded in the northern Tibetan Plateau. *Geology*, 47(10), 992-996. <https://doi.org/10.1130/g46422.1>
- Friedrich, O., Norris, R. D., & Erbacher, J. (2012). Evolution of middle to Late Cretaceous oceans—A 55 m.y. record of Earth's temperature and carbon cycle. *Geology*, 40(2), 107-110. <https://doi.org/10.1130/G32701.1>
- Gaillardet, J., Dupré, B., Louvat, P., & Allègre, C. J. (1999). Global silicate weathering and CO₂ consumption rates deduced from the chemistry of large rivers. *Chemical Geology*, 159(1), 3-30. [https://doi.org/https://doi.org/10.1016/S0009-2541\(99\)00031-5](https://doi.org/https://doi.org/10.1016/S0009-2541(99)00031-5)
- Galeotti, S., Krishnan, S., Pagani, M., Lanci, L., Gaudio, A., Zachos, J. C., Monechi, S., Morelli, G., & Lourens, L. (2010). Orbital chronology of Early Eocene hyperthermals from the Contessa Road section, central Italy. *Earth and Planetary Science Letters*, 290(1), 192-200. <https://doi.org/https://doi.org/10.1016/j.epsl.2009.12.021>
- Garrels, R. M., & Berner, R. A. (1983). The Global Carbonate-Silicate Sedimentary System — Some Feedback Relations. In P. Westbroek & E. W. de Jong (Eds.), *Biom mineralization and Biological Metal Accumulation: Biological and Geological Perspectives Papers presented at the Fourth International Symposium on Biom mineralization, Renesse, The Netherlands, June 2–5, 1982 (pp. 73-87)*. Springer Netherlands. https://doi.org/10.1007/978-94-009-7944-4_6
- Gartner, S. (1970). Sea-Floor Spreading, Carbonate Dissolution Level, and the Nature of Horizon A. *Science*, 169(3950), 1077-1079. <https://doi.org/doi:10.1126/science.169.3950.1077>
- Gibbs, S. J., Bralower, T. J., Bown, P. R., Zachos, J. C., & Bybell, L. M. (2006). Shelf and open-ocean calcareous phytoplankton assemblages across the Paleocene-Eocene Thermal Maximum: Implications for global productivity gradients. *Geology*, 34(4), 233-236. <https://doi.org/10.1130/g22381.1>

- Gibbs, S. J., Stoll, H. M., Bown, P. R., & Bralower, T. J. (2010). Ocean acidification and surface water carbonate production across the Paleocene–Eocene thermal maximum. *Earth and Planetary Science Letters*, 295(3), 583-592. <https://doi.org/https://doi.org/10.1016/j.epsl.2010.04.044>
- Gibson, T. G., & Towe, K. M. (1971). Eocene Volcanism and the Origin of Horizon A. *Science*, 172(3979), 152-154. <https://doi.org/doi:10.1126/science.172.3979.152>
- Gribble, G. W. (2003). The diversity of naturally produced organohalogens. *Chemosphere*, 52(2), 289-297. [https://doi.org/https://doi.org/10.1016/S0045-6535\(03\)00207-8](https://doi.org/https://doi.org/10.1016/S0045-6535(03)00207-8)
- Hartmann, J., Jansen, N., Dürr, H. H., Harashima, A., Okubo, K., & Kempe, S. (2010). Predicting riverine dissolved silica fluxes to coastal zones from a hyperactive region and analysis of their first-order controls. *International Journal of Earth Sciences*, 99(1), 207-230. <https://doi.org/10.1007/s00531-008-0381-5>
- Hesse, R. (1988). Diagenesis# 13. Origin of chert: Diagenesis of biogenic siliceous sediments. *Geoscience Canada*, 15(3), 171-192.
- Hessler, A. M., Zhang, J., Covault, J., & Ambrose, W. (2017). Continental weathering coupled to Paleogene climate changes in North America. *Geology*, 45(10), 911-914. <https://doi.org/10.1130/g39245.1>
- Hillenbrand, C. D., Kuhn, G., & Frederichs, T. (2009). Record of a Mid-Pleistocene depositional anomaly in West Antarctic continental margin sediments: an indicator for ice-sheet collapse? *Quaternary Science Reviews*, 28(13), 1147-1159. <https://doi.org/https://doi.org/10.1016/j.quascirev.2008.12.010>
- Hollis, C. J. (1997). Integrated Paleogene biostratigraphy of DSDP site 277 (Leg 29): foraminifera, calcareous nannofossils, Radiolaria, and palynomorphs. *Inst. Geol. Nuc. Sci. Rept.* 97/07, 1-87.
- Hollis, C. J., Dickens, G. R., Field, B. D., Jones, C. M., & Percy Strong, C. (2005). The Paleocene–Eocene transition at Mead Stream, New Zealand: a southern Pacific record of early Cenozoic global change. *Palaeogeography, Palaeoclimatology, Palaeoecology*, 215(3), 313-343. <https://doi.org/https://doi.org/10.1016/j.palaeo.2004.09.011>
- Ingram, W. C., Meyers, S. R., Brunner, C. A., & Martens, C. S. (2010). Late Pleistocene–Holocene sedimentation surrounding an active seafloor gas-hydrate and cold-seep field on the Northern Gulf of Mexico Slope. *Marine Geology*, 278(1), 43-53. <https://doi.org/https://doi.org/10.1016/j.margeo.2010.09.002>
- Jaccard, S. L., Galbraith, E. D., Sigman, D. M., & Haug, G. H. (2010). A pervasive link between Antarctic ice core and subarctic Pacific sediment records over the past 800kyrs. *Quaternary Science Reviews*, 29(1), 206-212. <https://doi.org/https://doi.org/10.1016/j.quascirev.2009.10.007>
- Jaccard, S. L., Haug, G. H., Sigman, D. M., Pedersen, T. F., Thierstein, H. R., & Röhl, U. (2005). Glacial/Interglacial Changes in Subarctic North Pacific Stratification. *Science*, 308(5724), 1003-1006. <https://doi.org/10.1126/science.1108696>
- John, C. M., Bohaty, S. M., Zachos, J. C., Sluijs, A., Gibbs, S., Brinkhuis, H., & Bralower, T. J. (2008). North American continental margin records of the Paleocene–Eocene thermal maximum: Implications for global carbon and hydrological cycling. *Paleoceanography*, 23(2). <https://doi.org/https://doi.org/10.1029/2007PA001465>
- JOIDES. (1967). Deep-Sea Drilling Project1. *AAPG Bulletin*, 51(9), 1787-1802. <https://doi.org/10.1306/5d25c183-16c1-11d7-8645000102c1865d>

- Kennett, J. P., & Stott, L. D. (1991). Abrupt deep-sea warming, palaeoceanographic changes and benthic extinctions at the end of the Palaeocene. *Nature*, 353(6341), 225-229. <https://doi.org/10.1038/353225a0>
- Khider, D., Emile-Geay, J., Zhu, F., James, A., Landers, J., Ratnakar, V., & Gil, Y. (2022). Pyleoclim: Paleoclimate timeseries analysis and visualization with Python. *Paleoceanography and Paleoclimatology*, 37, e2022PA004509. doi:10.1029/2022PA004509
- Kirtland Turner, S., Sexton, P. F., Charles, C. D., & Norris, R. D. (2014). Persistence of carbon release events through the peak of early Eocene global warmth. *Nature Geoscience*, 7(10), 748-751. <https://doi.org/10.1038/ngeo2240>
- Kirtland Turner, S., Ridgwell, A., Keller, A. L., Vahlenkamp, M., Aleksinski, A. K., Sexton, P. F., Penman, D. E., Hull, P. M., & Norris, R. D. (2024). Sensitivity of ocean circulation to warming during the Early Eocene greenhouse. *Proceedings of the National Academy of Sciences*, 121(24), e2311980121. <https://doi.org/doi:10.1073/pnas.2311980121>
- Kump, L. R., Brantley, S. L., & Arthur, M. A. (2000). Chemical Weathering, Atmospheric CO₂, and Climate. *Annual Review of Earth and Planetary Sciences*, 28(Volume 28, 2000), 611-667. <https://doi.org/https://doi.org/10.1146/annurev.earth.28.1.611>
- Lancelot, Y. (1973). Chert and Silica Diagenesis in Sediments from the Central Pacific.
- Laskar, J., Fienga, A., Gastineau, M., & Manche, H. (2011). La2010: a new orbital solution for the long-term motion of the Earth*. *A&A*, 532, A89. <https://doi.org/10.1051/0004-6361/201116836>
- Lauretano, V., Hilgen, F., Zachos, J. C., & Lourens, L. J. (2016). Astronomically tuned age model for the early Eocene carbon isotope events: A new high-resolution delta C-13 (benthic) record of ODP Site 1263 between similar to 49 and similar to 54 Ma. *Newsletters on stratigraphy*, 49(2), 383-400.
- Lauretano, V., Littler, K., Polling, M., Zachos, J. C., & Lourens, L. J. (2015). Frequency, magnitude and character of hyperthermal events at the onset of the Early Eocene Climatic Optimum. *Clim. Past*, 11(10), 1313-1324. <https://doi.org/10.5194/cp-11-1313-2015>
- Lauretano, V., Zachos, J. C., & Lourens, L. J. (2018). Orbitally Paced Carbon and Deep-Sea Temperature Changes at the Peak of the Early Eocene Climatic Optimum. *Paleoceanography and Paleoclimatology*, 33(10), 1050-1065. <https://doi.org/https://doi.org/10.1029/2018PA003422>
- Li, M., Huang, C., Ogg, J., Zhang, Y., Hinnov, L., Wu, H., Chen, Z.-Q., & Zou, Z. (2019). Paleoclimate proxies for cyclostratigraphy: Comparative analysis using a Lower Triassic marine section in South China. *Earth-Science Reviews*, 189, 125-146. <https://doi.org/https://doi.org/10.1016/j.earscirev.2019.01.011>
- Littler, K., Röhl, U., Westerhold, T., & Zachos, J. C. (2014). A high-resolution benthic stable-isotope record for the South Atlantic: Implications for orbital-scale changes in Late Paleocene–Early Eocene climate and carbon cycling. *Earth and Planetary Science Letters*, 401, 18-30. <https://doi.org/https://doi.org/10.1016/j.epsl.2014.05.054>
- Lourens, L. J., Sluijs, A., Kroon, D., Zachos, J. C., Thomas, E., Röhl, U., Bowles, J., & Raffi, I. (2005). Astronomical pacing of late Palaeocene to early Eocene global warming events. *Nature*, 435(7045), 1083-1087. <https://doi.org/10.1038/nature03814>
- Luciani, V., Dickens, G. R., Backman, J., Fornaciari, E., Giusberti, L., Agnini, C., & D'Onofrio, R. (2016). Major perturbations in the global carbon cycle and photosymbiont-bearing planktic foraminifera during the early Eocene. *Clim. Past*, 12(4), 981-1007. <https://doi.org/10.5194/cp-12-981-2016>

- Lyu, J., Auer, G., Bialik, O. M., Christensen, B., Yamaoka, R., & De Vleeschouwer, D. (2023). Astronomically-Paced Changes in Paleoproductivity, Winnowing, and Mineral Flux Over Broken Ridge (Indian Ocean) Since the Early Miocene. *Paleoceanography and Paleoclimatology*, 38(12), e2023PA004761. <https://doi.org/https://doi.org/10.1029/2023PA004761>
- Macellari, C. E., & De Vries, T. J. (1987). Late Cretaceous upwelling and anoxic sedimentation in northwestern South America. *Palaeogeography, Palaeoclimatology, Palaeoecology*, 59, 279-292. [https://doi.org/https://doi.org/10.1016/0031-0182\(87\)90086-1](https://doi.org/https://doi.org/10.1016/0031-0182(87)90086-1)
- Malcolm, S. J., & Price, N. B. (1984). The behaviour of iodine and bromine in estuarine surface sediments. *Marine Chemistry*, 15(3), 263-271. [https://doi.org/https://doi.org/10.1016/0304-4203\(84\)90022-7](https://doi.org/https://doi.org/10.1016/0304-4203(84)90022-7)
- Marsh, R., Mills, R. A., Green, D. R. H., Salter, I., & Taylor, S. (2007). Controls on sediment geochemistry in the Crozet region. *Deep Sea Research Part II: Topical Studies in Oceanography*, 54(18), 2260-2274. <https://doi.org/https://doi.org/10.1016/j.dsr2.2007.06.004>
- Mayer, L. M., Schick, L. L., Allison, M. A., Ruttenberg, K. C., & Bentley, S. J. (2007). Marine vs. terrigenous organic matter in Louisiana coastal sediments: The uses of bromine:organic carbon ratios. *Marine Chemistry*, 107(2), 244-254. <https://doi.org/https://doi.org/10.1016/j.marchem.2007.07.007>
- Misra, S., & Froelich, P. N. (2012). Lithium Isotope History of Cenozoic Seawater: Changes in Silicate Weathering and Reverse Weathering. *Science*, 335(6070), 818-823. <https://doi.org/doi:10.1126/science.1214697>
- Mitchell, R. N., Bice, D. M., Montanari, A., Cleaveland, L. C., Christianson, K. T., Coccioni, R., & Hinnov, L. A. (2008). Oceanic anoxic cycles? Orbital prelude to the Bonarelli Level (OAE 2). *Earth and Planetary Science Letters*, 267(1), 1-16. <https://doi.org/https://doi.org/10.1016/j.epsl.2007.11.02>
- Moore, T. C., Jr. (2008). Biogenic silica and chert in the Pacific Ocean. *Geology*, 36(12), 975-978. <https://doi.org/10.1130/g25057a.1>
- Müller, P. J., & Schneider, R. (1993). An automated leaching method for the determination of opal in sediments and particulate matter. *Deep Sea Research Part I: Oceanographic Research Papers*, 40(3), 425-444. [https://doi.org/https://doi.org/10.1016/0967-0637\(93\)90140-X](https://doi.org/https://doi.org/10.1016/0967-0637(93)90140-X)
- Muttoni, G., & Kent, D. V. (2007). Widespread formation of cherts during the early Eocene climate optimum. *Palaeogeography, Palaeoclimatology, Palaeoecology*, 253(3), 348-362. <https://doi.org/https://doi.org/10.1016/j.palaeo.2007.06.008>
- Nelson, D. M., Tréguer, P., Brzezinski, M. A., Leynaert, A., & Quéguiner, B. (1995). Production and dissolution of biogenic silica in the ocean: Revised global estimates, comparison with regional data and relationship to biogenic sedimentation. *Global Biogeochemical Cycles*, 9(3), 359-372. <https://doi.org/https://doi.org/10.1029/95GB01070>
- Nicolo, M. J., Dickens, G. R., Hollis, C. J., & Zachos, J. C. (2007). Multiple early Eocene hyperthermals: Their sedimentary expression on the New Zealand continental margin and in the deep sea. *Geology*, 35(8), 699-702. <https://doi.org/10.1130/g23648a.1>
- Niederbockstruck, B., Jones, H. L., Yasukawa, K., Raffi, I., Tanaka, E., Westerhold, T., Ikehara, M., & Röhl, U. (2024a). Apparent Diachroneity of Calcareous Nannofossil Datums During the Early Eocene

- in the High-Latitude South Pacific Ocean. *Paleoceanography and Paleoclimatology*, 39(4), e2023PA004801. <https://doi.org/https://doi.org/10.1029/2023PA004801>
- Niederbockstruck, B., Jones, H. L., Yasukawa, K., Raffi, I., Tanaka, E., Westerhold, T., et al. (2024b). Late Paleocene to early Eocene stable isotope records and calcareous nannofossil datums at IODP Site U1553 [Dataset]. PANGAEA. <https://doi.org/10.1594/PANGAEA.963554>
- Norris, R. D., & Röhl, U. (1999). Carbon cycling and chronology of climate warming during the Palaeocene/Eocene transition. *Nature*, 401(6755), 775-778. <https://doi.org/10.1038/44545>
- Pälike, H., Lyle, M. W., Nishi, H., Raffi, I., Ridgwell, A., Gamage, K., Klaus, A., Acton, G., Anderson, L., Backman, J., Baldauf, J., Beltran, C., Bohaty, S. M., Bown, P., Busch, W., Channell, J. E. T., Chun, C. O. J., Delaney, M., Dewangan, P., . . . Zeebe, R. E. (2012). A Cenozoic record of the equatorial Pacific carbonate compensation depth. *Nature*, 488(7413), 609-614. <https://doi.org/10.1038/nature11360>
- Panchuk, K., Ridgwell, A., & Kump, L. R. (2008). Sedimentary response to Paleocene-Eocene Thermal Maximum carbon release: A model-data comparison. *Geology*, 36(4), 315. <https://doi.org/10.1130/g24474a.1>
- Penman, D. E. (2016). Silicate weathering and North Atlantic silica burial during the Paleocene-Eocene Thermal Maximum. *Geology*, 44(9), 731-734. <https://doi.org/10.1130/g37704.1>
- Penman, D. E., Caves Rugenstein, J. K., Ibarra, D. E., & Winnick, M. J. (2020). Silicate weathering as a feedback and forcing in Earth's climate and carbon cycle. *Earth-Science Reviews*, 209, 103298. <https://doi.org/https://doi.org/10.1016/j.earscirev.2020.103298>
- Penman, D. E., Keller, A., D'haenens, S., Kirtland Turner, S., & Hull, P. M. (2019). Atlantic Deep-Sea Cherts Associated With Eocene Hyperthermal Events. *Paleoceanography and Paleoclimatology*, 34(2), 287-299. <https://doi.org/https://doi.org/10.1029/2018PA003503>
- PISCIOTTO, K. A. (1981). Diagenetic trends in the siliceous facies of the Monterey Shale in the Santa Maria region, California. *Sedimentology*, 28(4), 547-571. <https://doi.org/https://doi.org/10.1111/j.1365-3091.1981.tb01701.x>
- Ramachandra Rao, A., & Hamed, K. (2003). Multi-taper method of analysis of periodicities in hydrologic data. *Journal of Hydrology*, 279(1), 125-143. [https://doi.org/https://doi.org/10.1016/S0022-1694\(03\)00176-8](https://doi.org/https://doi.org/10.1016/S0022-1694(03)00176-8)
- Raymo, M. E., & Ruddiman, W. F. (1992). Tectonic forcing of late Cenozoic climate [Review]. *Nature*, 359(6391), 117-122. <https://doi.org/10.1038/359117a0>
- Rea, D. K., & Lyle, M. W. (2005). Paleogene calcite compensation depth in the eastern subtropical Pacific: Answers and questions. *Paleoceanography*, 20(1). <https://doi.org/https://doi.org/10.1029/2004PA001064>
- Ren, J., Jiang, H., Seidenkrantz, M.-S., & Kuijpers, A. (2009). A diatom-based reconstruction of Early Holocene hydrographic and climatic change in a southwest Greenland fjord. *Marine Micropaleontology*, 70(3), 166-176. <https://doi.org/https://doi.org/10.1016/j.marmicro.2008.12.003>
- Rickert, D., Schlüter, M., & Wallmann, K. (2002). Dissolution kinetics of biogenic silica from the water column to the sediments. *Geochimica et Cosmochimica Acta*, 66(3), 439-455. [https://doi.org/https://doi.org/10.1016/S0016-7037\(01\)00757-8](https://doi.org/https://doi.org/10.1016/S0016-7037(01)00757-8)

- Riech, V., von Rad, U., Tucholke, B., & Vogt, P. (1979). Eocene porcellanites and Early Cretaceous cherts from the western North Atlantic. *Initial Reports of the Deep Sea Drilling Project*, 43, 437-455.
- Riech, V., & von Rad, U. (1979). Silica Diagenesis in the Atlantic Ocean: Diagenetic Potential and Transformations. In *Deep Drilling Results in the Atlantic Ocean: Continental Margins and Paleoenvironment* (pp. 315-340). <https://doi.org/https://doi.org/10.1029/ME003p0315>
- Röhl, U., Westerhold, T., Bralower, T. J., & Zachos, J. C. (2007). On the duration of the Paleocene-Eocene thermal maximum (PETM). *Geochemistry, Geophysics, Geosystems*, 8(12). <https://doi.org/https://doi.org/10.1029/2007GC001784>
- Röhl, U., Thomas, D. J., Childress, L. B., Anagnostou, E., Ausín, B., Borba Dias, B., et al. (2022). Site U1553. In U. Röhl, D. J. Thomas, L. B. Childress, & Expedition 378 Scientists (Eds.), *South Pacific Paleogene climate. Proceedings of the International Ocean Discovery Program* (Vol. 378). International Ocean Discovery Program. <https://doi.org/10.14379/iodp.proc.378.103.2022>
- Schlanger, S. O., et al., *Initial Reports of the Deep Sea Drilling Project*, 33, 1976.
- Shackleton, N. J., & Kennett, J. P. (1975). Paleotemperature History of the Cenozoic and the Initiation of Antarctic Glaciation: Oxygen and Carbon Isotope Analyses in DSDP Sites 277, 279 and 281.
- Slotnick, B. S., Dickens, G. R., Hollis, C. J., Crampton, J. S., Percy Strong, C., & Phillips, A. (2015). The onset of the Early Eocene Climatic Optimum at Branch Stream, Clarence River valley, New Zealand. *New Zealand Journal of Geology and Geophysics*, 58(3), 262-280. <https://doi.org/10.1080/00288306.2015.1063514>
- Slotnick, B. S., Dickens, G. R., Nicolo, M. J., Hollis, C. J., Crampton, J. S., Zachos, J. C., & Sluijs, A. (2012). Large-Amplitude Variations in Carbon Cycling and Terrestrial Weathering during the Latest Paleocene and Earliest Eocene: The Record at Mead Stream, New Zealand. *The Journal of Geology*, 120(5), 487-505. <https://doi.org/10.1086/666743>
- Sluijs, A., Röhl, U., Schouten, S., Brumsack, H.-J., Sangiorgi, F., Sinninghe Damsté, J. S., & Brinkhuis, H. (2008). Arctic late Paleocene–early Eocene paleoenvironments with special emphasis on the Paleocene-Eocene thermal maximum (Lomonosov Ridge, Integrated Ocean Drilling Program Expedition 302). *Paleoceanography*, 23(1). <https://doi.org/https://doi.org/10.1029/2007PA001495>
- Sluijs, A., Schouten, S., Donders, T. H., Schoon, P. L., Röhl, U., Reichart, G.-J., Sangiorgi, F., Kim, J.-H., Sinninghe Damsté, J. S., & Brinkhuis, H. (2009). Warm and wet conditions in the Arctic region during Eocene Thermal Maximum 2. *Nature Geoscience*, 2(11), 777-780. <https://doi.org/10.1038/ngeo668>
- Smith, W. E. (1960). The siliceous constituents of chert. *Geol. en Mijnb*, 39, 1-8.
- Stoll, H. M., Shimizu, N., Archer, D., & Ziveri, P. (2007). Coccolithophore productivity response to greenhouse event of the Paleocene–Eocene Thermal Maximum. *Earth and Planetary Science Letters*, 258(1), 192-206. <https://doi.org/https://doi.org/10.1016/j.epsl.2007.03.037>
- Sutherland, R., Dickens, G. R., Blum, P., Agnini, C., Alegret, L., Bhattacharya, J., et al. (2019). Site U1510. In R. Sutherland, G. R. Dickens, & P. Blum (Eds.), *The expedition 371 Scientists, tasman frontier subduction initiation and Paleogene climate* (Vol. 371). International Ocean Discovery Program. <https://doi.org/10.14379/iodp.proc.371.107.2019>
- Tanaka, E., Yasukawa, K., Ohta, J., & Kato, Y. (2022). Enhanced continental chemical weathering during the multiple early Eocene hyperthermals: New constraints from the southern Indian Ocean.

Geochimica et Cosmochimica Acta, 331, 192-211.

<https://doi.org/https://doi.org/10.1016/j.gca.2022.05.022>

The pandas development team. (2024). pandas-dev/pandas: Pandas (v2.1.4). Zenodo.

<https://doi.org/10.5281/zenodo.10957263>

Thomas, D. J., Bralower, T. J., & Zachos, J. C. (1999). New evidence for subtropical warming during the Late Paleocene thermal maximum: Stable isotopes from Deep Sea Drilling Project Site 527, Walvis Ridge. *Paleoceanography*, 14(5), 561-570. <https://doi.org/https://doi.org/10.1029/1999PA900031>

Thomas, E., & Shackleton, N. J. (1996). The Paleocene-Eocene benthic foraminiferal extinction and stable isotope anomalies. Geological Society, London, Special Publications, 101(1), 401-441.

<https://doi.org/doi:10.1144/GSL.SP.1996.101.01.20>

Thomas, E., Zachos, J. C., & Bralower, T. J. (2000). Deep-sea environments on a warm earth: latest Paleocene-early Eocene.

Thomson, D. J. (1982). Spectrum estimation and harmonic analysis. *Proceedings of the IEEE*, 70(9), 1055-1096. <https://doi.org/10.1109/PROC.1982.12433>

Van Andel, T. H., Heath, G. R., Moore, T. C., Jr., van Andel, T. H., Heath, G. R., & Moore, T. C., Jr. (1975). Cenozoic History and Paleooceanography of the Central Equatorial Pacific Ocean: A Regional Synthesis of Deep Sea Drilling Project Data. In *Cenozoic History and Paleooceanography of the Central Equatorial Pacific Ocean* (Vol. 143, pp. 0). Geological Society of America.

<https://doi.org/10.1130/MEM143-p1>

von Rad, U., Riech, V., & Rösch, H. (1978). 31. Silica diagenesis in continental margin sediments off Northwest Africa. *Deep Sea Drilling*.

Walker, J. C. G., Hays, P. B., & Kasting, J. F. (1981). A negative feedback mechanism for the long-term stabilization of Earth's surface temperature [Article]. *Journal of Geophysical Research*, 86(C10), 9776-9782. <https://doi.org/10.1029/JC086iC10p09776>

Wang, Y., Cui, Y., Su, H., Jiang, J., Wang, Y., Yang, Z., Hu, X., & Jiang, S. (2022). Response of calcareous nannoplankton to the Paleocene–Eocene Thermal Maximum in the Paratethys Seaway (Tarim Basin, West China). *Global and Planetary Change*, 217, 103918.

<https://doi.org/https://doi.org/10.1016/j.gloplacha.2022.103918>

Wessel, P., Luis, J. F., Uieda, L., Scharroo, R., Wobbe, F., Smith, W. H. F., & Tian, D. (2019). The Generic Mapping Tools version 6. *Geochemistry, Geophysics, Geosystems*, 20, 5556–5564.

<https://doi.org/10.1029/2019GC008515>

Westerhold, T., Marwan, N., Drury, A. J., Liebrand, D., Agnini, C., Anagnostou, E., Barnet, J. S. K., Bohaty, S. M., De Vleeschouwer, D., Florindo, F., Frederichs, T., Hodell, D. A., Holbourn, A. E., Kroon, D., Laurentano, V., Littler, K., Lourens, L. J., Lyle, M., Pälike, H., . . . Zachos, J. C. (2020). An astronomically dated record of Earth's climate and its predictability over the last 66 million years. *Science*, 369(6509), 1383-1387. <https://doi.org/doi:10.1126/science.aba6853>

Westerhold, T., Röhl, U., Donner, B., & Zachos, J. C. (2018). Global Extent of Early Eocene Hyperthermal Events: A New Pacific Benthic Foraminiferal Isotope Record From Shatsky Rise (ODP Site 1209). *Paleoceanography and Paleoclimatology*, 33(6), 626-642.

<https://doi.org/https://doi.org/10.1029/2017PA003306>

- Westerhold, T., Röhl, U., Frederichs, T., Agnini, C., Raffi, I., Zachos, J. C., & Wilkens, R. H. (2017). Astronomical calibration of the Ypresian timescale: implications for seafloor spreading rates and the chaotic behavior of the solar system? *Clim. Past*, 13(9), 1129-1152. <https://doi.org/10.5194/cp-13-1129-2017>
- Westerhold, T., Röhl, U., Laskar, J., Raffi, I., Bowles, J., Lourens, L. J., & Zachos, J. C. (2007). On the duration of magnetochrons C24r and C25n and the timing of early Eocene global warming events: Implications from the Ocean Drilling Program Leg 208 Walvis Ridge depth transect. *Paleoceanography*, 22(2). <https://doi.org/10.1029/2006PA001322>
- Wilkens, R. H., Drury, A. J., Westerhold, T., & Röhl, U. (2022). Data report: Depths of site U1553 off-splice data adjusted to the site U1553 splice, IODP Expedition 378. In U. Röhl, D. J. Thomas, L. B. Childress, & Expedition 378 Scientists (Eds.), *South Pacific Paleogene climate. Proceedings of the International Ocean Discovery program (Vol. 378)*. International Ocean Discovery Program. <https://doi.org/10.14379/iodp.proc.378.202.2022>
- Witkowski, J., Penman, D. E., Bryłka, K., Wade, B. S., Matting, S., Harwood, D. M., & Bohaty, S. M. (2020). Early Paleogene biosiliceous sedimentation in the Atlantic Ocean: Testing the inorganic origin hypothesis for Paleocene and Eocene chert and porcellanite. *Palaeogeography, Palaeoclimatology, Palaeoecology*, 556, 109896. <https://doi.org/10.1016/j.palaeo.2020.109896>
- Yasukawa, K., Nakamura, K., Fujinaga, K., Ikehara, M., & Kato, Y. (2017). Earth system feedback statistically extracted from the Indian Ocean deep-sea sediments recording Eocene hyperthermals. *Scientific Reports*, 7(1), 11304. <https://doi.org/10.1038/s41598-017-11470-z>
- Zachos, J., Pagani, M., Sloan, L., Thomas, E., & Billups, K. (2001). Trends, Rhythms, and Aberrations in Global Climate 65 Ma to Present. *Science*, 292(5517), 686-693. <https://doi.org/10.1126/science.1059412>
- Zachos, J. C., McCarren, H., Murphy, B., Röhl, U., & Westerhold, T. (2010). Tempo and scale of late Paleocene and early Eocene carbon isotope cycles: Implications for the origin of hyperthermals. *Earth and Planetary Science Letters*, 299(1), 242-249. <https://doi.org/10.1016/j.epsl.2010.09.004>
- Zachos, J. C., Röhl, U., Schellenberg, S. A., Sluijs, A., Hodell, D. A., Kelly, D. C., Thomas, E., Nicolo, M., Raffi, I., Lourens, L. J., McCarren, H., & Kroon, D. (2005). Rapid Acidification of the Ocean During the Paleocene-Eocene Thermal Maximum. *Science*, 308(5728), 1611-1615. <https://doi.org/10.1126/science.1109004>
- Zeebe, R. E., Zachos, J. C., & Dickens, G. R. (2009). Carbon dioxide forcing alone insufficient to explain Palaeocene–Eocene Thermal Maximum warming. *Nature Geoscience*, 2(8), 576-580. <https://doi.org/10.1038/ngeo578>
- Zhang, Y., Huck, T., Lique, C., Donnadieu, Y., Ladant, J.-B., Rabineau, M., & Aslanian, D. (2020). Early Eocene vigorous ocean overturning and its contribution to a warm Southern Ocean. *Climate of the Past*, 16(4), 1263–1283. <https://doi.org/10.5194/cp-16-1263-2020>

7.7. Supplemental material

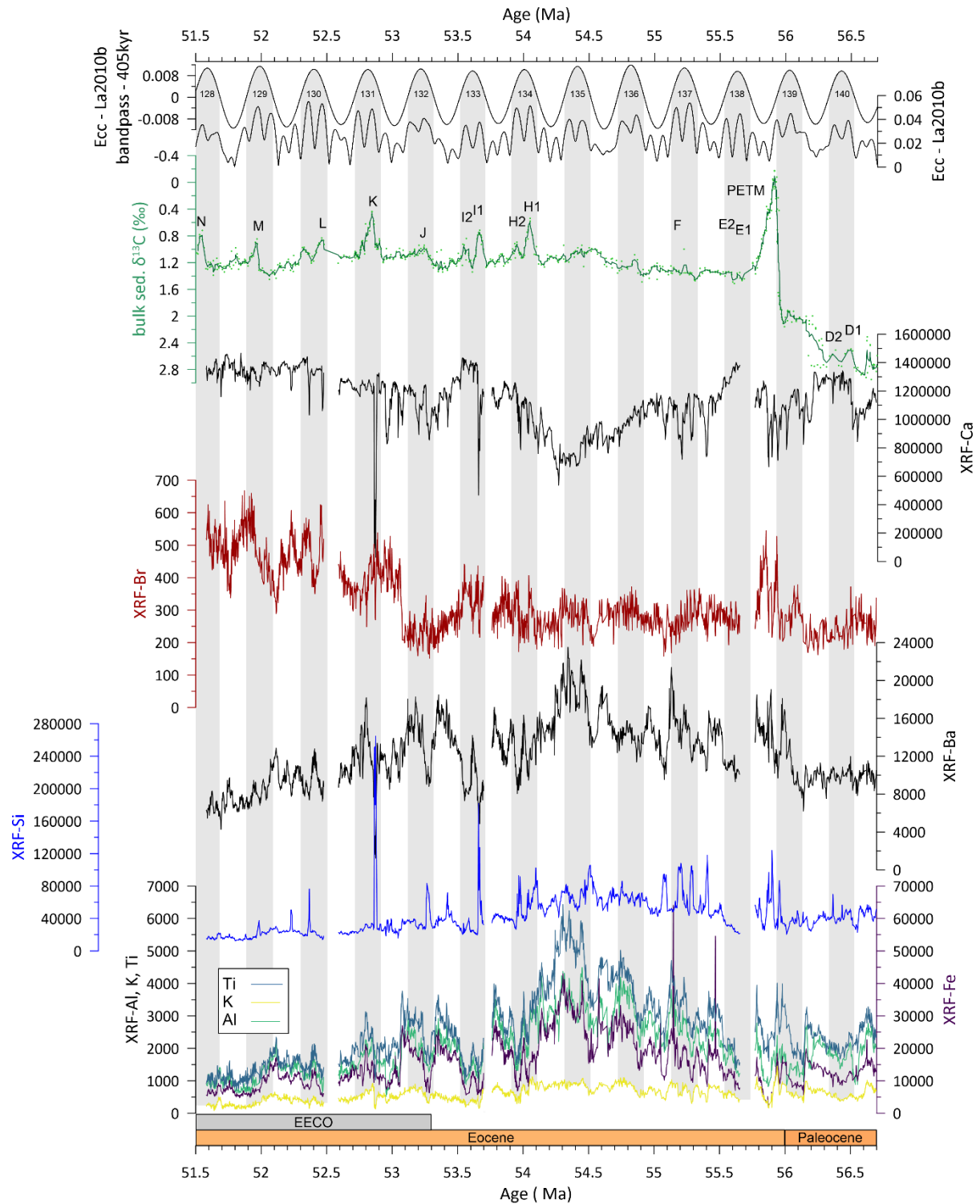


Figure S7.1. XRF elements Al, K, Ti, Fe, Si, Ba, Br, Sr and Ca (Röhl et al., 2022) used in this study. Bulk sediment $\delta^{13}\text{C}$ (Niederbockstruck et al., 2024b). Eccentricity cycle La2010b (Laskar et al., 2011) and an applied 405 kyr filter.

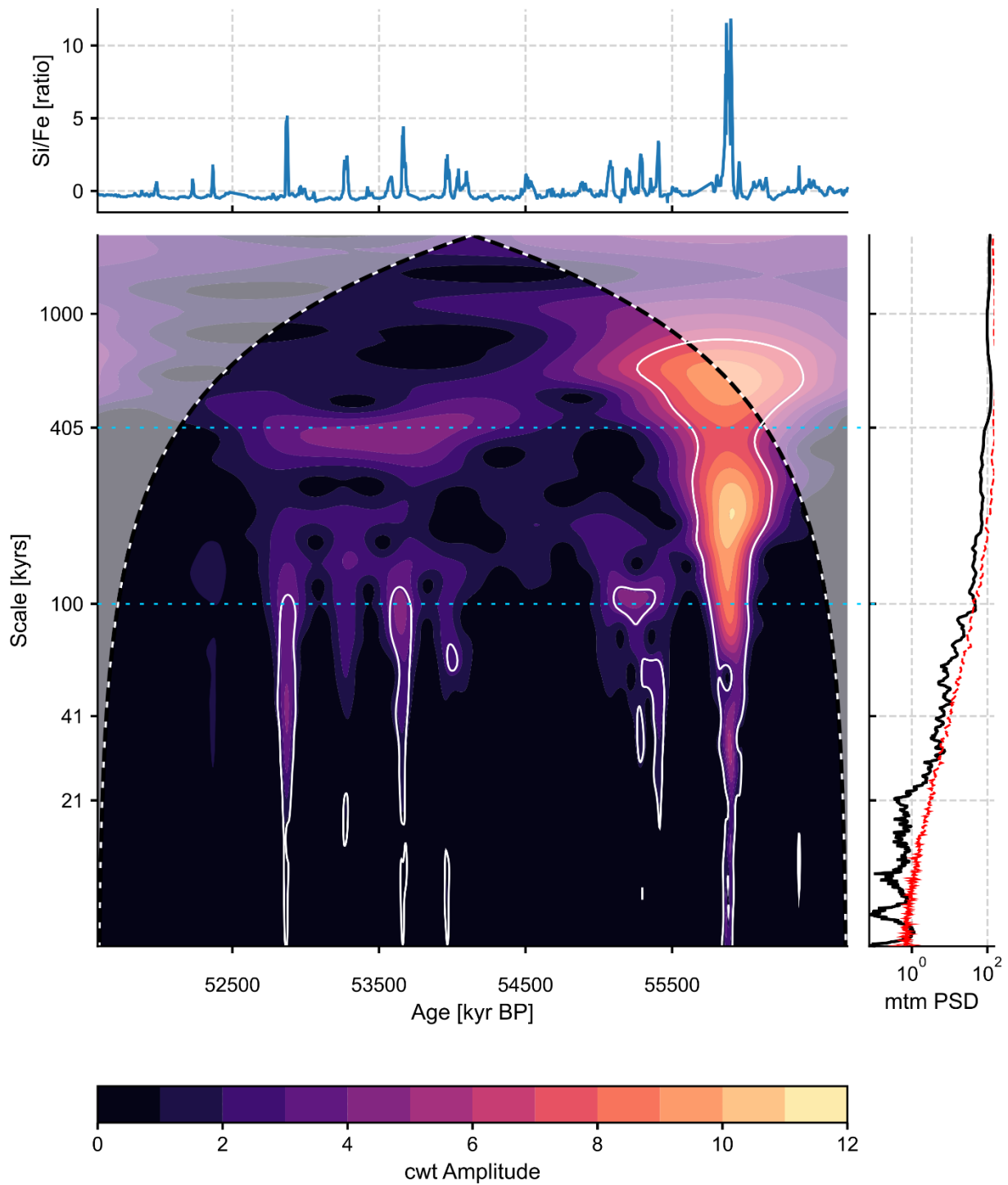


Figure S7.2. Wavelet analyses using the multitaper method (Thomson, 1982) of XRF Si/Fe ratio with highlighted 100 and 405 kyr signal (dashed blue lines). Analysis was performed using python package *Pyleoclim* (Khider et al., 2022).

Table S1. Result of a linear fit on the Br/Ti data for the studied interval.

	Equation	Average Y (Br/Ti)	Data points	Angle (°)
Onset EECO (51.58-53.30 Ma)	$Y = -0.24288433 * X + 13.029401$	0.30854013	616	-13.65°
Pre- EECO (53.3-56.70 Ma)	$Y = -0.0046348376 * X + 0.36388117$	0.10984942	922	-0.27°

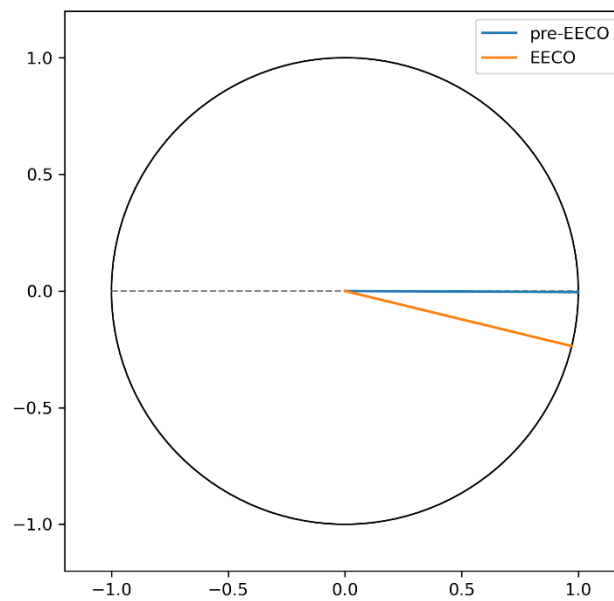


Figure S7.3. Comparison of the productivity increase (Bi/Ti) before the EECO in an interval from 56.70 to 53.30 Ma (Phase 1: blue line) and during the EECO 53.30 to 51.58 Ma (Phase 2: orange line), with horizontal line meaning no average change.

8. Synthesis

This doctoral thesis investigated the biotic response to carbon perturbation and warming events of the early Eocene using sediment records retrieved from IODP Site U1553, located south of New Zealand.

The main findings can be summarized as follows:

- 1) When developing an age model for the sediment record of Site U1553, I found that calcareous nannofossils related biostratigraphy and the correlation of $\delta^{13}\text{C}$ record to astronomically tuned records cannot be combined. The relative position of several first and last occurrences of calcareous nannofossil datums to hyperthermals were not in agreement to those of the Atlantic Sites ODP 1258 and ODP 1262. The observed diachroneity of several calcareous nannofossil datums between the Atlantic records and IODP Site U1553 is about 2 Myr or more. However, an age model based on the correlation of $\delta^{13}\text{C}$ records was successfully implemented and allows the identification of early Eocene hyperthermal events over a 7 Myr interval from 50.5 to 57.5 Ma.
- 2) I investigated the calcareous nannofossil assemblage at the genus level on 71 samples spanning a 1.1 Myr interval, covering four hyperthermals of different magnitude. The most significant change of calcareous nannofossil assemblage occurred between the I2 and J event, but more than 120 kyr before the suggested onset of the EECO. The changes in the calcareous nannofossil assemblage during the K event are consistent with those observed at IODP Site U1510.
- 3) I provide the first indication that enhanced silica burial is associated with multiple hyperthermal events in the South Pacific, appearing in a statistically significant 100 kyr cycle that is coinciding with the eccentricity cycle. This finding demonstrates that the association of silica burial with hyperthermals is not exclusive to the Atlantic Ocean.

9. Outlook

To improve future biostratigraphy related to calcareous nannofossil datums in the early Eocene, it is necessary to check the relative positions of the datums to the negative carbon excursions of hyperthermals at several sites. It is crucial to understand if the observed diachroneity at Site U1553 is more the rule than the exception. If so, are the diachroneities either 1) random, or 2) showing specific spatial patterns, such as low vs. high latitude, or are they related to ocean basins with calcareous nannofossil datums differing between the Atlantic and the Pacific? Therefore, it is important to increase the resolution of biostratigraphic shipboard data to confidently determine the last or first occurrence of a calcareous nannofossil datum in relation to hyperthermal events, indicated by $\delta^{13}\text{C}$ records.

The response of calcareous nannofossils does not appear to be related to the magnitude of carbon negative excursions in the early Eocene. Interestingly, the most significant change in the assemblage occurred between the small hyperthermal, the I2, and the J event. Finding the change in the calcareous nannofossil assemblage approximately 120 kyr before the EECO raises the question of whether this is a very site-specific observation or if similar changes in the assemblage can be detected elsewhere, indicating an early signal of the EECO recorded by the calcareous nanoplankton community.

The association of silica burial with hyperthermal events has so far been observed only in sediment cores from the Atlantic. However, new evidence from IODP Site U1553 in the South Pacific indicates that enhanced silica burial associated with hyperthermals leads to the hypothesis of a global phenomenon. Identifying signs of silicate weathering and increased siliceous productivity, particularly at other sites near continents, is vital for improving our understanding of global negative feedback mechanisms to carbon perturbations. This information can provide evidence that aligns with predictions from box models and Earth System Models.

10. References

- Agnini, C., Fornaciari, E., Raffi, I., Catanzariti, R., Pälke, H., Backman, J., & Rio, D. (2014). Biozonation and biochronology of Paleogene calcareous nannofossils from low and middle latitudes. *Newsletters on stratigraphy*, 47(2), 131-181.
- Agnini, C., Macrì, P., Backman, J., Brinkhuis, H., Fornaciari, E., Giusberti, L., Luciani, V., Rio, D., Sluijs, A., & Speranza, F. (2009). An early Eocene carbon cycle perturbation at ~52.5 Ma in the Southern Alps: Chronology and biotic response. *Paleoceanography*, 24(2).
<https://doi.org/https://doi.org/10.1029/2008PA001649>
- Agnini, C., Muttoni, G., Kent, D. V., & Rio, D. (2006). Eocene biostratigraphy and magnetic stratigraphy from Possagno, Italy: The calcareous nannofossil response to climate variability. *Earth and Planetary Science Letters*, 241(3), 815-830. <https://doi.org/https://doi.org/10.1016/j.epsl.2005.11.005>
- Anagnostou, E., John, E. H., Babila, T., Sexton, P., Ridgwell, A., Lunt, D. J., Pearson, P. N., Chalk, T., Pancost, R. D., & Foster, G. (2020). Proxy evidence for state-dependence of climate sensitivity in the Eocene greenhouse. *Nature communications*, 11(1), 1-9.
- Anagnostou, E., John, E. H., Edgar, K. M., Foster, G. L., Ridgwell, A., Inglis, G. N., Pancost, R. D., Lunt, D. J., & Pearson, P. N. (2016). Changing atmospheric CO₂ concentration was the primary driver of early Cenozoic climate. *Nature*, 533(7603), 380-384. <https://doi.org/10.1038/nature17423>
- Aubry, M.-P. (1986). Paleogene calcareous nannoplankton biostratigraphy of northwestern Europe. *Palaeogeography, Palaeoclimatology, Palaeoecology*, 55(2), 267-334.
[https://doi.org/https://doi.org/10.1016/0031-0182\(86\)90154-9](https://doi.org/https://doi.org/10.1016/0031-0182(86)90154-9)
- Backman, J., & Shackleton, N. J. (1983). Quantitative biochronology of Pliocene and early Pleistocene calcareous nannofossils from the Atlantic, Indian and Pacific oceans. *Marine Micropaleontology*, 8(2), 141-170. [https://doi.org/https://doi.org/10.1016/0377-8398\(83\)90009-9](https://doi.org/https://doi.org/10.1016/0377-8398(83)90009-9)
- Bijl, P. K., Houben, A. J. P., Schouten, S., Bohaty, S. M., Sluijs, A., Reichert, G.-J., Sinninghe Damsté, J. S., & Brinkhuis, H. (2010). Transient Middle Eocene Atmospheric CO₂ and Temperature Variations. *Science*, 330(6005), 819-821. <https://doi.org/doi:10.1126/science.1193654>
- Bijl, P. K., Schouten, S., Sluijs, A., Reichert, G. J., Zachos, J. C., & Brinkhuis, H. (2009). Early Palaeogene temperature evolution of the southwest Pacific Ocean. *Nature*, 461(7265), 776-779. <https://doi.org/10.1038/nature08399>
- Bown, P., & Pearson, P. (2009). Calcareous plankton evolution and the Paleocene/Eocene thermal maximum event: New evidence from Tanzania. *Marine Micropaleontology*, 71(1), 60-70. <https://doi.org/https://doi.org/10.1016/j.marmicro.2009.01.005>
- Bralower, T. J. (2002). Evidence of surface water oligotrophy during the Paleocene-Eocene thermal maximum: Nannofossil assemblage data from Ocean Drilling Program Site 690, Maud Rise, Weddell Sea. *Paleoceanography*, 17(2), 13-11-13-12. <https://doi.org/https://doi.org/10.1029/2001PA000662>
- Brassell, S. C., Eglinton, G., Marlowe, I. T., Pflaumann, U., & Sarnthein, M. (1986). Molecular stratigraphy: a new tool for climatic assessment. *Nature*, 320(6058), 129-133. <https://doi.org/10.1038/320129a0>
- Belkin, I.M. and Gordon, A.L. (1996). Southern Ocean fronts from the Greenwich meridian to Tasmania. *Journal of Geophysical Research: Oceans* (1978–2012), 101(C2), 3675-3696.

- Bukry, D. (1973). Low-attitude coccolith biostratigraphic zonation. Washington, DC, Initial Reports of the Deep Sea Drilling Project, 15, 127-149.
- Burke, K. D., Williams, J. W., Chandler, M. A., Haywood, A. M., Lunt, D. J., & Otto-Bliesner, B. L. (2018). Pliocene and Eocene provide best analogs for near-future climates. *Proceedings of the National Academy of Sciences*, 115(52), 13288-13293.
- Caballero, R., & Huber, M. (2013). State-dependent climate sensitivity in past warm climates and its implications for future climate projections. *Proceedings of the National Academy of Sciences*, 110(35), 14162-14167. <https://doi.org/doi:10.1073/pnas.1303365110>
- Carter, L., McCave, I. N., & Williams, M. J. M. (2008). Chapter 4 Circulation and Water Masses of the Southern Ocean: A Review. In F. Florindo & M. Siebert (Eds.), *Developments in Earth and Environmental Sciences* (Vol. 8, pp. 85-114). Elsevier. [https://doi.org/https://doi.org/10.1016/S1571-9197\(08\)00004-9](https://doi.org/https://doi.org/10.1016/S1571-9197(08)00004-9)
- Cramer, B. S., Wright, J. D., Kent, D. V., & Aubry, M.-P. (2003). Orbital climate forcing of $\delta^{13}\text{C}$ excursions in the late Paleocene–early Eocene (chrons C24n–C25n). *Paleoceanography*, 18(4). <https://doi.org/https://doi.org/10.1029/2003PA000909>
- Cramwinckel, M. J., Huber, M., Kocken, I. J., Agnini, C., Bijl, P. K., Bohaty, S. M., Frieling, J., Goldner, A., Hilgen, F. J., Kip, E. L., Peterse, F., van der Ploeg, R., Röhl, U., Schouten, S., & Sluijs, A. (2018). Synchronous tropical and polar temperature evolution in the Eocene. *Nature*, 559(7714), 382-386. <https://doi.org/10.1038/s41586-018-0272-2>
- D'Onofrio, R., Luciani, V., Fornaciari, E., Giusberti, L., Boscolo Galazzo, F., Dallanave, E., Westerhold, T., Sprovieri, M., & Telch, S. (2016). Environmental perturbations at the early Eocene ETM2, H2, and I1 events as inferred by Tethyan calcareous plankton (Terche section, northeastern Italy). *Paleoceanography*, 31(9), 1225-1247. <https://doi.org/https://doi.org/10.1002/2016PA002940>
- Deacon, G. E. R. (1982). Physical and biological zonation in the Southern Ocean. *Deep Sea Research Part A. Oceanographic Research Papers*, 29(1), 1-15. [https://doi.org/https://doi.org/10.1016/0198-0149\(82\)90058-9](https://doi.org/https://doi.org/10.1016/0198-0149(82)90058-9)
- Dedert, M., Stoll, H. M., Kroon, D., Shimizu, N., Kanamaru, K., & Ziveri, P. (2012). Productivity response of calcareous nannoplankton to Eocene Thermal Maximum 2 (ETM2). *Clim. Past*, 8(3), 977-993. <https://doi.org/10.5194/cp-8-977-2012>
- Falkowski, P. G., Barber, R. T., & Smetacek, V. (1998). Biogeochemical Controls and Feedbacks on Ocean Primary Production. *Science*, 281(5374), 200-206. <https://doi.org/doi:10.1126/science.281.5374.200>
- Friedlingstein, P., Meinshausen, M., Arora, V. K., Jones, C. D., Anav, A., Liddicoat, S. K., & Knutti, R. (2014). Uncertainties in CMIP5 Climate Projections due to Carbon Cycle Feedbacks. *Journal of Climate*, 27(2), 511-526. <https://doi.org/https://doi.org/10.1175/JCLI-D-12-00579.1>
- Galeotti, S., Krishnan, S., Pagani, M., Lanci, L., Gaudio, A., Zachos, J. C., Monechi, S., Morelli, G., & Lourens, L. (2010). Orbital chronology of Early Eocene hyperthermals from the Contessa Road section, central Italy. *Earth and Planetary Science Letters*, 290(1), 192-200. <https://doi.org/https://doi.org/10.1016/j.epsl.2009.12.021>
- Gibbs, S. J., Bown, P. R., Murphy, B. H., Sluijs, A., Edgar, K. M., Pälike, H., Bolton, C. T., & Zachos, J. C. (2012). Scaled biotic disruption during early Eocene global warming events. *Biogeosciences*, 9(11), 4679-4688. <https://doi.org/10.5194/bg-9-4679-2012>

- Gibbs, S. J., Bown, P. R., Sessa, J. A., Bralower, T. J., & Wilson, P. A. (2006). Nannoplankton Extinction and Origination Across the Paleocene-Eocene Thermal Maximum. *Science*, 314(5806), 1770-1773. <https://doi.org/doi:10.1126/science.1133902>
- Gutián, J., & Stoll, H. M. (2021). Evolution of Sea Surface Temperature in the Southern Mid-latitudes From Late Oligocene Through Early Miocene. *Paleoceanography and Paleoclimatology*, 36(9), e2020PA004199. <https://doi.org/https://doi.org/10.1029/2020PA004199>
- Hines, B. R., Hollis, C. J., Atkins, C. B., Baker, J. A., Morgans, H. E. G., & Strong, P. C. (2017). Reduction of oceanic temperature gradients in the early Eocene Southwest Pacific Ocean. *Palaeogeography, Palaeoclimatology, Palaeoecology*, 475, 41-54. <https://doi.org/https://doi.org/10.1016/j.palaeo.2017.02.037>
- Holland, M. M., & Bitz, C. M. (2003). Polar amplification of climate change in coupled models. *Climate Dynamics*, 21(3), 221-232. <https://doi.org/10.1007/s00382-003-0332-6>
- Hönisch, B., Ridgwell, A., Schmidt, D. N., Thomas, E., Gibbs, S. J., Sluijs, A., Zeebe, R., Kump, L., Martindale, R. C., Greene, S. E., Kiessling, W., Ries, J., Zachos, J. C., Royer, D. L., Barker, S., Marchitto, T. M., Moyer, R., Pelejero, C., Ziveri, P., . . . Williams, B. (2012). The Geological Record of Ocean Acidification. *Science*, 335(6072), 1058-1063. <https://doi.org/doi:10.1126/science.1208277>
- Hornibrook, N. d. B. (1992). New Zealand Cenozoic marine paleoclimates: a review based on the distribution of some shallow water and terrestrial biota. *Pacific Neogene: environment, evolution, and events*. University of Tokyo Press, Tokyo, 83-106.
- Huber, M., Brinkhuis, H., Stickley, C. E., Döös, K., Sluijs, A., Warnaar, J., Schellenberg, S. A., & Williams, G. L. (2004). Eocene circulation of the Southern Ocean: Was Antarctica kept warm by subtropical waters? *Paleoceanography*, 19(4). <https://doi.org/https://doi.org/10.1029/2004PA001014>
- Inglis, G. N., Bragg, F., Burls, N. J., Cramwinckel, M. J., Evans, D., Foster, G. L., Huber, M., Lunt, D. J., Siler, N., Steinig, S., Tierney, J. E., Wilkinson, R., Anagnostou, E., de Boer, A. M., Dunkley Jones, T., Edgar, K. M., Hollis, C. J., Hutchinson, D. K., & Pancost, R. D. (2020). Global mean surface temperature and climate sensitivity of the early Eocene Climatic Optimum (EECO), Paleocene–Eocene Thermal Maximum (PETM), and latest Paleocene. *Clim. Past*, 16(5), 1953-1968. <https://doi.org/10.5194/cp-16-1953-2020>
- Ito, A., Reyer, C. P. O., Gädeke, A., Ciais, P., Chang, J., Chen, M., François, L., Forrest, M., Hickler, T., Ostberg, S., Shi, H., Thiery, W., & Tian, H. (2020). Pronounced and unavoidable impacts of low-end global warming on northern high-latitude land ecosystems. *Environmental Research Letters*, 15(4), 044006. <https://doi.org/10.1088/1748-9326/ab702b>
- Jenkins, D. G. (1993). The Evolution of the Cenozoic Southern High- and Mid-Latitude Planktonic Foraminiferal Faunas. In *The Antarctic Paleoenvironment: A Perspective on Global Change: Part Two* (pp. 175-194). <https://doi.org/https://doi.org/10.1002/9781118668061.ch9>
- Jiang, S., & Wise, S. W. (2009). Distinguishing the influence of diagenesis on the paleoecological reconstruction of nannoplankton across the Paleocene/Eocene Thermal Maximum: An example from the Kerguelen Plateau, southern Indian Ocean. *Marine Micropaleontology*, 72(1), 49-59. <https://doi.org/https://doi.org/10.1016/j.marmicro.2009.03.003>
- Keeling, C. D., Piper, S. C., Bacastow, R. B., Wahlen, M., Whorf, T. P., Heimann, M., & Meijer, H. A. (2005). Atmospheric CO₂ and ¹³CO₂ Exchange with the Terrestrial Biosphere and Oceans from 1978 to 2000: Observations and Carbon Cycle Implications. In I. T. Baldwin, M. M. Caldwell, G. Heldmaier, R. B. Jackson, O. L. Lange, H. A. Mooney, E. D. Schulze, U. Sommer, J. R. Ehleringer, M. Denise Dearing, &

- T. E. Cerling (Eds.), *A History of Atmospheric CO₂ and Its Effects on Plants, Animals, and Ecosystems* (pp. 83-113). Springer New York. https://doi.org/10.1007/0-387-27048-5_5
- Kennett, J., Houtz, R., & Kennet, J. (1975). Introduction and explanatory remarks. In *Initial Reports of the Deep Sea Drilling Project*, 29 (pp. 3-16). US Govt. Printing Office Washington, DC.
- Kennett, J. P., & Stott, L. D. (1991). Abrupt deep-sea warming, palaeoceanographic changes and benthic extinctions at the end of the Palaeocene. *Nature*, 353(6341), 225-229. <https://doi.org/10.1038/353225a0>
- Kirtland Turner, S., Sexton, P. F., Charles, C. D., & Norris, R. D. (2014). Persistence of carbon release events through the peak of early Eocene global warmth. *Nature Geoscience*, 7(10), 748-751. <https://doi.org/10.1038/ngeo2240>
- Lauretano, V., Littler, K., Polling, M., Zachos, J. C., & Lourens, L. J. (2015). Frequency, magnitude and character of hyperthermal events at the onset of the Early Eocene Climatic Optimum. *Clim. Past*, 11(10), 1313-1324. <https://doi.org/10.5194/cp-11-1313-2015>
- Lawver, L. A., Gahagan, L. M., & Coffin, M. F. (1992). The Development of Paleoseaways Around Antarctica. In *The Antarctic Paleoenvironment: A Perspective on Global Change: Part One* (pp. 7-30). <https://doi.org/https://doi.org/10.1029/AR056p0007>
- Lei, Y., Jiang, S., Wise, S. W., Cui, Y., & Wang, Y. (2016). Contrasting response of the calcareous nannoplankton communities after the Eocene hyperthermal events in the tropical Atlantic Ocean. *Marine Micropaleontology*, 129, 24-31. <https://doi.org/https://doi.org/10.1016/j.marmicro.2016.11.001>
- Marsaglia, K., Milliken, K., Leckie, R., M., Tentori, D., Doran, L., 2015. IODP Smear Slide Digital Reference for Sediment Analysis of Marine Mud. Part 2: Methodology and Atlas of Biogenic Components. IODP Technical Note 2. doi:10.14379/iodp.tn.2.2015
- Martini, E. (1971). Standard Tertiary and Quaternary calcareous nannoplankton zonation. *Proceedings Second Planktonic Conference, Rome*,
- Müller, P. J., Kirst, G., Ruhland, G., von Storch, I., & Rosell-Melé, A. (1998). Calibration of the alkenone paleotemperature index U_{37K'} based on core-tops from the eastern South Atlantic and the global ocean (60°N-60°S). *Geochimica et Cosmochimica Acta*, 62(10), 1757-1772. [https://doi.org/https://doi.org/10.1016/S0016-7037\(98\)00097-0](https://doi.org/https://doi.org/10.1016/S0016-7037(98)00097-0)
- Müller, P. J., & Schneider, R. (1993). An automated leaching method for the determination of opal in sediments and particulate matter. *Deep Sea Research Part I: Oceanographic Research Papers*, 40(3), 425-444. [https://doi.org/https://doi.org/10.1016/0967-0637\(93\)90140-X](https://doi.org/https://doi.org/10.1016/0967-0637(93)90140-X)
- Mutterlose, J., Linnert, C., & Norris, R. (2007). Calcareous nannofossils from the Paleocene–Eocene Thermal Maximum of the equatorial Atlantic (ODP Site 1260B): Evidence for tropical warming. *Marine Micropaleontology*, 65(1), 13-31. <https://doi.org/https://doi.org/10.1016/j.marmicro.2007.05.004>
- Nelson, C. S., & Cooke, P. J. (2001). History of oceanic front development in the New Zealand sector of the Southern Ocean during the Cenozoic—a synthesis. *New Zealand Journal of Geology and Geophysics*, 44(4), 535-553. <https://doi.org/10.1080/00288306.2001.9514954>
- Newsam, C., Bown, P. R., Wade, B. S., & Jones, H. L. (2017). Muted calcareous nannoplankton response at the Middle/Late Eocene Turnover event in the western North Atlantic Ocean. *Newsletters on Stratigraphy*, 50(3), 297-309. <https://doi.org/10.1127/nos/2016/0306>

- Pagani, M. (2002). The alkenone-CO₂ proxy and ancient atmospheric carbon dioxide. *Philos Trans A Math Phys Eng Sci*, 360(1793), 609-632. <https://doi.org/10.1098/rsta.2001.0959>
- Penman, D. E., Keller, A., D'haenens, S., Kirtland Turner, S., & Hull, P. M. (2019). Atlantic Deep-Sea Cherts Associated With Eocene Hyperthermal Events. *Paleoceanography and Paleoclimatology*, 34(2), 287-299. <https://doi.org/https://doi.org/10.1029/2018PA003503>
- Prahl, F. G., & Wakeham, S. G. (1987). Calibration of unsaturation patterns in long-chain ketone compositions for palaeotemperature assessment. *Nature*, 330(6146), 367-369. <https://doi.org/10.1038/330367a0>
- Raffi, I., Backman, J., & Pälike, H. (2005). Changes in calcareous nannofossil assemblages across the Paleocene/Eocene transition from the paleo-equatorial Pacific Ocean. *Palaeogeography, Palaeoclimatology, Palaeoecology*, 226(1), 93-126. <https://doi.org/https://doi.org/10.1016/j.palaeo.2005.05.006>
- Raffi, I., & De Bernardi, B. (2008). Response of calcareous nannofossils to the Paleocene–Eocene Thermal Maximum: Observations on composition, preservation and calcification in sediments from ODP Site 1263 (Walvis Ridge — SW Atlantic). *Marine Micropaleontology*, 69(2), 119-138. <https://doi.org/https://doi.org/10.1016/j.marmicro.2008.07.002>
- Röhl, U., Thomas, D. J., Childress, L. B., Anagnostou, E., Ausín, B., Borba Dias, B., et al. (2022). Site U1553. In U. Röhl, D. J. Thomas, L. B. Childress, & Expedition 378 Scientists (Eds.), *South Pacific Paleogene climate. Proceedings of the International Ocean Discovery Program (Vol. 378)*. International Ocean Discovery Program. <https://doi.org/10.14379/iodp.proc.378.103.2022>
- Rubino, M., Etheridge, D. M., Thornton, D. P., Howden, R., Allison, C. E., Francey, R. J., Langenfelds, R. L., Steele, L. P., Trudinger, C. M., Spencer, D. A., Curran, M. A. J., van Ommen, T. D., & Smith, A. M. (2019). Revised records of atmospheric trace gases CO₂, CH₄, N₂O, and δ¹³C-CO₂ over the last 2000 years from Law Dome, Antarctica. *Earth Syst. Sci. Data*, 11(2), 473-492. <https://doi.org/10.5194/essd-11-473-2019>
- Schneider, L. J., Bralower, T. J., Kump, L. R., & Patzkowsky, M. E. (2013). Calcareous nannoplankton ecology and community change across the Paleocene-Eocene Thermal Maximum. *Paleobiology*, 39(4), 628-647. <https://doi.org/10.1666/12050>
- Self-Trail, J. M., Powars, D. S., Watkins, D. K., & Wandless, G. A. (2012). Calcareous nannofossil assemblage changes across the Paleocene–Eocene Thermal Maximum: Evidence from a shelf setting. *Marine Micropaleontology*, 92-93, 61-80. <https://doi.org/https://doi.org/10.1016/j.marmicro.2012.05.003>
- Sengupta, S., Gorain, P. C., & Pal, R. (2017). Aspects and prospects of algal carbon capture and sequestration in ecosystems: a review. *Chemistry and Ecology*, 33(8), 695-707. <https://doi.org/10.1080/02757540.2017.1359262>
- Serreze, M. C., Barrett, A. P., Stroeve, J. C., Kindig, D. N., & Holland, M. M. (2009). The emergence of surface-based Arctic amplification. *The Cryosphere*, 3(1), 11-19. <https://doi.org/10.5194/tc-3-11-2009>
- Taylor, P. C., Cai, M., Hu, A., Meehl, J., Washington, W., & Zhang, G. J. (2013). A Decomposition of Feedback Contributions to Polar Warming Amplification. *Journal of Climate*, 26(18), 7023-7043. <https://doi.org/https://doi.org/10.1175/JCLI-D-12-00696.1>

- Tierney, J. E., Poulsen, C. J., Montañez, I. P., Bhattacharya, T., Feng, R., Ford, H. L., Hönisch, B., Inglis, G. N., Petersen, S. V., Sagoo, N., Tabor, C. R., Thirumalai, K., Zhu, J., Burls, N. J., Foster, G. L., Goddérís, Y., Huber, B. T., Ivany, L. C., Turner, S. K., . . . Zhang, Y. G. (2020). Past climates inform our future. *Science*, 370(6517), eaay3701. <https://doi.org/doi:10.1126/science.aay3701>
- Toffanin, F., Agnini, C., Rio, D., Acton, G., & Westerhold, T. (2013). Middle Eocene to early Oligocene calcareous nannofossil biostratigraphy at IODP Site U1333 (equatorial Pacific). *Micropaleontology*, 59(1), 69-82. <http://www.jstor.org/stable/24413317>
- Wang, Y., Cui, Y., Su, H., Jiang, J., Wang, Y., Yang, Z., Hu, X., & Jiang, S. (2022). Response of calcareous nanoplankton to the Paleocene–Eocene Thermal Maximum in the Paratethys Seaway (Tarim Basin, West China). *Global and Planetary Change*, 217, 103918. <https://doi.org/https://doi.org/10.1016/j.gloplacha.2022.103918>
- Wessel, P., Luis, J. F., Uieda, L., Scharroo, R., Wobbe, F., Smith, W. H. F., & Tian, D. (2019). The Generic Mapping Tools version 6. *Geochemistry, Geophysics, Geosystems*, 20, 5556–5564. <https://doi.org/10.1029/2019GC008515>
- Westerhold, T., Marwan, N., Drury, A. J., Liebrand, D., Agnini, C., Anagnostou, E., Barnet, J. S. K., Bohaty, S. M., De Vleeschouwer, D., Florindo, F., Frederichs, T., Hodell, D. A., Holbourn, A. E., Kroon, D., Lauretano, V., Littler, K., Lourens, L. J., Lyle, M., Pälike, H., . . . Zachos, J. C. (2020). An astronomically dated record of Earth’s climate and its predictability over the last 66 million years. *Science*, 369(6509), 1383-1387. <https://doi.org/doi:10.1126/science.aba6853>
- Westerhold, T., Röhl, U., Donner, B., & Zachos, J. C. (2018). Global Extent of Early Eocene Hyperthermal Events: A New Pacific Benthic Foraminiferal Isotope Record From Shatsky Rise (ODP Site 1209). *Paleoceanography and Paleoclimatology*, 33(6), 626-642. <https://doi.org/https://doi.org/10.1029/2017PA003306>
- Westerhold, T., Röhl, U., Frederichs, T., Agnini, C., Raffi, I., Zachos, J. C., & Wilkens, R. H. (2017). Astronomical calibration of the Ypresian timescale: implications for seafloor spreading rates and the chaotic behavior of the solar system? *Clim. Past*, 13(9), 1129-1152. <https://doi.org/10.5194/cp-13-1129-2017>
- Westerhold, T., Röhl, U., Raffi, I., Fornaciari, E., Monechi, S., Reale, V., Bowles, J., & Evans, H. F. (2008). Astronomical calibration of the Paleocene time. *Palaeogeography, Palaeoclimatology, Palaeoecology*, 257(4), 377-403. <https://doi.org/https://doi.org/10.1016/j.palaeo.2007.09.016>
- Zachos, J., Pagani, M., Sloan, L., Thomas, E., & Billups, K. (2001). Trends, Rhythms, and Aberrations in Global Climate 65 Ma to Present. *Science*, 292(5517), 686-693. <https://doi.org/doi:10.1126/science.1059412>
- Zachos, J. C., Dickens, G. R., & Zeebe, R. E. (2008). An early Cenozoic perspective on greenhouse warming and carbon-cycle dynamics. *Nature*, 451(7176), 279-283. <https://doi.org/10.1038/nature06588>
- Zhang, Y. G., Pagani, M., Liu, Z., Bohaty, S. M., & DeConto, R. (2013). A 40-million-year history of atmospheric CO₂. *Philosophical Transactions of the Royal Society A: Mathematical, Physical and Engineering Sciences*, 371(2001), 20130096. <https://doi.org/doi:10.1098/rsta.2013.0096>

11. Appendix

For Part I, all data is published here: <https://doi.pangaea.de/10.1594/PANGAEA.963554>

Important note for PART II and Part III:

All appendices (Data and Python scripts for statistical analyses) are provided on the USB-stick enclosed to the thesis in the folder “Appendices”.

- Appendix_01: Counts of calcareous nannofossil assemblage (species level)
- Appendix_02: Relative abundance (%) of calcareous nannofossil assemblage (genus level)
- Appendix_03: Stable isotopes used for interpolation to samples of calcareous nannofossil assemblage
- Appendix_04: XRF-derived data
- Appendix_05: Opal concentration (wt%)

Statistical analyses for calcareous nannofossil assemblage

Data is accessible on the USB-stick, file:

Appendix_01.xlsx: Counts of calcareous nannofossils on species level

Appendix_02.xlsx: Relative abundance (%) of calcareous nannofossils on genus level

Appendix_03.xlsx: Stable Isotopes of Niederbockstruck et al. (2024) for linear interpolation

```
In [1]: %matplotlib inline
import numpy as np
import matplotlib.pyplot as plt
import pandas as pd
import seaborn as sns
from sklearn.preprocessing import StandardScaler
from sklearn.preprocessing import MinMaxScaler
from scipy.cluster.hierarchy import dendrogram, linkage, fcluster, leaves_list, set_link_color_palette
from scipy import interpolate
from scipy.interpolate import interp1d
from sklearn.decomposition import PCA
from sklearn import preprocessing
import seaborn as sns
```

```
In [2]: df_nannos = pd.read_excel("YOUR_PATH/Appendix_02.xlsx")
#replace with your path here
```

```
In [3]: df_nannos
```

```
Out[3]:
```

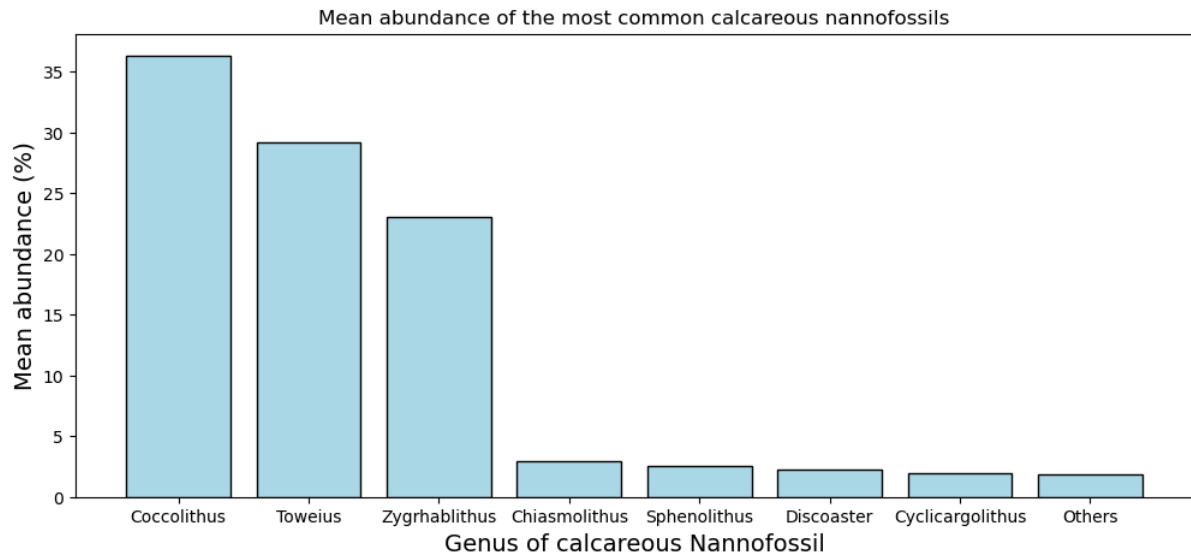
	Sample ID	U1553C-CSF	U1553C-CCSF	U1553C-CCSFadj	Age (Ma)	Cyclicargolithus	Reticulofenestra	Hornibrookina	Prinsius	Toweius	...	Pontosphaera	Neochiastozygus
	U1553C-28R-1,0-1 cm	428.605	459.435	459.692	52.710968	1.741294	0	0.0	0	25.124378	...	0.000000	0.000000
	U1553C-28R-1,1-3 cm	428.620	459.450	459.698	52.711830	1.724138	0	0.0	0	28.571429	...	0.000000	0.000000
	U1553C-28R-1,26-28 cm	428.870	459.700	459.807	52.727489	1.243781	0	0.0	0	26.616915	...	0.000000	0.000000
	U1553C-28R-1,30-31 cm	428.905	459.735	459.823	52.729787	2.912621	0	0.0	0	23.300971	...	0.000000	1.456311
	U1553C-28R-1,51-53 cm	429.120	459.950	459.916	52.743147	1.492537	0	0.0	0	28.606965	...	0.000000	1.243781
...
	U1553C-28R-CC,0-2 cm	437.370	468.200	468.200	53.700760	3.233831	0	0.0	0	34.577114	...	0.000000	0.497512
	U1553C-29R-1,14-16 cm	438.450	468.950	468.507	53.730837	0.977995	0	0.0	0	43.031785	...	0.000000	0.733496
	U1553C-29R-1,30-31 cm	438.605	469.105	468.685	53.748276	1.234568	0	0.0	0	37.283951	...	0.000000	1.481481
	U1553C-29R-1,60-61 cm	438.905	469.405	469.028	53.781880	2.977667	0	0.0	0	43.176179	...	0.248139	0.744417
	U1553C-29R-1,87-89 cm	439.180	469.680	469.343	53.812741	0.738916	0	0.0	0	50.000000	...	0.000000	0.738916

71 rows × 32 columns

```
In [4]: %matplotlib inline
barplot_columns = df_nannos[["Coccolithus", "Toweius", "Zygrhablithus", "Chiasmolithus", "Sphenolithus", "Discoaster",
                             "Cyclicargolithus", "Others"]]
mean_values = barplot_columns.mean()

plt.figure(figsize=(12, 5))
plt.bar(mean_values.index, mean_values.values, color="lightblue", edgecolor="black")
plt.xlabel('Genus of calcareous Nannofossil', fontsize=14)
plt.ylabel('Mean abundance (%)', fontsize=14)
plt.title('Mean abundance of the most common calcareous nannofossils')
plt.show()

total_mean = mean_values.sum()
print("Sum of all", total_mean, " - " "Sum of the most common genera:", total_mean - df_nannos["Others"].mean(), "%")
mean_values
```



```

Sum of all 100.0 - Sum of the most common genera: 98.18780714387697 %
Out[4]: Coccolithus      36.301815
        Toweius       29.227841
        Zygrhablithus 23.021474
        Chiasmolithus  2.914635
        Sphenolithus   2.582192
        Discoaster     2.229172
        Cyclicargolithus 1.910677
        Others         1.812193
dtype: float64

```

Recalculate the relative abundance of the seven genera (without others)

```

In [5]: df = df_nannos[["Coccolithus", "Toweius", "Zygrhablithus", "Chiasmolithus", "Discoaster", "Sphenolithus",
                       "Cyclicargolithus"]]
        row_sums = df.sum(axis=1)

        # Divide each value by the corresponding row sum
        df_rel = df.div(row_sums, axis=0)

```

```
In [6]: df_rel
```

```

Out[6]:
   Coccolithus  Toweius  Zygrhablithus  Chiasmolithus  Discoaster  Sphenolithus  Cyclicargolithus
0      0.323308  0.253133   0.348371      0.015038      0.025063      0.017544      0.017544
1      0.297500  0.290000   0.327500      0.010000      0.015000      0.042500      0.017500
2      0.357868  0.271574   0.299492      0.038071      0.012690      0.007614      0.012690
3      0.348148  0.237037   0.306173      0.024691      0.022222      0.032099      0.029630
4      0.356962  0.291139   0.281013      0.010127      0.022785      0.022785      0.015190
...      ...      ...      ...      ...      ...      ...      ...
66     0.336735  0.354592   0.155612      0.048469      0.028061      0.043367      0.033163
67     0.246193  0.446701   0.241117      0.035533      0.005076      0.015228      0.010152
68     0.420655  0.380353   0.083123      0.050378      0.030227      0.022670      0.012594
69     0.379397  0.437186   0.082915      0.042714      0.007538      0.020101      0.030151
70     0.246753  0.527273   0.192208      0.015584      0.002597      0.007792      0.007792

```

71 rows × 7 columns

Hierarchical clustering

Scaling the data

```

In [7]: scaler1 = StandardScaler()
        standardized_data = scaler1.fit_transform(df_rel)
        df_scaled = standardized_data
        df_scaled = pd.DataFrame(standardized_data, columns=df_rel.columns)

```

```
In [8]: df_scaled
```

```
Out[8]:
```

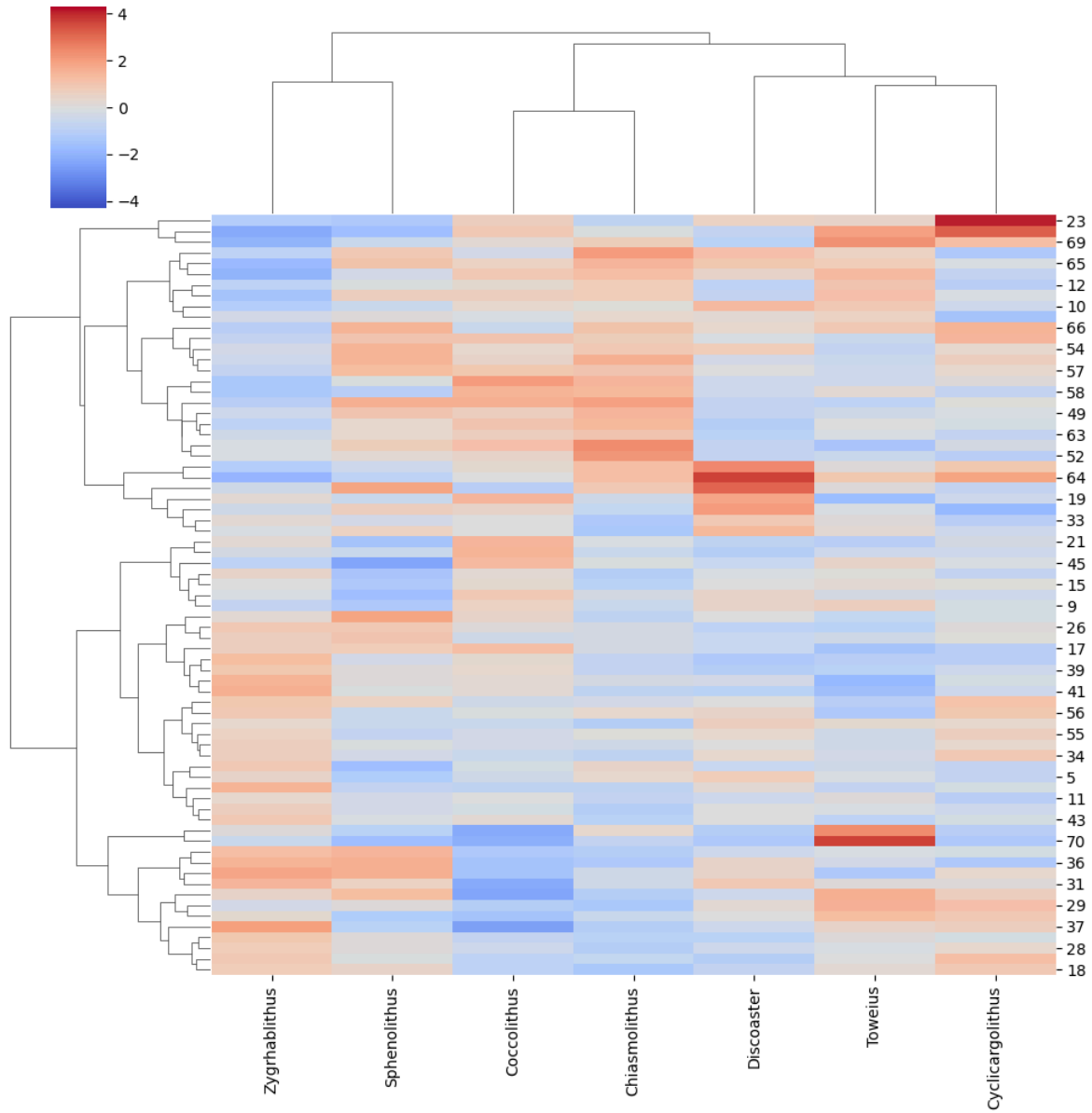
	Coccolithus	Toweius	Zygrhablithus	Chiasmolithus	Discoaster	Sphenolithus	Cyclicargolithus
0	-0.819729	-0.721966	1.511752	-0.820023	0.144784	-0.768138	-0.209610
1	-1.276582	-0.129331	1.235466	-1.101725	-0.479835	1.431948	-0.214364
2	-0.207960	-0.425533	0.864705	0.468011	-0.623201	-1.643517	-0.735692
3	-0.380019	-0.980703	0.953140	-0.280184	-0.031531	0.514995	1.100393
4	-0.223997	-0.111018	0.620073	-1.094647	0.003391	-0.306106	-0.464764
...
66	-0.582058	0.908973	-1.039960	1.049486	0.330913	1.508411	1.483411
67	-2.184810	2.389607	0.091936	0.326082	-1.095838	-0.972262	-1.010799
68	0.903481	1.323075	-1.999557	1.156206	0.465331	-0.316225	-0.746086
69	0.173142	2.236662	-2.002322	0.727620	-0.943043	-0.542749	1.156878
70	-2.174891	3.684794	-0.555513	-0.789444	-1.249701	-1.627825	-1.266613

71 rows x 7 columns

Two-way cluster analysis

```
In [9]: plt.figure(figsize=(4,4))
sns.clustermap(df_scaled[["Coccolithus", "Toweius", "Zygrhablithus", "Chiasmolithus", "Discoaster", "Sphenolithus",
"Cyclicargolithus"]], method='ward', metric='euclidean', cmap='coolwarm', row_cluster=True,
linecolor="grey",
vmin=-4.3, vmax=4.3, dendrogram_ratio=0.2, cbar_pos=(0.06, 0.82, 0.05, 0.18))
plt.show()
```

<Figure size 400x400 with 0 Axes>



Principle Component Analyses

```
In [10]: # Visualize the distribution with histograms for each genus
plt.figure(figsize=(20, 10))
for i, column in enumerate(df_rel.columns, 1):
    plt.subplot(2, 4, i)
    df_rel[column].hist(bins=12, alpha=0.7, color='silver', edgecolor='black')
```

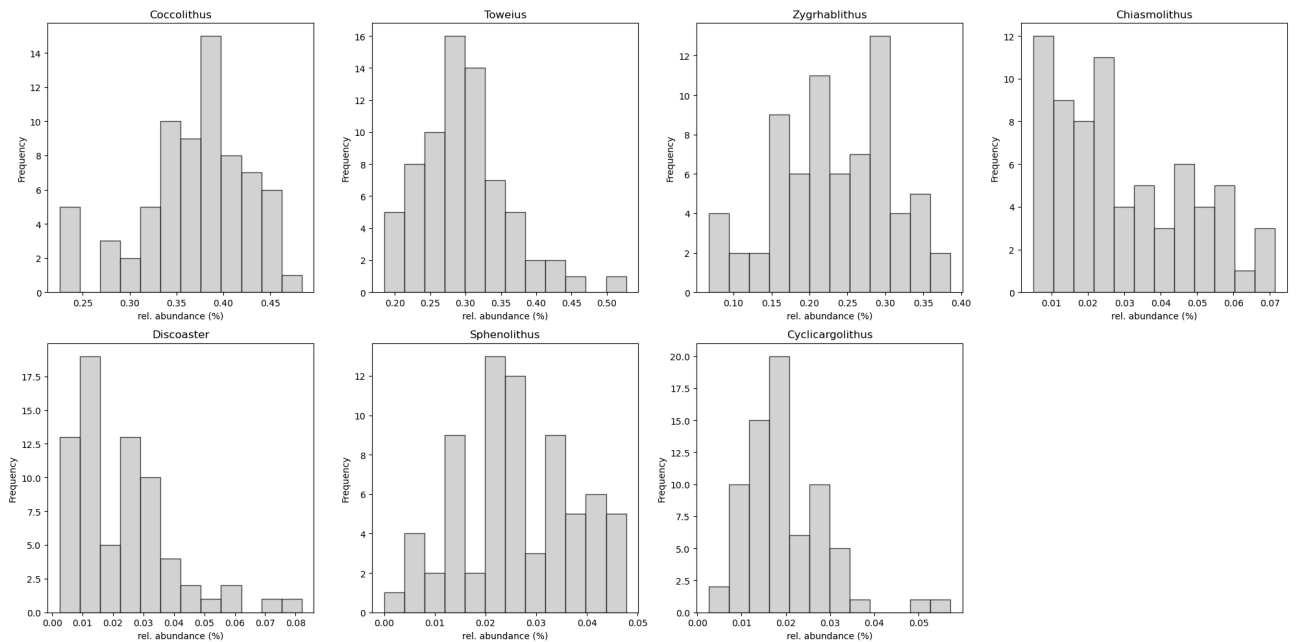


```

plt.xlabel('rel. abundance (%)')
plt.ylabel('Frequency')
plt.grid(False)
plt.title(column)
plt.tight_layout()
plt.show()

skewness_rel = df_rel.skew().to_frame(name='Skewness')
print(skewness_rel)

```



Genus	Skewness
Coccolithus	-0.584493
Toweius	0.953834
Zygrhablithus	-0.200205
Chiasmolithus	0.577638
Discoaster	1.430887
Sphenolithus	0.008475
Cyclicargolithus	1.412332

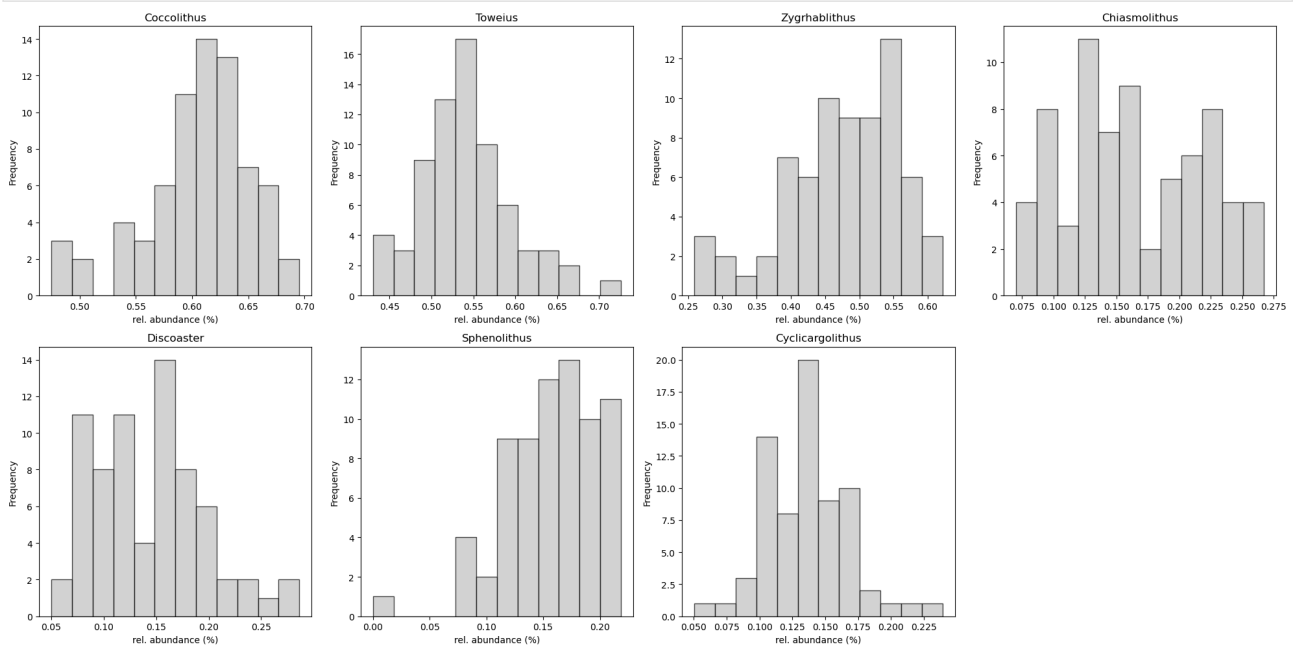
```

In [11]: # Visualize the square-root distribution with histograms for each genus
df_sqrt = np.sqrt(df_rel)

plt.figure(figsize=(20, 10))
for i, column in enumerate(df_sqrt.columns, 1):
    plt.subplot(2, 4, i)
    df_sqrt[column].hist(bins=12, alpha=0.7, color='silver', edgecolor='black')
    plt.xlabel('rel. abundance (%)')
    plt.ylabel('Frequency')
    plt.grid(False)
    plt.title(column)
    plt.tight_layout()
plt.show()

skewness_sqrt = df_sqrt.skew().to_frame(name='Skewness')
print(skewness_sqrt)

```



```

                Skewness
Coccolithus    -0.806572
Toweius        0.566992
Zygrhablithus -0.599919
Chiasmolithus 0.145898
Discoaster     0.514225
Sphenolithus  -0.958459
Cyclicargolithus 0.389715

```

```
In [12]: df_sqrt
```

```

Out[12]:
   Coccolithus  Toweius  Zygrhablithus  Chiasmolithus  Discoaster  Sphenolithus  Cyclicargolithus
0    0.568602  0.503123    0.590230    0.122628    0.158312    0.132453    0.132453
1    0.545436  0.538516    0.572276    0.100000    0.122474    0.206155    0.132288
2    0.598221  0.521127    0.547259    0.195118    0.112651    0.087259    0.112651
3    0.590041  0.486864    0.553329    0.157135    0.149071    0.179161    0.172133
4    0.597463  0.539573    0.530106    0.100631    0.150946    0.150946    0.123247
...
66   0.580288  0.595476    0.394477    0.220158    0.167515    0.208248    0.182108
67   0.496178  0.668357    0.491036    0.188502    0.071247    0.123404    0.100759
68   0.648579  0.616727    0.288311    0.224450    0.173858    0.150566    0.112225
69   0.615952  0.661200    0.287949    0.206673    0.086820    0.141776    0.173640
70   0.496743  0.726135    0.438415    0.124838    0.050965    0.088273    0.088273

```

71 rows × 7 columns

```
In [13]: pca = PCA()
pca.fit(df_sqrt)
```

```
Out[13]:
PCA
```

```
In [14]: explained_variance = pca.explained_variance_ratio_
eigenvalues = pca.explained_variance_
print("Eigenvalues", eigenvalues)
print("Explained variance", explained_variance)
```

```

Eigenvalues [9.59729607e-03 4.31412249e-03 2.71599211e-03 1.84640768e-03
1.07941600e-03 9.39650557e-04 3.51924715e-05]
Explained variance [0.46752045 0.21015716 0.13230621 0.08994548 0.05258242 0.04577392
0.00171436]

```

```
In [15]: n_components = 7
df_pca = pca.transform(df_sqrt)[: , :n_components]
```

```
In [16]: plt.figure(figsize=(10, 8))
scatter= plt.scatter(df_pca[:, 0], df_pca[:,1],label='Data Points',c=df_nannos.index, cmap='cool')

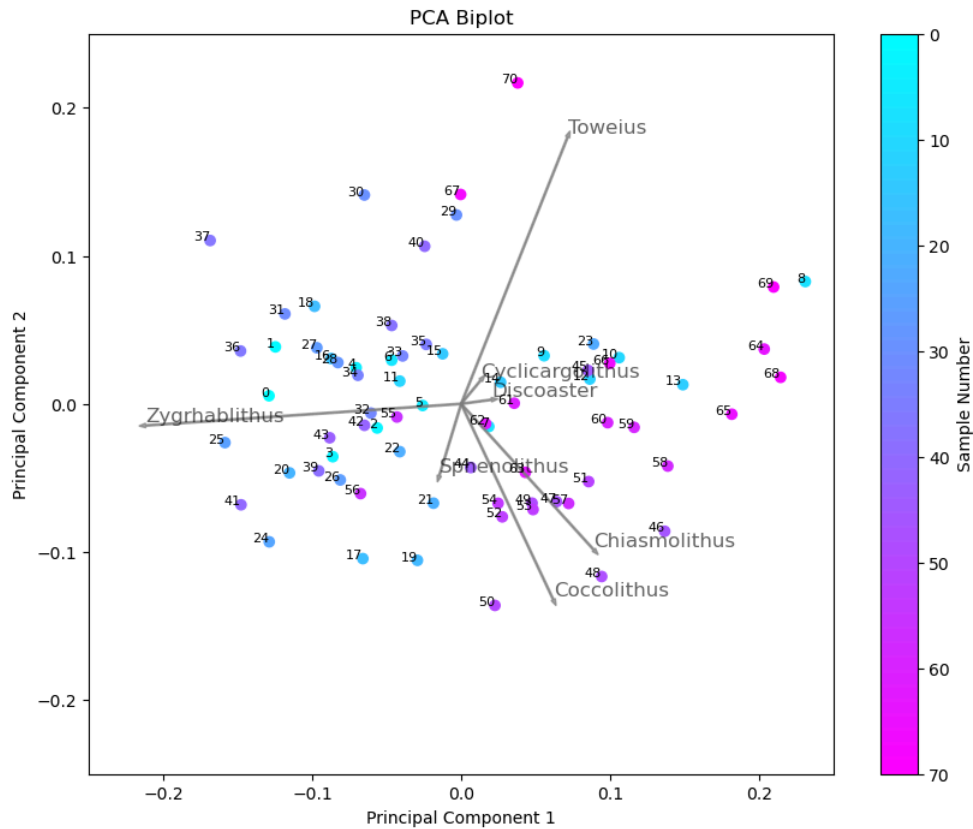
loadings = pca.components_.T
scale_factor = 0.25
loadings1 = loadings * scale_factor

# Biplot arrows using the loadings
for i, (loading1, loading2) in enumerate(loadings1[:, [0, 1]]):
    plt.arrow(0, 0, loading1, loading2, color='grey', alpha=0.7)
    plt.text(loading1, loading2, df_sqrt.columns[i], fontsize=12, ha='left', va='bottom', alpha=0.6)

plt.xlabel('Principal Component 1')
plt.ylabel('Principal Component 2')
# Annotate data points with row numbers
for i, txt in enumerate(range(df_pca.shape[0])):
    plt.annotate(txt, (df_pca[i, 0], df_pca[i, 1]), fontsize=8, ha='right')

# Legend
plt.title('PCA Biplot')
plt.xlim(-0.25,+0.25)
plt.ylim(-0.25,+0.25)

# Colorbar
cbar = plt.colorbar(scatter, label='Sample Number')
cbar.ax.invert_yaxis()
plt.show()
```



```
In [17]: df_pca_scores = pd.DataFrame(df_pca)
df_pca_scores
```

```
Out[17]:
```

	0	1	2	3	4	5	6
0	-0.128988	0.005456	0.019297	0.021999	-0.021403	-0.022301	0.002665
1	-0.124701	0.038479	0.003561	-0.036416	0.028503	0.023312	0.002311
2	-0.056400	-0.016311	-0.044793	0.017416	-0.070517	-0.044851	-0.002823
3	-0.086202	-0.035688	0.021049	-0.010708	0.027114	-0.034446	-0.001825
4	-0.070506	0.024398	0.010014	0.031053	0.002851	0.024197	-0.003954
...
66	0.099745	0.027380	0.036698	-0.068652	0.036725	-0.023985	-0.006838
67	-0.000392	0.141432	-0.074077	-0.076609	-0.065006	-0.018385	-0.000094
68	0.214404	0.017904	0.014384	-0.002203	-0.018171	0.033205	0.008055
69	0.209696	0.078902	-0.065226	-0.019216	0.036077	-0.005126	0.006998
70	0.037931	0.216762	-0.103985	-0.029253	-0.055809	0.019891	0.011407

71 rows x 7 columns

```
In [18]: df_loadings_scores = pd.DataFrame(loadings)
new_index = ['Coccolithus', 'Toweius', 'Zygrhablithus', 'Chiasmolithus', 'Discoaster', 'Sphenolithus', 'Cyclicargolithus']
# Assign the new index
df_loadings_scores.index = new_index

new_columns = ['PC1', 'PC2', 'PC3', 'PC4', 'PC5', 'PC6', 'PC7']
# Assign the new column headers
df_loadings_scores.columns = new_columns
df_loadings_scores
```

```
Out[18]:
```

	PC1	PC2	PC3	PC4	PC5	PC6	PC7
Coccolithus	0.247159	-0.528874	-0.158571	0.458911	0.103325	0.267195	-0.584287
Toweius	0.285713	0.720716	-0.103043	-0.147188	-0.098989	0.107020	-0.587710
Zygrhablithus	-0.847179	-0.058507	-0.022145	-0.067755	-0.190778	-0.160852	-0.459907
Chiasmolithus	0.356038	-0.394429	-0.048196	-0.527216	-0.425927	-0.471216	-0.184186
Discoaster	0.081205	0.011121	0.951498	0.186414	-0.182801	-0.035426	-0.136058
Sphenolithus	-0.058799	-0.194084	0.228741	-0.665174	0.492585	0.448863	-0.141340
Cyclicargolithus	0.052484	0.063805	0.061260	0.089343	0.696892	-0.683010	-0.171110

```
In [19]: # Figure of Loadings
fig, (ax1, ax2) = plt.subplots(nrows=1, ncols=2, figsize=(10, 8))

# Define colors for PC1
pos_color1 = 'royalblue'
neg_color1 = 'cornflowerblue'
bar_width = 0.5

# Horizontal bar chart for PC1 on the first axis with y-axis in reverse order
```

```

for index, value in enumerate(df_loadings_scores['PC1'][::-1]):
    color = pos_color1 if value >= 0 else neg_color1
    ax1.barh(df_loadings_scores.index[::-1][index], value, color=color, height=bar_width)

ax1.axvline(0, color='black', linestyle='-')
ax1.set_xlabel('PC1 Loading', fontsize=12)
ax1.tick_params(axis='y', labelsize=12)

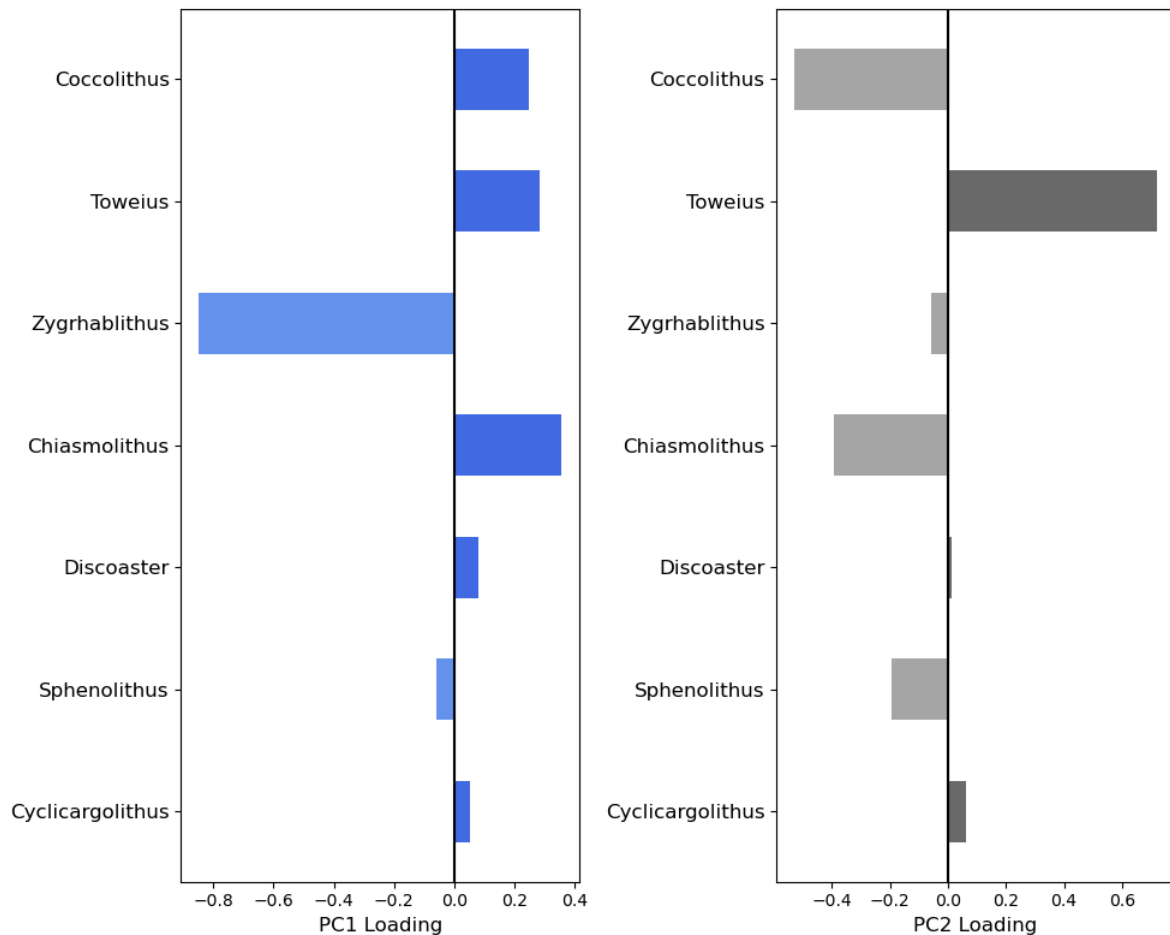
# Define colors for PC2
pos_color2 = 'dimgrey'
neg_color2 = 'darkgrey'

# Horizontal bar chart for PC2 on the second axis with y-axis in reverse order
for index, value in enumerate(df_loadings_scores['PC2'][::-1]):
    color = pos_color2 if value >= 0 else neg_color2
    ax2.barh(df_loadings_scores.index[::-1][index], value, color=color, height=bar_width)

ax2.axvline(0, color='black', linestyle='-')
ax2.set_xlabel('PC2 Loading', fontsize=12)
ax2.tick_params(axis='y', labelsize=12)

plt.tight_layout()

```



Interpolation of $\delta^{13}\text{C}$

Stable isotopes from Niederbockstruck et al. (2024) and can be found here: <https://doi.pangaea.de/10.1594/PANGAEA.963447>

```
In [26]: df_d13C = pd.read_excel("YOUR_PATH/Appendix_03.xlsx")
#replace with your path here
```

```
In [27]: df_d13C
```

```
Out[27]:
```

	ID	mid CSF	mid CCSF	mid_adjCCSF	Age (Ma)	U1553_d13C	U1553_d18O	Lab
0	378-U1553C-25R-1,20-21 cm	399.605	430.945000	430.945000	48.874634	1.762	-0.989	MARUM
1	378-U1553D-2R-1,20-21 cm	399.605	430.945000	431.162960	48.910056	1.800	-0.949	MARUM
2	378-U1553C-25R-1,50-51 cm	399.905	431.245000	431.245000	48.923389	1.773	-1.015	MARUM
3	378-U1553D-2R-1,50-51 cm	399.905	431.245000	431.502170	48.965183	1.809	-0.866	MARUM
4	378-U1553C-25R-1,80-81 cm	400.205	431.545000	431.545000	48.972143	1.729	-0.975	MARUM
...
478	378-U1553D-8R-2,139-140 cm	460.695	494.724999	494.724999	58.044068	2.780	-1.010	MARUM
479	378-U1553C-33R-3,74-75 cm	461.405	494.775003	494.774990	58.052226	2.640	-0.950	MARUM
480	378-U1553D-8R-9,6-7 cm	460.805	494.834999	494.834999	58.062018	2.780	-0.780	MARUM
481	378-U1553D-8R-9,25-26 cm	460.995	495.024999	495.024999	58.093023	3.120	-0.390	MARUM
482	378-U1553C-33R-3,104-105 cm	461.705	495.075003	495.075010	58.101183	2.900	-0.910	MARUM

483 rows x 8 columns

```
In [22]: ages = df_d13C['Age (Ma)'].values
d13C_values = df_d13C['U1553_d13C'].values

# Creating the interpolation function
interp_function = interp1d(ages, d13C_values, kind='linear', fill_value='extrapolate')

# Applying the interpolation function to the ages in df_nannos
interpolated_d13C_values = interp_function(df_nannos['Age (Ma)'].values)

# Creating the new dataframe with interpolated values
df_interpolated = pd.DataFrame({
    'Age (Ma)': df_nannos['Age (Ma)'],
    'Interpolated_d13C': interpolated_d13C_values})
```

```
In [23]: df_interpolated
```

```
Out[23]:
```

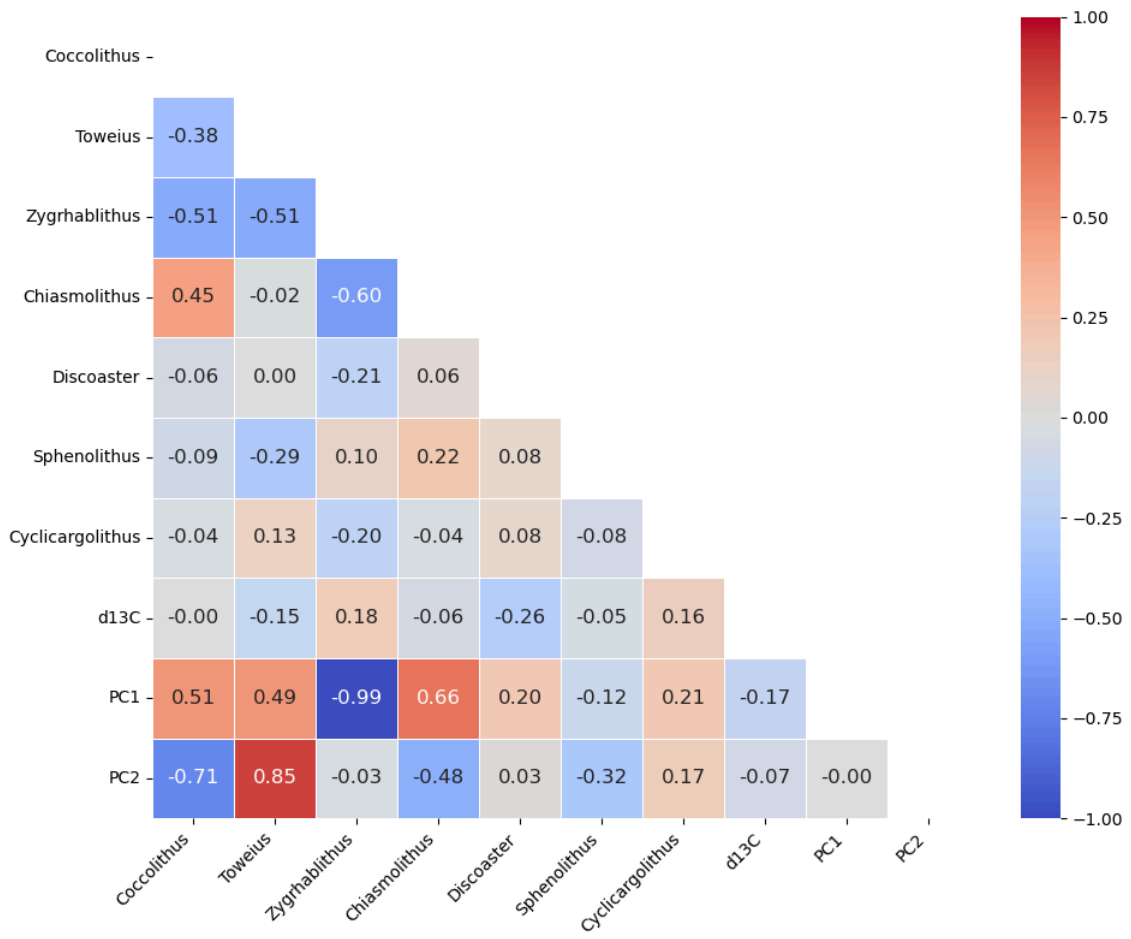
	Age (Ma)	Interpolated_d13C
0	52.710968	1.090277
1	52.711830	1.097497
2	52.727489	1.087865
3	52.729787	1.090124
4	52.743147	1.141976
...
66	53.700760	1.091340
67	53.730837	1.210468
68	53.748276	1.189960
69	53.781880	1.259969
70	53.812741	1.195768

71 rows x 2 columns

Pearson correlation

```
In [24]: df_heatmap=df_re1.reset_index(drop=True)
df_heatmap['d13C']=df_interpolated[['Interpolated_d13C']].reset_index(drop=True)
df_heatmap['PC1']=df_pca_scores.iloc[:, 0].reset_index(drop=True)
df_heatmap['PC2']=df_pca_scores.iloc[:, 1].reset_index(drop=True)
df_heatmap1=df_heatmap.corr(method='pearson')
```

```
In [25]: mask = np.triu(np.ones_like(df_heatmap1, dtype=bool))
# Plot the heatmap with the mask
plt.figure(figsize=(10, 8))
sns.heatmap(df_heatmap1, cmap="coolwarm", annot=True, annot_kws={"size": 12}, fmt=".2f", linewidths=.5,
            vmin=-1, vmax=1, mask=mask)
plt.xticks(rotation=45, ha='right')
plt.tight_layout()
plt.show()
```



Spectral- and wavelet analyses using pyleoclim (<https://pyleoclim-util.readthedocs.io/en/latest/>)

Data is accessible on the USB-stick, file: Appendix_04.xlsx

```
In [1]: import matplotlib.pyplot as plt
from matplotlib.ticker import LogLocator, NullFormatter
import pandas as pd
import pyleoclim as pyleo
import numpy as np
from matplotlib.ticker import StrMethodFormatter
pyleo.set_style('matplotlib')
```

```
In [24]: df_XRF = pd.read_excel("YOUR_PATH/Appendix_04.xlsx")
```

```
In [25]: df_XRF
```

```
Out[25]:
```

	U1553splice_XRF2_Site	U1553splice_XRF2_Hole	U1553splice_XRF2_Core	U1553splice_XRF2_Type	U1553splice_XRF2_Section	U1553splice_XRF2_Interval	U1
0	U1553	D	4	R	1	7	
1	U1553	D	4	R	1	8	
2	U1553	D	4	R	1	12	
3	U1553	D	4	R	1	14	
4	U1553	D	4	R	1	16	
...
1533	U1553	C	32	R	1	54	
1534	U1553	C	32	R	1	56	
1535	U1553	C	32	R	1	58	
1536	U1553	C	32	R	1	60	
1537	U1553	C	32	R	1	62	

1538 rows x 35 columns

```
In [6]: SiFe_ts = pyleo.Series(time=df_XRF['Age (Ma)']*1000, value=df_XRF['SiFe'], time_name='Age', time_unit='kyr BP',
value_name='Si/Fe', value_unit='ratio', label='SiFe')
```

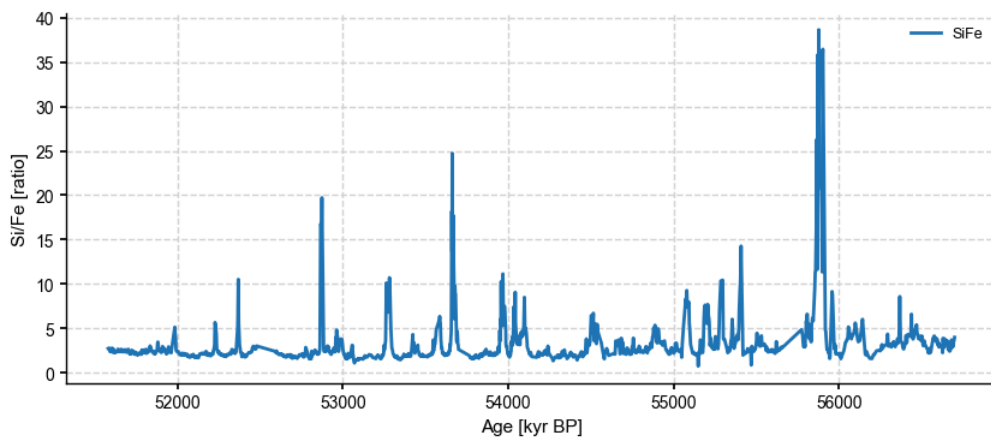
Time axis values sorted in ascending order

C:\Users\bniederbockstruck\AppData\Local\Temp\ipykernel_15572\1004109436.py:1: UserWarning: auto_time_params is not specified. Currently default behavior sets this to True, which might modify your supplied time metadata. Please set to False if you want a different behavior.

```
SiFe_ts = pyleo.Series(time=df_XRF['Age (Ma)']*1000, value=df_XRF['SiFe'], time_name='Age', time_unit='kyr BP', value_name='Si/Fe', value_unit='ratio', label='SiFe')
```

```
In [7]: SiFe_ts.plot()
```

```
Out[7]: (<Figure size 1000x400 with 1 Axes>,
<Axes: xlabel='Age [kyr BP]', ylabel='Si/Fe [ratio]'>)
```



```
In [8]: fig, ax = plt.subplots()
plt.hist(np.diff(SiFe_ts.time), bins=16)
plt.xlabel(r'$\Delta t$ (kyr)')
plt.ylabel('# occurrences')
plt.title('Distribution of age increments', weight='bold')
```

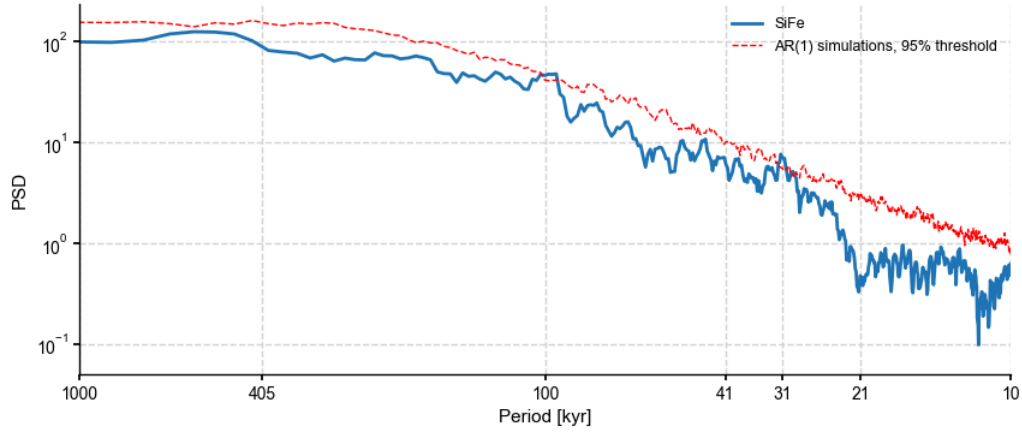
```
Out[8]: Text(0.5, 1.0, 'Distribution of age increments')
```



```

new_ticks = np.unique(np.concatenate((current_ticks, custom_ticks)))
plt.gca().set_xticks(new_ticks)
plt.gca().get_xaxis().set_major_formatter(plt.ScalarFormatter())
plt.xlim(1000, 10)
plt.show()

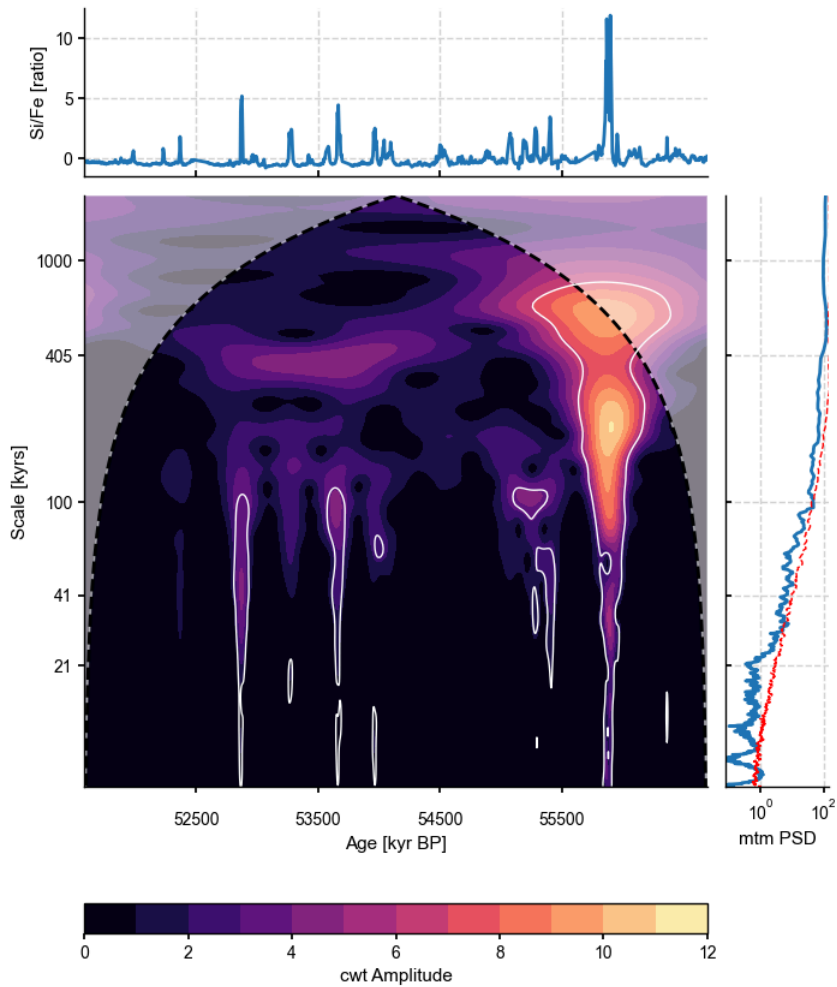
```



Wavelet analysis

```
In [21]: scal = SiFe_33.standardize().wavelet()
```

```
In [22]: scal_sig = scal.signif_test(method='ar1asym')
fig, axes_dict = SiFe_33.summary_plot(psd=psd_mtm_sig, scalogram=scal_sig)
scalogram_axis = axes_dict['scal']
# Set y-ticks
scalogram_axis.set_yticks([21, 41, 100, 405, 1000])
plt.show()
```



Pearson Correlation of XRF-derived data in Part III

Data is accessible on the USB-stick, file: Appendix_04.xlsx

```
In [2]: %matplotlib inline
import numpy as np
import matplotlib.pyplot as plt
import pandas as pd
import seaborn as sns
from scipy.cluster.hierarchy import dendrogram, linkage, fcluster, leaves_list, set_link_color_palette
from scipy import interpolate
from sklearn import preprocessing
from sklearn.decomposition import PCA
import seaborn as sns
from matplotlib.ticker import AutoMinorLocator
import matplotlib.cm as cm
```

```
In [6]: df_XRF = pd.read_excel("YOUR_PATH/Appendix_04.xlsx")
#replace with your path here
```

```
In [8]: df_data = df_XRF[['U1553splice_XRF2_10kV_Fe_Area', 'U1553splice_XRF2_10kV_Ti_Area', 'U1553splice_XRF2_10kV_Al_Area',
                        'U1553splice_XRF2_10kV_K_Area', 'U1553splice_XRF2_50kV_Ba_Area', 'U1553splice_XRF2_10kV_Si_Area',
                        'U1553splice_XRF2_10kV_Ca_Area', 'U1553splice_XRF2_30kV_Br_Area', 'SiFe', 'CaFe']]
```

```
In [10]: df_data = df_data.rename(columns={
        'U1553splice_XRF2_10kV_Fe_Area': 'Fe',
        'U1553splice_XRF2_10kV_Ti_Area': 'Ti',
        'U1553splice_XRF2_10kV_Al_Area': 'Al',
        'U1553splice_XRF2_10kV_K_Area': 'K',
        'U1553splice_XRF2_50kV_Ba_Area': 'Ba',
        'U1553splice_XRF2_10kV_Si_Area': 'Si',
        'U1553splice_XRF2_10kV_Ca_Area': 'Ca',
        'U1553splice_XRF2_30kV_Br_Area': 'Br',
    })
```

```
In [12]: df_heatmap = df_data.corr(method='pearson')
```

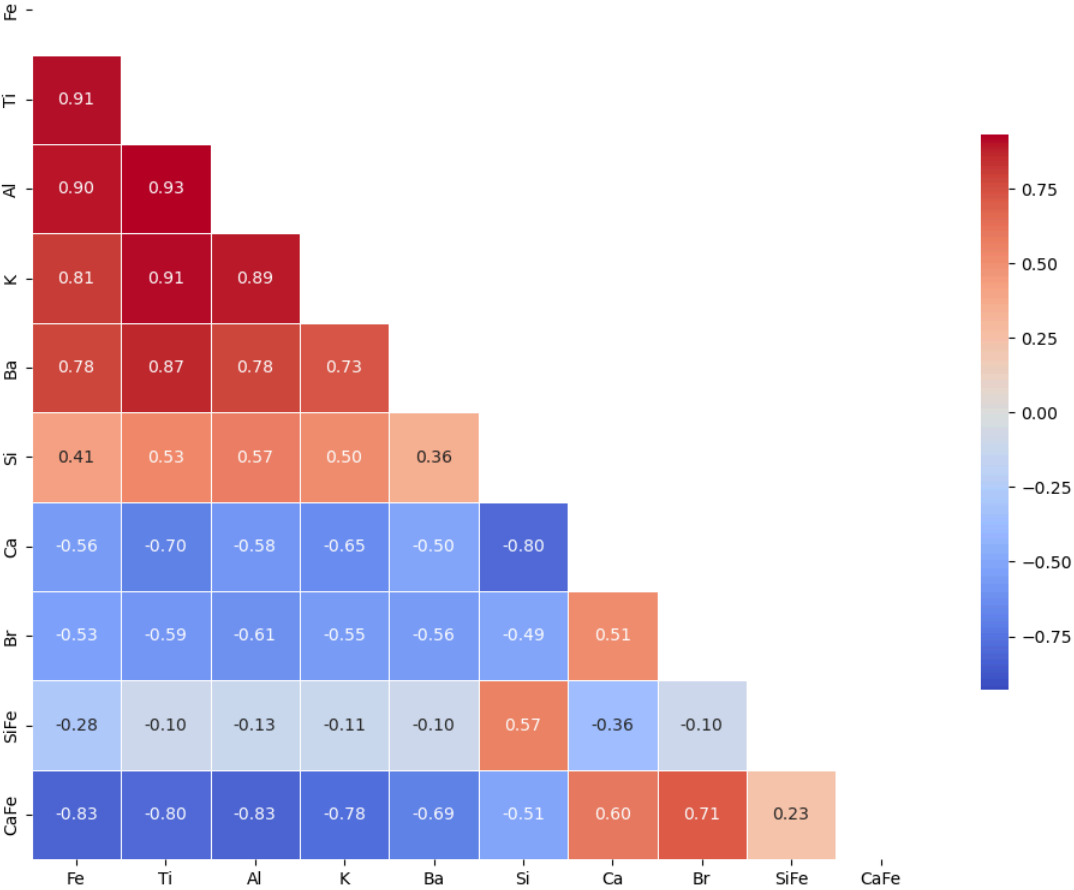
```
In [13]: df_heatmap
```

```
Out[13]:
```

	Fe	Ti	Al	K	Ba	Si	Ca	Br	SiFe	CaFe
Fe	1.000000	0.906443	0.900012	0.806403	0.781061	0.414374	-0.563966	-0.527711	-0.279825	-0.825618
Ti	0.906443	1.000000	0.925158	0.912579	0.871557	0.533587	-0.695424	-0.589151	-0.104385	-0.797618
Al	0.900012	0.925158	1.000000	0.891218	0.779011	0.569241	-0.577864	-0.608630	-0.130606	-0.825330
K	0.806403	0.912579	0.891218	1.000000	0.731708	0.503213	-0.645748	-0.554393	-0.112391	-0.775746
Ba	0.781061	0.871557	0.779011	0.731708	1.000000	0.361724	-0.497473	-0.556372	-0.098735	-0.690800
Si	0.414374	0.533587	0.569241	0.503213	0.361724	1.000000	-0.795644	-0.494557	0.565152	-0.513985
Ca	-0.563966	-0.695424	-0.577864	-0.645748	-0.497473	-0.795644	1.000000	0.511996	-0.356169	0.602088
Br	-0.527711	-0.589151	-0.608630	-0.554393	-0.556372	-0.494557	0.511996	1.000000	-0.097010	0.705627
SiFe	-0.279825	-0.104385	-0.130606	-0.112391	-0.098735	0.565152	-0.356169	-0.097010	1.000000	0.233911
CaFe	-0.825618	-0.797618	-0.825330	-0.775746	-0.690800	-0.513985	0.602088	0.705627	0.233911	1.000000

```
In [18]: plt.figure(figsize=(12, 12))
mask = np.triu(np.ones_like(df_heatmap, dtype=bool))
sns.heatmap(df_heatmap, mask=mask, annot=True, cmap='coolwarm', fmt=".2f", vmin=-0.93, vmax=0.93,
            square=True, linewidths=.5, cbar_kws={"shrink": .5})
plt.title('Heatmap of Pearson Correlation Matrix')
plt.show()
```

Heatmap of Pearson Correlation Matrix



Appendix 05:

Opal concentration (wt%) of Part III (Chapter 7). Ages after Niederbockstruck et al. (2024).

Sample ID	mid CSF (m)	mid CCSF (m)	midCCSFadj (m)	Age (Ma)	Opal (wt%)
378-U1553C-28R-1,90-91 cm	429.505	460.335	460.084	52.767	0.53
378-U1553C-28R-2,40-41 cm	430.505	461.335	460.818	52.868	8.53
378-U1553C-28R-2,50-51 cm	430.605	461.435	460.911	52.879	6.87
378-U1553C-28R-4,2-3 cm	433.105	463.935	463.935	53.242	3.24
378-U1553C-28R-4,32-33 cm	433.405	464.235	464.235	53.278	17.73
378-U1553C-28R-4,77-78 cm	433.855	464.685	464.685	53.330	0.22
378-U1553C-28R-5,1-2 cm	434.605	465.435	465.435	53.418	2.9
378-U1553C-28R-5,16-17 cm	434.755	465.585	465.585	53.436	2.2
378-U1553C-28R-5,31-32 cm	434.905	465.735	465.735	53.454	5.89
378-U1553C-28R-5,109-110 cm	435.685	466.515	466.515	53.545	0.69
378-U1553C-28R-6,9-10 cm	436.105	466.935	466.935	53.583	6.68
378-U1553C-28R-6,24-25 cm	436.255	467.085	467.085	53.597	1.8
378-U1553C-28R-6,99-100 cm	437.005	467.835	467.835	53.665	23.6
378-U1553C-28R-6,114-115 cm	437.155	467.985	467.985	53.680	5.02
378-U1553C-29R-2,29-30 cm	440.105	470.605	470.401	53.916	2.08
378-U1553C-29R-2,59-60 cm	440.405	470.905	470.744	53.950	6.06
378-U1553C-29R-2,74-75 cm	440.555	471.055	470.916	53.967	19.15
378-U1553C-29R-2,104-105 cm	440.855	471.355	471.259	54.000	2.27
378-U1553C-29R-2,119-120 cm	441.005	471.505	471.431	54.017	3.65
378-U1553C-30R-4,54-55 cm	447.605	479.185	480.004	55.630	1.32
378-U1553C-31R-1,110-111 cm	449.105	481.775	481.762	55.892	20.64
378-U1553C-31R-2,27-28 cm	449.705	482.375	482.310	55.958	19.15
378-U1553C-31R-3,56-57 cm	450.705	483.375	483.147	56.130	1.11
378-U1553D-5R-1,73-74 cm	429.235	459.555	459.555	52.691	0.86
378-U1553D-5R-2,57-58 cm	430.445	460.765	460.765	52.862	0.83
378-U1553D-5R-2,73-74 cm	430.605	460.925	460.925	52.881	0.98
378-U1553D-5R-4,100-101 cm	433.605	463.925	463.926	53.241	1.59
378-U1553D-5R-4,128-129 cm	433.885	464.205	464.197	53.273	19.81
378-U1553D-5R-5,25-26 cm	434.215	464.535	464.500	53.309	3.29
378-U1553D-5R-5,84-85 cm	434.805	465.125	465.041	53.372	7.89
378-U1553D-5R-6,23-24 cm	435.405	465.725	465.591	53.437	1.06
378-U1553D-6R-1,30-31 cm	438.605	471.125	471.028	53.978	10.6
378-U1553D-6R-1,60-61 cm	438.905	471.425	471.333	54.007	1.3
378-U1553D-6R-1,90-91 cm	439.205	471.725	471.618	54.035	5.13
378-U1553D-6R-1,120-121 cm	439.505	472.025	472.025	54.098	5.67
378-U1553D-6R-2,64-65 cm	440.405	472.925	472.925	54.271	5.6
378-U1553D-6R-5,13-14 cm	444.305	476.825	476.825	55.020	4.02
378-U1553D-6R-5,48-49 cm	444.655	477.175	477.175	55.087	9.63
378-U1553D-6R-5,103-104 cm	445.205	477.725	477.725	55.192	19.98
378-U1553D-6R-6,74-75 cm	446.405	478.925	478.925	55.423	3.92
378-U1553D-6R-7,27-28 cm	447.305	479.825	479.825	55.595	2.59

378-U1553D-7R-1,50-51 cm	448.605	481.235	481.235	55.829	2.05
378-U1553D-7R-1,115-116 cm	449.255	481.885	481.885	55.906	7.09
378-U1553D-7R-1,119-120 cm	449.295	481.925	481.925	55.911	26.06
378-U1553D-7R-2,30-31 cm	449.705	482.335	482.335	55.961	8.05
378-U1553D-7R-2,35-36 cm	449.755	482.385	482.385	55.967	4.61
378-U1553D-7R-2,60-61 cm	450.005	482.635	482.635	56.013	2.67
378-U1553D-7R-2,140-141 cm	450.805	483.435	483.435	56.196	1.43
